Developing Zwitterionic Hydrogel for Biomedical Applications

Tao Bai

A dissertation
Submitted in partial fulfillment of the
Requirements for the degree of

Doctor of Philosophy

University of Washington

2017

Reading Committee:

Shaoyi Jiang, Chair

Buddy D. Ratner

Ying Zheng

Program Authorized to Offer Degree:
Chemical Engineering

University of Washington

Abstract

Developing Zwitterionic Hydrogel for Biomedical Applications

Tao Bai
Chair of the Supervisory Committee:
Professor Shaoyi Jiang
Department of Chemical Engineering

Ultra-low fouling zwitterionic hydrogels offer unique advantages over conventional biomaterials in biomedical applications. By exclusively using zwitterionic monomer and crosslinker, pure zwitterionic hydrogels are prepared with highly tunable mechanical properties and functionalities for diverse applications. This thesis summarizes recent studies in zwitterionic hydrogels. First, we demonstrated that zwitterionic hydrogel can repair itself independent of time after damage under physiological conditions via a new mechanism, "zwitterionic fusion". Second, we explored the properties of zwitterionic hydrogels in controlling the self-renewal and differentiation of mesenchymal stem cells. Finally, we realized *ex vivo* expansion of mesenchymal stem cells and hematopoietic stem cells without differentiation in a biodegradable zwitterionic hydrogel.

Table of Contents

List of Tables

List of Figures

Acknowledgements

The author would like to thank his advisor, Professor Shaoyi Jiang for support, monetary, inspiration and funding for all studies presented here. The author also thanks all members in Prof. Jiang’s research group for their kind help and helpful discussions, Dr. Colleen Delaney and her group for collaboration and Profs. Buddy Ratner, Ying Zheng and Nathan Sniadecki for serving on the supervisory committee. The author especially thanks his family for support.

Chapter 1 Introduction

Hydrogels are crosslinked polymeric networks with high water content. They have been considered as one important form of biomaterials due to their biomimetic mechanical properties[1-3] and widely used in biomedical applications such as tissue scaffolds, medical implants, controlled drug delivery vehicles and sensors[4-7]. In the past few decades, particular interest has been given to poly(2-hydroxyethyl methacrylate) (PHEMA) and poly(ethylene glycol) (PEG) synthetic hydrogels since they are widely considered as biocompatible, and versatile for practical uses[1, 8]. Hydrogels based on hyaluronic acid, dextran, and other natural hydrophilic polymers are also fully developed for biomedical applications[9,10]. Furthermore, many promising high-strength and intelligent hydrogels are demonstrated[11-15]. However, limited nonfouling properties and/or *in vivo* stability in complex media remain as the bottleneck, hindering their applications.

Biofouling is a major cause of medical device complications and failure [16-20]. Even a minimal level of surface adhesion by undesirable proteins or other biomolecules can lead to the recognition and rejection of a device by the body's immune system or the formation of a biofilm by microorganisms, a leading cause of nosocomial infection [17, 21, 22]. Therefore, nonfouling properties are crucial for modern biomedical applications. Biomaterials that can highly resist fouling in complex media are rare. PHEMA and other natural polymers can only offer limited nonfouling properties and regarded as "low-fouling" materials. The synthetic polymer, PEG, has been regarded as the "gold standard", and has been widely used in nonfouling applications for decades [23-26]. However, PEG has been found to lose stability in biologically relevant environments, limiting its applications [27, 28]. Moreover, it has also been reported that PEG is immunogenic, [25] leading to a foreign body rejection by the host. Zwitterionic materials, such as carboxybetaine (CB), sulfobetaine (SB), and phosphorylcholine (PC), have emerged as a new class of nonfouling materials [29-35]. They have been found to not only work as an effective alternative to PEG, but also possess many distinct advantages over PEG. Poly(phosphorylcholine) (PPC) is structurally similar to lecithin, a component of cell membranes [36]. Phosphorylcholine monomers, such as 2-methacryloyloxyethyl phosphorylcholine (MPC), are used [37]. Poly(sulfobetaine) (PSB) is structurally similar to taurine or 2-aminoethane sulfonic acid. Commercially available sulfobetaine monomer, 2-(methacryloyloxy) ethyl dimethyl-(3-sulfopropyl) ammonium hydroxide, is used [38, 39].

Among zwitterionic materials, PCB is unique in several aspects [17]. First, it is structurally similar to that of glycine betaine, which is one of the compatible solutes vital to the osmotic regulation of living organisms [40, 41]. Second, it was demonstrated that PCB showed undetectable nonspecific protein adsorption (<0.3 ng cm^{-2}) in complex medias such as undiluted human serum or plasma. Third, unlike PPC and PSB, each CB monomer has one carboxyl group as a functionalizable group for the immobilization of biomolecules via simple 1-ethyl-3-(3-dimethylaminopropyl)-carbodiimide/N-hydroxysuccinimide (EDC/NHS) chemistry. Furthermore, unreacted carboxylic acids can then be easily restored to their original nonfouling form. Thus, functionalized PCB can specifically immobilize target molecules while highly resisting any other non-specific adhesion. In comparison, PEG is relatively difficult to functionalize, and unreacted functional groups (such as –COOH or –NH_2), still carry charge and remain as fouling moieties after this process [42]. Fourth, PCB is ionic and “super-hydrophilic” while PEG is non-ionic and amphiphilic [42-44]. The amphiphilicity of PEG can cause significant bioactivity loss when conjugated to a protein or destabilize self-assembled nanoparticles with hydrophobic cores. Super-hydrophilic PCB avoids interference with the hydrophobic regions of proteins or nanoparticles, solving these persistent problems. PCB is also stable in complex media and *in vivo* [45, 46]. In addition, a self-assembling monolayer (SAM) of zwitterionic molecules can stabilize nanoparticles better than that of short-chain PEG groups [47-49].

PCB hydrogels were firstly developed by crosslinking zwitterionic monomers with commercially available crosslinkers, such as N,N'-methylenebis(acrylamide) (MBAA). The use of conventional crosslinkers can inevitably introduce fouling moieties into the hydrogels, compromising their performance, particularly under complex environments. These hydrogels suffer poor mechanical strength as well [50]. PCB had to be copolymerized with PHEMA to form hydrogels with enough mechanical strength for *in vivo* tests, leading to capsule formation. Both biocompatibility and mechanical strength problems were solved with CB crosslinkers (CBX), which also contain CB units. The mechanical properties of CB hydrogels can be tuned by introducing different ratios of CBX without introducing any impurities into the hydrogels. It has been demonstrated that the incorporation of CBX does not compromise the nonfouling properties of hydrogels [45, 50]. Another interesting property of CBX is that the reactivity of its carboxyl group can be tuned by changing the carbon spacer length between the quaternary amine group and the carboxyl group [51]. As shown in Figure 1, two types of CB crosslinkers have been developed: CBX-1 has one carbon spacer while CBX-2 has two carbon spacers. Due to its pKa, CBX-1 can only be functionalized under low pH values such as 1 or 2. In comparison, CBX-2 can be functionalized under mild conditions via NHS/EDC chemistry [45, 51, 52]. CB-1 and CB-2 monomers have similar properties as their CBX counterparts in term of functionalization. Therefore, CB hydrogels can be tunable. Both mechanical and functionalizable properties can be easily tuned by changing the ratio of CB monomer (CB-1 or CB-2) to CB crosslinker (CBX-1 or CBX-2) while their nonfouling properties remain unchanged [51]. In this thesis, recent developments and biomedical applications of zwitterionic hydrogels will be discussed.

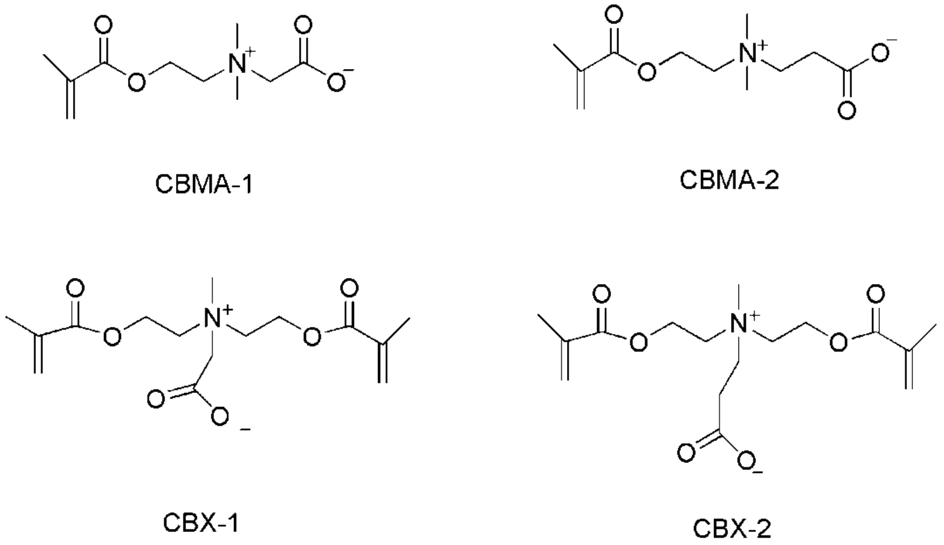

CBMA-1

CBMA-2

CBX-1

CBX-2

Figure 1.1. Chemical structures of CBMA-1 monomer and CBX-1 crosslinker (left column) and CBMA-2 monomer and CBX-2 crosslinker (right column).

References

1 Wichterle O, Lim D. Hydrophilic gels for biological use. Nature. 1960;185:117-8.

2 Peppas NA, Hilt JZ, Khademhosseini A, Langer R. Hydrogels in biology and medicine: From molecular principles to bionanotechnology. Advanced Materials. 2006;18:1345-60.

3 Benoit DSW, Schwartz MP, Durney AR, Anseth KS. Small functional groups for controlled differentiation of hydrogel-encapsulated human mesenchymal stem cells. Nature Materials. 2008;7:816-23.

4 Hoffman AS. Hydrogels for biomedical applications. Advanced Drug Delivery Reviews. 2012;64:18-23.

5 Seliktar D. Designing Cell-Compatible Hydrogels for Biomedical Applications. Science. 2012;336:1124-8.

6 Slaughter BV, Khurshid SS, Fisher OZ, Khademhosseini A, Peppas NA. Hydrogels in Regenerative Medicine. Advanced Materials. 2009;21:3307-29.

7 DeForest CA, Anseth KS. Cytocompatible click-based hydrogels with dynamically tunable properties through orthogonal photoconjugation and photocleavage reactions. Nature Chemistry. 2011;3:925-31.

8 Lin CC, Metters AT, Anseth KS. Functional PEG-peptide hydrogels to modulate local inflammation induced by the pro-inflammatory cytokine TNF alpha. Biomaterials. 2009;30:4907-14.

9 Bajaj G, Kim MR, Mohammed SI, Yeo Y. Hyaluronic acid-based hydrogel for regional delivery of paclitaxel to intraperitoneal tumors. Journal of Controlled Release. 2012;158:386-92.

10 Sun GM, Zhang XJ, Shen YI, Sebastian R, Dickinson LE, Fox-Talbot K, et al. Dextran hydrogel scaffolds enhance angiogenic responses and promote complete skin regeneration during burn wound healing. Proceedings of the National Academy of Sciences of the United States of America. 2011;108:20976-81.

11 Bai T, Zhang P, Han YJ, Liu YA, Liu WG, Zhao XL, et al. Construction of an ultrahigh strength hydrogel with excellent fatigue resistance based on strong dipole-dipole interaction. Soft Matter. 2011;7:2825-31.

12 Gong JP, Katsuyama Y, Kurokawa T, Osada Y. Double-network hydrogels with extremely high mechanical strength. Advanced Materials. 2003;15:1155-+.

13 Han YJ, Bai T, Liu Y, Zhai XY, Liu WG. Zinc Ion Uniquely Induced Triple Shape Memory Effect of Dipole-Dipole Reinforced Ultra-High Strength Hydrogels. Macromolecular Rapid Communications. 2012;33:225-31.

14 Ehrbar M, Schoenmakers R, Christen EH, Fussenegger M, Weber W. Drug-sensing hydrogels for the inducible release of biopharmaceuticals. Nature Materials. 2008;7:800-4.

15 Nath N, Chilkoti A. Creating "Smart" surfaces using stimuli responsive polymers. Advanced Materials. 2002;14:1243-+.

16 Ratner BD, Hoffman, A.S., Schoen, F.J., and Lemons, J.E. Biomaterials Science. 3nd ed: Amsterdam: Elsevier.; 2012.

17 Jiang SY, Cao ZQ. Ultralow-Fouling, Functionalizable, and Hydrolyzable Zwitterionic Materials and Their Derivatives for Biological Applications. Advanced Materials. 2010;22:920-32.

18 Langer R. Perspectives and Challenges in Tissue Engineering and Regenerative Medicine. Advanced Materials. 2009;21:3235-6.

19 Langer R, Tirrell DA. Designing materials for biology and medicine. Nature. 2004;428:487-92.

20 Anderson JM, Rodriguez A, Chang DT. Foreign body reaction to biomaterials. Seminars in Immunology. 2008;20:86-100.

21 Zhang L, Cao ZQ, Bai T, Carr L, Ella-Menye JR, Irvin C, et al. Zwitterionic hydrogels implanted in mice resist the foreign-body reaction. Nature Biotechnology. 2013;31:553-6.

22 Zhang L, Cao ZQ, Li YT, Ella-Menye JR, Bai T, Jiang SY. Softer Zwitterionic Nanogels for Longer Circulation and Lower Splenic Accumulation. ACS Nano. 2012;6:6681-6.

23 Niidome T, Yamagata M, Okamoto Y, Akiyama Y, Takahashi H, Kawano T, et al. PEG-modified gold nanorods with a stealth character for *in vivo* applications. Journal of Controlled Release. 2006;114:343-7.

24 Perrault SD, Walkey C, Jennings T, Fischer HC, Chan WCW. Mediating Tumor Targeting Efficiency of Nanoparticles Through Design. Nano Letters. 2009;9:1909-15.

25 Hu CMJ, Zhang L, Aryal S, Cheung C, Fang RH, Zhang LF. Erythrocyte membrane-camouflaged polymeric nanoparticles as a biomimetic delivery platform. Proceedings of the National Academy of Sciences of the United States of America. 2011;108:10980-5.

26 Gref R, Minamitake Y, Peracchia MT, Trubetskoy V, Torchilin V, Langer R. Biodegradable long-circulating polymeric nanospheres. Science. 1994;263:1600-3.

27 Ostuni E, Chapman RG, Holmlin RE, Takayama S, Whitesides GM. A survey of structure-property relationships of surfaces that resist the adsorption of protein. Langmuir. 2001;17:5605-20.

28 Shen MC, Martinson L, Wagner MS, Castner DG, Ratner BD, Horbett TA. PEO-like plasma polymerized tetraglyme surface interactions with leukocytes and proteins: *in vitro* and *in vivo* studies. Journal of Biomaterials Science-Polymer Edition. 2002;13:367-90.

29 Ishihara K, Ziats NP, Tierney BP, Nakabayashi N, Anderson JM. Protein adsorption from human plasma is reduced on phospholipid polymers. Journal of Biomedical Materials Research. 1991;25:1397-407.

30 Lalani R, Liu LY. Electrospun Zwitterionic Poly(Sulfobetaine Methacrylate) for Nonadherent, Superabsorbent, and Antimicrobial Wound Dressing Applications. Biomacromolecules. 2012;13:1853-63.

31 Zhang Z, Chen SF, Jiang SY. Dual-functional biomimetic materials: Nonfouling poly(carboxybetaine) with active functional groups for protein immobilization. Biomacromolecules. 2006;7:3311-5.

32 Butun V, Liu S, Weaver JVM, Bories-Azeau X, Cai Y, Armes SP. A brief review of 'schizophrenic' block copolymers. Reactive & Functional Polymers. 2006;66:157-65.

33 Li CM, Madsen J, Armes SP, Lewis AL. A new class of biochemically degradable, stimulus-responsive triblock copolymer gelators. Angewandte Chemie-International Edition. 2006;45:3510-3.

34 Lowe AB, McCormick CL. Synthesis and solution properties of zwitterionic polymers. Chemical Reviews. 2002;102:4177-89.

35 Flores JD, Xu XW, Treat NJ, McCormick CL. Reversible "Self-Locked" Micelles from a Zwitterion-Containing Triblock Copolymer. Macromolecules. 2009;42:4941-5.

36 Iwasaki Y, Ishihara K. Phosphorylcholine-containing polymers for biomedical applications. Analytical and Bioanalytical Chemistry. 2005;381:534-46.

37 Ishihara K, Goto Y, Takai M, Matsuno R, Inoue Y, Konno T. Novel polymer biomaterials and interfaces inspired from cell membrane functions. Biochimica Et Biophysica Acta-General Subjects. 2011;1810:268-75.

38 Zhang Z, Chen SF, Chang Y, Jiang SY. Surface grafted sulfobetaine polymers via atom transfer radical polymerization as superlow fouling coatings. Journal of Physical Chemistry B. 2006;110:10799-804.

39 Zhang Z, Zhang M, Chen SF, Horbetta TA, Ratner BD, Jiang SY. Blood compatibility of surfaces with superlow protein adsorption. Biomaterials. 2008;29:4285-91.

40 Nyyssola A. Dissertation for the degree of Doctor: Helsinki University of Technology 2001.

41 Ueland PM, Holm PI, Hustad S. Betaine: a key modulator of one-carbon metabolism and homocysteine status. Clin Chem Lab Med. 2005;43:1069-75.

42 Cao ZQ, Yu QM, Xue H, Cheng G, Jiang SY. Nanoparticles for Drug Delivery Prepared from Amphiphilic PLGA Zwitterionic Block Copolymers with Sharp Contrast in Polarity between Two Blocks. Angewandte Chemie-International Edition. 2010;49:3771-6.

43 Cao ZQ, Jiang SY. Super-hydrophilic zwitterionic poly(carboxybetaine) and amphiphilic non-ionic poly(ethylene glycol) for stealth nanoparticles. Nano Today. 2012;7:404-13.

44 Cao ZQ, Zhang L, Jiang SY. Superhydrophilic Zwitterionic Polymers Stabilize Liposomes. Langmuir. 2012;28:11625-32.

45 Carr LR, Zhou YB, Krause JE, Xue H, Jiang SY. Uniform zwitterionic polymer hydrogels with a nonfouling and functionalizable crosslinker using photopolymerization. Biomaterials. 2011;32:6893-9.

46 Li LY, Chen SF, Jiang SY. Protein interactions with oligo(ethylene glycol) (OEG) self-assembled monolayers: OEG stability, surface packing density and protein adsorption. Journal of Biomaterials Science-Polymer Edition. 2007;18:1415-27.

47 Choi HS, Liu W, Misra P, Tanaka E, Zimmer JP, Ipe BI, et al. Renal clearance of quantum dots. Nature Biotechnology. 2007;25:1165-70.

48 Murthy AK, Stover RJ, Hardin WG, Schramm R, Nie GD, Gourisankar S, et al. Charged Gold Nanoparticles with Essentially Zero Serum Protein Adsorption in Undiluted Fetal Bovine Serum. Journal of the American Chemical Society. 2013;135:7799-802.

49 Uyeda HT, Medintz IL, Jaiswal JK, Simon SM, Mattoussi H. Synthesis of compact multidentate ligands to prepare stable hydrophilic quantum dot fluorophores. Journal of the American Chemical Society. 2005;127:3870-8.

50 Carr LR, Xue H, Jiang SY. Functionalizable and nonfouling zwitterionic carboxybetaine hydrogels with a carboxybetaine dimethacrylate crosslinker. Biomaterials. 2011;32:961-8.

51 Carr LR, Krause JE, Ella-Menye JR, Jiang SY. Single nonfouling hydrogels with mechanical and chemical functionality gradients. Biomaterials. 2011;32:8456-61.

52 Vaisocherova H, Yang W, Zhang Z, Cao ZQ, Cheng G, Piliarik M, et al. Ultralow fouling and functionalizable surface chemistry based on a zwitterionic polymer enabling sensitive and specific protein detection in undiluted blood plasma. Analytical Chemistry. 2008;80:7894-901.

Chapter 2 Zwitterionic Fusion in Hydrogels and Spontaneous and Time-Independent Self-Healing under Physiological Conditions

The biomedical applications of current self-healing materials are largely impeded by their healing conditions, which usually require heating, UV exposure or harsh pH environments. At the same time, for very few existing spontaneously self-healing materials, healing can only be achieved immediately after rupture occurs. Here, we developed a spontaneously healing material, driven by a new mechanism, "zwitterionic fusion", which is repairable independent of time after damage under physiological conditions. We also tested the anti-fatigue property of this zwitterionic hydrogel. Furthermore, we utilized this zwitterionic fusion to link different cell-hydrogel constructs together.

2.1 Introduction

Self-healing materials can eliminate damage or fatigue during normal utilization, thus holding promise for enhanced lifetimes and enduring strength.[1-4] They have been demonstrated by exploiting polymer-clay interactions,[5] phase segregation,[6] redox reactions,[7] photo-reactive groups,[8, 9] and microvascular networks.[10-12] Currently, few materials have been reported to effectively and spontaneously repair themselves under physiological conditions after damage. For these scarce existing spontaneously self-healing materials, healing can only be achieved either immediately after rupture occurs[5], [13-16] (e.g. in less than one minute) or at low pH values.[17, 18] Materials capable of spontaneous self-healing are typically constructed from either single-charged or non-ionic amphiphilic components. Their healing abilities rely on hydrogen-bond donors/acceptors[5, 13, 17] or hydrophobic interactions.[14] For example, Phadke et al.[17] recently developed a self-healing single-charged hydrogel. However, the driving force for this reconstruction is superseded by electrostatic repulsion among the ionized carboxyl groups under physiological pH conditions: this problem is depicted in Fig. 1a. As a result, these single-charged hydrogels cannot undergo healing unless the pH is reduced to as low as 3, which limits their applications in biologically relevant systems. Another type of self-healing material is non-ionic and amphiphilic, with an outermost layer assembled from hydrophobic components in contact with air. When damage occurs, hydrophilic healable functional groups are initially exposed to air. In order to minimize the surface free energy of the system, hydrophobic components then move to the surface and bury the hydrophilic groups inside over time—the so-called "hydrophobic regeneration" process[19, 20] (Fig. 1a). However, interactions among these hydrophobic components are not strong enough to mediate the movement of polymer chains across a rupture junction for further healing. Consequently, the newly formed hydrophobic outer layer prevents broken pieces from fusing. For example, Wang et al.[5] designed a spontaneously self-healing hydrogel based on amphiphilic polyethylene glycol (PEG) dendrimers. As they pointed out, deposited water droplets spread over a cut surface immediately but beaded on an uncut surface. Therefore, fusion did not take place unless the blocks were cut to obtain fresh surfaces. Moreover, if the blocks were cut but left alone for more than a minute, they also lost their adhering ability. This time-dependent self-healing behavior is attributed to surface reconstruction resulting from the amphiphilic nature of current self-healing materials. In order to achieve time-independent self-healing, this surface reconstruction must be avoided.

In sharp contrast to the amphiphilic character of most materials, the superhydrophilic nature of zwitterionic materials has made them uniquely suited for protein protection,[21] nanoparticle formation,[22] and nonfouling surface coatings.[23] In this work, we endeavored to prevent surface reconstruction by utilizing one zwitterionic material, carboxybetaine acrylamide (AAZ). For control materials, we used anionic 7-acrylamidoheptanoate acid (AAS, Fig. 1b), and non-ionic hydroxyhexylacrylamide (AAN, Fig. 1b), both possessing backbone and side chain lengths equivalent to AAZ. Hydrogels based on these materials were synthesized and their healing properties demonstrated.

2.2 Experimental Section

2.2.1 Materials

Ammonium persulfate (APS) and N,N,N',N'-Tetramethylethylenediamine (TEMED) was purchased from Bio-Rad Laboratories (Hercules, CA). Dulbecco's Modified Eagle Medium (DMEM), fetal bovine serum (FBS), nonessential amino acids, and penicillin-streptomycin were purchased from Invitrogen Corp (Carlsbad, CA). Human fibronectin was purchased from Alfa Aesar. COS-7 and NIH/3T3 cells were purchased from the American Tissue Culture Collection (Manassas, VA). Ethanol was purchased from Decon Laboratories (King of Prussia, PA). Tetrahydrofuran (THF) was purchased from Mallinckrodt Chemicals (Phillipsburg, NJ). All water used had been purified to 18.2mU with a Millipore Simplicity water purification system. AAZ and carboxybetaine methacrylate (MAZ) monomers were prepared following a previously published method.[24] AAS and AAN were synthesized in a similar way as reported,[17] with the process briefly shown in Fig. 2.7.

2.2.2 Preparation of hydrogels

An appropriate amount of AAZ, MAZ, AAS, AAN monomer, APS initiator (2% w/w, relative to the total monomer mass), and TEMED accelerator (10% w/w, relative to total APS mass) were dissolved in water at a fixed concentration of 0.1M. The mixture was cast into disc molds (diameter 12.6 mm, thickness 10 mm) or tubular molds (inner diameter 10 mm, length 12 mm), and the polymerization was carried out for 24 hours at room temperature. Zwitterionic (AAZ), single-charged (AAS) and non-ionic (AAN) hydrogels were synthesized. All the hydrogels were equilibrated in PBS for at least three days prior to tests. Solutions were refreshed every 3 hours.

For all chemically crosslinked hydrogels, the monomer concentration is fixed at 0.1M and PBS will be used as polymerization solution. An appropriate amount of AAZ monomer, N,N'-Methylenebisacrylamide crosslinker (MBAA), APS initiator (2% w/w, relative to the total monomer mass), and TEMED accelerator (10% w/w, relative to total APS mass) were dissolved. The mixture was cast into disc molds (diameter 12.6 mm, thickness 10 mm) or tubular molds (inner diameter 10 mm, length 12 mm), and the polymerization was carried out for 24 hours at room temperature. Zwitterionic (AAZ-x) hydrogels and non-ionic (AAN-x) hydrogels were synthesized, where x is the concentration of the crosslinker. (a: 0.5mM; b: 5mM; c: 50mM; d: 125mM). Unless specifically noted, all the hydrogels were equilibrated in PBS for at least three days prior to experiments. PBS was refreshed every three hours.

2.2.3 Dynamic equilibrium water content (EWC) test in air

The AAZ, AAN and AAS hydrogels were left in air for different times (up to 24 h) before testing. The EWCs of the hydrogels were measured using a gravimetric method. The samples were immersed in water (pH=7.4) for at least 24 h and then taken out, blotted with wet filter paper to remove water on the surface, and weighed on a microbalance. The EWC was defined as: $m_{eq}=(m_{wet}-m_{dry})/m_{wet}\times 100\%$, Where m_{wet} and m_{dry} denote the wet weight and dry weight of hydrogel, respectively. The average values of three measurements were taken for each sample.

2.2.4 Measurement of mechanical properties

Dynamic viscoelasticity was measured with a Kinexus Pro rheometer (Malvern Instruments Ltd) using parallel plates of 40-mm diameter and a plate-to-plate distance of 900µm. The frequency-sweep spectra were recorded in a constant-strain (10%) mode over the frequency range of 0.1-100 rad/s at 25 ºC. The time-sweep spectra were recorded at a constant-strain (10%) mode and constant frequency of 10 rad/s over time at 25 ºC. The strain-sweep spectra were recorded in a constant frequency of 10 rad/s over the strain range of 0.01-10 at 25 ºC. The temperature dependence of the storage and loss moduli was determined by oscillatory shear deformation over a temperature range of 20 ºC to 50 ºC.

The tensile stresses of hydrogels were measured on an Instron 5543 Amechanical tester (Instron Corp., Norwood, MA) at room temperature. Hydrogels were cut into rectangular pieces with dimensions of 20 mm×2 mm×0.50 mm for tensile strength tests. Crosshead speed was set at 100 mm/min, and at least three specimens were tested for each hydrogel sample.

Cylindrical hydrogel samples (8 mm in diameter and 10 mm thick) were used for the cyclic compression test. We performed 10,000 cycles with 45 % displacement of gel height at a frequency of 0.5 Hz in a 25 ºC water bath. The compression modulus was obtained from the linear regression of the stress-strain curve.

2.2.5 Quantification of the self-healing efficiency

We have demonstrated the viability of the AAZ hydrogel platform for the formation of a one-piece integrated block hydrogel from original individual hydrogels with differing mechanical properties. Then, we utilized tensile tests to quantify the efficiency of the self-healing effect. Using a razor blade, one AAZ sample was cut into two completely separate pieces and these cut parts were then kept apart for different times before being gently rejoined. The fusion process happened immediately upon rejoining. After remaining under ambient conditions for 24 hours without additional treatment, each sample was subjected to a tensile test. The tensile strength and modulus of the mended samples were recorded.

2.2.6 Cell adhesion assay

Three AAZ hydrogel disks of 0.5 cm diameter (0.5 mm thickness when cast) were placed individually into the wells of a 48-well plate with PBS. To sterilize the hydrogels, they were irradiated with UV light for 30 min and refrigerated overnight in 1x penicillin-streptomycin. COS-7 and NIH/3T3 cells were seeded onto the hydrogels at a concentration of 10^4 cells/ml in supplemented DMEM. Cells were allowed to grow for 24 h at 37°C, 5% CO_2, and 100% humidity, after which time the hydrogels were photographed at 10x magnification on a Nikon Eclipse TE2000-U microscope.

2.2.7 Cell encapsulation assay

For 3D cell-hydrogel constructs, variable amounts of COS-7 or NIH/3T3 cells were mixed and suspended inside a PBS solution of monomers as described in the manuscript. After adding initiators, the solution was allowed to polymerize at 37°C for 10min. The cell-encapsulated AAZ hydrogels were cultured in medium. The viability of encapsulated cells was examined by using a commercial LIVE/DEAD assay kit (Invitrogen).

2.2.8 Quantification of the hydration free energy of AAZ, AAS and AAN

Molecular simulations were employed to calculate the hydration free energy of AAZ, AAS and AAN. The initial simulation system was a periodic water box (initial size: 2.7 × 2.7 × 2.7 nm) containing one solute molecule and certain number of water molecules with the density as $1 g/cm^3$. The potential energy of intermolecular interactions is calculated as a combination of a Lennard−Jones (L-J) 12−6 potential and a Coulombic potential, as shown in Equation 1:

$$U_{ij} = 4\varepsilon_{ij}\left[\left(\frac{\sigma_{ij}}{r_{ij}}\right)^{12} - \left(\frac{\sigma_{ij}}{r_{ij}}\right)^{6}\right] + \frac{q_i q_j}{r_{ij}} \qquad (1)$$

The force field parameters for AA and ACA were obtained from the OPLSAA force field. We employed the SPC/E model[25] for water molecules in this work. Long-range electrostatic interactions were computed with the particle mesh Ewald method with periodic boundary conditions in all three dimensions and the short-range van der Waals interactions were calculated with a cutoff distance of 1.0 nm.

For each system, an energy minimization and a 10.0 ns molecular dynamics (MD) simulation with an integral step of 1.0 fs in NPT (T=300 K, P=100 bar) ensemble were performed for equilibrium. The system was maintained at 298 K (0.1 ps time constant) and 100.0 KPa with the Berendsen algorithm. For each system, the equilibrated configurations from the 5.0, 7.5 and 10 ns were used for the calculation of hydration free energy.

Hydration free energies of AAZ, AAS and AAN were calculated with the free energy perturbation (FEP) method, which mimics the reversible process of dehydration process. The negative of the free energy change of this process is the hydration free energy. As shown in Equation 2, we change the interaction energy between the solute molecule and water molecules, including the van der Waals interaction energy and electrostatic interaction energy, from the normal values to zero gradually as λ changes from zero to 1.

$$U(\lambda) = 4\varepsilon_{ij}(1-\lambda)\left[\left(\frac{\sigma_{ij}}{r_{ij}}\right)^{12} - \left(\frac{\sigma_{ij}}{r_{ij}}\right)^{6}\right] + \frac{(1-\lambda)q_i q_j}{r_{ij}} \qquad (2)$$

This interaction change causes the potential energy of the system to vary gradually from UA(λ =0) to UB(λ =1). λ should decrease small enough in every step to preserve reversibility. In this work, we divided λ into 20 intervals from zero to one evenly. For every λ_{n+1}, a 1000 ps MD simulation with 1fs as the integral step was carried out with the initial structure obtained from the final structure of MD simulation of λ_n. The potential energy is the average of the last 500 ps MD simulations. Three independent FEP calculations with different initial configurations were carried out for each molecule. All the MD simulations and FEP calculations in this work were carried out with Gromacs 4.5.4.26

2.3 Results and Discussion

Physically crosslinked AAZ hydrogels were synthesized as described in the Methods. The samples presented in this report contain a fixed monomer concentration of 25% and were dyed with different colors for easy inspection (Fig. 1d). As illustrated in Fig. 1c, by gently bringing the original surfaces of an AAZ hydrogel together without adding any healing agents or external energy, we observed excellent fusion between hydrogel blocks (Fig. 1e). In order to demonstrate the effectiveness of zwitterionic fusion, we stretched and bent the block hydrogel. As shown, it can withstand a rather large deformation of ~300% (Fig. 1f) and bending does not tear apart the joined connections (Fig. 1g).

As presented in Fig. 2.6, superhydrophilic AAZ is particularly hygroscopic, adsorbing water from the air to form droplets in a very short time. We further quantified the hydration free energy of AAZ using the free energy perturbation (FEP) method, which mimics the reversible dehydration process as described above. In this work, the simulation results show the hydration free energy of AAZ (-404.0±9.9 KJ/mol) is much lower than AAS (-256±4 KJ/mol) and AAN (-18.53±2 KJ/mol), indicating that the zwitterionic AAZ can be hydrated much more easily than single-charged and non-ionic materials. Therefore, in contrast to amphiphilic materials, it is expected that AAZ moieties surround themselves with a compact hydration layer, shielding them from direct contact with air. As a result, surface reconstruction can be effectively avoided by using a single superhydrophilic material. The dynamic equilibrium water content (EWC) of AAZ, AAN and AAS hydrogels can be found in Fig. 2.8, where the EWC of an AAZ hydrogel in air does not change with time. It is expected that, contrary to single-charged or amphiphilic materials, superhydrophilic AAZ hydrogels respond differently upon damage due to a unique process of zwitterionic fusion. As illustrated in Fig. 1a, after damage, the hydrophilic functional groups in AAZ hydrogels will remain exposed to the air without surface reconstruction due to the stable hydration layer. Consequently, when two gel surfaces are brought into contact, regardless of whether they have been freshly cut, positively and negatively charged groups in the zwitterionic material will easily fuse across the boundary through electrostatic attraction and form zwitterionic pairs (Fig. 1c). This zwitterionic fusion can thus reconnect separate pieces to form one integrated material, avoiding the electrostatic repulsion experienced by single-charged hydrogels. AAZ hydrogels also exhibit excellent rheological stability under various rheological tests; these results can be found in Fig. 2.9-2.10.

Because the formation of an AAZ hydrogel is based on reversible interactions, it should exhibit self-healing properties by virtue of dynamic bond formation. Here, we utilized step-strain measurements to conduct a break test of the AAZ hydrogel. When conducting a strain sweep on an AAZ hydrogel from a small to a large strain, as presented in Fig. 2a, G' is larger than G" under 100% strain, suggesting the formation of a freestanding hydrogel. Additionally, G' and G" were observed to remain constant from 0%-30% strain, reflecting that no apparent damage was conferred to the AAZ hydrogel within that range. We observed that the values of G' and G" decayed sharply when the strain increased above 50%, suggesting plastic deformation due to dislocation and cutoff of polymer chains under large strains. The relative positions of G' and G" inverted when the strain grew larger than 300%, showing that the AAZ hydrogel can revert to a sol state under higher strain. We also conducted a cyclic test on the AAZ hydrogel by toggling strain between 1% and 1,000%. As presented in Fig. 2b, when reverting from 1,000% strain back to 1%, the values of G' and G" were able to recover to their initial state in 100 seconds. Over the time scale we observed, this recovery behavior was reproducible for cycles. This quick sol-gel transformation is due to the topological structure built by forming dynamic physical interactions under small strain. Then, under large strain, the severing of these physical interactions absorbs energy before chemical bonds break, leaving less permanent damage to the hydrogel. As a result, when the strain recovered to 1%, the secondary interactions re-formed on-site and restored the hydrogel to its original state.

Based on the superhydrophilic nature of AAZ discussed above and illustrated in Fig. 1a, we expected AAZ hydrogels to exhibit spontaneous self-healing independent of time after damage or cutting. In order to investigate this further, we measured the tensile strength of the healed AAZ hydrogel. Cut samples were kept apart in PBS for different waiting times before they were brought back into contact. After the cut hydrogel pieces were linked together, the healed samples were left for 24 hours prior to tensile tests. The results were compared with those from both an uncut sample and a healed sample whose separate parts were brought into contact immediately after being cut. As presented in Fig. 2c, the tensile strength of the healed samples varied minimally over the time scale we observed, even though the pieces were kept apart for up to 24 hours before being rejoined. Modulus changes showed similar trends, as shown in Fig. 2d. In this work, we also investigated fused hydrogels based on another zwitterionic material, carboxybetaine methacrylate (MAZ). Results (Fig. 2.11) show the time-independent self-healing behavior of MAZ and the importance of zwitterionic fusion.

In contrast to the time-independent healing behavior of the AAZ hydrogel, cut AAS and AAN hydrogels performed differently upon rejoining. As shown in Fig. 2c-d, due to the electronic repulsion between the charged carboxyl groups, cut AAS hydrogels could not be healed under physiological pH. For the non-ionic and amphiphilic hydrogel AAN, even though they exhibited some self-healing property with freshly cut surfaces, increasing the waiting time dramatically compromised their healing efficiency. As shown in Fig. 2c-d, the healing efficiency of an AAN hydrogel decreased almost 90% even though the waiting time was increased by only 1 min, and it completely lost its healing capacity when the waiting time was prolonged to 60 min.

In order to understand the time-independent healing behavior further, we tested changes in hydrophilicity at the break point. Here, we measured the contact angle (θ) of water on the cut surface of the superhydrophilic AAZ hydrogel at different times after damage (Fig. 2e), with the non-ionic and amphiphilic AAN hydrogel used for comparison. As shown in Fig. 2e, the contact angle θ changes as a function of time after the gel is cut. For the amphiphilic AAN hydrogel, θ increased significantly after cutting and the entire "hydrophobic regeneration" process was accomplished in 20 min. However, for the AAZ hydrogel, θ at the cut interface increased only slightly during the entire time range. We also compared the morphology of water droplets on the freshly cut surface with those on the uncut surface. As seen in Fig. 2f (i, ii), the droplet morphology on the AAZ hydrogel varies minimally between the uncut and freshly cut surface. In contrast, the uncut surface (Fig. 2f (iii)) of AAN is more hydrophobic than its freshly cut surface (Fig. 2f (iv)). This supports the expectation that hydrophobic surface regeneration can be effectively avoided by constructing the hydrogel from only one superhydrophilic component, AAZ. This allows the aforementioned zwitterionic fusion to occur across the interface and fuse hydrogels at any time without the need for external energy or regeneration agents.

It is generally difficult for chemically crosslinked hydrogels to heal themselves due to their fixed backbones. Here, we endeavored to demonstrate the effect of chemical crosslinkers on the healing behavior of zwitterionic AAZ hydrogels, using MBAA as a model crosslinker. Non-ionic AAN hydrogels were used as a control. When the hydrogel system was augmented with MBAA, new nomenclature was used as described below. The crosslinker concentrations were chosen as 0.5mM (AAZ/N-a), 5mM (AAZ/N-b), 50mM (AAZ/N-c), and 125mM (AAZ/N-d, maximum solubility of MBAA in PBS). As presented in Fig. 3a-b, the introduction of MBAA into polymeric networks significantly increases the mechanical strength of AAZ hydrogels. While most chemically crosslinked hydrogels lose their healing capacity due to the limited chain mobility, we found the MBAA-crosslinked AAZ hydrogels to behave differently. As seen in Fig. 3c, the healing efficiency of a non-ionic AAN hydrogel decreased significantly from 76.3% to 5.8% when 0.5mM MBAA was added, and its self-healing capacity was completely lost when the crosslinker content reached 5mM. In contrast, compared with a physically crosslinked AAZ hydrogel, the healing efficiency of AAZ-a was reduced by only 1.5% when 0.5mM MBAA was added. Moreover, even though the crosslinker concentration increased ten-fold, its healing efficiency decreased only 5.1% from AAZ-a to AAZ-b. We believe the zwitterionic nature of AAZ is able to compensate for the limited chain mobility. Similar to magnetic interaction, the zwitterionic fusion does not require the direct molecular contact needed for hydrophobic interactions14 and the formation of covalent bonds.27-29 Additionally, the superhydrophilic long pendant side chains of AAZ play an important role in healing these hydrogels. Unlike hydrophobic or amphiphilic moieties, the hydrophilic zwitterionic moieties do not aggregate in aqueous solution. With moderate crosslinker content, even though the backbones are fixed by the crosslinker, the flexible zwitterionic side chains are still able to bridge the hydrogel boundaries and form associations with their counterparts. The mobility of the pendant chains can be limited with high crosslinker content. As presented in Fig. 3c, the healing efficiency decreased to 55.1% when the crosslinker content reached 50mM, and healing capability was lost when the crosslinker content reached 125mM.

Like physically crosslinked AAZ hydrogels, the healing efficiency of the chemically crosslinked samples is also independent of the separation time. As presented in Fig. 3d, even though the healing efficiency decreased with high crosslinker content, it did not change with a greater separation time. The superhydrophilic nature of AAZ can still avoid surface regeneration and enable time-independent healing behavior when chemical crosslinker is present. Due to the excellent healing capability of the chemically crosslinked AAZ hydrogels, we expected they would be able to resist fatigue under cyclic loading and unloading. In order to prevent water loss in the anti-fatigue test, we conducted 10,000 cycles of continuous compression loading and unloading in a water bath.30 Taking mechanical properties and healing efficiency into account, AAZ-b hydrogels were used. As presented in Fig. 3e-f, the cyclic force curves overlap very well and no significant difference was observed between the moduli of selected cycles. Based on our discussion above, these excellent anti-fatigue properties can be attributed to zwitterionic fusion in the AAZ hydrogels. When loaded, the zwitterionic interactions break prior to the breaking of chemical bonds, resulting in the hysteresis loop in Fig. 3e. When the load is removed, zwitterionic fusion allows these interactions to be re-formed on-site and the mechanical properties are recovered.

We further evaluated whether the zwitterionic fusion process is able to mediate cell patterning by linking different cell-hydrogel constructs together under physiological conditions. As we have reported previously, zwitterionic hydrogels show a remarkable capacity for resisting non-specific biofouling.31-33 Here, COS-7 and NIH/3T3 cells were seeded onto antibiotic-sterilized AAZ hydrogels and human fibronectin (FNT) functionalized32, 34 AAZ hydrogels. After incubating for three days, as presented in Fig. 4, both COS-7 and NIH/3T3 cells were able to grow on the surface of FNT-functionalized AAZ hydrogels, while non-functionalized AAZ hydrogels did not support any cell adhesion. Notably, cells grown on the FNT-functionalized AAZ hydrogels were prone to attain a round rather than a spread shape, since the nonfouling background prevented most non-specific binding. To demonstrate the zwitterionic fusion process, a non-functionalized AAZ hydrogel section was brought into contact with a piece of FNT-functionalized AAZ. After 24 hours of room-temperature healing, COS-7 cells were seeded onto the block hydrogel and cell adhesion was observed after another 24-hour growth period, as depicted in Fig. 5a. One can see that COS-7 cells did not adhere to the non-functionalized AAZ hydrogel portion (bottom), while the functionalized portion (top) was wholly covered with COS-7 cells. A quantitative description of the adhered cells can be found in Fig. 5b, which shows a significantly heterogeneous cell distribution.

We have demonstrated above that the self-healing process induced by zwitterionic fusion does not require an external stimulus such as heat, chemical reagents, harsh pH conditions, or UV exposure. One could thus envision using these materials to assemble cell-gel constructs and build hierarchically structured tissues. Therefore, we further examined the fusion and biocompatibility of zwitterionic hydrogels containing cells. We first encapsulated NIH/3T3 and COS-7 cells in an AAZ hydrogel and measured their viability with a LIVE/DEAD assay after culture in standard growth medium. As presented in Fig. 5c, the AAZ hydrogel was able to maintain full viability of the encapsulated cells. We then proceeded to examine the cell viability in fused zwitterionic hydrogels containing cells. In order to distinguish between different hydrogel segments, we seeded COS-7 cells into AAZ hydrogels at densities of 10^5 or 10^6 cells/mL. After 3 days of culture, we removed two portions of AAZ hydrogels with different seeding densities from the growth medium, connected the pieces for 5 minutes to initialize the healing process, and placed them back into the medium for another 24 hours. When the fusion process completed, we cut out a section around the connection area and used the LIVE/DEAD assay to evaluate cell viability in this region. As seen in Fig. 5d, the cell density is noticeably higher in the left portion than in the right portion. It is noteworthy that zwitterionic fusion did not cause significant loss of cell viability, which is of great concern in other self-healing systems requiring heat, toxic chemicals, harsh pH conditions, or UV exposure.

2.4 Conclusions

In summary, we herein report a unique single-component zwitterionic hydrogel with a capability for spontaneous healing under physiological conditions without the need for additional healing reagents or the input of external energy. This hydrogel can be physically crosslinked via electrostatic interactions among zwitterionic moieties, a process we refer to as zwitterionic fusion. Zwitterionic fusion resulting from the unique nature of AAZ endows the hydrogel with time-independent healing behavior: increasing the separation time of cut fragments does not compromise healing efficiency even in chemically crosslinked samples. Furthermore, distinct from most self-healing systems, we demonstrate that this zwitterionic fusion enables the connection of different cell-hydrogel constructs without compromising cell viability.

Reference:

1 Hager MD, Greil P, Leyens C, van der Zwaag S, Schubert US. Self-healing materials. Adv Mater 2010;22:5424-30.

2 Wu DY, Meure S, Solomon D. Self-healing polymeric materials: A review of recent developments. Prog Polym Sci 2008;33:479-522.

3 Guimard NK, Oehlenschlaeger KK, Zhou J, Hilf S, Schmidt FG, Barner-Kowollik C. Current trends in the field of self-healing materials. Macromol Chem Phys 2012;213:131-43.

4 Sun J-Y, Zhao X, Illeperuma WRK, Chaudhuri O, Oh KH, Mooney DJ, et al. Highly stretchable and tough hydrogels. Nature 2012;489:133-6.

5 Wang Q, Mynar JL, Yoshida M, Lee E, Lee M, Okuro K, et al. High-water-content mouldable hydrogels by mixing clay and a dendritic molecular binder. Nature 2010;463:339-43.

6 Sivakova S, Bohnsack DA, Mackay ME, Suwanmala P, Rowan SJ. Utilization of a combination of weak hydrogen-bonding interactions and phase segregation to yield highly thermosensitive supramolecular polymers. J Am Chem Soc 2005;127:18202-11.

7 Nakahata M, Takashima Y, Yamaguchi H, Harada A. Redox-responsive self-healing materials formed from host-guest polymers. Nat Commun 2011;2.

8 Burnworth M, Tang LM, Kumpfer JR, Duncan AJ, Beyer FL, Fiore GL, et al. Optically healable supramolecular polymers. Nature 2011;472:334-U230.

9 Froimowicz P, Frey H, Landfester K. Towards the Generation of self-healing materials by means of a reversible photo-induced approach. Macromol Rapid Commun 2011;32:468-73.

10 Toohey KS, Sottos NR, Lewis JA, Moore JS, White SR. Self-healing materials with microvascular networks. Nat Mater 2007;6:581-5.

11 Hamilton AR, Sottos NR, White SR. Self-healing of internal damage in synthetic vascular materials. Adv Mater 2010;22:5159-63.

12 Cho SH, Andersson HM, White SR, Sottos NR, Braun PV. Polydimethylsiloxane-based self-healing materials. Adv Mater 2006;18:997-1000.

13 Cordier P, Tournilhac F, Soulie-Ziakovic C, Leibler L. Self-healing and thermoreversible rubber from supramolecular assembly. Nature 2008;451:977-80.

14 Chen YL, Kushner AM, Williams GA, Guan ZB. Multiphase design of autonomic self-healing thermoplastic elastomers. Nat Chem 2012;4:467-72.

15 Zhang H, Xia H, Zhao Y. Poly(vinyl alcohol) hydrogel can autonomously self-heal. Acs Macro Letters 2012;1:1233-6.

16 Lin L-J, Larsson M, Liu D-M. A novel dual-structure, self-healable, polysaccharide based hybrid nanogel for biomedical uses. Soft Matter 2011;7:5816-25.

17 Phadke A, Zhang C, Arman B, Hsu CC, Mashelkar RA, Lele AK, et al. Rapid self-healing hydrogels. Proc Natl Acad Sci USA 2012;109:4383-8.

18 Holten-Andersen N, Harrington MJ, Birkedal H, Lee BP, Messersmith PB, Lee KYC, et al. pH-induced metal-ligand cross-links inspired by mussel yield self-healing polymer networks with near-covalent elastic moduli. Proc Natl Acad Sci USA 2011;108:2651-5.

19 Yasuda T, Okuno T, Yasuda H. Contact-angle of water on polymer surfaces. Langmuir 1994;10:2435-9.

20 Bodas D, Khan-Malek C. Hydrophilization and hydrophobic recovery of PDMS by oxygen plasma and chemical treatment—An SEM investigation. Sensors and Actuators B: Chemical 2007;123:368-73.

21 Keefe AJ, Jiang S. Poly(zwitterionic)protein conjugates offer increased stability without sacrificing binding affinity or bioactivity. Nat Chem 2012;4:60-4.

22 Cao Z, Yu Q, Xue H, Cheng G, Jiang S. Nanoparticles for drug delivery prepared from amphiphilic PLGA zwitterionic block copolymers with sharp contrast in polarity between two blocks. Angew Chem Int Ed 2010;49:3771-6.

23 Zhang L, Cao Z, Bai T, Carr L, Ella-Menye J-R, Irvin C, et al. Zwitterionic hydrogels implanted in mice resist the foreign-body reaction. Nat Biotech 2013;31:553-6.

24 Zhang Z, Chao T, Chen SF, Jiang SY. Superlow fouling sulfobetaine and carboxybetaine polymers on glass slides. Langmuir 2006;22:10072-7.

25 Berendsen HJC, Grigera JR, Straatsma TP. The missing term in effective pair potentials. J. Phys Chem 1987;91:6269-71.

26 Van der Spoel D, Lindahl E, Hess B, Groenhof G, Mark AE, Berendsen HJC. GROMACS: Fast, flexible, and free. J Comput Chem 2005;26:1701-18.

27 Gragert M, Schunack M, Binder WH. Azide/Alkyne-“Click”-Reactions of encapsulated reagents: Toward Self-Healing Materials. Macromol Rapid Commun 2011;32:419-25.

28 Kolmakov GV, Matyjaszewski K, Balazs AC. Harnessing labile bonds between nanogel particles to create self-healing materials. ACS nano 2009;3:885-92.

29 Canadell J, Goossens H, Klumperman B. Self-healing materials based on disulfide links. Macromolecules 2011;44:2536-41.

30 Bai T, Zhang P, Han YJ, Liu YA, Liu WG, Zhao XL, et al. Construction of an ultrahigh strength hydrogel with excellent fatigue resistance based on strong dipole-dipole interaction. Soft Matter 2011;7:2825-31.

31 Carr LR, Krause JE, Ella-Menye JR, Jiang SY. Single nonfouling hydrogels with mechanical and chemical functionality gradients. Biomaterials 2011;32:8456-61.

32 Carr LR, Xue H, Jiang SY. Functionalizable and nonfouling zwitterionic carboxybetaine hydrogels with a carboxybetaine dimethacrylate crosslinker. Biomaterials 2011;32:961-8.

33 Carr LR, Zhou YB, Krause JE, Xue H, Jiang SY. Uniform zwitterionic polymer hydrogels with a nonfouling and functionalizable crosslinker using photopolymerization. Biomaterials 2011;32:6893-9.

34 Yang W, Bai T, Carr LR, Keefe AJ, Xu J, Xue H, et al. The effect of lightly crosslinked poly(carboxybetaine) hydrogel coating on the performance of sensors in whole blood. Biomaterials 2012;33:7945-51.

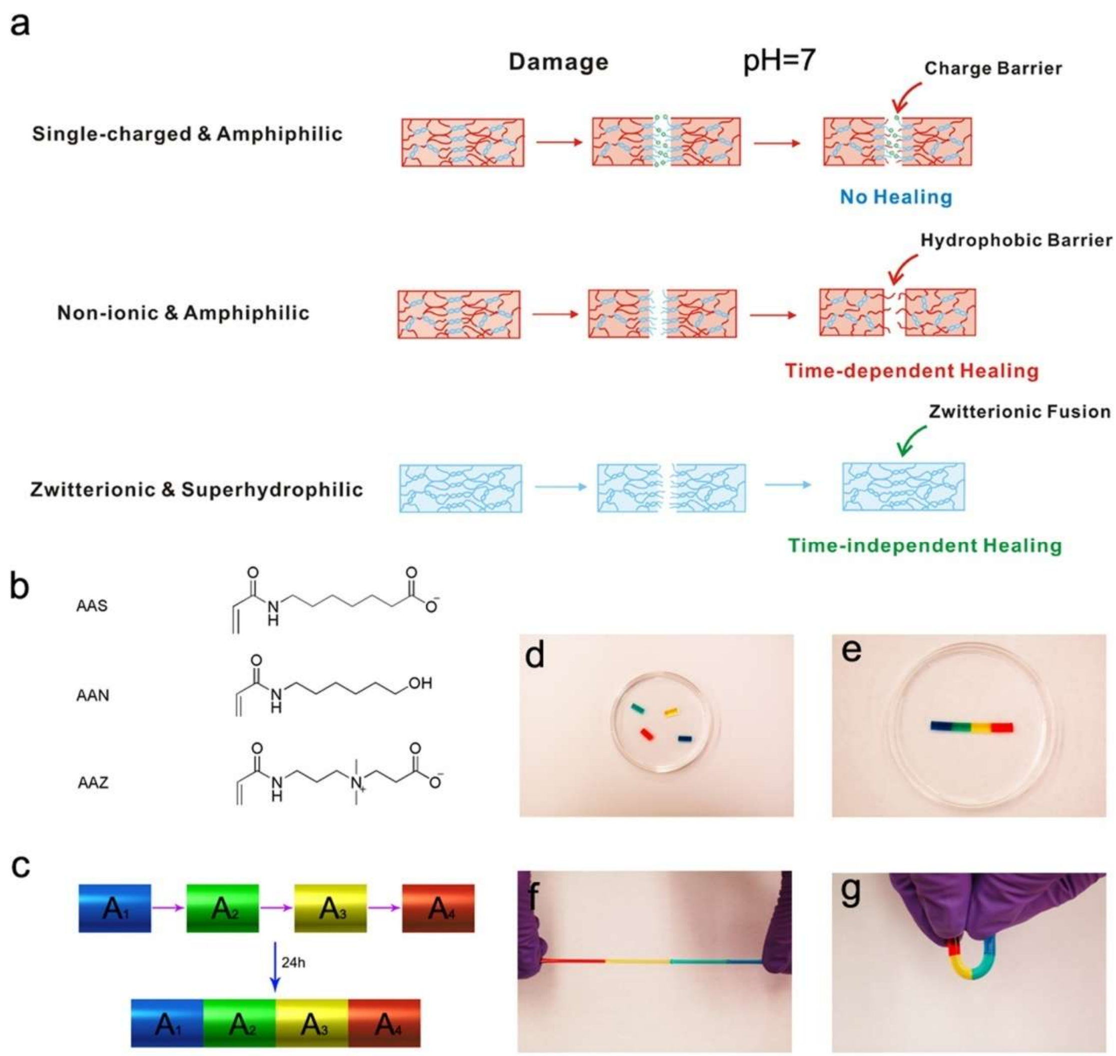

Figure 2.1. Illustration and demonstration of zwitterionic fusion induced time-independent self-healing behavior. **a,** Different healing behaviors of single-charged, non-ionic and zwitterionic materials. **b**, Chemical structure of single-charged AAS, non-ionic AAN, and zwitterionic AAZ. **c**, The construction process of a block hydrogel from different AAZ hydrogels. **d**, Individual AAZ hydrogel building blocks dyed with different colors **e,** A block hydrogel constructed from the building blocks. **f,** The block hydrogel upon large deformation. **g,** The block hydrogel upon bending.

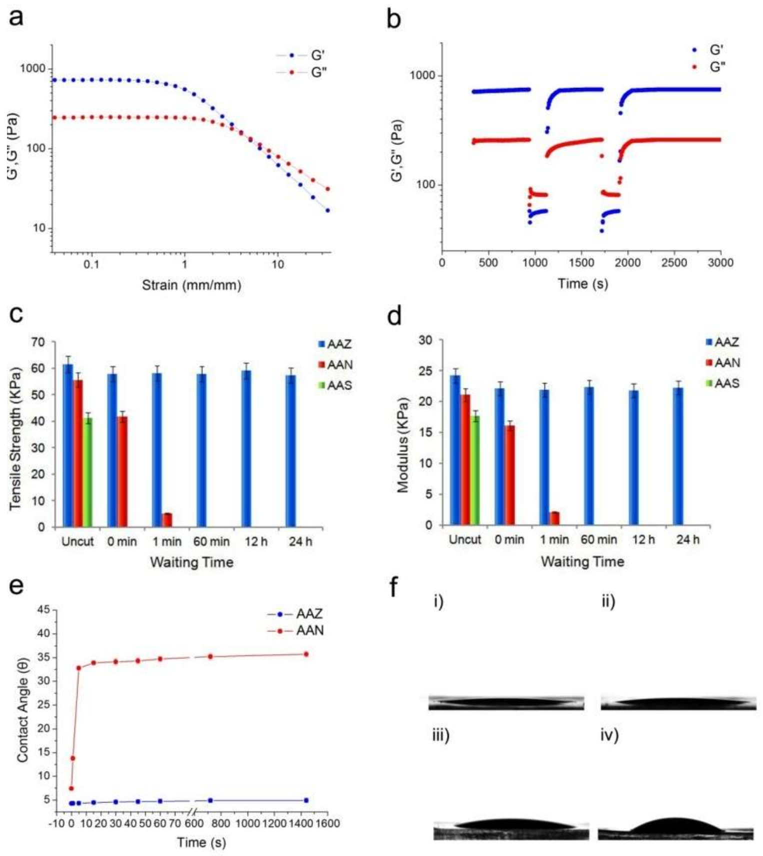

Figure 2.2. Mechanical properties and surface wettability tests. **a**, G' and G" of AAZ hydrogel for a strain sweep with ω= 10 rad s^{-1}. **b**, G' and G" of AAZ hydrogel in continuous step strain measurements (25ºC). Large strain (1,000%) inverted the values of G' and G" to give the sol state, while G' recovered under a small strain (1%) within 100 seconds. **c**, Tensile strength of the mended samples; mending was performed at room temperature after cut samples were kept apart for up to 24 hours. **d**, Young's Modulus of the mended samples; mending was performed in the same way as in (c). **e**, Influence of wait time (time after cutting) on the value of the advancing water contact angle on the cut surfaces of the physically crosslinked AAZ hydrogel and AAN hydrogel at 25ºC. **f**, The morphology of water droplets on the surface of freshly cut surface of AAZ (i), AAN (iii) and uncut surface of AAZ (ii), AAN (iv) hydrogels.

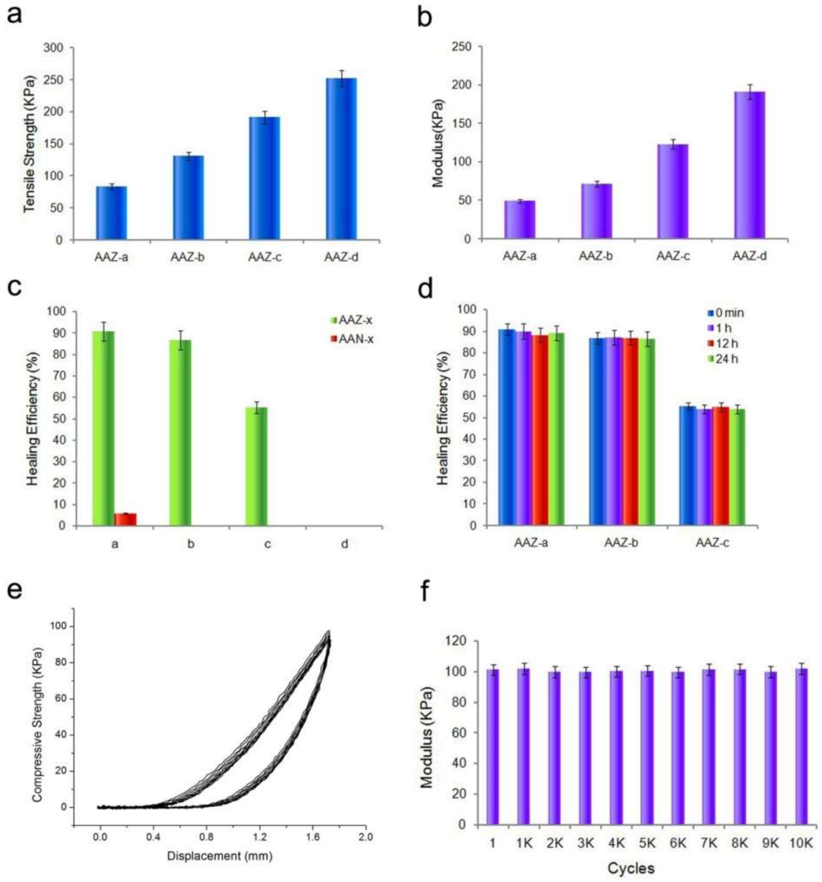

Figure 2.3. The effect of additional crosslinkers on AAZ and AAN hydrogels. **a-b**, Tensile strength (a) and moduli (b) of chemically crosslinked AAZ hydrogels with different crosslinker concentrations. **c**, The effect of increasing concentration of chemical crosslinker on the healing efficiency of AAZ and AAN hydrogels. **d**, The effect of separation time on the healing efficiency of chemically crosslinked AAZ-x hydrogels. The separation time causes no significant difference among the healing efficiency of each sample. **e**. Cyclic compressive force curves for AAZ-b with 45% displacement of height at a rate of 0.5Hz in 25ºC water bath. Representative curves were selected every 1000 cycles. **f**. Compressive moduli recorded at the selected cycles. There is no significant difference among the moduli of selective cycles.

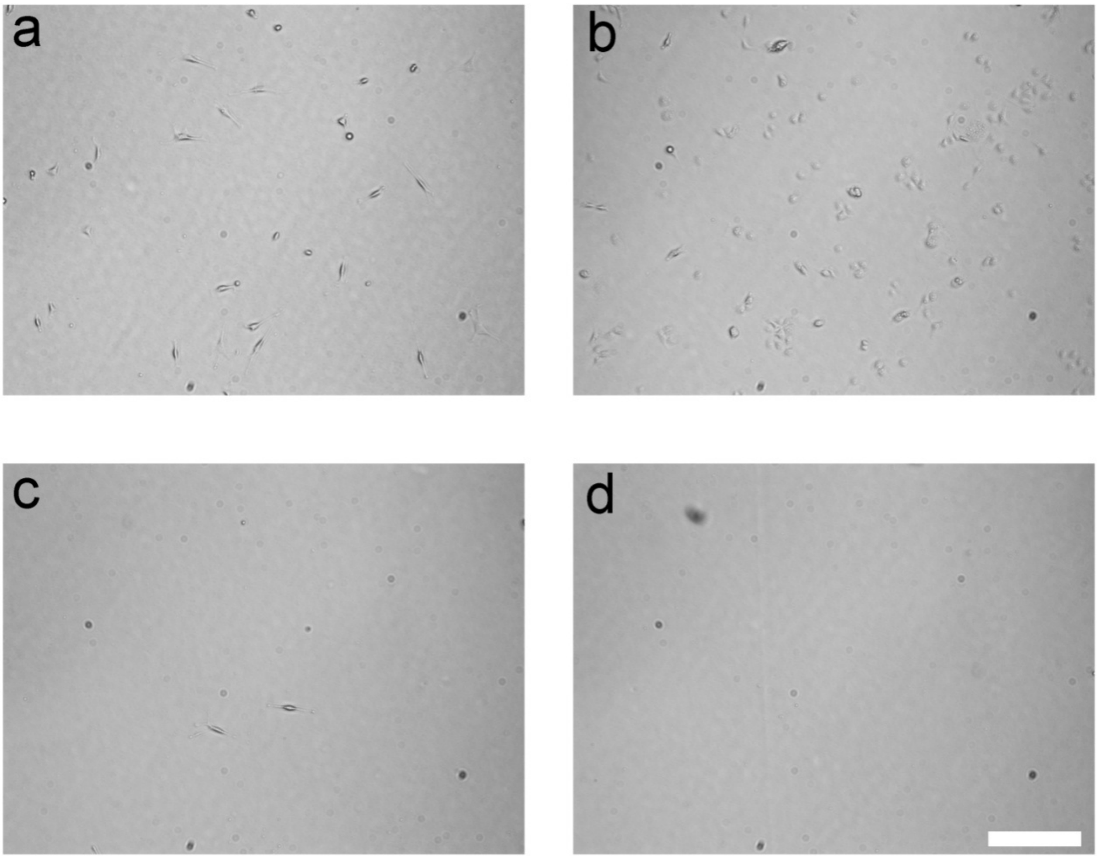

Figure 2.4. Representative images of NIH/3T3 and COS-7 cells on AAZ hydrogels either functionalized with FNT **a-b** or without FNT **c-d**. Scale Bar: 150μm.

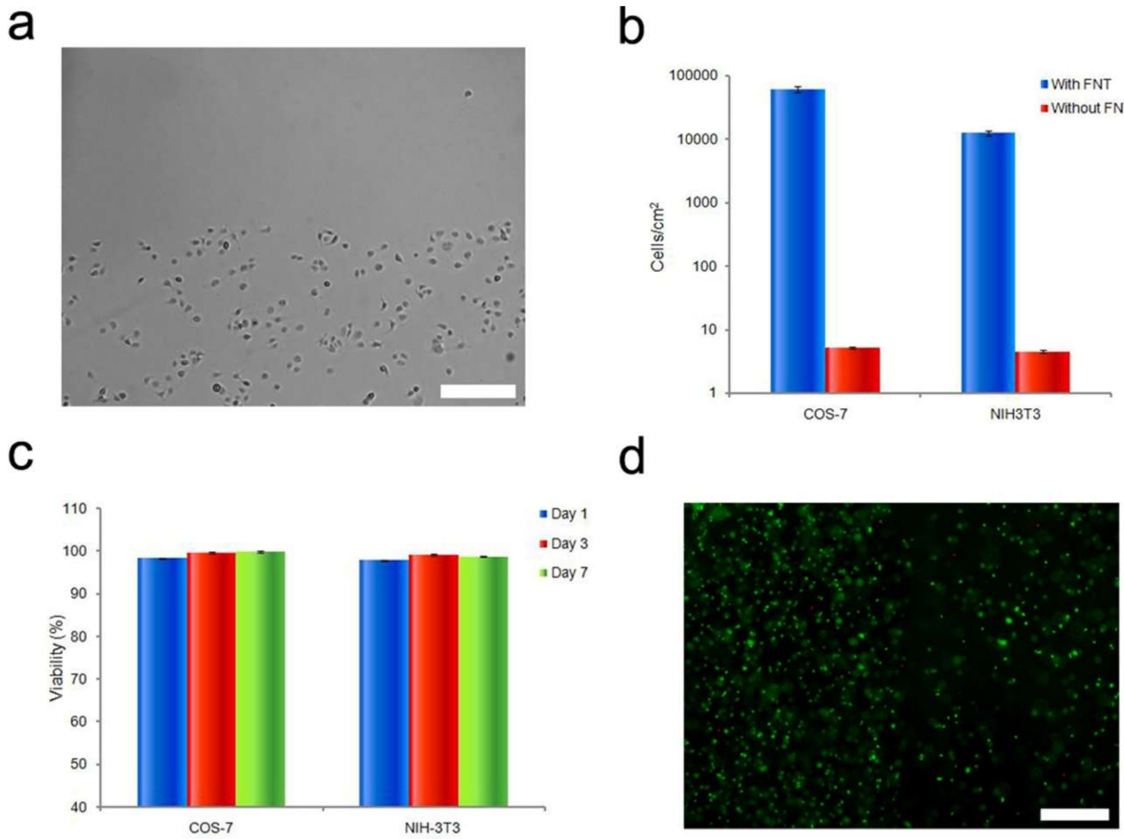

Figure 2.5. Demonstration of the biocompatibility of zwitterionic hydrogels as well as the zwitterionic fusion healing process. **a.** Representative images of COS-7 adhesion on a block hydrogel constructed with FNT-functionalized AAZ (top) and original AAZ (bottom). Scale Bar: 100μm. **b.** Quantitative data on the number of adhered cells on AAZ hydrogels either functionalized with FNT or not. **c.** The viability of NIH/3T3 and COS-7 cells when encapsulated into AAZ hydrogels for different days. **d.** Representative LIVE/DEAD assay image of AAZ hydrogels with different seeding densities of COS-7 cells after zwitterionic fusion healing process. Scale Bar: 150μm.

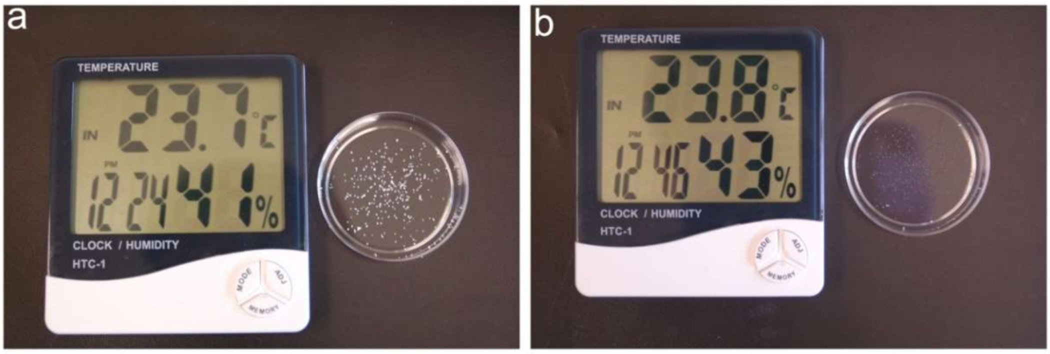

Figure 2.6. Superhydrophilic AAZ can strongly absorb water from the air in a short time and turn from solid (a) into droplets (b).

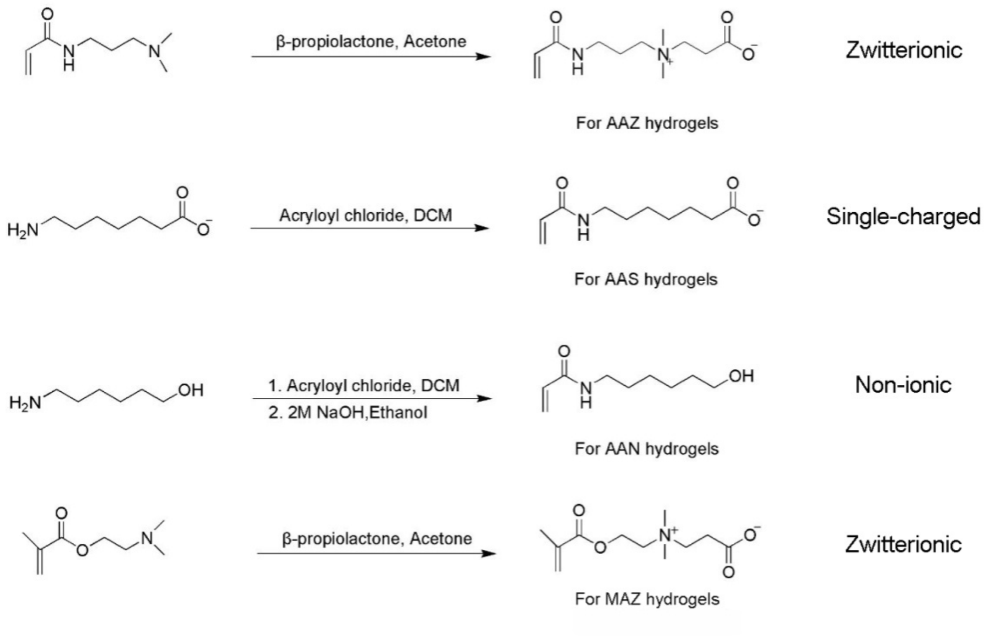

Figure 2.7. Synthesis route of AAZ, AAS, AAN and MAZ.

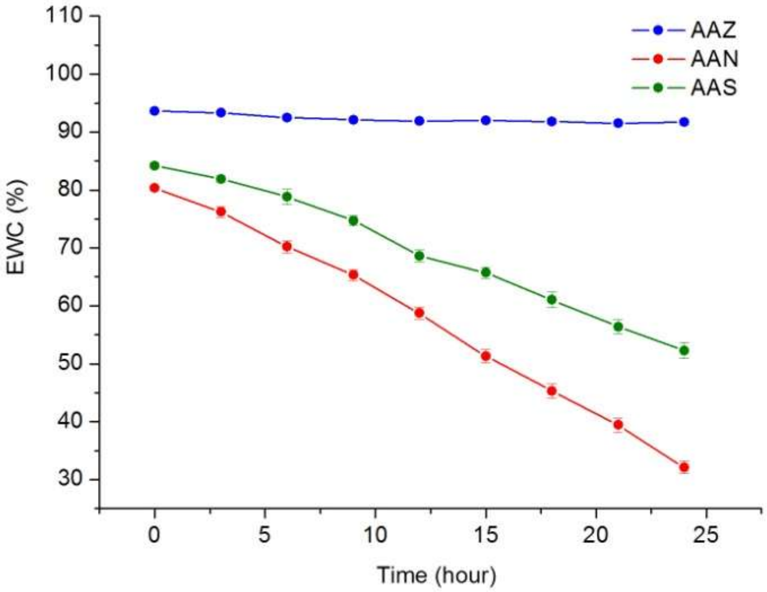

Figure 2.8. The dynamic EWC of AAZ, AAN and AAS hydrogels in air.

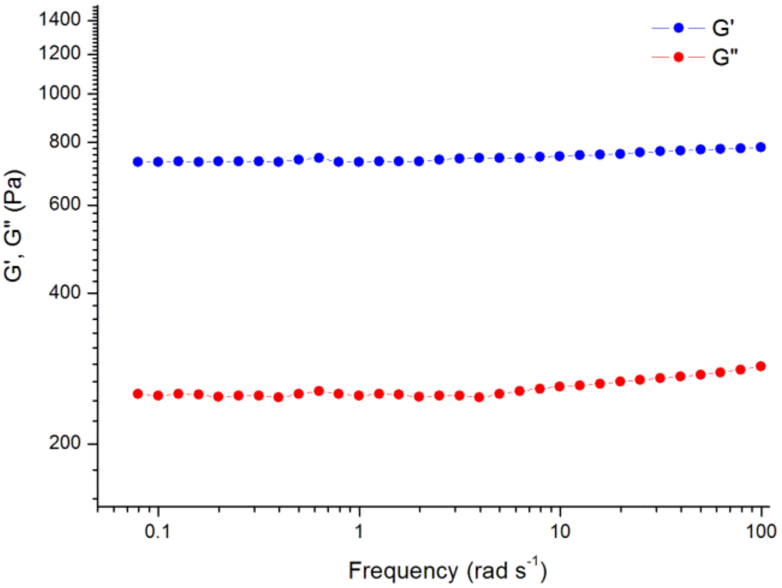

Figure 2.9. Dependence of the storage and loss moduli on angular frequency (ω) for AAZ hydrogel. (Strain = 10%, 25°C)

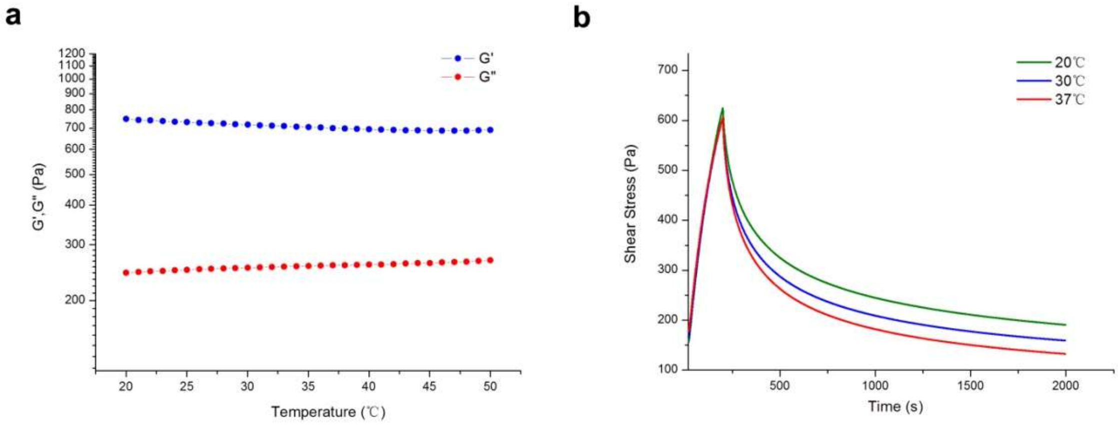

Figure 2.10. a. Dependency of the storage and loss moduli on temperature for AAZ hydrogel (Frequency =10 rad s^{-1}, Strain = 10%). **b.** Stress data as a function of time during typical shear stress relaxation experiments with different temperatures.

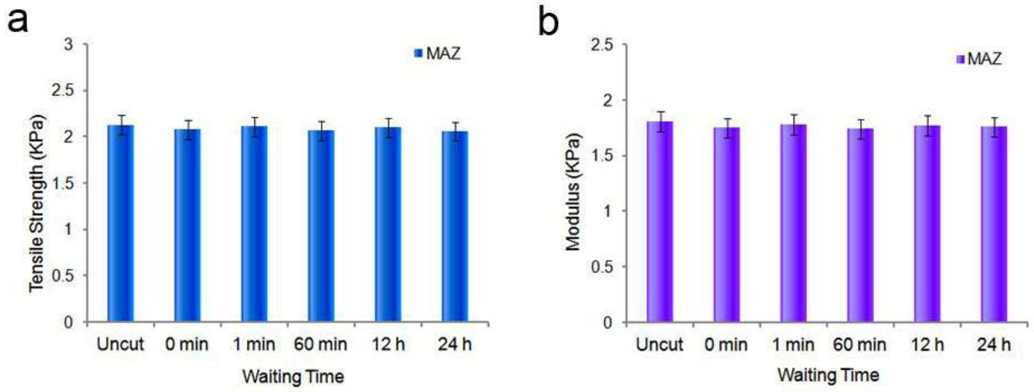

Figure 2.11. a, Tensile strength of the mended samples; mending was performed at room temperature after cut samples were kept apart for up to 24 hours. **b**, Young's Modulus of the mended samples; mending was performed in the same way as in (a).

Chapter 3 Restraint of the Differentiation of Mesenchymal Stem Cells by a Nonfouling Zwitterionic Hydrogel

The success of human mesenchymal stem cell (hMSC) therapies is largely dependent on the ability to maintain the multipotency of cells and control their differentiation. External biochemical and biophysical cues can easily trigger hMSCs to spontaneously differentiate, resulting in a rapid decrease of the multipotent cell population and thus compromising their regenerative capacity. In this work, we demonstrate for the first time that nonfouling hydrogels composed of pure poly(carboxybetaine) (PCB) allow hMSCs to retain their stem cell phenotype and multipotency, independent of differentiation-promoting media, cytoskeletal manipulation agents, and the stiffness of the hydrogel matrix. Moreover, encapsulated hMSCs can be specifically induced to differentiate down osteogenic or adipogenic pathways by controlling the content of fouling moieties in the PCB hydrogel. This work examines the critical role of nonspecific interactions in stem cell differentiation and highlights the importance of materials chemistry in maintaining stem cell multipotency and controlling differentiation.

3.1 Introduction

The extensive potential applications of human stem cells make it highly significant to reveal the fundamental mechanism by which to control their differentiation. According to reports, stem cell fate can be affected by altering various factors, which can be classified into biochemical[4,5] and biophysical signals[6-9]. For biochemical signaling, several soluble chemicals such as growth factors, hormones, and small molecules have been identified to upregulate stem cell differentiation into certain lineages. Mechanical determinism is another prevalent theory in the regulation of stem cell fate. Researchers have observed that biophysical cues, including substrate stiffness[7], porosity[10], geometry[11], or even external forces[12], are able to direct stem cells to differentiate. The belief that integrin-mediated cellular traction plays a vital role in translating mechanical signals into "decision-making" information can explain the influence of these mechanical factors[13].

In recent years, researchers have begun to realize that the material surrounding a stem cell is highly important in determining its fate[14-17]. Among current 2D substrates or 3D matrixes used to culture stem cells, naturally occurring polymers such as collagen[10], alginate[13], agarose[13] and hyaluronic acid[18] are commonly chosen due to their high biocompatibility. Though these natural materials can provide a biocompatible niche, their complex composition makes it difficult to elucidate the stem cell differentiation mechanism and the fate choice of stem cells cultured inside is highly dependent on their surrounding biochemical and biophysical cues[4,6]. Variable material processing techniques can also substantially change the outcome—stem cells cultured in chemically crosslinked[19] and physically crosslinked[13] alginate hydrogels differ markedly in their differentiation behavior. Artificial materials are usually easier to control[20], but generally not biocompatible with stem cells, especially for 3D cell encapsulation. High-molecular-weight poly(ethylene glycol) (PEG) is presently the most popular among the very limited synthetic materials suitable for stem cell culture[21-24]. Similar to their behavior in naturally derived polymer matrixes, the fate of stem cells living in PEG hydrogels is highly influenced by chemical and physical cues[13,23]. However, uniform external forces and chemical diffusion will be very hard to implement in upcoming clinical applications. The development of a platform allowing stem cells to maintain their pluripotency regardless of biochemical or biophysical influence has been a great challenge.

In sharp contrast to the natural polymers mentioned and the artificial amphiphilic material PEG, the superhydrophilic zwitterionic material polycarboxybetaine (PCB)[25] exhibits an unmatched capability for resisting nonspecific binding[26,27]. In the present work, to assess the influence of a nonfouling background on the fate of encapsulated hMSCs, carboxybetaine derived monomer carboxybetaine acrylamide (CBAA) and crosslinker carboxybetaine dimethacrylate (CBDMA) were used to construct a hydrogel platform designated CBX (Fig. 1a). The mechanical strength, or stiffness, of these hydrogels was varied by altering the crosslinker content while holding monomer concentration constant. Prior to cell encapsulation, integrin binding molecule cyclic-RGD was functionalized to the matrix components in order to support stem cell attachment and mediate cellular traction. Hydrogen bonding between the amide and carboxyl groups in the material allowed the encapsulation process to be completed quickly. The viability of the encapsulated hMSCs is presented in SI Fig. 1. As seen in this figure, a CBX hydrogel can support encapsulated hMSCs with almost 100% viability over a 3-day culture in basal media. We then transferred the hydrogel-hMSC constructs to a bipotential differentiation medium (osteogenic and adipogenic) and cultured them for 7 days after an initial 3-day culture in basal media. As seen in SI Fig. 2, differentiation media did not compromise the viability of encapsulated hMSCs. After confirming PCB hydrogel biocompatibility, we endeavored to explore the differentiation of hMSCs in this environment using immunohistochemistry (IHC), histological staining and RNA analysis.

3.2. Experimental Section

3.2.1 Culture of hMSCs. Human mesenchymal stem cells (hMSCs) were purchased from Lonza Corporation (Wakersville, MD). For encapsulation studies, hMSCs were expanded in hMSC growth media (MSCGM™, Lonza Corporation) and used between passages 3-4 in both 3D and 2D studies.

3.2.2 Preparation of hMSCs lysates. hMSCs at passage 3-4 were pelleted (1000 rpm, 4°C) and lysed into RIPA buffer (Sigma) which enables efficient cell lysis and protein solubilization while avoiding protein degradation and interference with the proteins immunoreactivity and biological activity. The protein content of clarified cell lysates was determined via BCA.

3.2.3 Preparation of 2D/3D hMSCs-PCB Hydrogel Constructs. An appropriate amount of CBAA monomer, and CBDMA or EGDMA crosslinker were dissolved in 40uL PBS. The molar concentration of CBAA was fixed at 2M and the molar concentration of crosslinker was adjusted to 2mM, 4mM and 20mM respectively. Before mixing with hMSCs, Cyclo(RGDYKEG) peptide (cRGD) or Cyclo(RGEYKEG) peptide (cRGE) was functionalized to the system. In brief, equimolar N-(3-Dimethylaminopropyl)-N'-ethylcarbodiimide hydrochloride (EDC) (Sigma) and N-Hydroxysuccinimide (NHS) (Sigma) were added to the solution mentioned above. After incubation at 25℃ for 1 hour to activate the carboxylate group, equimolar cRGD or cRGE was added to the activated system. The molar concentration of cRGD or cRGE in the reaction solution was chosen as 30μM, 150μM and 500μM. The reaction was allowed to proceed at 25℃ for 24 hours before polymerization. The efficiency of the reaction was calculated by LC-MS and shown in Table 2.1.

For 3D cell-hydrogel constructs, hMSCs were mixed with and suspended in the solution described above. Each sample contained 60.5 million hMSCs. Photoinitiator 2-hydroxy-2-methylpropiophenone was then added and the solution was placed between two glass slides separated by 2 mm-thick polytetrafluoroethylene spacers and allowed to polymerize in a crosslink oven (XL-1500B UV Crosslinker, Spectronics Corporation, NY, USA) for 1min. The cell-encapsulating CB hydrogels were equilibrated in basal media. The viability of encapsulated cells was examined by using a live/dead assay kit (Invitrogen). The total cell expansion ratio was tested by Vybrant® MTT Cell Proliferation Assay Kit (Invitrogen) as per the manufacture instruction and was measured on a microplate reader (Cytation 3 Cell Imaging Multi-Mode Reader, BioTek). The Click-iT EdU Alexa Fluor 594 Imaging Kit (Invitrogen) was used to label proliferating cells as per the manufacture instruction. DAPI was used to label the nuclei and counted the total number of hMSCs. In order to remove the influence of the cells on the surface, the 20μm hydrogel near the surface were removed. Zeiss LSM 510 META confocal microscope was used for quantifying the proliferating hMSCs within CBE and CBX hydrogels. At least three independent constructs were used and each one was sampled at three different depths. A Z-sampling rate of 3.6μm was used for image acquisition

For 2D cell-hydrogel constructs, after functionalization with cRGD, photoinitiator 2-hydroxy-2-methylpropiophenone was added and the solution was allowed to polymerize by using the same method to the 3D work. After polymerization, CB hydrogels were removed from casts and dialyzed in PBS for 3 days. Then, CB hydrogels were seeded with hMSCs at 20,000 cells cm^{-2} and cultured in stem cell medium for 3 days before transfer into bipotential medium.

3.2.4 Efficiency of peptide functionalization. The data were collected using an Agilent 1200 LC 6520 Q-Tof MS system (Agilent Technologies, Santa Clara, CA). 1 μL of each sample was injected. The chromatographic separation was performed in hydrophilic interaction chromatography (HILIC) mode on a SeQuant ZIC-cHILIC column (150 x 2.1

mm, 3.0 μm particle size, Merck KGaA, Darmstadt, Germany). The flow rate was 0.500 mL/min, auto-sampler temperature was kept at 4℃, the column compartment was set at 40℃, and total separation time for both ionization modes was 40 min. The mobile phase was composed of Solvents A (5 mM ammonium acetate in 90% H_2O/10% acetonitrile + 0.2% acetic acid) and B (5mM ammonium acetate in 90% acetonitrile/10% H_2O + 0.2% acetic acid). The gradient conditions are shown below.

Time Segment, min.	Solvent A, %	Solvent B, %
0 – 1	25	75
1 - 5	from 25 to 70	from 75 to 30
5 - 9	70	30
9 – 9.1	from 70 to 25	from 30 to 75
9.1 – 40 (equilibration)	25	75

The Q-Tof mass spectrometer was equipped with an electrospray ionization (ESI) source. The instrument was controlled by Agilent MassHunter Workstation (Agilent Technologies, Santa Clara, CA). The ESI voltage was set at 3800 volts. The source gas was N_2 (99.999% purity). The ion source conditions in positive mode were: drying gas = 10 l/min, nebulizer gas = 45 psi, temperature = 325℃. The extracted ion chromatography (EIC, cRGD m/z=804.3602, cRGE m/z=818.3801) peaks were integrated using Agilent Mass Hunter Qualitative Analysis (Agilent Technologies, Santa Clara, CA).

The functionalization efficiency was determined as $(V_f - V_c) / V_c \times 100$ (%), where V_f was the integrated value of the free cRGD or cRGE after the reaction and V_c was the integrated value of the free cRGD or cRGE in the according CBE or CBX aqueous solutions where no coupling agents (EDC or NHS) were added.

3.2.5 Characterization of CBE and CBX hydrogels. The hydrogels were obtained as described above and placed into PBS to reach equilibrium for at least five days before mechanical tests. At least five 0.5 cm diameter disks of each formulation (1.5 mm thickness when cast) were compressed at a rate of 1 mm/min using an Instron 5543A mechanical tester

(Instron Corp., Norwood, MA) with a 10 kN load cell. The Young's modulus was calculated from 3% to 13% strain to avoid any complications in an instance in which the top plate may not be completely engaged with the specimen when compression begins.

The swelling ratios were determined as $(D_s/D_o) \times 100$ (%), where D_s was the diameter of the fully swollen hydrogels and D_o was the diameter of the relaxed (unswollen, but not dehydrated) hydrogels.

3.2.6 Pore size distribution by uptake of dextran particles. As reported before[1] , the relative uptake of dextran of various molar masses can be used to determine the pore size distribution of a hydrogel. FITC–dextran of molar masses 4, 40, 70, 150, 250, 500, 1000 and 2000 kDa were dissolved in PBS buffer (100 mM) to yield a final concentration of 0.2 mg/mL. CBE and CBX hydrogels were immersed in the dextran solution and the samples were sealed and kept in a box covered with aluminium foil in order to prevent exposure to light. After 3 days of equilibration, the dextran-loaded hydrogels were examined by using a Zeiss LSM 510 META confocal microscope. The partition coefficients were measured as follows:

$R=(I_{gel}-I_{background})/(I_{solution}-I_{background}) \times 100\%$

I_{gel}: fluorescence intensity inside gel

$I_{solution}$: fluorescence intensity in solution

$I_{background}$: fluorescence intensity for background

3.2.7 Preparation of self-assembled monolayers. Glass chips were first coated with an adhesion-promoting chromium layer (thickness 2 nm) and a surface-plasmon-active gold layer (48nm) by electron beam evaporation under vacuum. Before self-assembled monolayer (SAM) preparation, the gold-coated glass substrate was rinsed with ethanol and water in sequence, dried with filtered air, then further cleaned in a UV ozone cleaner (Jelight, model 42) for 20 min. The cleaned chip was immediately soaked in a 0.1 mM ethanol solution of ATRP initiator for 24 h to form a SAM on the gold surface[2]. The chip was subsequently rinsed with THF, then ethanol, and dried with a stream of filtered air just prior to surface-initiated polymerization.

3.2.8 Surface-initiated atom transfer radical polymerization. Surface-initiated ATRP was carried out on SAM-coated gold substrates following a method similar to one previously reported[3]. Briefly, CuBr, $CuBr_2$, BPY, and gold chips with immobilized initiators were placed in a sealed reaction tube and deoxygenated via vacuum and nitrogen purging. CBAA monomer was deoxygenated in a separate sealed tube, and then dissolved in a deoxygenated solution of methanol and pure water in a 10:1 volume ratio. The monomer solution was transferred to the reaction tube using a syringe under nitrogen protection. In a shaker at 120 RPM and 25℃, PCBAA was allowed to react for 3 h. After polymerization, chips were removed, rinsed with pure water and PBS, and stored overnight in PBS. Chips were rinsed with Milli-Q water and dried with filtered air just prior to any experiments. Dry film thickness was measured with an ellipsometer (J.A. Woollam, Alpha-SE), and chips with thicknesses of 20-30 nm were used for SPR measurements.

3.2.9 Peptides functionalization of PCBAA polymer films. The PCBAA coated gold chips described above were placed in 20ml petri dishes and immersed in PBS before peptides conjugation. Then, appropriate amount of EDC and NHS were added to the petri dishes. After incubation at 25℃ for 1 hour to activate the carboxylate group, appropriate amount of cRGD or cRGE was added to the activated system. The concentration of cRGD or cRGE in the reaction solution was chosen as 30μM, 150μM and 500μM. The molar ratio of EDC, NHS and peptides are fixed at 1:1:1. The reaction was allowed to proceed at 25℃ for 24 hours and the obtained chips will be used for protein adsorption tests.

3.2.10 Measurements of protein adsorption: 100% Human Serum, 1 μg/ml α_5-integrin (CD49e, BD Biosciences) and 1 μg/ml α_v-integrin (CD51, BD Biosciences) were used for the protein absorption assay. This study used a custom-built surface plasmon resonance (SPR) sensor from the Institute of Photonics and Electronics, Academy Sciences (Prague, Czech Republic). A prepared chip was attached to the base of the prism and optical contact was established using refractive index matching fluid (Cargille). A quadruple-channel flow cell with four independent parallel flow channels was used to contain liquid samples during experiments. A peristaltic pump (Ismatec) was utilized to deliver liquid samples to the four channels of the flow cell. A stable baseline was first established with water, PBS, or divalent salt solution with different concentrations of running buffer, then serum solution was delivered to the surface at a flow rate of 0.050 mL/min for 30 min, and the same buffer flowed again for 10 min before determining final wavelength shifts. A surface-sensitive SPR detector was used to monitor surface interactions in real time, and wavelength shift was used as an indication of changes on the surface.

3.2.11 Nonspecific protein adsorption on CBE and CBX hydrogels. FITC tagged FBS was prepared by using FluoroTag™ FITC Conjugation Kit (Sigma) and Rhodamine tagged cell lysates (CLS) was prepared by using Rhodamine Conjugation Kit (Abcam) as per the manufacture instruction. To evaluate nonspecific protein interactions, hydrogels were exposed to 0.1 mg/mL of FITC tagged FBS or Rhodamine tagged CLS in PBS for overnight at 4℃ followed by washing with PBS for 3 times. Protein adsorption was detected by using Zeiss LSM 510 META confocal microscope. For all stacking images, a Z-sampling rate of 2.5μm was used for image acquisition

3.2.12 FRET Measurement and Calculation. For FRET measurements, hMSCs were labeled with 5-hexadecanoylaminofluorescein (4 nmol/cm^2; Invitrogen) in tissue culture flasks for 24 hr, before being prepared for encapsulation as per differentiation studies. Cell suspensions were mixed with CBE or CBX system mentioned above while cRGD was replaced by Cyclo{RGDYKEGK(5,6-TAMRA)} (cRGD-TAMRA). The density of RGD-TAMRA peptides was controlled by varying the concentration of peptides and corresponding coupling agents. After mixing cells with CBE or CBX solutions and crosslinking, hydrogel discs (500μm thick, 5mm diameter) were incubated for 2 hr on an orbital shaker in phenol red free medium (10% FBS) at 37°C, 5% CO_2 before FRET measurements. The 2 hr time-point was chosen to minimize any effects of new protein synthesis on integrin-RGD bond formation. Cyclo{RGEYKEGK(5,6-TAMRA)} (RGE-TAMRA) peptides were used as negative controls.

We carried out FRET measurements in CBE and CBX hydrogels on a fluorescent microplate reader (Cytation 3 Cell Imaging Multi-Mode Reader, BioTek). In order to rule out the influence of the autofluorescence of polymer molecules as well as the fluorescence bleeding through phenomena, the ‘donor-only’ samples, the ‘acceptor-only’ samples, and the ‘FRET’ samples which contain both donor and acceptor were generated in parallel for FRET calibration. Fluorescence of all samples in three filter sets (acceptor, donor, and FRET filter set) was measured, and the calibration was accomplished with "specified bleed through with donor and acceptor only correction" as reported before[4]. The FRET signals of the donor-only samples were used to normalized FRET signals of donor–acceptor samples and expressed as 'Normalized FRET'.

3.2.13 Immunohistochemistry. After induced differentiation for 7 days, cell-hydrogel constructs were fixed in 4% paraformaldehyde in PBS for 8 hours, transferred to 30 wt% sucrose for 72 h, frozen in Cryo-gel (Instrumedics, Inc.) and cryosectioned (10μm sections). Vinculin-containing focal adhesion is stained by using ProteoExtract® Cytoskeleton Enrichment and Isolation Kit (EMD Millipore) per the manufacture instruction. The F-actin filaments is stained with CytoPainter F-actin Staining Kit (Abcam) and mounted with ProLong Gold antifade reagent with DAPI and allowed to cure overnight.

Triple-label immunofluorescence staining was used to visualize differentiation markers and pluripotent markers. Mouse anti-RUNX2 (Abcam) and rabbit anti-OPN (Abcam) were used to visualize osteogenesis. Rabbit anti-PPARG (Abcam) and mouse anti-FABP4 (Abcam) were used to visualize adipogenesis. Mouse Anti-STRO-1 (Invitrogen) and Rabbit Anti-ALCAM (Abcam) were used to visualize pluripotency. The cells were permeabilized for 10 minutes with PBT (0.1% Triton X-100 in PBS). After blocking for 1h in 10% fetal bovine serum, substrates were incubated with primary antibodies for 8 hours at room temperature. Then, two types of secondary antibodies with different fluorescence tags, donkey anti-rabbit IgG (Invitrogen), and donkey anti-mouse IgG (Invitrogen), were used to visualize the antibodies of differentiation markers. Goat anti-mouse IgM (Invitrogen) and Donkey anti-rabbit IgG (Invitrogen) were used to visualize antibodies of pluripotency markers. 4,6-diamidino-2-phenylindole (DAPI; Molecular Probes) was included in the secondary solution and samples were mounted on glass slides with ProLong® Gold reagent.

3.2.14 Biochemical assays. Dried cell-hydrogel constructs from each group (n=5) were obtained by lyophilization. The dried constructs were crushed with a tissue grinder and digested in 1ml of papainase for 15h at 60 ºC. The DNA content (nanograms of DNA per milligram dry weight of the hydrogel) was determined with Hoechst 33258.

3.2.15 Quantitative Real Time PCR. At certain time points, constructs were removed from the culture media. Then, the constructs were transferred in TRI REAGENT (Sigma) in RNase-free test tubes and were homogenized with a tissue homogenizer. Total RNA was extracted according to the manufacturer's instructions. Total RNA for each sample was quantified with a UV spectrophotometer and converted to cDNA using the QuantiTect Reverse Transcription Kit. After amplification by using SYBR Green PCR Master mix (Qiagen), thermocycling was carried out in a solution with primers (Integrated DNA Technologies) and cDNA. PCR conditions were as follows: 15s at 94 ºC, 30s at 55ºC, and 30s at 72ºC. The primer sequence is summarized in Table 3.1 as reported before[5-14]. Here, we used RNase-free DNase (Qiagen) to prevent genomic DNA contamination.

3.2.16 Osteogenic/Adipogenic Differentiation. Cell-Hydrogel constructs were cultured in basal medium for 3 days. Following this time point, the basal medium was replaced with bipotential differentiation medium—low glucose DMEM supplemented with 20% FBS and 1% penicillin/streptomycin (Invitrogen); Adipogenic supplement: 1μM dexamethasone, 50μM indomethacin (Sigma), 0.5μM 3-isobutyl-1-methylxanthine (IBMX; Sigma) and 10μg/mL human recombinant insulin (Invitrogen); Osteogenic supplement: 10mM β-glycerol phosphate (Sigma), 50μg/mL ascorbic acid (Sigma)). Media changes were performed every 3 days.

As a parallel control, a mixed adipogenic/osteogenic inductive media was made by combining commercially available osteogenic and adipogenic inductive media (R&D Systems) in a 1:1 ratio and supplementing with 1% (v/v) penicillin-streptomycin (Gibco). The mixed media was also used for the differentiation experiment mentioned above and no significant difference was observed compared to the lab-made bipotential differentiation medium.

3.2.17 Histological Analysis on hMSC differentiation. After incubation for 1 week, cell-hydrogel constructs were fixed in 4% paraformaldehyde in PBS for 8 hours, transferred to 30 wt% sucrose for 72 h, frozen in Cryo-gel (Instrumedics, Inc.) and cryosectioned (10μm sections). ALP activity (osteogenic biomarker) and lipid accumulation (adipogenic biomarker) were visualized by Fast Blue BB (Sigma) and Oil Red O (Sigma). The total cell counts were obtained by staining the nuclei with DAPI. By dividing the positive stained cells for ALP and Oil Red O, respectively by the total cell counts, percentage of differentiated hMSCs of osteogenesis and adipogenesis was calculated. Color micrographs were acquired using a Nikon E800 upright microscope.

3.2.18 Inhibition assays. Inhibitors were added to cell culture media at the following concentrations without causing apparent changes to the viability of encapsulated hMSCs. Nocodazole (1.1μM), Cytochalasin D (0.25μM), Blebbistatin (1μM), and Y-27632 (1.8μM) (Calbiochem). Integrin blocking antibodies (α5 and β1, Chemicon) were added at 1.1ug/mL in the process of cell encapsulation.

3.2.19 Metabolites analysis. hMSCs were cultured within CBE and CBX hydrogels for 3 days in basal medium and 7 days in bi-potential differentiation medium as described above. All the media were collected for glucose consumption measurement. The value obtained was normalized to the value of fresh media. For the amino acid metabolic assay, cell-hydrogel constructs were washed in PBS and crushed with a tissue grinder before metabolites were extracted using an extraction solvent (1:3:1 Chloroform: Methanol: Water), and placed on a rotary shaker for 1 hour at 4℃. The solution was then centrifuged for 3 minutes at 13000g at 4℃ after which supernatant were collected and dried at 30 °C for ~2hr in a SpeedVac. The samples were analyzed using LC-MS QqQ method system as described below.

3.2.20 Liquid chromatography conditions. The LC system was composed of two Agilent 1260 binary pumps, an Agilent 1260 auto-sampler, and Agilent 1290 column compartment containing a column-switching valve (Agilent Technologies, Santa Clara, CA). Each sample was injected twice, 10 μL for analysis using negative ionization mode and 2 μL for analysis using positive ionization mode. Both chromatographic separations were performed in hydrophilic interaction chromatography (HILIC) mode on two SeQuant ZIC-cHILIC columns (150 x 2.1 mm, 3.0 μm particle size, Merck KGaA, Darmstadt, Germany) connected in parallel. Our setup allows one column performing separation while the other column is getting reconditioned and ready for the next injection. The flow rate was 0.300 mL/min, auto-sampler temperature was kept at 4℃, the column compartment was set at 40℃, and total separation time for both ionization modes was 20 min. The mobile phase was composed of Solvents A (5 mM ammonium acetate in 90% H_2O / 10% acetonitrile + 0.2% acetic acid) and B (5 mM ammonium acetate in 90% acetonitrile/ 10% H_2O + 0.2% acetic acid). The gradient conditions for both separations were identical and are shown below.

Time Segment, min.	Solvent A, %	Solvent B, %
0 - 2	25	75
2 - 5	from 25 to 70	from 75 to 30
5 - 9	70	30
9 - 11	from 70 to 25	from 30 to 75
11 - 20	25	75

The metabolite identities were confirmed by spiking the sample used for method development with mixtures of standard compounds (each mixture contained five standard metabolites). All the samples were analyzed over a 12-day period and the retention times (RT) did not undergo any significant shift (each peak was within 6 seconds throughout 12 days of analysis), which proved the robustness of our HILIC method.

3.2.21 Mass spectrometry conditions. After the chromatographic separation, MS ionization and data acquisition were performed using an AB Sciex QTrap 5500 mass spectrometer (AB Sciex, Toronto, ON, Canada) equipped with an electrospray ionization (ESI) source. The instrument was controlled by Analyst 1.5 software (AB Sciex, Toronto, ON, Canada). Targeted data acquisition was performed in multiple-reaction-monitoring (MRM) mode. We monitored 99 and 59 MRM transitions in negative and positive mode, respectively (158 transitions in total). The source and collision gas was N_2 (99.999% purity). The ion source conditions in negative/positive mode were: curtain gas (CUR) = 25 psi, collision gas (CAD) = high, ion spray voltage (IS) = -3.8/3.8 KV, temperature (TEM) = 500℃, ion source gas 1 (GS1) = 50 psi, and ion source gas 2 (GS2) = 40 psi.. The extracted MRM peaks were integrated using MultiQuant 2.1 software (AB Sciex, Toronto, ON, Canada).

3.2.22 Data analysis, model development and cross validation. A custom metabolite database incorporating HMDB was used to identify compounds. After exporting from MultiQuant software, spectral data were normalized using average values from the data of quality control (QC) injections (at least five in each batch, 33 QC samples in total). Means and standard errors of the mean were generated for all groups of picked peaks.

3.2.23 Flow Cytometry. Multicolor analysis for progenitor and stem cell phenotyping was performed on a LSR II flow cytometer (Becton Dickinson). Cells were stained in staining media (HBSS supplemented with FBS 2% and EDTA 2 mM) at 4°C for 1 h with Alexa Fluor® 647 anti-STRO-1 (Biolegend), FITC anti-ALCAM (AbD Serotec), Alexa Fluor® 647 anti-RUNX2 (Bioss Inc.), FITC anti-OPN (Biorbyt), and Alexa Fluor® 647 anti-PPARG (Bioss Inc.) and FITC anti-FABP4 (Biorbyt), then washed with staining media and analyzed. At least 10,000 events were acquired for each analysis.

3.2.24 Statistical analysis. Examination and quantification of histological sections was done by three independent researchers blinded to sample identity with at least five random images/fields in each section per sample. A two-tailed Student's *t*-test was used for all statistical analyses, with $*p<0.01$ being considered as statistically significant.

3.3. Results and Discussion

al media. We then transferred the hydrogel-hMSC constructs to the bipotential differentiation medium mentioned above and cultured them for 7 days after an initial 3-day culture in basal media. As seen in Fig. 3.14, differentiation media did not compromise the viability of encapsulated hMSCs. We also quantified the expansion of the hMSCs in CBX and CBE hydrogels. As presented in Fig. 3.15, since no growth factor was added and hMSCs are not able to degrade the CBX or CBE matrixes, no significant proliferation was observed in both CBE and CBX hydrogels. After confirming the biocompatibility of PCB hydrogel, we endeavored to explore the differentiation of hMSCs in this environment using immunohistochemistry (IHC), histological staining and RNA analysis.

3.3.1 IHC assay and histological staining for hMSCs within 3D nonfouling CBX and fouling CBE hydrogels. According to current differentiation theories, the fate of hMSCs can be tuned by adjusting the mechanical properties of their support[7]. As we mentioned above, three different moduli were chosen for both CBE and CBX hydrogels. To examine the differentiation results after a 7-day culture in the bipotential media, we first utilized IHC to visualize nuclei (DAPI), osteogenic biomarkers, and adipogenic biomarkers. To test for osteogenesis, we visualized RUNX2[29], a key transcription factor essential for osteogenic differentiation, and Osteopontin (OPN), an important factor in bone remodeling expressed predominantly by osteoblasts, osteocyctes and osteoclasts[30]. Similarly, two biomarkers of adipogenesis were also examined; PPARG is a crucial regulator of adipogenesis and highly related to the uptake and storage of lipids[31], and fatty acid binding protein 4 (FABP4) is a carrier protein primarily expressed in adipocytes[32]. Interestingly, as presented in Fig. 1b, both osteogenic and adipogenic biomarkers remained absent from cells grown in CBX hydrogels prepared in a wide range of moduli, from soft (3.1KPa) to stiff (71.2KPa). These results suggested that neither mechanical-property-associated cell traction nor soluble differentiation factors conclusively drive stem cell differentiation choices.

From the IHC results, it appeared that nonspecific binding plays an important role in directing stem cells to differentiate. The superhydrophilic CBX hydrogel matrix does not interact with the cell surface and cannot induce hMSC differentiation. In sharp contrast to the lack of differentiation we observed in CBX hydrogels, adipogenic biomarkers were robustly expressed in cells cultured in soft CBE hydrogels (2.6KPa), and disappeared quickly when the modulus was increased. Compared with the soft CBX constructs, it was apparent that a minimal concentration of hydrophobic components encouraged hMSCs to differentiate to an adipogenic lineage. On the other hand, osteogenic biomarkers were clearly expressed in the stiffer (medium- and high-modulus) CBE hydrogel samples, with increased nonspecific binding sites resulting in increased expression. This indicates that increasing the mechanical strength of the matrix in the presence of nonspecific binding can help hMSCs shift their differentiation choice from adipogenesis to osteogenesis.

After visualizing the characteristic surface antigens, we further aimed to explore certain chemicals and enzymes secreted within specifically differentiated hMSCs. Adipogenesis in hMSCs can be indicated by the presence of neutral lipids[33], visualized by staining with Oil Red O. Likewise, osteogenesis can be reflected by alkaline phosphatase (ALP)[33], stained with Fast Blue salts. We conducted this histological staining for both lipid and ALP content in hMSCs encapsulated in CBX and CBE hydrogels. As presented in Fig. 1c (i-iii), stem cells differentiate positively in CBE hydrogels. Nearly all the differentiated cells commit to adipogenesis in a soft CBE matrix (2.6KPa), and begin to choose the osteogenic pathway as the stiffness is increased. In contrast, nearly all hMSCs in CBX hydrogels remain in an undifferentiated state, with the very few differentiated cells randomly committed (Fig. 1c (iv-vi)). We also extended the differentiation culture period to 21 days and tried to functionalize the CBX hydrogels with cRGD of different densities. As presented in Fig. 3.17, neither extended culture period nor varied cRGD density was able to compromise the viability of encapsulated hMSCs or cause active differentiation of hMSCs.

Furthermore, we demonstrated the fate choice of hMSCs within PCBAA hydrogels can be conclusively controlled by the amount of hydrophobic components. PCBAA hydrogels were crosslinked by a combination of hydrophilic CBDMA crosslinker and hydrophobic EGDMA crosslinker while the total molar concentration of crosslinker and monomer concentration are fixed. As presented in Fig. 3.18a, the moduli of PCBAA hydrogels did not vary significantly with increasing percentage of added CBDMA crosslinker. However, the fate choice of hMSCs differed markedly with increasing percentage of CBDMA. As seen in Fig. 3.18b, the osteogenesis dominated even though the share of the CBDMA reached 75%. However, it decreased sharply with further increasing percentage of CBDMA. In contrast to osteogenesis, the adipogenesis increased significantly with the reduced osteogenesis and decreased again when the share of CBDMA increased higher than 95%. Both osteogenesis and adipogenesis were observed to be negative in 100% CBDMA crosslinked PCBAA hydrogels.

We hypothesize that different cell-matrix interactions in CBX hydrogels or CBE hydrogels significantly influence the fate choice of hMSCs. As illustrated in Fig. 2, when cultured in nonfouling CBX hydrogels, hMSCs cannot fully interact with the matrix surrounding them, even though the matrix is anchored with c-RGD moieties. Therefore, neither physical or chemical factors can promote these hMSCs to differentiate. In contrast to the CBX hydrogels, the CBE hydrogels can provide sufficient nonspecific cues to those anchored hMSCs, mediating them to fully interact with their surrounding matrix. Therefore, as illustrated in Fig. 2, hMSCs are prone to commit to the osteogenic pathway when cultured in CBE hydrogels with a high modulus. On the other hand, hMSCs are prone to commit to the adipogenic pathway when cultured in CBE hydrogels with a low modulus.

To confirm our hypothesis, we further aimed to visualize biomarkers signifying multipotency in hMSCs encapsulated in CBX and CBE hydrogels. STRO-1 is one such biomarker found in bone marrow samples, used for enriching subsets of marrow stromal cells through recognition of a surface antigen unique to this lineage[34]. The CD166 antigen (encoded by the ALCAM gene) is a transmembrane glycoprotein that has been used as a potential stem cell marker[34]. As presented in Fig. 3, hMSCs cultured in the completely nonfouling CBX hydrogels were positive for stem cell markers STRO-1 and ALCAM, independent of matrix modulus. The same phenomenon was observed even we extended the differentiation culture period to 21 days (Fig. 3.19). In contrast, most of the hMSCs in CBE hydrogels were not able to express these stem cell biomarkers, as also shown in Fig. 3. This suggests that nonspecific-binding-mediated differentiation has been triggered, and hMSCs in CBE hydrogels lose their multipotency when cultured with differentiation media.

3.3.2 qRT-PCR assessment of hMSC differentiation within 3D CBX and CBE hydrogels.

The expression of characteristic genes can accurately reveal the propensity of stem cells to differentiate. Thus, we next endeavored to examine the behavior of stem cells within CBX and CBE hydrogels from the RNA level. RNAs were isolated and we conducted quantitative real-time PCR (qRT-PCR) to test the expression levels of certain characteristic genes. The expression was normalized to cells at the time of encapsulation, with β-actin used as the housekeeping gene. Since hMSCs are potentially able to differentiate into many different lineages, we first tested the characteristic gene expression in the process of adipogenesis, osteogenesis, chondrogenesis, myogenesis and neurogenesis. In addition to PPARG (adipogenic marker) and RUNX2 (osteogenic marker) mentioned above, three more RNA biomarkers were visualized to characterize the other differentiation pathways. AGGRECAN is a cartilage-specific proteoglycan core protein associated with chondrogenesis[35], MyoD is one of the earliest markers of myogenic commitment and plays a role in regulating muscle repair[36], and β3 TUBULIN is expressed exclusively in neurons and serves as a popular identifier specific to nervous tissue[37]. As exhibited in Fig. 4a, hMSCs encapsulated in CBX hydrogels exhibit no commitment to any differentiation lineage. However, while hMSCs in CBE hydrogels did not show any significant commitment to chondrogenesis, myogenesis, or neurogenesis, they presented noteworthy expression of the adipogenic biomarker (PPARG) in the soft sample and the osteogenic biomarker (RUNX2) in the stiffer samples (Fig. 4b).

Fig. 4c-d summarizes the expression of a panel of adipogenic genes in hMSCs cultured in CBX and CBE hydrogels. In addition to PPARG and FABP4 mentioned previously, we tested for adiponectin (encoded by ADIPQ), which regulates fatty acid breakdown[38], and lipoprotein lipase (LPL), a water-soluble enzyme that hydrolyzes triglycerides in lipoproteins[39]. As presented in Fig. 4c-d, without nonspecific binding sites there is no enhanced expression of adipogenic genes in hMSCs cultured in any CBX hydrogel, regardless of mechanical properties. However, when encapsulated in CBE hydrogels, the nonspecific binding sites lead to positive expression of the adipogenic genes, which decreases with an increasing modulus.

Fig. 4e-f summarizes the expression of osteogenic genes by hMSCs in CBX and CBE hydrogels. We quantified the expression of two more osteogenic biomarkers as well as OPN and RUNX2: collagen, type I, alpha 1 (COL1A1), a human gene found in osteoprogenitor cells encoding the major component of collagen I[40], and the gene encoding osteocalcin (OCN), a noncollagenous protein secreted exclusively by osteoblasts[41]. Normalized to cells at the time of encapsulation, the hMSCs in nonfouling CBX hydrogels did not express any of the osteogenic biomarkers at a significant level, once again regardless of matrix stiffness and differentiation-promoting media, as shown in Fig. 4e. And again, nonspecific binding sites produced dramatic changes in expression. As delineated in Fig. 4f, compared to the negligible expression of osteogenic genes in CBX hydrogels, expression was hundreds of times higher in CBE hydrogels. There are also significant differences when the concentration of nonspecific binding sites changes; stem cells in the CBE hydrogel with a lower concentration of hydrophobic crosslinker express the osteogenic genes at a much lower level than those surrounded by a higher concentration of hydrophobic components in the CBE hydrogels of higher moduli.

3.3.3Metabolic analysis in hMSC within 3D CBX and CBE hydrogels. Stem cells have been proved to be able to present in different stages of activation such as in quiescence or in the cell cycle, which is regulated by their metabolisms[42-44]. For example, hypoxia cultures which reduce the amino acid metabolism[45] can promote the adipogenic differentiation of hMSCs while normoxic cultures promote osteogenic and chondrocytic differentiation[46]. In this study, we endeavored to test the influence of a nonfouling background on the glucose consumption and amino acids metabolism of encapsulated hMSCs. After the 7 days differentiation, the total media were collected and analyzed by liquid chromatography–mass spectrometry (LC-MS) method involved a quadrupole time-of-flight (QTOF) mass spectrometer. As seen in Fig. 5a, the hMSCs cultured within CBE hydrogels consumed a large amount of glucose in the media. In contrast to the active glucose consumption of hMSCs within CBE hydrogels, as presented in Fig. 5b, hMSCs within CBX hydrogels exhibited a significant low level of glucose consumption, independent of the amount of added zwitterionic crosslinkers. This suggests the hMSCs can interpret the nonfouling background as a signal to remain quiescent and are able to keep the glucose metabolism at a very slow rate.

In addition to the glucose consumption, we further tested the amino acids metabolism of hMSCs within CBX and CBE hydrogels. After 7 days culture in the differentiation media, we tested the amount of 20 basic amino acids in aminoacyl tRNA synthesis of peptides from the hMSCs within CBE and CBX hydrogels by using LC-MS method involved a triple quadrupole (QqQ) mass spectrometer. The signal for each amino acid was normalized to the total DNA content and then normalized to the corresponding value of hMSCs before encapsulation. As presented in Fig. 5c, the peptide biosynthesis in hMSCs within CBE hydrogels was up-regulated after the induction of differentiation media. In contrast to the hMSCs within the CBE hydrogels, the peptide biosynthesis in hMSCs within all CBX hydrogels was down-regulated to a great extent compared to the proliferating hMSCs, independent of the amount of added zwitterionic crosslinkers. The metabolism analysis suggests the hMSCs interpret the nonfouling background as a signal to remain quiescent and we believe the restrained metabolic activity in hMSCs is critical of keeping them in a naïve state even after the induction of differentiation media for a long time.

3.3.4Modulating differentiation by cytoskeletal manipulation. It is believed that the differentiation behavior of hMSCs is directly dependent on the cytoskeletal contractility[11,12]. Here, we further evaluated the effect of several pharmacological agents known to modulate the cytoskeleton on the differentiation behavior of encapsulated hMSCs in CBX and CBE hydrogels. The percentage of hMSCs differentiating to adipocytes or osteoblasts in control culture media without the addition of pharmacological agents is shown in Fig. 6a (i) and Fig. 6b (i). It is known that nocodazole can interfere with the polymerization of microtubules, thus increasing the cell contractility[12]. As seen in Fig. 6a (ii), the agent indeed reversed the fate choice of hMSCs in a CBE hydrogel with low modulus and gave a high rate of osteogenesis in all cases. Three other agents that are able to directly inhibit contractility of the cytoskeleton—blebbistatin, which inhibits myosin II, cytochalasin D, which inhibits F-actin polymerization and Y-27632, which inhibits ROCK—resulted in a significant decrease in osteogenesis with a corresponding increase in adipogenesis, with the mechanical property of the CBE hydrogel having no influence on differentiation (Fig. 6a(iii-v)). It is also known that α5β1 integrin can mediate coupling of the cytoskeleton to the extracellular matrix and enable the mechanical signal transduction[12]. Here, we examined cells encapsulated in cRGD-modified CBE hydrogels of varying rigidity in the presence of function-blocking antibodies against α5β1 integrin. We found that most hMSCs committed to adipogenesis in CBE hydrogels in the presence of these antibodies, and the influence of mechanical property on differentiation was removed (Fig. 6a(vi)). We also tested the influence of these pharmacological agents on the differentiation of hMSCs in CBX hydrogels. As presented in Fig. 6b, unlike in CBE hydrogels, the hMSCs in CBX hydrogels of varying rigidity exhibit a very low rate (< 5%) of differentiation and no significant difference was observed among CBX hydrogels treated with different pharmacological agents. These results further demonstrate that actomyosin contractility is not able to influence the fate choice of hMSCs in the absence of non-specific interactions and the non-specific interactions between extracellular matrix and cells are indispensable for hMSCs to initiate the differentiation process.

3.4 Conclusions

In summary, as evidenced by IHC, histological staining and RNA analysis, we show that the absence of nonspecific interactions prevents hMSC differentiation in both 2D and 3D cultures. Stem cells do not undergo differentiation in completely nonfouling hydrogels or on completely nonfouling substrates regardless of materials stiffness even after long-term culture in differentiation media or in the presence of cytoskeletal manipulation agents. The metabolic analysis reveals that the nonfouling background can down-regulate glucose and amino acid metabolism, which restrains hMSCs from differentiation for a long time. Furthermore, as demonstrated by the 2D work, the quiescent hMSCs can be activated again when transferred to a fouling environment such as petri dishes. This work demonstrates the behavior of stem cells under the extreme condition in which non-specific interactions are eliminated. Furthermore, this work demonstrates that varying levels of nonspecific interactions between stem cells and platforms are responsible for their fate choice. These new findings reveal the fundamental mechanism of cell-material interactions in directing stem cell fate and highlight the importance of material chemistry for the long-term maintenance of stem cell multipotency.

Reference

1 Jiang, Y. H. et al. Pluripotency of mesenchymal stem cells derived from adult marrow. Nature 418, 41-49, (2002).

2 Nombela-Arrieta, C., Ritz, J. & Silberstein, L. E. The elusive nature and function of mesenchymal stem cells. Nature Reviews Molecular Cell Biology 12, 126-131, (2011).

3 Discher, D. E., Mooney, D. J. & Zandstra, P. W. Growth Factors, Matrices, and Forces Combine and Control Stem Cells. Science 324, 1673-1677, (2009).

4 Zhu, S., Wei, W. & Ding, S. in Annual Review of Biomedical Engineering, Vol 13 Vol. 13 Annual Review of Biomedical Engineering (eds M. L. Yarmush, J. S. Duncan, & M. L. Gray) 73-90 (2011).

5 Yao, S. et al. Long-term self-renewal and directed differentiation of human embryonic stem cells in chemically defined conditions. Proceedings of the National Academy of Sciences of the United States of America 103, 6907-6912, (2006).

6 Sun, Y., Chen, C. S. & Fu, J. in Annual Review of Biophysics, Vol 41 Vol. 41 Annual Review of Biophysics (ed D. C. Rees) 519-542 (2012).

7 Guilak, F. et al. Control of Stem Cell Fate by Physical Interactions with the Extracellular Matrix. Cell Stem Cell 5, 17-26, (2009).

8 Higuchi, A., Ling, Q.-D., Chang, Y., Hsu, S.-T. & Umezawa, A. Physical Cues of Biomaterials Guide Stem Cell Differentiation Fate. Chemical Reviews 113, 3297-3328, (2013).

9 Engler, A. J., Sen, S., Sweeney, H. L. & Discher, D. E. Matrix elasticity directs stem cell lineage specification. Cell 126, 677-689, (2006).

10 Trappmann, B. et al. Extracellular-matrix tethering regulates stem-cell fate. Nature Materials 11, 642-649, (2012).

11 Kilian, K. A., Bugarija, B., Lahn, B. T. & Mrksich, M. Geometric cues for directing the differentiation of mesenchymal stem cells. Proceedings of the National Academy of Sciences of the United States of America 107, 4872-4877, (2010).

12 Riveline D, Zamir E, Balaban N Q. Schwarz US, Ishizaki T, Narumiya S, Kam Z, Geiger B and Bershadsky AD. Focal contacts as mechanosensors externally applied local

mechanical force induces growth of focal contacts by an mdia1-dependent and rock-independent mechanism. The Journal of cell biology 153, 1175-1186, (2001).

13 Huebsch, N. et al. Harnessing traction-mediated manipulation of the cell/matrix interface to control stem-cell fate. Nature Materials 9, 518-526, (2010).

14 Khetan, S. et al. Degradation-mediated cellular traction directs stem cell fate in covalently crosslinked three-dimensional hydrogels. Nature materials, (2013).

15 Lutolf, M. P., Gilbert, P. M. & Blau, H. M. Designing materials to direct stem-cell fate. Nature 462, 433-441, (2009).

16 Scadden, D. T. The stem-cell niche as an entity of action. Nature 441, 1075-1079, (2006).

17 Higuchi, A., Ling, Q.-D., Hsu, S.-T. & Umezawa, A. Biomimetic Cell Culture Proteins as Extracellular Matrices for Stem Cell Differentiation. Chemical Reviews 112, 4507-4540, (2012).

18 Kilian, K. A. & Mrksich, M. Directing Stem Cell Fate by Controlling the Affinity and Density of Ligand-Receptor Interactions at the Biomaterials Interface. Angewandte Chemie-International Edition 51, 4891-4895, (2012).

19 Mei, Y. et al. Combinatorial development of biomaterials for clonal growth of human pluripotent stem cells. Nature Materials 9, 768-778, (2010).

20 Benoit, D. S. W., Schwartz, M. P., Durney, A. R. & Anseth, K. S. Small functional groups for controlled differentiation of hydrogel-encapsulated human mesenchymal stem cells. Nature Materials 7, 816-823, (2008).

21 Singh, A., Zhan, J., Ye, Z. & Elisseeff, J. H. Modular Multifunctional Poly(ethylene glycol) Hydrogels for Stem Cell Differentiation. Advanced Functional Materials 23, 575-582, (2013).

22 Kloxin, A. M., Kasko, A. M., Salinas, C. N. & Anseth, K. S. Photodegradable Hydrogels for Dynamic Tuning of Physical and Chemical Properties. Science 324, 59-63, (2009).

23 Cao, Z. & Jiang, S. Super-hydrophilic zwitterionic poly (carboxybetaine) and amphiphilic non-ionic poly (ethylene glycol) for stealth nanoparticles. Nano Today 7, 404-413, (2012).

24 Keefe, A. J. & Jiang, S. Poly(zwitterionic)protein conjugates offer increased stability without sacrificing binding affinity or bioactivity. Nature Chemistry 4, 60-64, (2012).

25 Zhang, L. et al. Zwitterionic hydrogels implanted in mice resist the foreign-body reaction. Nature biotechnology, (2013).

26 Jiang, S. & Cao, Z. Ultralow-Fouling, Functionalizable, and Hydrolyzable Zwitterionic Materials and Their Derivatives for Biological Applications. Advanced Materials 22, 920-932, (2010).

27 Kane, R. S., Deschatelets, P. & Whitesides, G. M. Kosmotropes Form the Basis of Protein-Resistant Surfaces. Langmuir 19, 2388-2391, (2003).

28 Kong, H. J., Boontheekul, T. & Mooney, D. J. Quantifying the relation between adhesion ligand-receptor bond formation and cell phenotype. Proceedings of the National Academy of Sciences of the United States of America 103, 18534-18539, (2006).

29 Lian, J. B. et al. Regulatory controls for osteoblast growth and differentiation: role of Runx/Cbfa/AML factors. Critical Reviews™ in Eukaryotic Gene Expression 14, (2004).

30 Reinholt, F. P., Hultenby, K., Oldberg, A. & Heinegård, D. Osteopontin--a possible anchor of osteoclasts to bone. Proceedings of the National Academy of Sciences 87, 4473-4475, (1990).

31 Kliewer, S. A. et al. Fatty acids and eicosanoids regulate gene expression through direct interactions with peroxisome proliferator-activated receptors α and γ. Proceedings of the National Academy of Sciences 94, 4318-4323, (1997).

32 Furuhashi, M. & Hotamisligil, G. S. Fatty acid-binding proteins: role in metabolic diseases and potential as drug targets. Nature Reviews Drug Discovery 7, 489-503, (2008).

33 Pittenger, M. F. et al. Multilineage potential of adult human mesenchymal stem cells. science 284, 143-147, (1999).

34 Barry, F. P. & Murphy, J. M. Mesenchymal stem cells: clinical applications and biological characterization. The international journal of biochemistry & cell biology 36, 568-584, (2004).

35 Kiani, C., Liwen, C., WU, Y. J., Albert, J. Y. & Burton, B. Y. Structure and function of aggrecan. Cell research 12, 19-32, (2002).

36 Berkes, C. A. & Tapscott, S. J. in Seminars in cell & developmental biology. 585-595 (Elsevier).

37 Katsetos, C. D., Herman, M. M. & Mörk, S. J. Class III β - tubulin in human development and cancer. Cell motility and the cytoskeleton 55, 77-96, (2003).

38 Nedvidkova, J., Smitka, K., Kopsky, V. & Hainer, V. Adiponectin, an adipocyte-derived protein. Physiol Res 54, 133-140, (2005).

39 Goldberg, I. J. Lipoprotein lipase and lipolysis: central roles in lipoprotein metabolism and atherogenesis. Journal of Lipid Research 37, 693-707, (1996).

40 Chamberlain, J. R. et al. Gene targeting in stem cells from individuals with osteogenesis imperfecta. Science 303, 1198-1201, (2004).

41 Nakamura, A. et al. Osteocalcin secretion as an early marker of *in vitro* osteogenic differentiation of rat mesenchymal stem cells. Tissue Engineering Part C: Methods 15, 169-180, (2009).

42 Shyh-Chang, N., Daley, G. Q. & Cantley, L. C. Stem cell metabolism in tissue development and aging. Development 140, 2535-2547, (2013).

43 McGraw, T. E. & Mittal, V. Stem cells: Metabolism regulates differentiation. Nat Chem Biol 6, 176-177, (2010).

44 Vacanti, N. M. & Metallo, C. M. Exploring metabolic pathways that contribute to the stem cell phenotype. Biochimica Et Biophysica Acta-General Subjects 1830, 2361-2369, (2013).

45 Gibson, G. E., Peterson, C. & Sansone, J. Decreases in amino acid and acetylcholine metabolism during hypoxia. Journal of neurochemistry 37, 192-201, (1981).

46 Mohyeldin, A., Garzon-Muvdi, T. & Quinones-Hinojosa, A. Oxygen in Stem Cell Biology: A Critical Component of the Stem Cell Niche. Cell Stem Cell 7, 150-161, (2010).

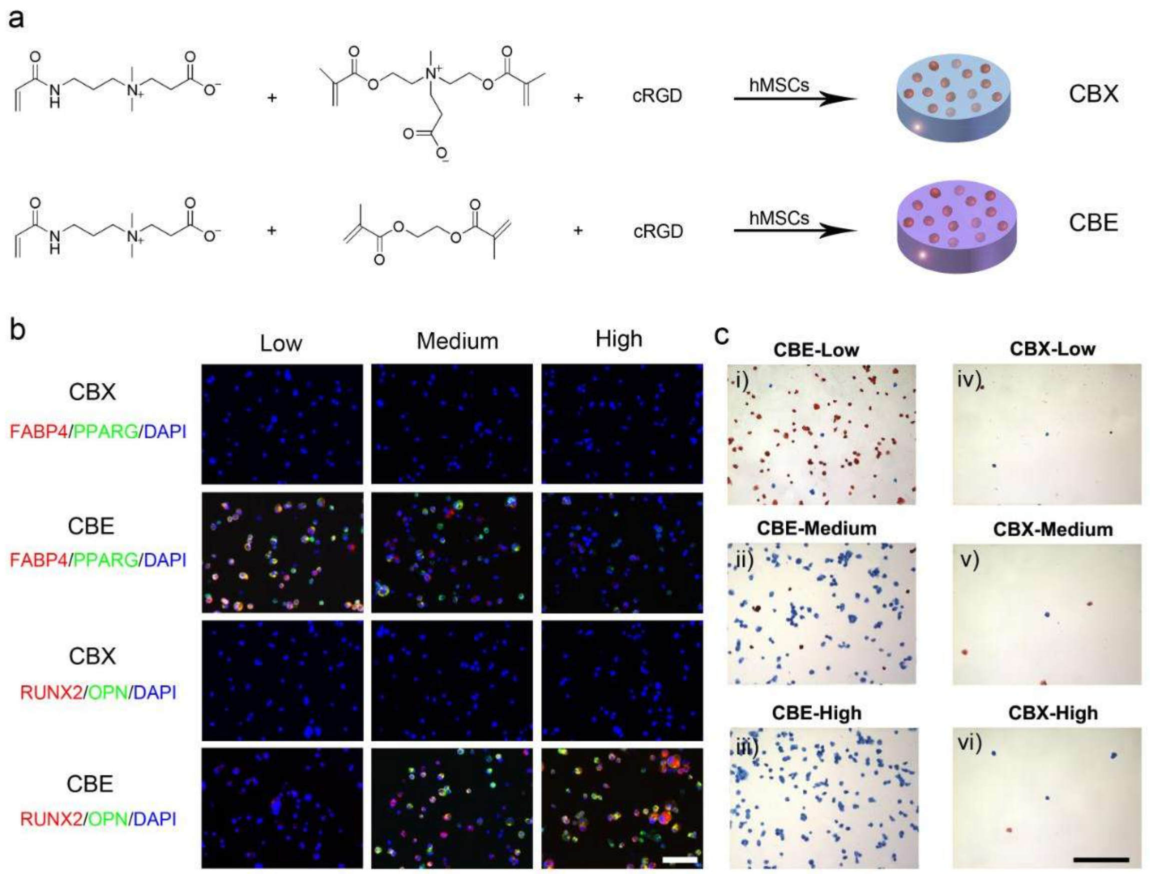

Figure 3.1. Fate determination of hMSCs within 3D nonfouling CBX and fouling CBE hydrogels. a. Schematic illustration of cRGD conjugation to carboxybetaine monomer or crosslinker and cell encapsulation in CBX and CBE hydrogels. **b.** After 7 days of culture in bipotential differentiation medium, cell-hydrogel constructs of CBX and CBE samples were immunostained for adipogenic (PPARG, FABP4) and osteogenic (RUNX2, OPN) biomarkers. Scale bar, 20μm. **c.** Representative bright-field images of Oil Red O and ALP stained hMSCs following 7-day bipotential differentiation medium incubation within CBE, Low (**i**); CBE, Medium (**ii**); CBE, High (**iii**); CBX, Low (**iv**); CBX, Medium (**v**); CBX, High (**vi**). Scale bar, 100μm.

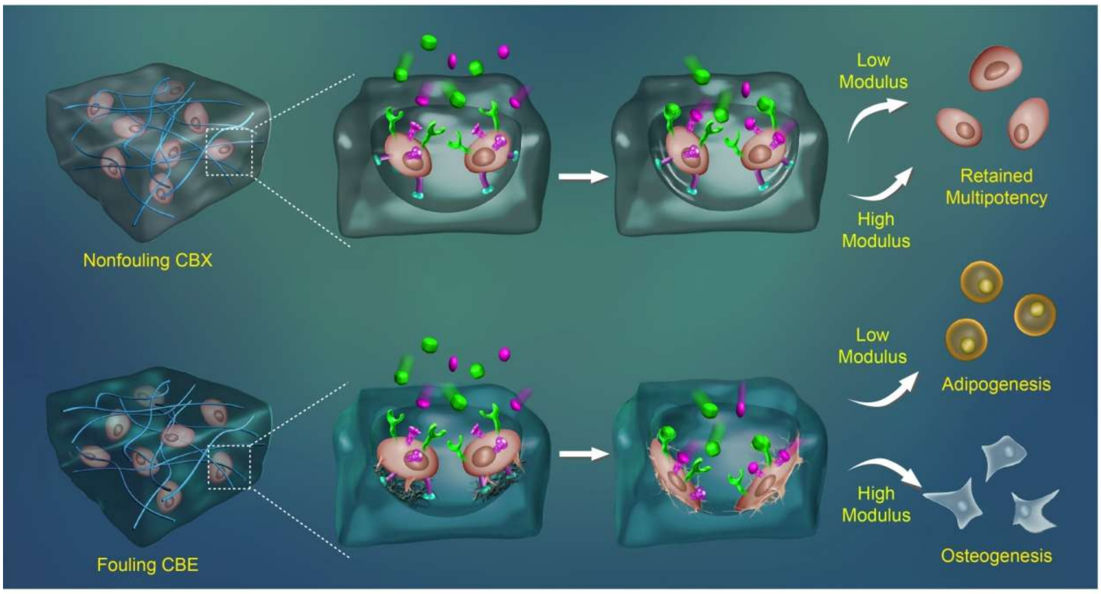

Figure 3.2. Schematic illustration of the behavior and fate choice of hMSCs in CBX or CBE hydrogels. In both CBX and CBE hydrogels, hMSCs were first attached to the matrix by c-RGD moieties (denoted as cyan hemispheres). In nonfouling CBX hydrogels, hMSCs cannot fully interact with the surrounding environment due to the absence of nonspecific binding. The hMSCs in both hard and soft CBX hydrogels will retain their multipotency in the presence of various differentiation factors (denoted as colorful particles). On the other hand, in fouling CBE hydrogels, hMSCs can fully interact with their surrounding matrix, mediated by the nonspecific binding. The hMSCs commit to the adipogenic pathway in soft CBE hydrogels and commit to the osteogenic pathway in hard CBE hydrogels.

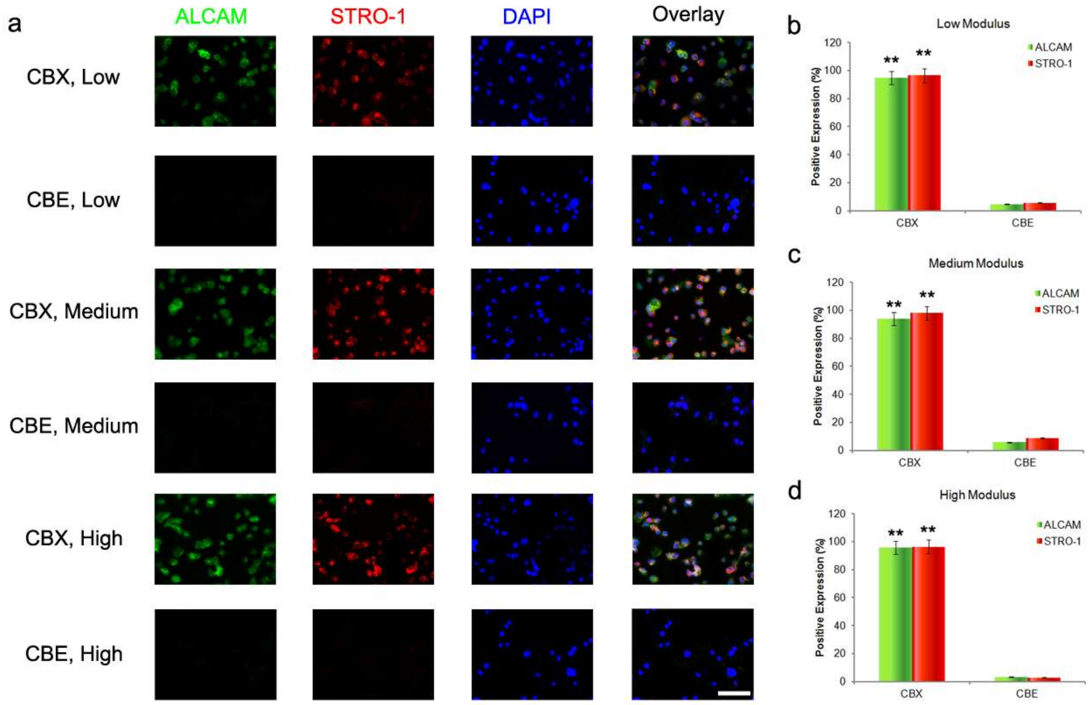

Figure 3.3. The multipotency of hMSCs within 3D CBX and CBE hydrogels. a. By using immunofluorescence staining, undifferentiated hMSCs were detected by visualizing undifferentiated cell markers ALCAM (green) and STRO-1 (red) (nuclei: blue) in CBX hydrogels from low modulus to high modulus. With the introduction of a hydrophobic crosslinker, hMSCs differentiated and hMSC markers were barely detected. Scale bar, 30μm. **b-d.** Percentage of cells expressing either ALCAM or STRO-1 when encapsulated in CBX and CBE hydrogels with different moduli (Low: **b**; Medium: **c**; High: **d**) following incubation for 7 days in bipotential differentiation medium. Asterisks denote statistical significance compared with CBE hydrogels (**$p<0.001$, *t*-test). Error bars represent standard error of the mean from 5 individual experiments.

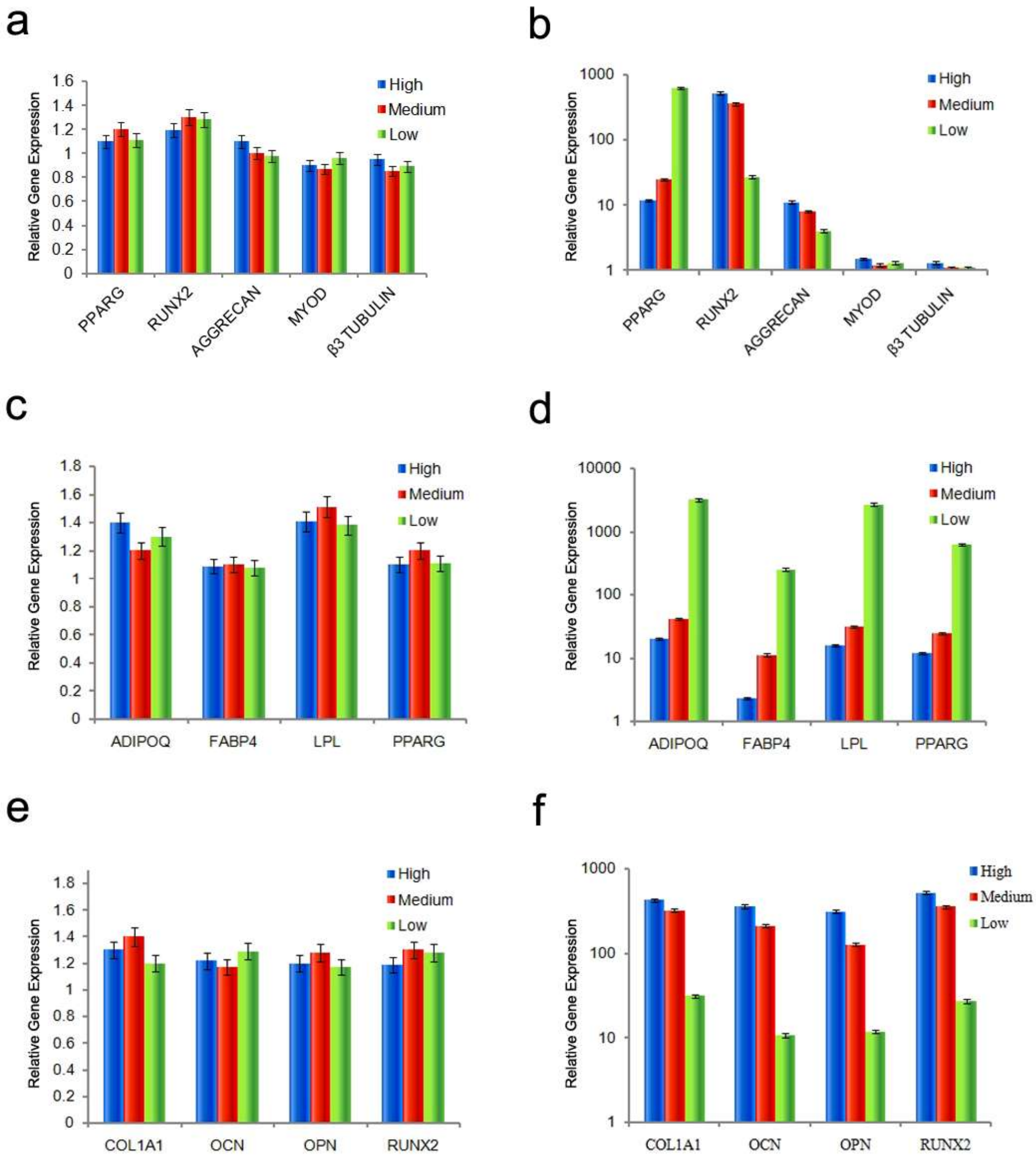

Figure 3.4. qRT-PCR assessment of hMSC differentiation within 3D CBX and CBE hydrogels. a-b. Characteristic differentiation gene activity of hMSCs cultured within CBX and CBE hydrogels in bipotential differentiation medium for 7 days. **c-d.** Adipogenic gene activity of hMSCs cultured in CBX and CBE hydrogels in bipotential differentiation medium for 7 days. **e-f.** Osteogenic gene activity of hMSCs cultured in CBX and CBE hydrogels in bipotential differentiation medium for 7 days. For all osteogenic and adipogenic genes, the percent expression was significantly different between CBX and CBE hydrogels with similar mechanical properties (*p<0.001, *t*-test). Error bars represent standard error of the mean from 5 individual experiments.

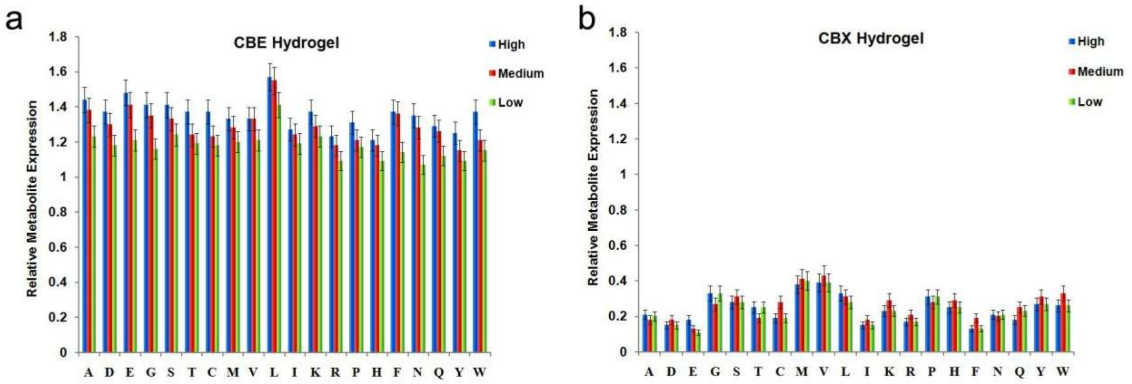

Figure 3.5. Metabolomic analysis of hMSC within 3D CBX and CBE hydrogels. (**a-b**) Total glucose consumption in media of hMSCs within CBE (**a**) and CBX (**b**) hydrogels. Amino acid metabolism of hMSCs in fouling CBE (**c**) and nonfouling CBX (**d**) are displayed in aminoacyl tRNA synthesis after cultured in CBX and CBE hydrogels in bipotential differentiation medium for 7 days.

a. CBE Hydrogel

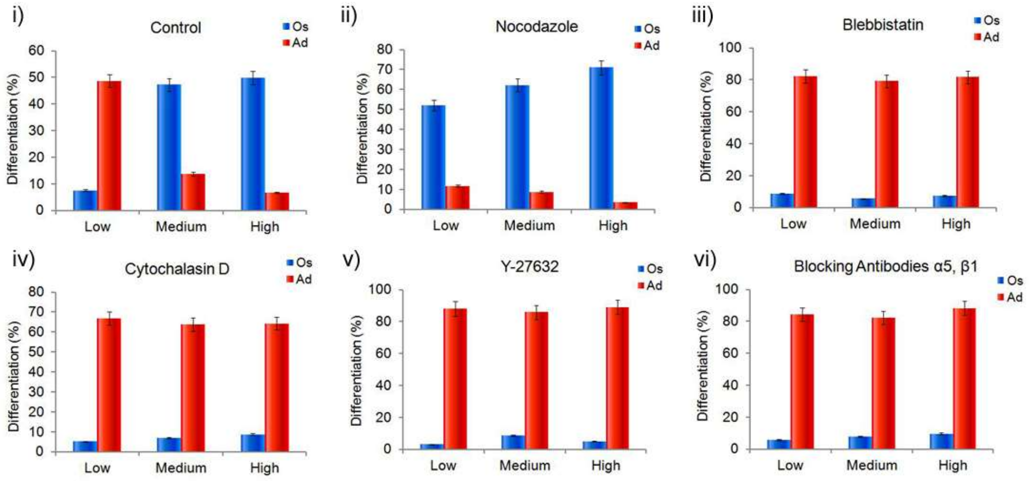

b. CBX Hydrogel

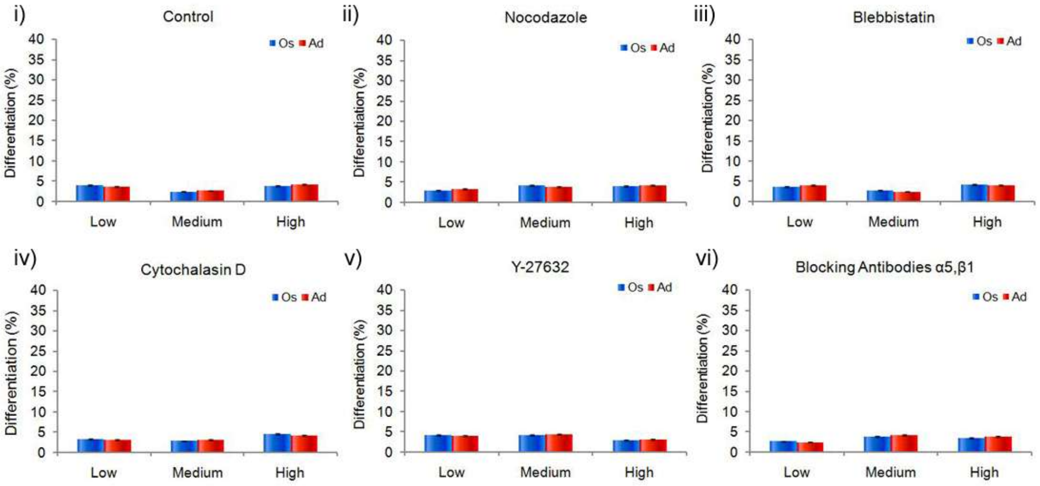

Figure 3.6. Percentage differentiation of hMSCs within CBE (a) and CBX (b) hydrogels after pharmacological agents induced cytoskeletal manipulation. a (i), b (i), Percentage of cells in CBE or CBX hydrogels differentiating to adipocytes or osteoblasts in bipotential differentiation media. **a (ii-vi), b (ii-vi)**, Percentage of cells in CBE or CBX hydrogels differentiating to adipocytes or osteoblasts in the presence of cytoskeleton disruptors and integrin blocking antibodies.

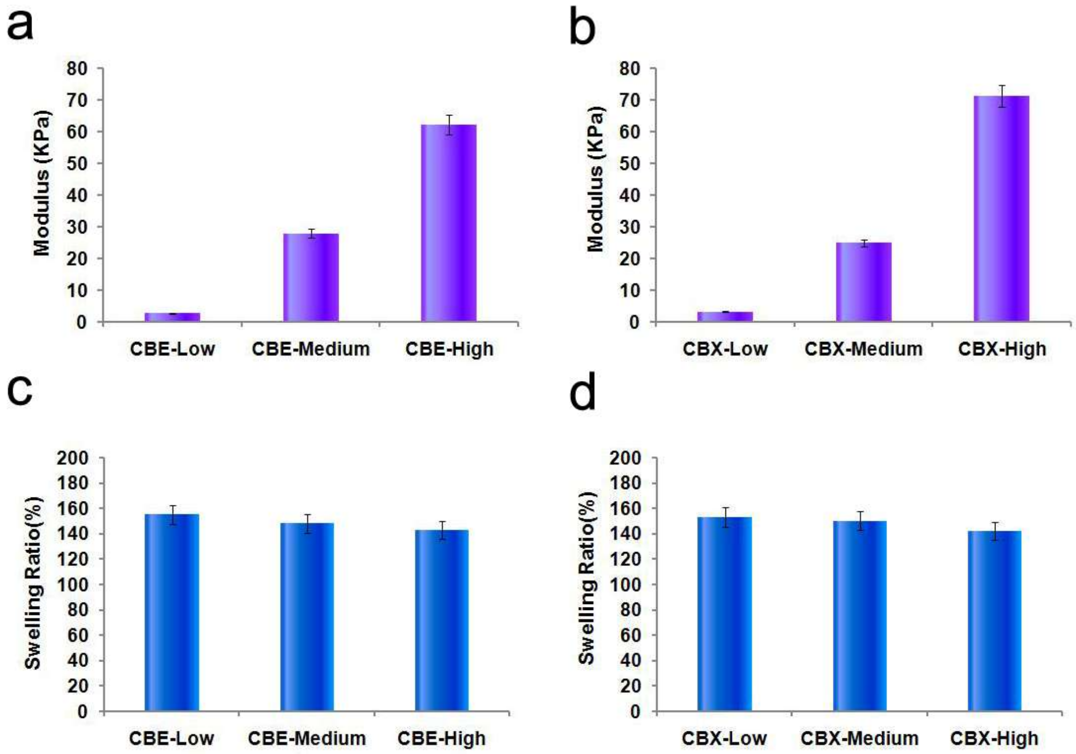

Figure 3.7. Characterization of CBE and CBX hydrogels. (**a-b**) Moduli of CBX and CBE hydrogels. (**c-d**) Swelling ratios of CBE and CBX hydrogels.

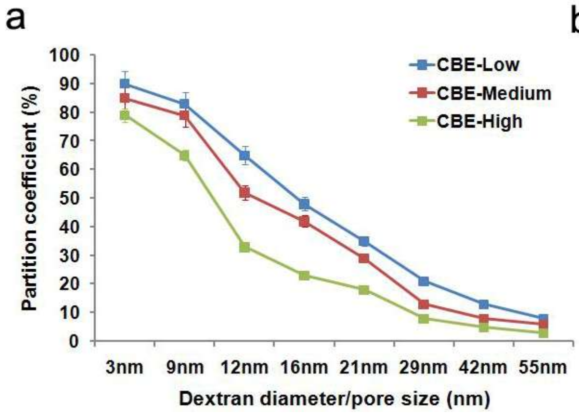

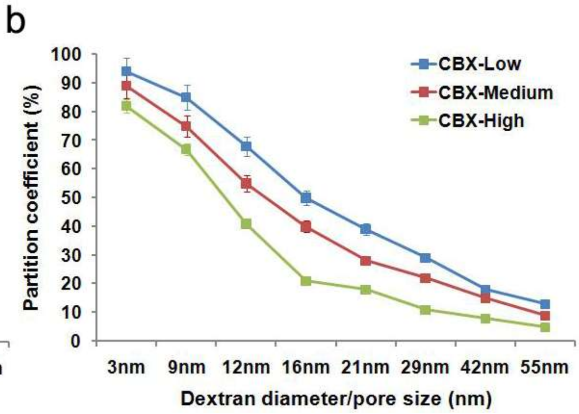

Figure 3.8. Pore size distribution in CBX hydrogels of varying stiffness as measured by diffusion of dextran particles.

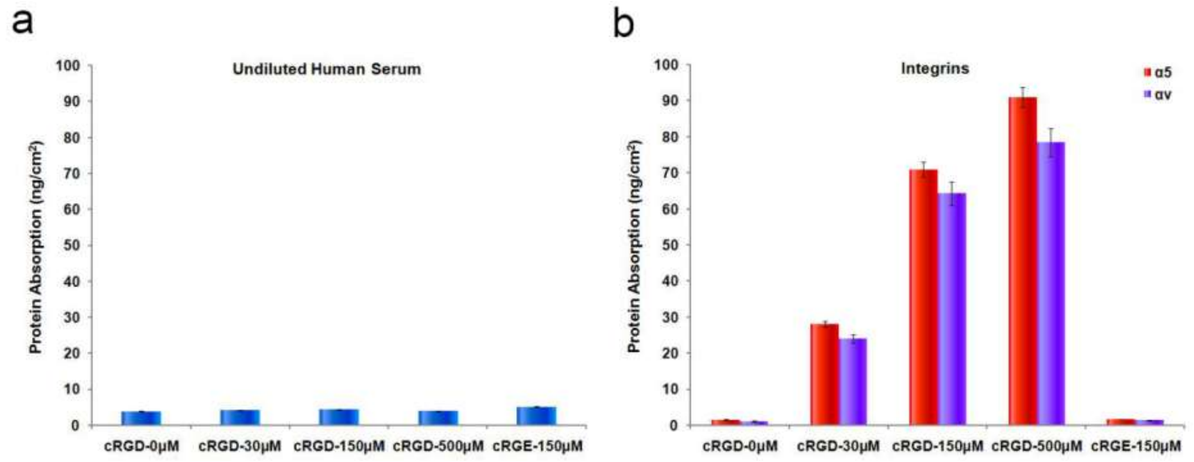

Figure 3.9. Total protein adsorption was measured on a SPR sensor after injection of undiluted human blood serum (**a**) and α_5-integrin and α_v-integrin (**b**) on unfunctionalized, cRGD functionalized and cRGE functionalized polyCBAA surface coatings.

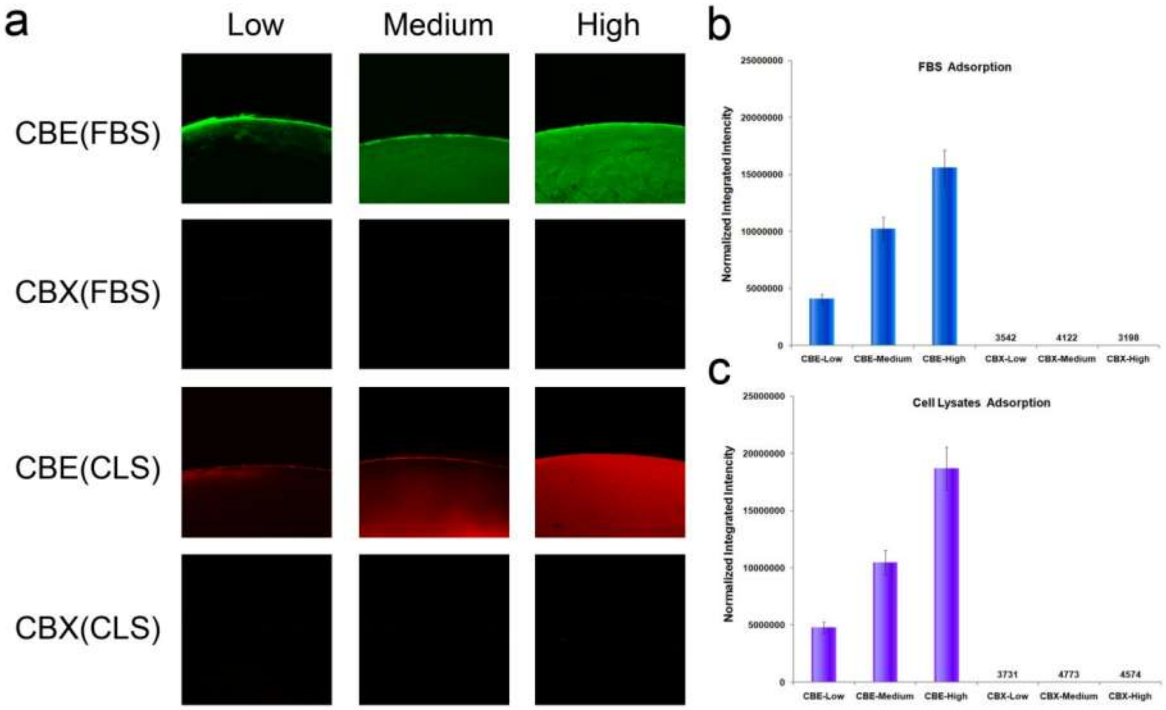

Figure 3.10. Fluorescent characterization of nonspecific protein adsorption on CBE and CBX hydrogels. (**a**) FITC tagged FBS and Rho tagged CLS adsorption on CBE and CBX hydrogels with different mechanical properties. Normalized integrated fluorescent intensity of CBX and CBE hydrogels with different mechanical properties after incubated with FITC tagged FBS (**b**) and Rho tagged CLS (**c**) for 24 h.

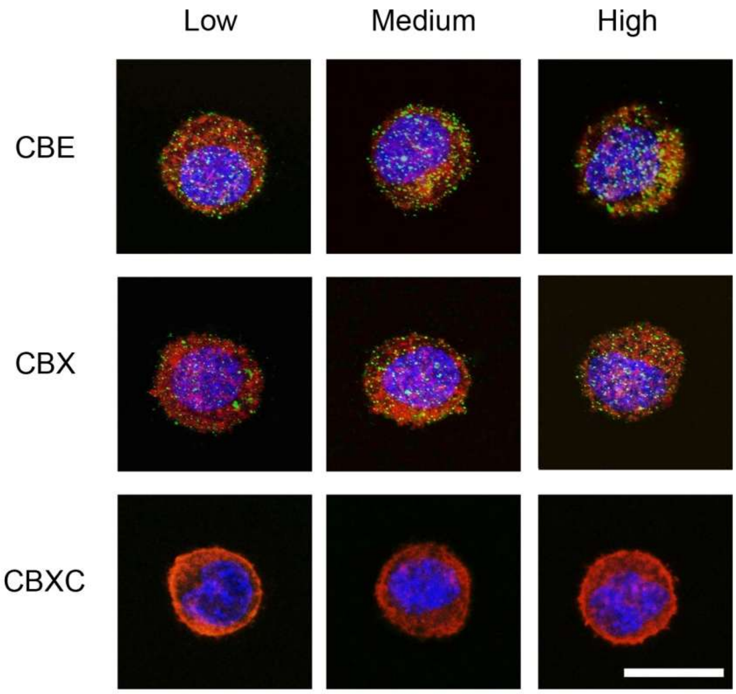

Figure 3.11. Cytoskeletal organization of hMSCs and interaction between them and surrounding matrixes within 3D environment. Immunofluorescence images of hMSCs stained for filamentous actin (red), vinculin (green), and nuclei (blue). CBE and CBX hydrogel presenting 150μM cRGD peptide and controlled CBX hydrogel (CBXC) presenting 150μM cRGE peptide. Scale Bar: 10μm.

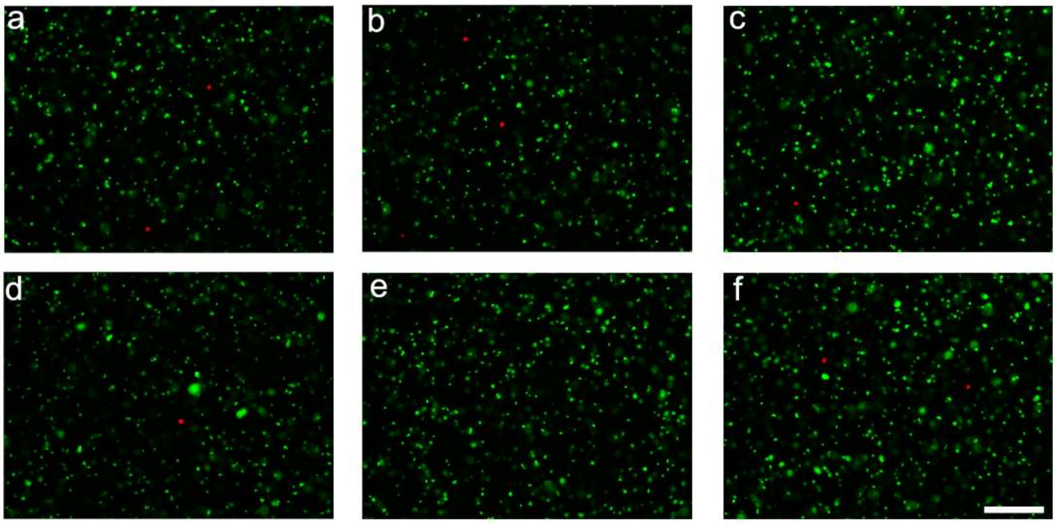

Figure 3.13. Live-Dead stain performed after encapsulating cells in CBX, Low (**a**); CBX, Medium (**b**); CBX, High (**c**); CBE, Low (**d**); CBE, Medium (**e**); CBE, High (**f**) after being cultured in basal medium for 3 days. Scale Bar: 200μm

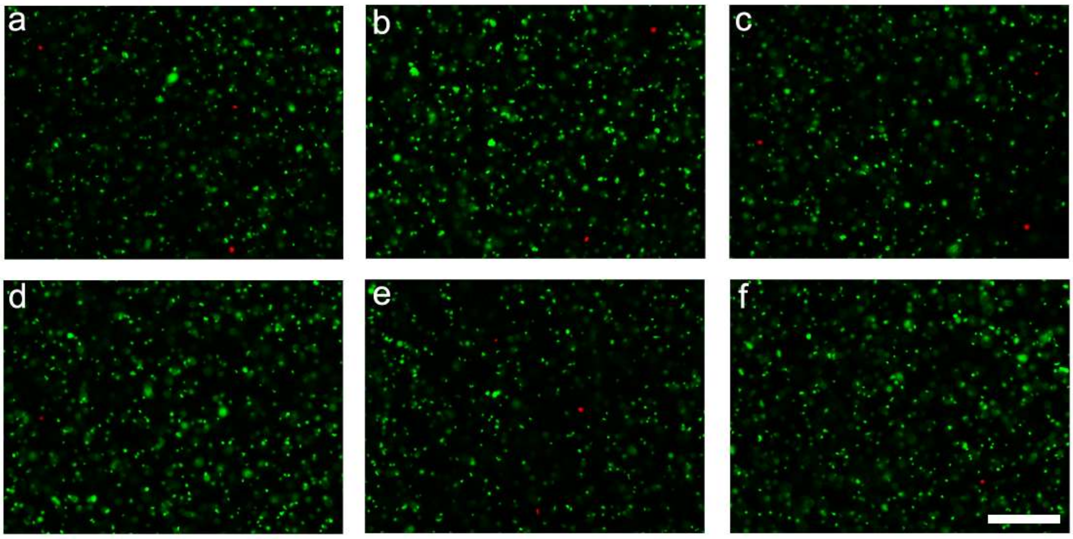

Figure 3.14. After being cultured in basal medium for 3 days and in bipotential differentiation medium for 7 days, Live-Dead stain performed for encapsulated cells in CBX, Low (**a**); CBX, Medium (**b**); CBX, High (**c**); CBE, Low (**d**); CBE, Medium (**e**); CBE, High (**f**). Scale Bar: 200μm

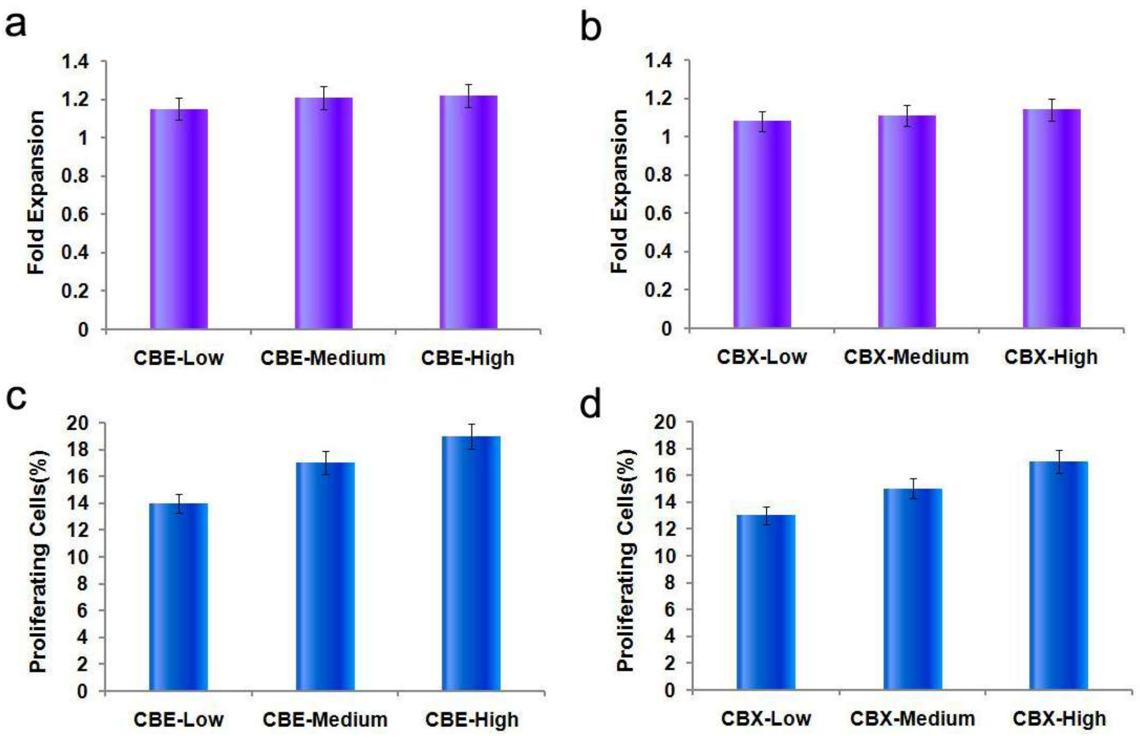

Figure 3.15. The fold expansion of hMSCs in the 3D encapsulation of CBE (**a**) and CBX (**b**) hydrogels examined for 3 day culture in basal medium using MTT assay. hMSCs encapsulated in CBE and CBX hydrogels for 3 days in basal media and tested with Click-iT® EdU Kit. The percentage of proliferating hMSCs in CBE (**c**) and CBX (**d**) hydrogels was quantified shown. Error bars represent standard error of the mean from 5 individual experiments.

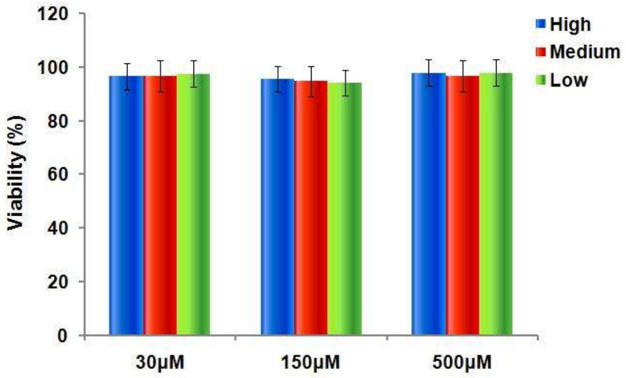

Figure 3.16. The viability of hMSCs when encapsulated into CBE hydrogels with different mechanical properties and cRGD densities following a differentiation culture for 21 days. The data were generated from LIVE/DEAD assay. Error bars represent standard error of the mean from 5 individual experiments.

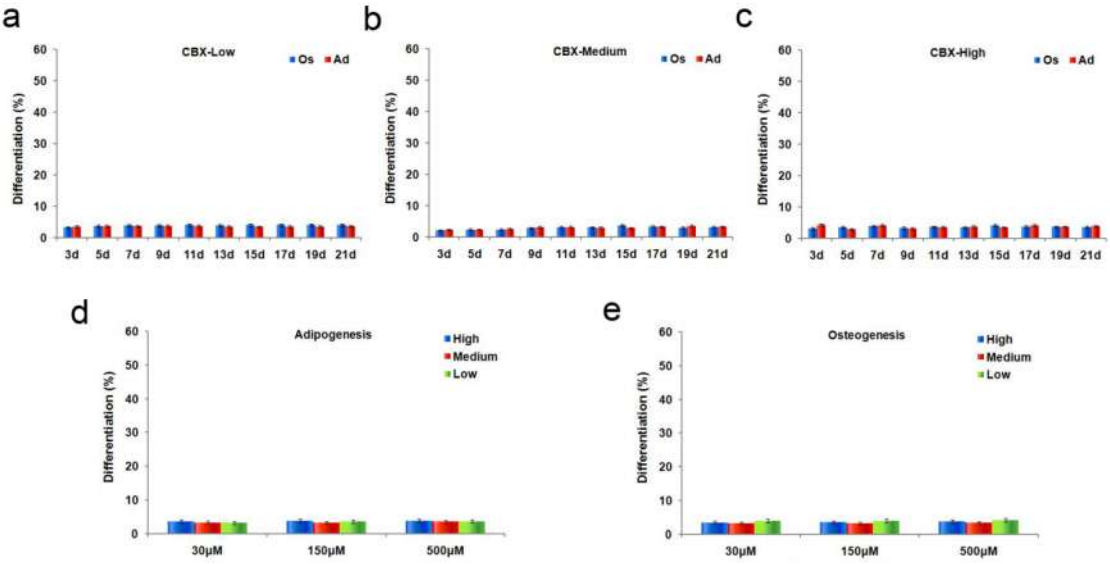

Figure 3.17. The effect of extended differentiation culture period on the differentiation behavior of hMSCs within CBX hydrogels with different mechanical properties and different cRGD concentration for up to 21days. (**a-c**) Percentage of cells in CBX hydrogels (cRGD-150μM) differentiating to adipocytes (Lipid was stained red by Oil Red O) or osteoblasts (ALP was stained blue by Fast Blue salt) in bipotential differentiation media for 21 days. (**d-f**) The effect of varying concentration of presented cRGD on the expression of ALP (**d**) and neutral lipid (**e**) of hMSCs within CBX hydrogels with different mechanical properties.

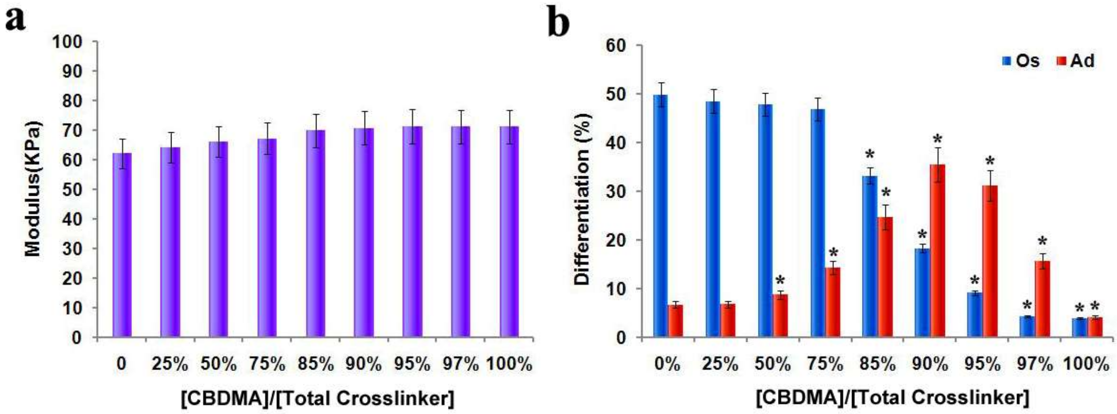

Figure 3.18. PCBAA hydrogels were crosslinked by a combination of hydrophilic CBDMA crosslinker and hydrophobic EGDMA crosslinker while the total molar concentration of crosslinker and monomer concentration are fixed. (**a**) The mechanical property of selected PCBAA hydrogels did not vary significantly with increasing percentage of added CBDMA crosslinker. (**b**) Percentage of hMSCs in PCBAA hydrogels differentiating to adipocytes or osteoblasts as a function of the composition of mixed crosslinkers in normal bipotential differentiation media.

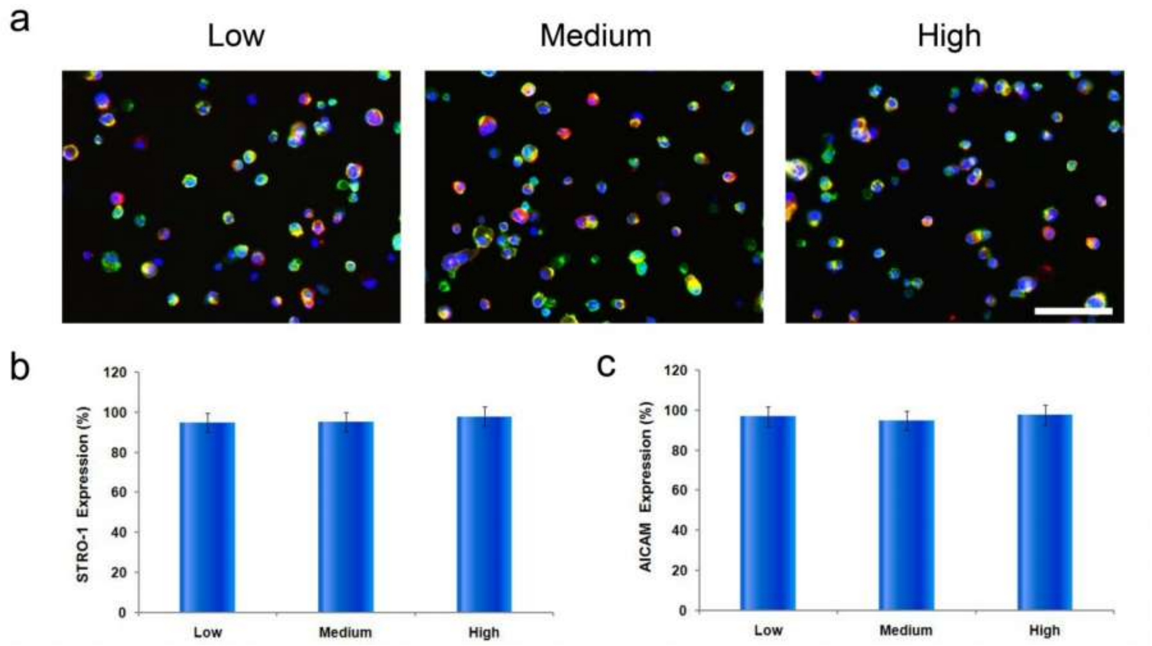

Figure 3.19. The effect of extended differentiation culture period on the multipotency of hMSCs within CBX hydrogels with different mechanical properties for up to 21days.The multipotency of hMSCs within 3D CBX and CBE hydrogels. **a.** By using immunofluorescence staining, undifferentiated hMSCs were detected by visualizing undifferentiated cell markers ALCAM (green) and STRO-1 (red) (nuclei: blue) in CBX hydrogels from low modulus to high modulus. Scale bar, 50μm. **b-c**. Percentage of cells expressing either STRO-1 (**b**) or ALCAM (**c**) when encapsulated in CBX hydrogels with different moduli following incubation for 7 days in bipotential differentiation medium. Error bars represent standard error of the mean from 5 individual experiments.

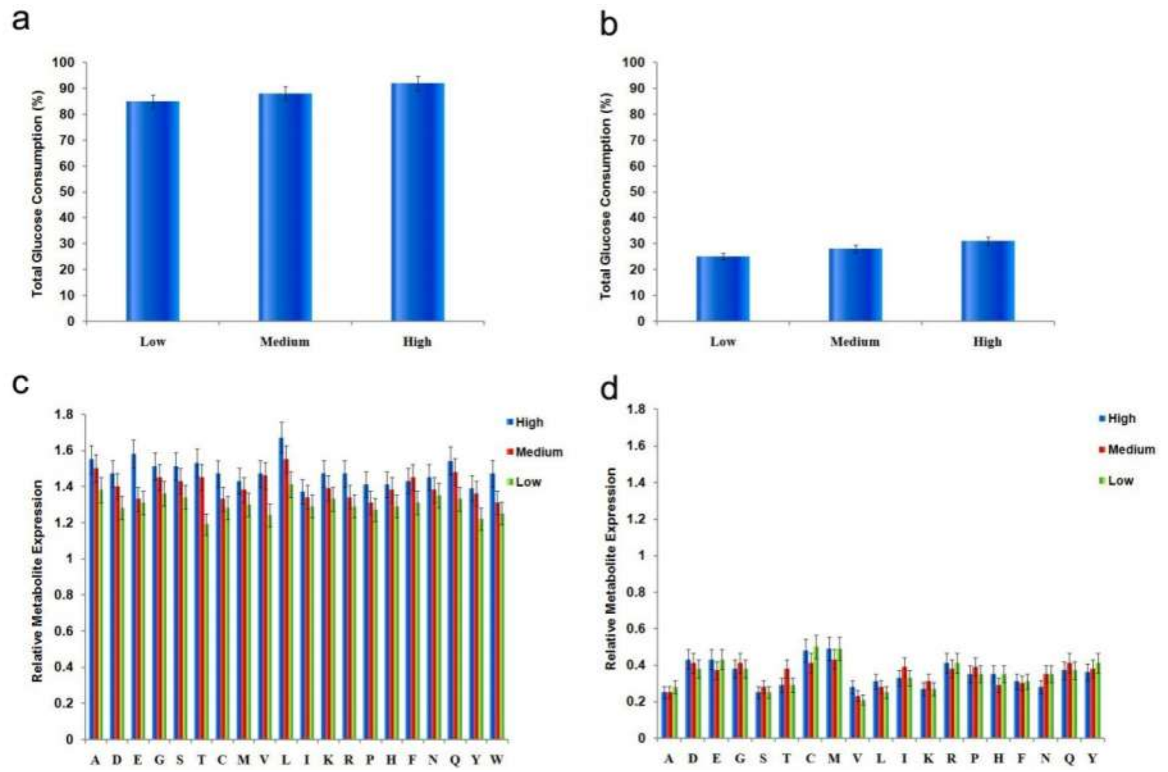

Figure 3.20. Metabolomic analysis of hMSC within 3D CBX and CBE hydrogels. (**a-b**) Total glucose consumption in media of hMSCs within CBE (**a**) and CBX (**b**) hydrogels. Amino acid metabolism of hMSCs in fouling CBE (**c**) and nonfouling CBX (**d**) are displayed in aminoacyl tRNA synthesis after cultured in CBX and CBE hydrogels in bipotential differentiation medium for 7 days.

Chapter 4 Harnessing Isomerization-mediated Manipulation of Nonspecific Cell/matrix Interactions to Reversibly Trigger and Suspend Stem Cell Differentiation

Specific interactions such as protein-cell interaction and drug-cell interaction have been widely used for the manipulation of stem cell fate. Despite extensive studies, most current platforms cannot realize reversible manipulation of stem cell differentiation. In this work, we report a photodynamic zwitterionic hydrogel capable of reversibly triggering and suspending the differentiation process via manipulating nonspecific interactions between cultured stem cells and the hydrogel. The state of differentiated stem cells can be altered when the hydrogel is exposed to a selected light program, while the differentiation can be immediately suspended when the hydrogel is converted into a pure zwitterionic form by light. Unlike other existing studies controlling the fate of stem cells via specific interactions, this work provides a completely different approach, allowing reversible, real-time and site-specific manipulation of the fate choice of stem cells via nonspecific interactions.

4.1 Introduction

Hydrogels with advanced integrated functions have numerous potential applications in the biomedical field, especially for stem cell-based tissue engineering[1-3]. Strategies to provide 'smart' capabilities to hydrogels primarily seek to achieve matrices that are instructive/inductive to neighboring stem cells, or that stimulate/trigger desired stem cell responses that are crucial in the tissue regeneration processes[4, 5]. The ability to control biophysical and biochemical properties of a hydrogel with an external stimulus is highly desirable and actively studied[5, 6]. Conventional smart hydrogels can be actuated via a change in pH, temperature or ionic strength as a bulk material[7, 8]. However, the most desired type of scaffold would realize dynamic heterogeneity like natural tissues, which is unrealistic to achieve via the bulk stimuli mentioned above[9]. Unlike these bulk stimuli-responsive hydrogel systems, light-induced hydrogels have numerous advantages—specific wavelengths can be delivered with high spatial and temporal precision, no chemical contamination is introduced, and closed systems such as a hydrogel-cell constructs can be conveniently and easily actuated[9-13]. For example, the biophysical properties of photoresponsive hydrogels can be tuned by photolysis with the utilization of photoscissile bonds[11, 14-16] or by means of bulk photodegradation[17-21]. Moreover, the biochemical properties of photoresponsive hydrogels can be manipulated by conjugating signaling ligands via site-specific photoconjugation chemistries such as thiol-ene addition[10, 12, 22], Michael-type chemistry[23, 24] and photo-induced click cycloaddition[25] with the aim to upregulate specific stem cell activity pathways. These biophysical and biochemical manipulations can also be employed simultaneously, providing dynamic environments with the scope to answer fundamental questions about material regulation of live cell functions and advancing applications from drug delivery platform design to tissue engineering systems[11]. Investigations of photoswitchable molecules including azobenzenes[26], stilbenes[27], spiropyrans[28, 29], diarylethenes[30], fulgides[31], and others[32-34], have built a helpful toolbox employable for the construction of light-responsive systems and materials. However, none of these aforementioned light-induced materials enable both reversible photocleavage/conjugation reactions[29] and restraint of stem cell differentiation, making it hard to realize continuously programmed manipulation of stem cell fate and to provide a reference state from which biophysical and biochemical cues can be introduced and studied.

In our previous study, ultra-low fouling zwitterionic poly(carboxybetaine)-based materials have been demonstrated to be capable of restraining the differentiation of human mesenchymal stem cells (hMSCs) due to the complete elimination of nonspecific interactions with cells[35-41]. This finding encouraged us to develop a zwitterionic hydrogel platform responsive to external stimuli and explore the influence of nonspecific interactions on the differentiation behavior of stem cells using this hydrogel platform and its useful reference state. Spiropyran is a unique photoresponsive molecule we hypothesized would complement this platform, as its two isomers have vastly different properties. It can assume a zwitterionic hydrophilic form (Merocyanine, MC), a closed-ring hydrophobic form (Spiropyran, SP), or switch in between continuously and reversibly when exposed to invisible near-infrared (NIR) or visible green light[29]. In a polar solution[42] such as water, exposure to NIR light is able to convert SP moieties into MC moieties via two-photon excitation (TPE), while visible green light converts MC moieties back to SP moieties via single-photon excitation (SPE)[43].

In this work, a dynamic photoresponsive zwitterionic hydrogel containing spiropyran was developed, comprising a copolymer of static zwitterionic monomer carboxybetaine acrylamide (CBAA) and photoswitchable monomer spiropyran methacrylate (SPMA), crosslinked with zwitterionic carboxybetaine dimethacrylate (CBDMA). Prior to gel formation, CBAA was functionalized with cellular recognition peptide cyclic-RGD (cRGD) to mediate stem cell adhesion. As we have previously demonstrated, the sequence of cRGD allows functionalized CB molecules to maintain a neutral charge and remain highly resistant to nonspecific protein binding[41]. HMSCs were encapsulated within the described hydrogel during gel formation. The resulting cell-hydrogel constructs were then incubated in a bipotential (osteogenic and adipogenic) differentiation medium under photoirradiation by two constructively interacting NIR and green lights. Tuning the strength of each light enables the balance between hydrophobic SP and hydrophilic MC moieties in the construct to be deliberately modulated. Consequently, nonspecific interactions between hMSCs and their culture platform can be tuned spatially and temporally. The results show that the differentiation restraint, lineage programming, and precise spatiotemporal control of differentiated hMSC can be achieved with this photoactuated zwitterionic hydrogel platform.

4.2 Experimental Section

4.2.1 Preparation of hMSC lysates. hMSCs at passage 3-4 were pelleted (1000 rpm, 4°C) and lysed into RIPA buffer (Sigma) which enables efficient cell lysis and protein solubilization while avoiding protein degradation and interference with the proteins' immunoreactivity and biological activity. The protein content of purified cell lysates was determined via BCA assay.

4.2.2 Preparation and purification of cRGD-functionalized CBAA monomer. As we reported before, Cyclo(RGDYKEG) peptide (cRGD) was functionalized to the system. In brief, appropriate amounts of N-(3-Dimethylaminopropyl)-N'-ethylcarbodiimide hydrochloride (EDC) (Sigma) and N-Hydroxysuccinimide (NHS) (Sigma) were added to CBAA monomer solution. After incubation at 25°C for 1 hour to activate the carboxylate group, an appropriate amount of cRGD was added to the activated system. The molar concentration of cRGD in the reaction solution was set at 150μM. The molar ratio of EDC, NHS and peptides was fixed at 1:1:1. The reaction was allowed to proceed at 25°C for 24 hours before purification. The efficiency of the reaction was calculated by LC-MS (Yield 78%).

An Agilent 1200 LC 6520 Q-Tof MS system (Agilent Technologies, Santa Clara, CA) was employed to purify the functionalized monomer and quantify the efficiency of the conjugation reaction. In brief, after the reaction, monomer sample was injected. The chromatographic separation was performed in hydrophilic interaction chromatography (HILIC) mode on a SeQuant ZIC-cHILIC column (150 x 2.1 mm, 3.0 μm particle size, Merck KGaA, Darmstadt, Germany). The flow rate was 0.500 mL/min, auto-sampler temperature was kept at 4°C, the column compartment was set at 40°C, and total separation time for both ionization modes was 40 min. The mobile phase was composed of Solvents A (5 mM ammonium acetate in 90% H_2O/10% acetonitrile + 0.2% acetic acid) and B (5 mM ammonium acetate in 90% acetonitrile/10% H_2O + 0.2% acetic acid). The gradient conditions are shown below.

Time Segment, min.	Solvent A, %	Solvent B, %
0 – 1	25	75
1 - 5	from 25 to 70	from 75 to 30
5 - 9	70	30
9 – 9.1	from 70 to 25	from 30 to 75
9.1 – 40 (equilibration)	25	75

The Q-Tof mass spectrometer was equipped with an electrospray ionization (ESI) source. The instrument was controlled by an Agilent Mass Hunter Workstation (Agilent Technologies, Santa Clara, CA). The ESI voltage was set at 3800 volts. The source gas was N_2 (99.999% purity). The ion source conditions in positive mode were: drying gas = 10 L/min, nebulizer gas = 45 psi, temperature=325°C. The extracted ion chromatography (EIC, cRGD m/z=804.3602, cRGD-CBAA m/z=1015.5102,) peaks were integrated using Agilent Mass Hunter Qualitative Analysis software (Agilent Technologies, Santa Clara, CA). The functionalized monomers were purified by the LC system and obtained via lyophilization.

The functionalization efficiency was determined using $(V_c - V_f) / V_c \times 100$ (%), where V_f was the integrated value of the free cRGD after the reaction and V_c was the integrated value of the free cRGD in the aqueous solutions in which no coupling agents (EDC or NHS) were added.

4.2.3 Preparation of 3D hMSCs-PCB hydrogel constructs. An appropriate amount of CBAA, cRGD-functionalized CBAA, SPMA and CBDMA were dissolved in 40uL PBS. The molar concentration of CBAA, cRGD-functionalized CBAA, SPMA was fixed at 2M, 150mM, 10mM respectively and the molar concentration of crosslinker was adjusted to 20mM to produce hydrogels of desired mechanical rigidity.

For 3D cell-hydrogel constructs, cell/precursor solution (40μL) containing 6.1×10^7 cells ml^{-1} was used. Photoinitiator 2-hydroxy-2-methylpropiophenone was then added and mixed thoroughly to produce a final concentration of 0.05% (w/v). The solution was placed between two glass slides separated by 1.5 mm-thick polytetrafluoroethylene spacers and allowed to polymerize in a crosslink oven (XL-1500B UV Crosslinker, Spectronics Corporation, NY, USA) for 30s. The cell-encapsulating PCB hydrogels were equilibrated in basal media. During the first 5-hour equilibration, the basal media was refreshed every hour, and then refreshed every day. Visible and infrared light exposure was applied by employing customized MaxMax lighting system.

4.2.4 Viability assay. The viability of encapsulated cells was examined by using a LIVE/DEAD assay kit (Invitrogen). In order to remove the influence of cells on the surface of the gel, a 20 μm slice of the hydrogel from the surface was removed. Representative micrographs were acquired using a Zeiss LSM 510 META confocal microscope. At least three independent constructs were used. Three sections were sampled every 250-300 μm across the depth of the hydrogel and at least five different fields were randomly examined in each section. A Z-sampling rate of 2.1 μm was used for image acquisition.

4.2.5 Characterization of hydrogels. The hydrogels were obtained as described above and placed into PBS to reach equilibrium for at least five days before mechanical tests. At least five 0.5 cm diameter disks of each formulation (1.5 mm thickness when cast) were compressed at a rate of 1 mm/min using an Instron 5543A mechanical tester (Instron Corp., Norwood, MA) with a 10 kN load cell. The Young's modulus was calculated from 3% to 13% strain to avoid any complications in an instance in which the top plate may not be completely engaged with the specimen when compression begins.

The swelling ratios were determined using $(D_s/D_o) \times 100$ (%), where D_s was the diameter of the fully swollen hydrogels and D_o was the diameter of the relaxed (unswollen, but not dehydrated) hydrogels.

4.2.6 Preparation of self-assembled monolayers. Glass chips were first coated with an adhesion-promoting chromium layer (thickness 2 nm) and a surface-plasmon-active gold layer (48nm) by electron beam evaporation under vacuum. Before self-assembled monolayer (SAM) preparation, the gold-coated glass substrate was rinsed with ethanol and water in sequence, dried with filtered air, then further cleaned in a UV ozone cleaner (Jelight, model 42) for 20 min. The cleaned chip was immediately soaked in a 0.1 mM ethanol solution of ATRP initiator for 24 h to form a SAM on the gold surface[1]. The chip was subsequently rinsed with THF, then ethanol, and dried with a stream of filtered air just prior to surface-initiated polymerization.

4.2.7 Surface-initiated atom transfer radical polymerization. Surface-initiated ATRP was carried out on SAM-coated gold substrates following a method similar to one previously reported[1]. Briefly, CuBr, $CuBr_2$, BPY, and gold chips with immobilized initiators were placed in a sealed reaction tube and deoxygenated via vacuum and nitrogen purging. CBAA monomer was deoxygenated in a separate sealed tube, and then dissolved in a deoxygenated solution of methanol and pure water in a 10:1 volume ratio. The monomer solution was transferred to the reaction tube using a syringe under nitrogen protection. In a shaker at 120 RPM and 25°C, PCBAA was allowed to react for 3 h. After polymerization, chips were removed, rinsed with pure water and PBS, and stored overnight in PBS. Chips were rinsed with Milli-Q water and dried with filtered air just prior to any experiments. Dry film thickness was measured with an ellipsometer (J.A. Woollam, Alpha-SE), and chips with thicknesses of 20-30 nm were used for SPR measurements.

4.2.8 Measurements of protein adsorption: HMSCs lysates and FBS were used for the protein absorption assay. This study used a custom-built surface plasmon resonance (SPR) sensor from the Institute of Photonics and Electronics, Academy Sciences (Prague, Czech Republic). A prepared chip was attached to the base of the prism and optical contact was established using refractive index matching fluid (Cargille). A quadruple-channel flow cell with four independent parallel flow channels was used to contain liquid samples during experiments. A peristaltic pump (Ismatec) was utilized to deliver liquid samples to the four channels of the flow cell. A stable baseline was first established with PBS, then protein solution was delivered to the surface at a flow rate of 0.050 mL/min for 30 min, and finally the PBS was flowed again for 10 min before determining final wavelength shifts. A surface-sensitive SPR detector was used to monitor surface interactions in real time, and wavelength shift was used as an indication of changes on the surface.

4.2.9 Nonspecific protein adsorption on photodynamic hydrogels. After incubation with CLS or FBS, the hydrogel were rinsed with PBS before fluorescent detection. FluoroTag™ FITC Conjugation Kit (Sigma) and Rhodamine Conjugation Kit (Abcam) were used to label CLS and FBS as per manufacturer's instructions. Protein adsorption was detected by using Zeiss LSM 510 META confocal microscope. For all stacking images, a Z-sampling rate of 2.5μm was used for image acquisition.

4.2.10 Immunohistochemistry. After induced differentiation for 21 days, cell-hydrogel constructs were fixed in 4% paraformaldehyde in PBS for 8 hours, transferred to 30 wt% sucrose for 72 h, frozen in Cryo-gel (Instrumedics, Inc.) and cryosectioned (10μm sections). In order to remove the influence of the cells on the surface, a 20 μm slice of the hydrogel from the surface was removed. Vinculin-containing focal adhesion was stained by using ProteoExtract® Cytoskeleton Enrichment and Isolation Kit (EMD Millipore) per the manufacture instruction. The F-actin filaments were stained with CytoPainter F-actin Staining Kit (Abcam) and mounted with ProLong Gold antifade reagent with DAPI and allowed to cure overnight.

Triple-label immunofluorescence staining was used to visualize differentiation markers and pluripotent markers. Mouse anti-RUNX2 (Abcam) and rabbit anti-OPN (Abcam) were used to visualize osteogenesis. Rabbit anti-PPARG (Abcam) and mouse anti-FABP4 (Abcam) were used to visualize adipogenesis. The cells were permeabilized for 10 minutes with PBT (0.1% Triton X-100 in PBS). After blocking for 1h in 10% fetal bovine serum, substrates were incubated with primary antibodies for 8 h at room temperature. Then, two types of secondary antibodies with different fluorescence tags, donkey anti-rabbit IgG (Invitrogen), and donkey anti-mouse IgG (Invitrogen), were used to visualize the antibodies of differentiation markers. 4,6-diamidino-2-phenylindole (DAPI; Molecular Probes) was included in the secondary solution and samples were mounted on glass slides with ProLong® Gold reagent. Representative micrographs were acquired using a Zeiss LSM 510 META confocal microscope. At least three independent constructs were used. Three sections were sampled every 250-300 μm across the depth of the hydrogel and at least five different fields were randomly examined in each section.

4.2.11 Quantitative Real Time PCR. At appropriate time points, constructs were removed from the culture media. Then, the constructs were transferred in TRI REAGENT (Sigma) in RNase-free test tubes and were homogenized with a tissue homogenizer. Total RNA was extracted according to the manufacturer's instructions. Total RNA for each sample was quantified with a UV spectrophotometer and converted to cDNA using the QuantiTect Reverse Transcription Kit. After amplification by using SYBR Green PCR Master mix (Qiagen), thermocycling was carried out in a solution with primers (Integrated DNA Technologies) and cDNA. PCR conditions were as follows: 15s at 94 ºC, 30s at 55ºC, and 30s at 72ºC. The primer sequence is summarized in Table 1[2-11]. Here, we used RNase-free DNase (Qiagen) to prevent genomic DNA contamination.

4.2.12 Osteogenic/Adipogenic Differentiation. Cell-hydrogel constructs were cultured in basal medium for 3 days. Following this time point, the basal medium was replaced with bipotential differentiation medium—low glucose DMEM supplemented with 20% FBS and 1% penicillin/streptomycin (Invitrogen); Adipogenic supplement: 1μM dexamethasone, 50μM indomethacin (Sigma), 0.5μM 3-isobutyl-1-methylxanthine (IBMX; Sigma) and 10μg/mL human recombinant insulin (Invitrogen); Osteogenic supplement: 10mM β-glycerol phosphate (Sigma), 50μg/mL ascorbic acid (Sigma). Media changes were performed every 3 days.

As a parallel control, a mixed adipogenic/osteogenic inductive media was made by combining commercially available osteogenic and adipogenic inductive media (R&D Systems) in a 1:1 ratio and supplementing with 1% (v/v) penicillin-streptomycin (Gibco). The mixed media was also used for the differentiation experiment mentioned above and no significant difference was observed compared to the lab-made bipotential differentiation medium.

4.2.13 Histological Analysis on hMSC differentiation. After incubation for 3 weeks, cell-hydrogel constructs were fixed in 4% paraformaldehyde in PBS for 8 hours, transferred to 30 wt% sucrose for 72 h, frozen in Cryo-gel (Instrumedics, Inc.) and cryosectioned (10μm sections). In order to remove the influence of the cells on the surface, a 20 μm slice of the hydrogel from the surface was removed. At least three independent constructs were used. Three sections were sampled every 250-300 μm across the depth of the hydrogel and at least five different fields were randomly examined in each section. ALP activity (osteogenic biomarker) and neutral lipids (adipogenic biomarker) were visualized by Fast Blue BB (Sigma) and Oil Red O (Sigma). The total cell counts were obtained by staining the nuclei with DAPI. By dividing the positive stained cells for ALP and Oil Red O, respectively, by the total cell counts, the percentage of differentiated hMSCs proceeding through osteogenesis and adipogenesis was calculated. Color micrographs were acquired using a Nikon E800 upright microscope.

4.2.14 Inhibition assays. Inhibitors were added to cell culture media at the following concentrations without causing apparent changes to the viability of encapsulated hMSCs. Nocodazole (1.1μM), Cytochalasin D (0.25μM), Blebbistatin (1μM), and Y-27632 (1.8μM) (Calbiochem). Integrin blocking antibodies (α5 and β1, Chemicon) were added at 1.1ug/mL in the process of cell encapsulation.

4.2.15 Statistical analysis. Examination and quantification of histological sections was done by three independent researchers blinded to sample identity with at least five random images/fields in each section per sample. A two-tailed Student's *t*-test was used for all statistical analyses, with $^*p<0.05$ being considered as statistically significant.

4.2.16 Synthesis of 1-(2-Hydroxyethyl)-2,3,3-trimethyl-3H-indolium bromide

A mixture of 2,3,3-trimethyl-3H-indole (25.0 g, 0.157 mol) and 2-bromoethanol (24.5 g, 0.196 mol) and acetonitrile (192 mL) were placed in a flask. The solution was heated at 90 °C for 24 h under nitrogen protection. After cooling down to ambient temperature, the solvent was evaporated under reduced pressure. The solid obtained was purified by solvent extraction with benzene for 24 h, and then dried overnight in vacuum. The product was further recrystallized from a mixed solvent of methanol (50 mL) and diethylether (150 mL) to obtain 1-(2-hydroxyethyl)-2,3,3-trimethyl-3H-indolium bromide (32.8 g, 71.6 %) as pink solid. ^{1}H NMR (300 MHz, DMSO d6): d: 7.79 (m, 2H), 7.73 (m, 2H), 4.70 (t, 2H, J ¼ 8 Hz), 4.13 (t, 2H, J ¼ 8 Hz), 2.18 (s, 3H), 1.6 (s, 6H). ^{13}C (50 MHz, DMSO d6) d: 200.74, 144.4, 143.36, 132.48, 131.56, 126.1,117.74, 60.85, 57.4, 52.84, 24.69, 12.68.

4.2.17 Synthesis of 9,9,9a-trimethyl-2,3,9,9a-tetrahydro-oxazolo3,2-aindole. A solution of 1-(2-hydroxyethyl)-2,3,3-trimethyl-3H-indolium bromide (4.30 g, 15.90 mmol) and KOH (0.93g, 16.57mmol) in water (50 mL) was stirred at room temperature for 20 min. The product was extracted with ether and obtained under reduced pressure as yellow oil (Yield: 96.23%). 1H-NMR ($CDCl_3$): δ = 7.2-7.07 (m, 2H), 6.91 (t, 1H), 6.73 (d, 1H,), 3.79-3.62 (m, 2H), 3.53-3.46 (m, 2H), 1.38 (s, 3H), 1.34 (s, 3H), 1.18 (s, 3H). ^{13}C-NMR ($CDCl_3$): δ= 150.30, 139.76, 127.30, 122.23, 121.49, 111.75, 108.75, 62.77, 49.83, 46.72, 27.91, 15.08.

4.2.18 Synthesis of 1'-(2-Hydroxyethyl)-3',3'-dimethyl-6-nitrospiro(2H-1-benzopyran-2,2'- indoline). A solution of 2-hydroxy-5-nitorobenzaldehyde(25.0g,0.150mol) and 9,9,9a-trimethyl -2,3,9,9a- tetrahydro-oxazolo3,2-aindole (20.7 g, 0.102 mol) in ethanol (238 mL) was heated at 80°C for 16 h under nitrogen atmosphere. After cooling down to ambient temperature, the mixture was filtrated. The resulting solid was washed with ethanol (100mL) and dried to obtain the product as dark purple solid. ^{1}H NMR (300 MHz, CDCl3): δ 1.21 (3H, s), 1.31 (3H, s), 3.33-3.50 (2H, m), 3.71-3.82 (2H, m), 5.98 (1H, d), 6.68-7.22 (6H, m), 8.00-8.04 (2H, m). ^{13}C-NMR ($CDCl_3$): δ = 167.12, 159.29, 146.58, 141.09, 136.17, 135.44, 128.34, 127.91, 125.80, 122.71, 121.67, 119.84, 118.49, 115.41, 106.69, 106.37, 62.51, 52.67, 42.28, 29.57, 26.34, 25.77, 19.56, 18.38.

4.2.19 Synthesis of 1' -(2 -Methacryloyloxyethyl)-3',3' -dimethyl-6-nitrospiro(2H-1benzopyran-2,2' -indoline) (SPMA). To a vigorously stirred solution of 2 (4.50 g, 12.8 mmol) and a catalytic amount of N,N-dimethylaminopyridine (0.22g, 1.8 mmol) in 50 mL CH_2Cl_2 at 0 ºC under an nitrogen atmosphere were simultaneously added CH_2Cl_2 solutions (each 20mL) of freshly distilled methacryolyl chloride (1.50 mL, 15.3 mmol) and triethylamine (2.14 mL, 15.3mmol) over a period of ca. 30 min. The reaction mixture was allowed to warm to room temperature overnight. The crude product was then subsequently washed with aqueous solution. The crude product in the organic phase was purified on a silica gel column using a hexanes/Ethyl acetate system. The purified product was further purified by recrystallization (hexanes; freezer) to give light yellow solid. Yield: 3.33 g (62%). crystals. Yield: 3.33 g (62%). ^1H NMR (300 MHz, $CDCl_3$): δ 8.00-7.88 (2H, m), 7.22 (1H, td,), 7.10 -7.08 (1H, dd), 6.93 -6.86 (2H, m), 6.78 -6.67 (2H, m), 6.08 (1H, m), 5.91 (1H, d), 5.58 (1H, m), 4.27 (2H, t), 3.60 -3.41 (2H, m), 1.93-1.90 (3H, m), 1.26 (3H, s), 1.19 (3H, s). ^{13}C NMR ($CDCl_3$): δ 166.9, 158.1, 146.2, 140.1, 135.8, 135.3, 128.2, 128.0, 126.0, 125.9, 122.4, 121.3, 120.0, 118.9, 115.3, 106.5, 106.3, 62.4, 52.1, 42.3, 25.5, 20.0, 18.2.

4.3 Results and Discussion

4.3.1 Characterization of photo-responsive zwitterionic hydrogels. Synthesis of the photoswitchable SPMA monomer is described above and presented in Fig. 4.6 [44, 45]. In this work, as presented in Fig. 1a, a hydrogel was constructed with monomers, CBAA, cRGD-functionalized CBAA, SPMA and crosslinker CBDMA. The photochromic mechanism and property of the synthesized hydrogel were presented and evaluated in Fig. 1b-f. As presented in Fig. 1b, we speculated the synthesized hydrogel could be dynamically manipulated between two different states via the exposure of different lights. To test this, we exposed the hydrogel to infrared light (800 nm, 50mW), green light (560nm, 50mW), or a combination of the wavelengths at different powers (50mW infrared, 10mW green (NG-1)), or 50mW infrared, 30mW green (NG-2)) for 14 days. Photographs of hydrogels receiving different light exposures are summarized in Fig. 1c. As shown, the hydrogels appeared starkly different after exposure to each light program despite their chemically identical initial compositions. The hydrogel receiving pure NIR exposure developed a dark purple color, constructively interacting green light gradually discolored the hydrogel dependent on the intensity of each wavelength, and the hydrogel appeared colorless under pure green light exposure. The UV-Vis spectrum also confirmed this MC⇌SP balance. As presented in Fig. 1d, NIR exposure converted SP to MC and led to a significant adsorption at the MC characteristic band (548nm). The applied green light reversed this conversion and diminished adsorption at 548nm. The dynamic process of this photochromism is summarized in Fig. 1e-f. As shown, the MC⇌SP conversion can be completed within 30 minutes and this photodynamic balance was reversible and stable (up to 14 days). In addition, as presented in Fig. 4.7, the mechanical and swelling properties of the synthesized hydrogels did not change significantly under different light exposures, suggesting that this photochromism has little influence on the physical properties of the reported hydrogel.

In our previous studies, we have demonstrated the ultra-low fouling properties of polyCBAA, cRGD-functionalized polyCBAA and polyCBDMA[35, 41]. In this work, we thus evaluated protein adsorption on the photodynamic polySPMA surface. Surface plasmon resonance (SPR) was used to measure protein adsorption on the polymer film from hMSC lysate and fetal bovine serum (FBS). These protein-containing media were selected to evaluate the nonspecific protein interactions from either cells or cell culture medium. The SPMA was grafted from a gold chip via surface-initiated atom transfer radical polymerization (ATRP) under previously reported conditions (Fig. 4.8). We exposed the pSPMA films to NIR, NG-1, NG-2 and green light for one hour before evaluation. The ability of the polymer films to resist nonspecific protein fouling differs starkly after exposure to various light conditions (Fig. 4.8b-c). While pSPMA films exhibited low fouling after exposure to pure NIR light, increased protein fouling was observed when the green wavelength was added, with the highest fouling produced after exposure to pure green light. This demonstrates that nonspecific interactions on SP-based substrates are highly dependent on the light system applied to them. We proceeded to encapsulate hMSCs within the aforementioned hydrogel. The hydrogel-hMSC constructs were placed in a bipotential medium and cultured for 14 days under continuous exposure to pure NIR, NG-1, NG-2, or pure green light. As presented in Fig. 4.9, the encapsulated hMSCs exposed to each light condition retained nearly 100% viability during the 14 days. We then proceeded to explore their differentiation behavior by examining the expression of characteristic surface antigens, histological substances and mRNAs by the encapsulated cells.

4.3.2Assessing the differentiation of encapsulated hMSCs in 3D photodynamic zwitterionic hydrogels. To examine the differentiation behavior of hMSCs encapsulated in photoactuated gels, we first assessed the expression of surface antigens characteristic to adipocyte (PPARG and FABP4) and osteocyte (OPN and RUNX2) lineages. When hMSC-hydrogel constructs were incubated under pure NIR exposure, neither adipogenic nor osteogenic surface antigens were observed (Fig. 2a). This suggests the differentiation potential of hMSCs is restrained when nonspecific interactions between the matrix and cells are eliminated, which is consistent with our previous finding[41]. When nonspecific interactions were slightly enhanced under NIR-dominant mixed wavelength (NG-1) exposure, we observed clear expression of adipogenic surface antigens (PPARG and FABP4) by cells within the hydrogel. However, this adipogenic antigen expression was largely absent under green-dominant mixed (NG-2) and pure green photoirradiation, whereas osteogenic surface antigen (RUNX2 and OPN) expression was heightened when nonspecific interactions were further increased in these conditions (Fig. 2a). Quantitative results are summarized in Fig. 2b. We further evaluated encapsulated hMSC differentiation via histological staining for neutral lipids (indicating adipogenesis) with Oil Red O, and for alkaline phosphatase (ALP, an osteogenic marker) with Fast Blue salt. As presented in Fig. 3a, these results corroborate the IHC analysis. Neither marker was prominently found in the hydrogel-hMSC scaffolds exposed to NIR, while supplemental green light exposure progressively increased nonspecific binding sites and initiated differentiation. Encapsulated hMSCs were prone to commit to an adipogenic lineage when fewer nonspecific interactions were available (NG-1) but increasingly committed to osteogenesis as more nonspecific interactions were possible (NG-2 and green). Quantitative results are summarized in Fig. 3b-c.

In addition, we tested the expression of characteristic mRNA via qRT-PCR (Fig. 4.10) and observed the same trend found by IHC analysis and histological staining. Moreover, we also demonstrated the influence of cytoskeletal manipulation on the differentiation of encapsulated hMSCs in different systems. The results are summarized in Fig. 4.11.

4.3.3 Assessing the differentiation of hMSCs on 2D photodynamic zwitterionic hydrogels. The results presented above demonstrate the crucial role played by nonspecific binding in signal transfer and therefore the fate of hMSCs grown in 3D hydrogels. Compared to 3D culture, a 2D culture gives hMSCs more room to expand and grow; we therefore cultured hMSCs on the surface of photoswitchable hydrogels under the same light and media conditions described above to further explore their morphologies and lineage commitment. As presented in Fig. 4a, hMSCs form a small round shape under NIR exposure, as the nonfouling substrate greatly inhibits spreading. In contrast, hMSCs develop larger spread morphologies under the other light conditions, suggesting that hMSCs cultured on the surface of the reported hydrogel can retain their stem cell phenotype under NIR exposure and commit to differentiated phenotypes under visible light. Based on the larger round adipocyte-like shape observed under NG-1 exposure and outstretched osteoblast morphology presented under NG-2 and green light systems (Fig. 4a), we speculated that the cells were prone to commit to adipogenesis under weak visible light and osteogenesis under stronger visible light exposure as observed in 3D culture experiments.

We repeated histological staining analysis of the surface-cultured cells grown under each light condition. As presented in Fig. 4b, hMSCs cultured under visible light exposure differentiated predictably according to the degree of nonspecific interactions present, committing to adipogenesis under weaker green light intensity (NG-1) and increasingly osteogenesis under higher intensity (NG-2) or pure green light. Furthermore, we isolated mRNAs from the surface-cultured hMSCs and utilized qRT-PCR to examine genes characteristic to each lineage. Congruent with our other analyses of 2D- and 3D-cultured cells, adipogenic gene expression was highest under NG-1 exposure and osteogenic gene expression dominated under NG-2 and green conditions (Fig. 4c). None of the lineage-specific genes were expressed at significant levels by hMSCs on the nonfouling NIR-exposed gel, again indicating their multipotency was maintained.

4.3.4 Controlling hMSC differentiation with high spatial and temporal precision. Achieving robust spatiotemporal control of cell-scaffold constructs is a key challenge in the regeneration of complex tissues or organs. We hypothesized the photoactuated platform presented here would allow hMSC differentiation lineages to be precisely programmed in real time and with respect to their location in the gel. A patterned and constructively interacting irradiation method was employed first to evaluate spatial control. In brief, the entire hydrogel sample was exposed to NIR light from the bottom, and green light at varying strengths was applied through a patterned chrome photomask from the top. In the example shown in Fig. 5, 30mW green light is applied through the 1st and 3rd patterned rows of the photomask and 10mwW green light is applied through the 2nd patterned row. Green light sources with different powers were isolated to avoid crosstalk. During the patterned light exposure, we added protein solutions from either culture medium (FBS) or hMSC lysate (CLS) onto the gel and incubated them for 24 hours. The resulting protein adsorption was evaluated with fluorescent tagging by Rhodamine (FBS) and FITC (CLS), as described above. As presented in Fig. 5a, the 1st and the 3rd rows presented strong binding affinity to both FBS and CLS proteins while the 2nd row presented weaker binding affinity to these solutions. At the same time, the remainder of the hydrogel exposed to pure NIR resisted fouling by either FBS or CLS proteins, in sharp contrast to the patterned area exposed to visible light. After confirming the spatially controlled protein fouling, we proceeded to test hMSC differentiation on the patterned hydrogel. We seeded hMSCs on the gel surface and applied the aforementioned exposure pattern while culturing the cell-hydrogel construct in bipotential media for 14 days. The differentiation behavior of the hMSCs was examined by histological staining and the result is summarized in Fig. 5a. As presented, most hMSCs did not differentiate under pure NIR exposure while they actively differentiated on the patterned area exposed to added green light. In addition, one can clearly see that the power of green light used can delicately specify the differentiation behavior of cultured stem cells. As seen, hMSCs grown on the 1st and 3rd rows conclusively underwent osteogenic differentiation, while those grown on the 2nd row preferred adipogenesis.

Furthermore, we intended to manipulate the fate choice of encapsulated hMSCs in real time in order to delicately control the differentiation composition on one hydrogel section. We exposed the hMSC-encapsulating hydrogel to a continuous wavelength-sweep program (NIR, 3 days→ NG-2, 1 day→ NIR, 3 days→ NG-1, 1 day→ NIR, 3 days) in the bipotential differentiation media. NIR was applied during the whole process and visible light with different powers (i.e. NG-1 and NG-2) was applied for 1 day every 3 days. As presented in Fig. 5b (i), during the first 3 days of culture under NIR exposure, the differentiation potential of encapsulated hMSCs was largely restrained. When we switched NIR to NG-2 for one day, we began to observe significant osteogenesis on the hydrogel while their adipogenic potential was still largely inhibited. Notably, when we switched from NG-2 back to NIR exposure, the differentiation process was suspended due to the elimination of nonspecific interactions. As presented in Fig. 5b (iii), we did not observe significantly enhanced differentiation during the entire process of the 2nd pure NIR exposure. We further exposed the construct to the NG-1 system for one day and observed differentiation—as seen in Fig. 5b (iv), significant adipogenesis was observed on the platform while enhanced osteogenesis was not seen. Furthermore, this adipogenesis was again suspended by switching NG-1 exposure back to NIR exposure. As shown in Fig. 5b (v) when compared to 5b (iv), we did not observe significantly enhanced adipogenesis during the final 3-day exposure to NIR. A quantitative summary of the stem cell differentiation during this continuous wavelength-sweep program is summarized in Fig. 5c. We finally examined the cultured cells via flow cytometry after this 12-day programmed culture. As presented in Fig. 5d (i), after this 12-day culture, the cells showed neither significant death nor apoptosis on the reported platform, indicating the high biocompatibility of the platform and differentiation programming strategy. Examination of the expression of characteristic surface antigens and mRNAs from cells on the hydrogel surface further confirmed the positive differentiation of hMSCs after this 12-day culture program. The quantitative differentiation profiles as assayed through each method are summarized in Fig. 5c-e.

4.4 Conclusions

In this work, we demonstrate a photoswitchable zwitterionic hydrogel platform used for the dynamic control of hMSC differentiation spatially and temporally. This hydrogel can be switched between a zwitterionic hydrophilic state and a hydrophobic state continuously and reversibly when exposed to a combination of green and NIR lights, without causing cell damage. The combined abilities to control the degree of nonspecific interactions in a photodynamic hydrogel without changing its composition, and to restrain the differentiation of stem cells in a zwitterionic hydrogel free of nonspecific interactions, make it possible to precisely control stem cell self-renewal and differentiation. As a result, the composition, location, and differentiation status of stem cells can be easily manipulated and adjusted at will on a single hydrogel piece by controlling lights without chemical contamination. This strategy can advance fundamental understanding of the mechanism of stem cell differentiation, as well as provide a platform for hMSC-based regenerative medicine.

References

1. Roy, I. & Gupta, M.N. Smart polymeric materials: emerging biochemical applications. Chemistry & biology 10, 1161-1171 (2003).

2. Kopeček, J. Hydrogel biomaterials: a smart future? Biomaterials 28, 5185-5192 (2007).

3. Fernández-Barbero, A. et al. Gels and microgels for nanotechnological applications. Adv. Colloid Interface Sci. 147, 88-108 (2009).

4. Hoffman, A.S. Stimuli-responsive polymers: Biomedical applications and challenges for clinical translation. Adv Drug Deliv Rev. 65, 10-16 (2013).

5. Qiu, Y. & Park, K. Environment-sensitive hydrogels for drug delivery. Adv Drug Deliv Rev. 64, 49-60 (2012).

6. Lutolf, M.P. Biomaterials: Spotlight on hydrogels. Nat. Mater. 8, 451-453 (2009).

7. Theato, P., Sumerlin, B.S., O'Reilly, R.K. & Epps III, T.H. Stimuli responsive materials. Chem. Soc. Rev. 42, 7055-7056 (2013).

8. Oliveira, M.B. & Mano, J.F. Natural ‐ Based and Stimuli ‐ Responsive Polymers for Tissue Engineering and Regenerative Medicine. Polymers in Regenerative Medicine: Biomedical Applications from Nano-to Macro-Structures, 49-90 (2015).

9. Tomatsu, I., Peng, K. & Kros, A. Photoresponsive hydrogels for biomedical applications. Adv Drug Deliv Rev. 63, 1257-1266 (2011).

10. DeForest, C.A. & Anseth, K.S. Cytocompatible click-based hydrogels with dynamically tunable properties through orthogonal photoconjugation and photocleavage reactions. Nat. Chem. 3, 925-931 (2011).

11. Kloxin, A.M., Kasko, A.M., Salinas, C.N. & Anseth, K.S. Photodegradable hydrogels for dynamic tuning of physical and chemical properties. Science 324, 59-63 (2009).

12. DeForest, C.A., Polizzotti, B.D. & Anseth, K.S. Sequential click reactions for synthesizing and patterning three-dimensional cell microenvironments. Nat. Mater. 8, 659-664 (2009).

13. Ercole, F., Davis, T.P. & Evans, R.A. Photo-responsive systems and biomaterials: photochromic polymers, light-triggered self-assembly, surface modification, fluorescence modulation and beyond. Polym. Chem. 1, 37-54 (2010).

14. Wirkner, M. et al. Triggered cell release from materials using bioadhesive photocleavable linkers. Adv. Mater. 23, 3907-3910 (2011).

15. Griffin, D.R. et al. Synthesis of photodegradable macromers for conjugation and release of bioactive molecules. Biomacromolecules 14, 1199-1207 (2013).

16. DeForest, C.A. & Tirrell, D.A. A photoreversible protein-patterning approach for guiding stem cell fate in three-dimensional gels. Nat. Mater. (2015).

17. Kloxin, A.M., Tibbitt, M.W. & Anseth, K.S. Synthesis of photodegradable hydrogels as dynamically tunable cell culture platforms. Nat. Protoc. 5, 1867-1887 (2010).

18. Fairbanks, B.D., Singh, S.P., Bowman, C.N. & Anseth, K.S. Photodegradable, photoadaptable hydrogels via radical-mediated disulfide fragmentation reaction. Macromolecules 44, 2444-2450 (2011).

19. Griffin, D.R. & Kasko, A.M. Photodegradable macromers and hydrogels for live cell encapsulation and release. J. Am. Chem. Soc. 134, 13103-13107 (2012).

20. Azagarsamy, M.A., Alge, D.L., Radhakrishnan, S.J., Tibbitt, M.W. & Anseth, K.S. Photocontrolled nanoparticles for on-demand release of proteins. Biomacromolecules 13, 2219-2224 (2012).

21. He, M., Li, J., Tan, S., Wang, R. & Zhang, Y. Photodegradable supramolecular hydrogels with fluorescence turn-on reporter for photomodulation of cellular microenvironments. J. Am. Chem. Soc. 135, 18718-18721 (2013).

22. DeForest, C.A., Sims, E.A. & Anseth, K.S. Peptide-functionalized click hydrogels with independently tunable mechanics and chemical functionality for 3D cell culture. Chem. Mater 22, 4783-4790 (2010).

23. Luo, Y. & Shoichet, M.S. A photolabile hydrogel for guided three-dimensional cell growth and migration. Nat. Mater. 3, 249-253 (2004).

24. Wylie, R.G. et al. Spatially controlled simultaneous patterning of multiple growth factors in three-dimensional hydrogels. Nat. Mater. 10, 799-806 (2011).

25. Adzima, B.J. et al. Spatial and temporal control of the alkyne–azide cycloaddition by photoinitiated Cu (II) reduction. Nat. Chem. 3, 256-259 (2011).

26. Bandara, H.D. & Burdette, S.C. Photoisomerization in different classes of azobenzene. Chem. Soc. Rev. 41, 1809-1825 (2012).

27. Fuß, W., Kosmidis, C., Schmid, W.E. & Trushin, S.A. The Photochemical cis‐trans Isomerization of Free Stilbene Molecules Follows a Hula‐Twist Pathway. Angew. Chem. Int. Edit. 43, 4178-4182 (2004).

28. Minkin, V.I. Photo-, thermo-, solvato-, and electrochromic spiroheterocyclic compounds. Chem. Rev. 104, 2751-2776 (2004).

29. Klajn, R. Spiropyran-based dynamic materials. Chem. Soc. Rev. 43, 148-184 (2013).

30. der Molen, S.J. & ávan Wees, B.J. Uni-and bi-directional light-induced switching of diarylethenes on gold nanoparticles. Chem. Commun., 3597-3599 (2006).

31. Heinz, B. et al. Comparing a photoinduced pericyclic ring opening and closure: Differences in the excited state pathways. J. Am. Chem. Soc. 129, 8577-8584 (2007).

32. Koumura, N., Zijlstra, R.W., van Delden, R.A., Harada, N. & Feringa, B.L. Light-driven monodirectional molecular rotor. Nature 401, 152-155 (1999).

33. Zhao, P. et al. A possible anthracene-based optical molecular switch driven by a reversible photodimerization reaction. Appl. Phys. Lett. 93, 013113 (2008).

34. di Nunzio, M.R., Gentili, P.L., Romani, A. & Favaro, G. Photochromic, thermochromic, and fluorescent spirooxazines and naphthopyrans: a spectrokinetic and thermodynamic study. ChemPhysChem 9, 768-775 (2008).

35. Jiang, S. & Cao, Z. Ultralow-Fouling, Functionalizable, and Hydrolyzable Zwitterionic Materials and Their Derivatives for Biological Applications. Adv. Mater. 22, 920-932 (2010).

36. Zhang, L. et al. Zwitterionic hydrogels implanted in mice resist the foreign-body reaction. Nat. Biotech. 31, 553-556 (2013).

37. Keefe, A.J. & Jiang, S. Poly(zwitterionic)protein conjugates offer increased stability without sacrificing binding affinity or bioactivity. Nat. Chem. 4, 60-64 (2012).

38. Bai, T. et al. Zwitterionic fusion in hydrogels and spontaneous and time-independent self-healing under physiological conditions. Biomaterials 35, 3926-3933 (2014).

39. Chien, H.-W., Tsai, W.-B. & Jiang, S. Direct cell encapsulation in biodegradable and functionalizable carboxybetaine hydrogels. Biomaterials 33, 5706-5712 (2012).

40. Carr, L.R., Zhou, Y., Krause, J.E., Xue, H. & Jiang, S. Uniform zwitterionic polymer hydrogels with a nonfouling and functionalizable crosslinker using photopolymerization. Biomaterials 32, 6893-6899 (2011).

41. Bai, T. et al. Restraint of the Differentiation of Mesenchymal Stem Cells by a Nonfouling Zwitterionic Hydrogel. Angew. Chem. Int. Edit. 126, 12943-12948 (2014).

42. Wojtyk, J.T., Wasey, A., Kazmaier, P.M., Hoz, S. & Buncel, E. Thermal reversion mechanism of N-functionalized merocyanines to spiropyrans: a solvatochromic, solvatokinetic, and semiempirical study. J. Phys. Chem. A 104, 9046-9055 (2000).

43. Zhu, M.-Q. et al. Reversible two-photon photoswitching and two-photon imaging of immunofunctionalized nanoparticles targeted to cancer cells. J. Am. Chem. Soc. 133, 365-372 (2010).

44. Elizalde, L.E., Ledezma, R. & López, R.G. Synthesis of Photochromic Monomers Derived from 1′ - (2 - Methacryloxyethyl) - 3, 3 - Dimethyl - 2 - 2H - Spirobenzopyran Indoline. Synthetic Commun. 35, 603-610 (2005).

45. Friedle, S. & Thomas, S.W. Controlling contact electrification with photochromic polymers. Angew. Chem. Int. Edit. 122, 8140-8143 (2010).

Table 1. Description of the primers sequence utilized for qRT-PCR.

Gene Symbol	Forward Primer	Reverse Primer
β3 TUBULIN	5'-GGCCTTTGGACATCTCTTCA	5'-CGGTCGGGATACTCCTCA
MYOD	5'-AGCACTACAGCGGCGACT	5'-GCGACTCAGAAGGCACGTC
AGGRECAN	5'-CACGCTACACCCTGGACTTG	5'-CCATCTCTCAGGAAGCAGT
RUNX2	5'-GATGACACTGCCACCTCTGA	5'-GACTGGCGGGGTGTAAGTAA
PPARG	5'-GCTGTTATGGGTGAAACTCTG	5'-ATAAGGTGGAGATGCAGGTTC
COL1A1	5'-TGAGAGACCAAGAACTG	5'-CCATCCAAACCACTGAAACC
OCN	5'-ATGAGAGCCCTCACACTCCTC	5'-CGTAGAAGCGCCGATAGGC
OPN	5'-CTAGGCATCACCTGTGCCATACC	5'-CAGTGACCAGTTCATCAGATTCATC
ADIPOQ	5'-CCTGGTGAGAAGGGTGAGAA	5'-CTCCTTTCCTGCCTTGGATT
FABP4	5’-GCCAGGAATTTGACGAAGTCAC	5’- TTCTGCACATGTACCAGGACAC
LPL	5'-GTGGCCGAGAGTGAGAACAT	5'-GAAGGAGTAGGTCTTATTTGTGGAA

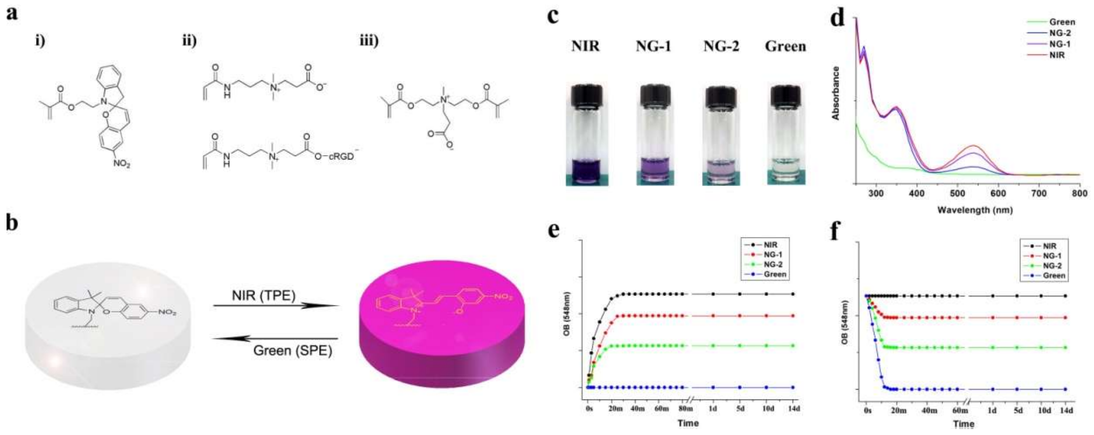

Figure 4.1. a) Photoresponsive hydrogel components spiropyran methacrylate (i, SPMA), carboxybetaine acrylamide (ii, CBAA), cRGD-functionalized CBAA (ii) and crosslinker carboxybetaine dimethacrylate (CBDMA). **b)** Reversible photochromism of spiropyran between its hydrophobic spiropyran (SP) and hydrophilic merocyanine (MC) forms. **c)** Representative photograph of photodynamic hydrogels receiving NIR, NG-1, NG-2 and Green light exposure. **d)** UV-VIS absorption spectra of photodynamic hydrogels receiving NIR, NG-1, NG-2 and Green light exposure. **e-f)** Photodynamic process of the MC⇌SP conversion in hydrogels receiving different light exposures starting from either a green hydrogel (**e**) or NIR hydrogel (**f**).

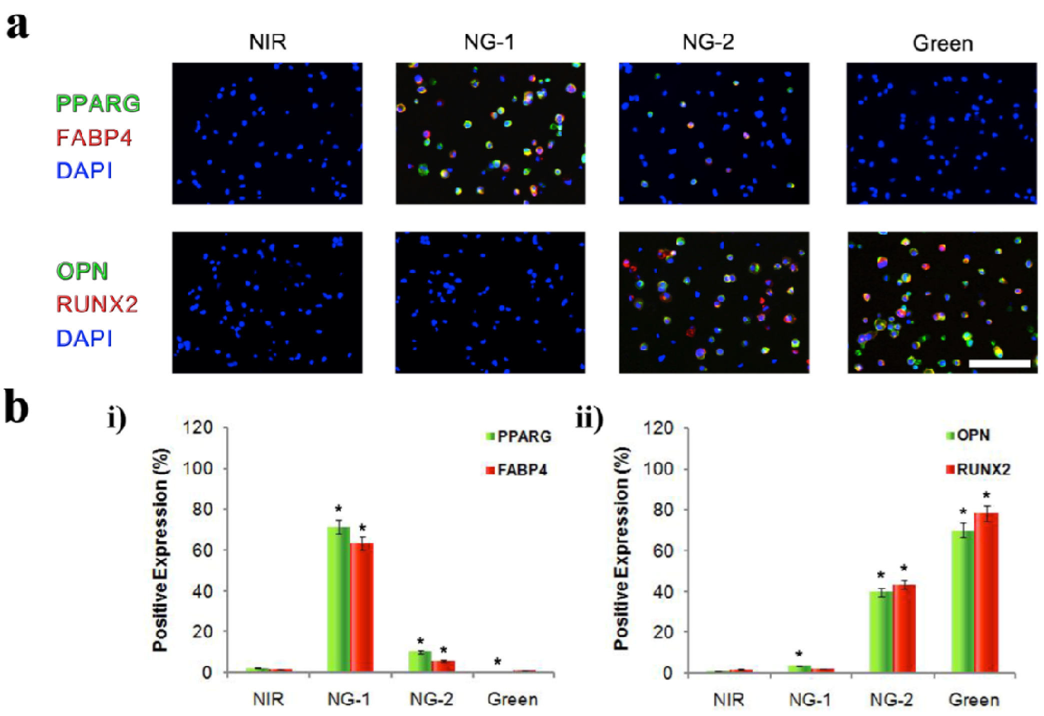

Figure 4.2. a) After 14 days of culture in bipotential differentiation media, cell-hydrogel constructs exposed to NIR, NG-1, NG-2 and green light conditions were immunostained for adipogenic (PPARG, FABP4) and osteogenic (RUNX2, OPN) biomarkers. Scale bar, 50 μm. **b)** Percentage of cells expressing either adipogenic (i) or osteogenic (ii) biomarkers when encapsulated in hydrogels after exposure to different light conditions during a 14-day incubation in bipotential differentiation media. Asterisks denote statistical significance compared with NIR hydrogels (**$p<0.001$, t-test). Error bars represent standard error of the mean from 5 individual experiments.

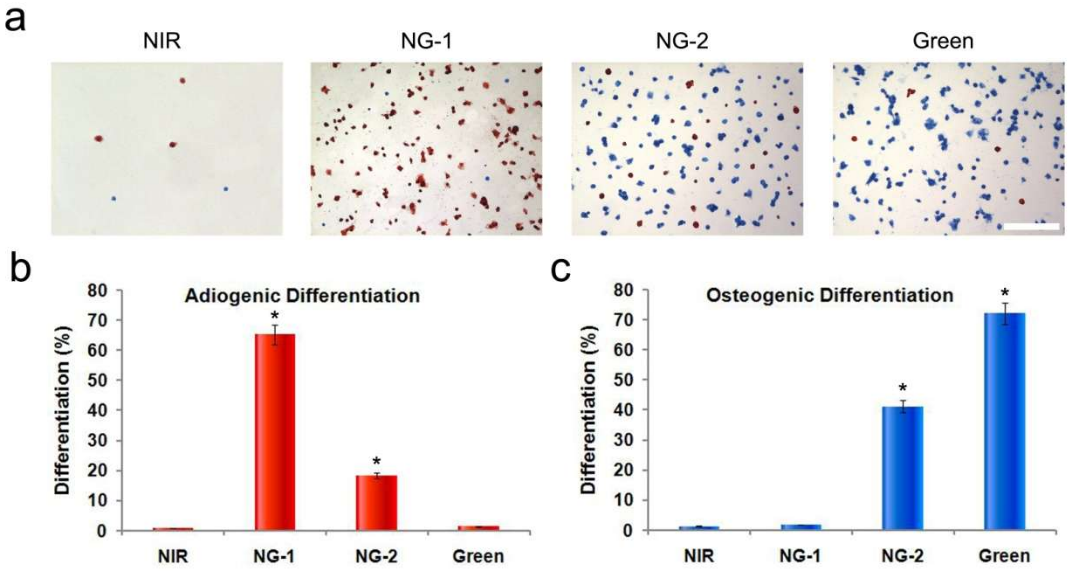

Figure 4.3. a) Representative bright-field images of Oil Red O and Fast Blue salt-stained hMSC-hydrogel constructs following a 14-day incubation in bipotential differentiation media while exposed to different light conditions. Scale bar, 100 μm. Percentage of cells expressing neutral lipids (**b**) and alkaline phosphatase (ALP, **c**). Asterisks denote statistical significance compared with NIR hydrogels (**$p<0.05$, t-test). Error bars represent standard error of the mean from 5 individual experiments.

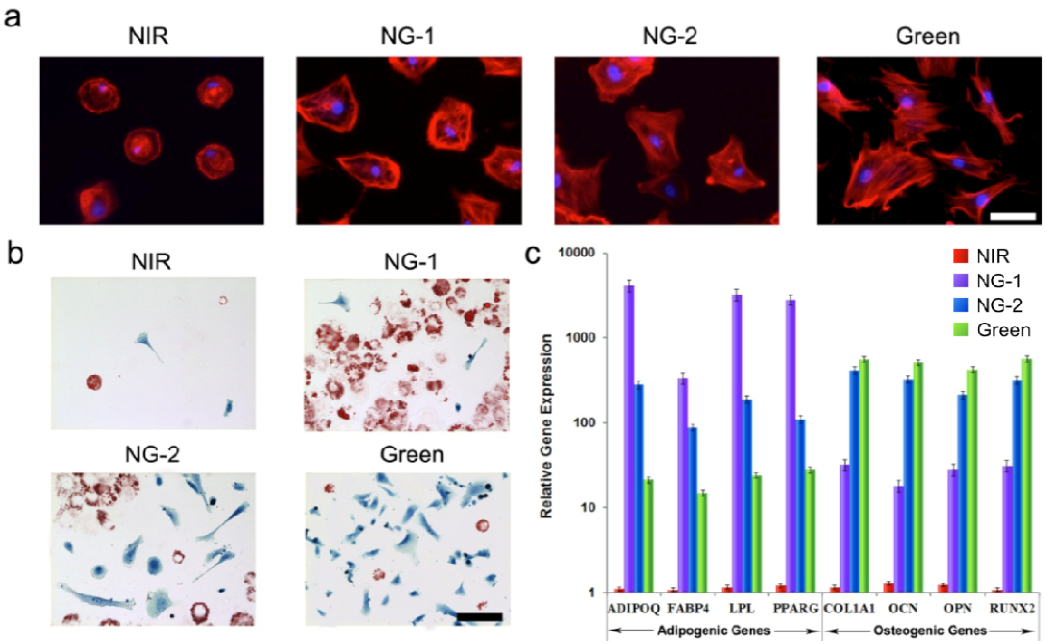

Figure 4.4. a) Representative fluorescent micrographs of hMSCs stained with TRITC-phalloidin (red) and DAPI (blue) grown under different light conditions. Scale bars, 15μm. **b)** Representative bright-field images of Oil Red O- and Fast Blue salt-stained hMSCs grown under the same set of light conditions as in **a**. Scale bars, 100μm. **c)** Adipogenic and osteogenic gene activities of hMSCs cultured under each light condition. The percent expression of all osteogenic and adipogenic genes was significantly different between hydrogels exposed to each light condition (*p<0.05, t-test). All cells presented in this figure were grown on the surface of the photoresponsive gel for 14 days in bipotential differentiation media. Error bars represent standard error of the mean from 5 individual experiments.

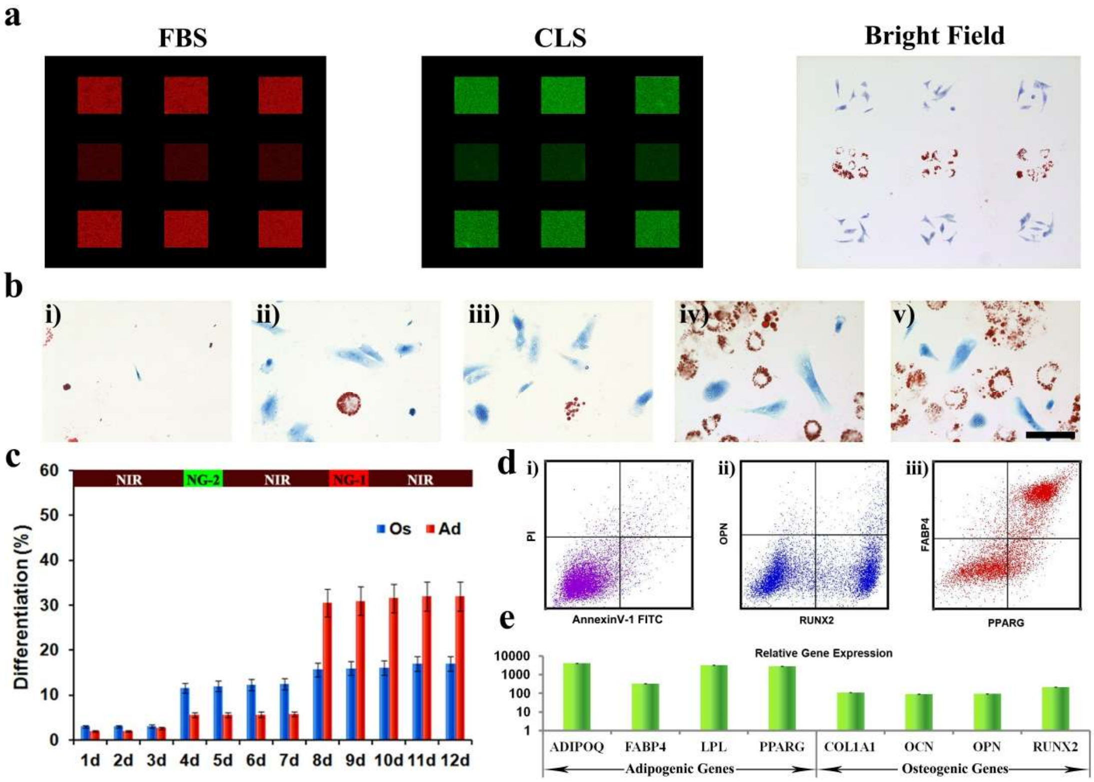

Figure 4.5. a) FBS and CLS protein adsorption and hMSC differentiation on the hydrogel receiving patterned exposure. **b)** Representative bright-field images of Oil Red O and Fast Blue salt-stained hMSCs following 12-day bipotential differentiation media incubation within hydrogels exposed to programmed light conditions. Scale bar, 30 μm. **c)** Percentage of cells differentiating to adipocytes (Lipid was stained red by Oil Red O) or osteoblasts (ALP was stained blue by Fast Blue salt) in bipotential differentiation media for 12 days when exposed to a light program. **d)** Representative flow cytometry profile of cell apoptosis/necrosis (i) and the expression of the osteogenic biomarkers (ii) and the adipogenic biomarkers (iii) for hMSCs grown on the hydrogel surface receiving the 12-day light program. **e)** Representative gene expression profile of hMSCs grown on the hydrogel surface receiving the 12-day light program.

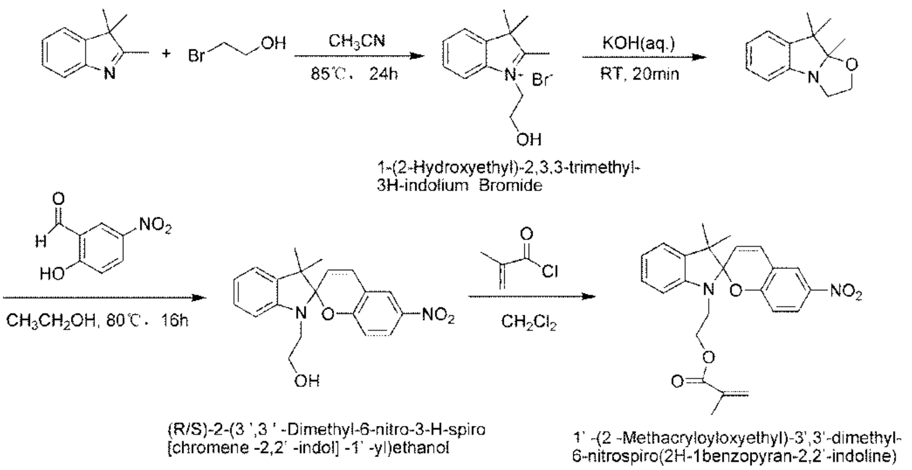

Figure 4.6. Synthetic route of 1’ -(2 -Methacryloyloxyethyl)-3’,3’ -dimethyl-6-nitrospiro(2H-1benzopyran-2,2’-indoline) (SPMA).

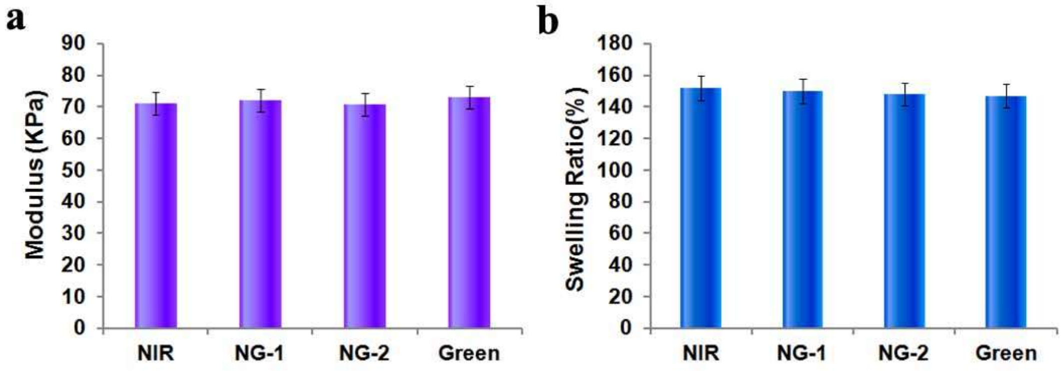

Figure 4.7. Characterization of NIR, NG-1, NG-2 and Green hydrogels. **a)** Moduli of NIR, NG-1, NG-2 and Green hydrogels. **b)** Swelling ratios of NIR, NG-1, NG-2 and Green hydrogels.

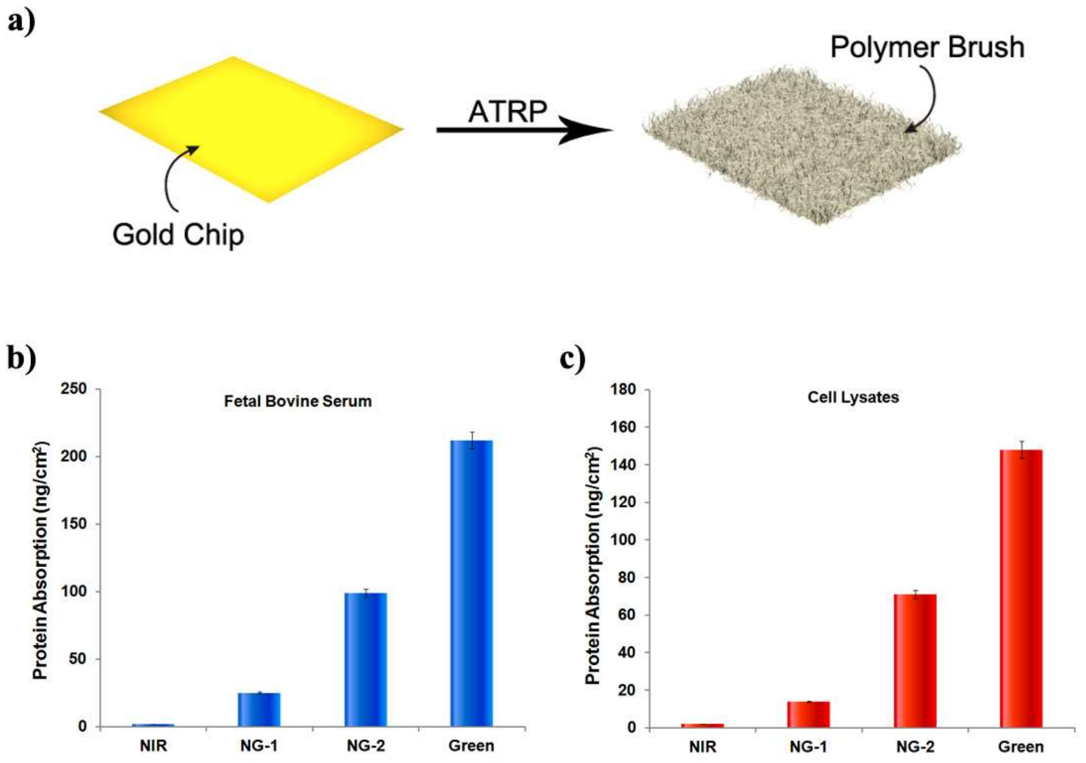

Figure 4.8. a) Schematic illustration of grafting pSPMA polymer brush from gold chip by ATRP. **b-c)** Total protein adsorption was measured on an SPR sensor after injection of fetal bovine serum (FBS) and hMSCs lysates on pSPMA film receiving NIR, NG-1, NG-2 and Green light exposure.

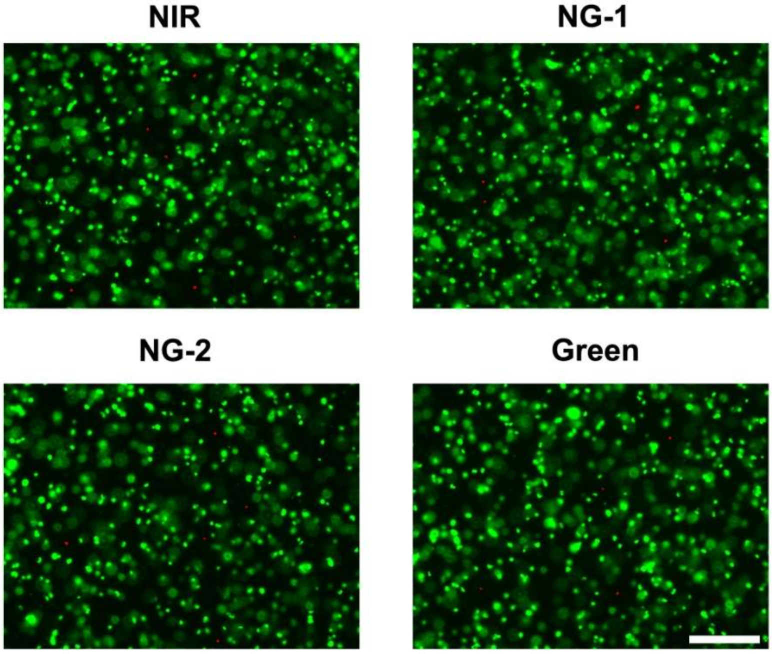

Figure 4.9. LIVE-DEAD stain performed after encapsulating cells in NIR, NG-1, NG-2 and Green hydrogels after being cultured in bipotential medium for 14 days. Scale Bar: 200μm

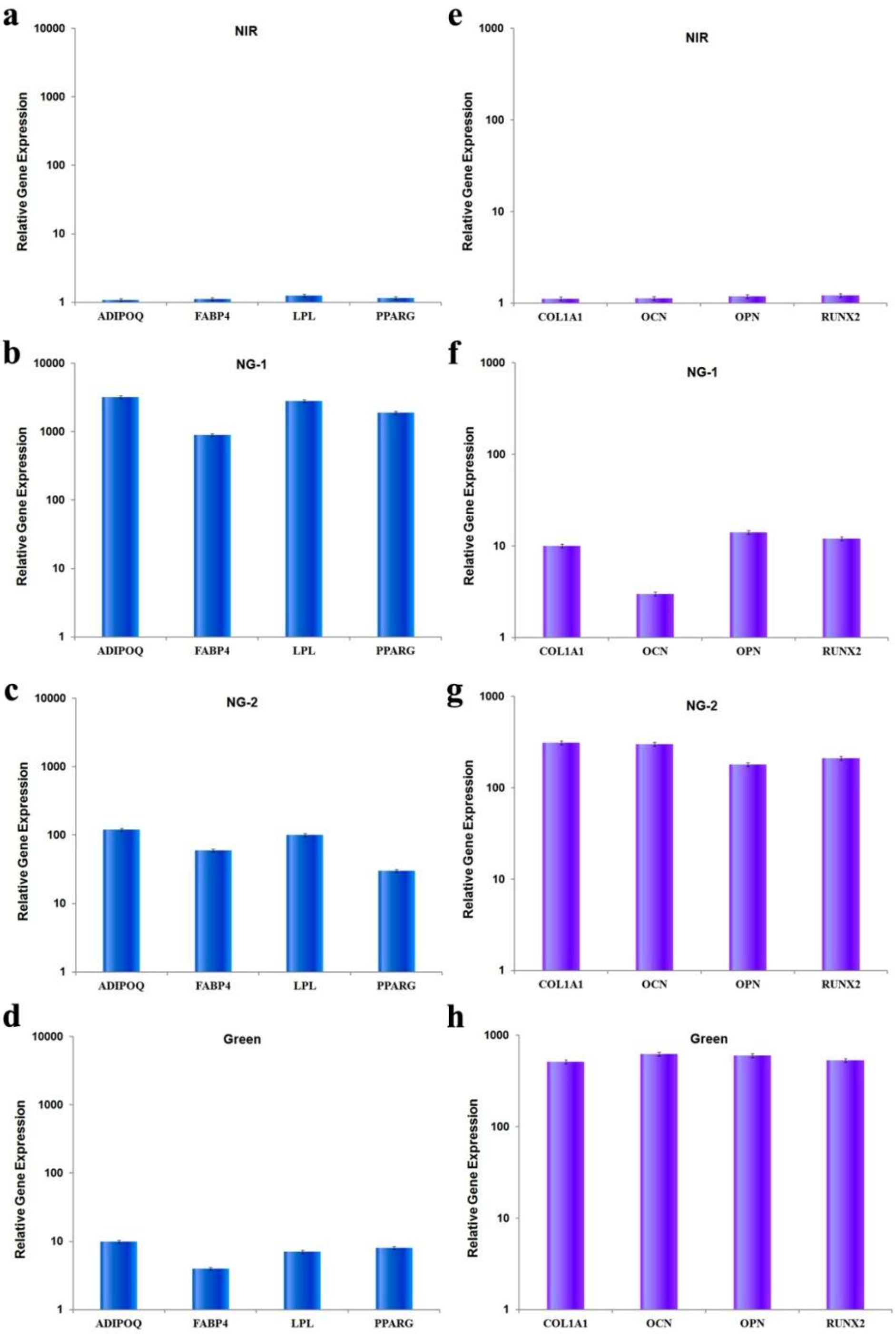

Figure 4.10. Adipogenic (**a-d**) and osteogenic (**e-h**) gene activity of hMSCs cultured in photodynamic hydrogels receiving different light exposure in bipotential differentiation medium for 14 days. For all osteogenic and adipogenic genes, the percent expression was significantly different among NIR, NG-1, NG-2 and Green hydrogels (*$p<0.001$, t-test). Error bars represent standard error of the mean from 5 individual experiments.

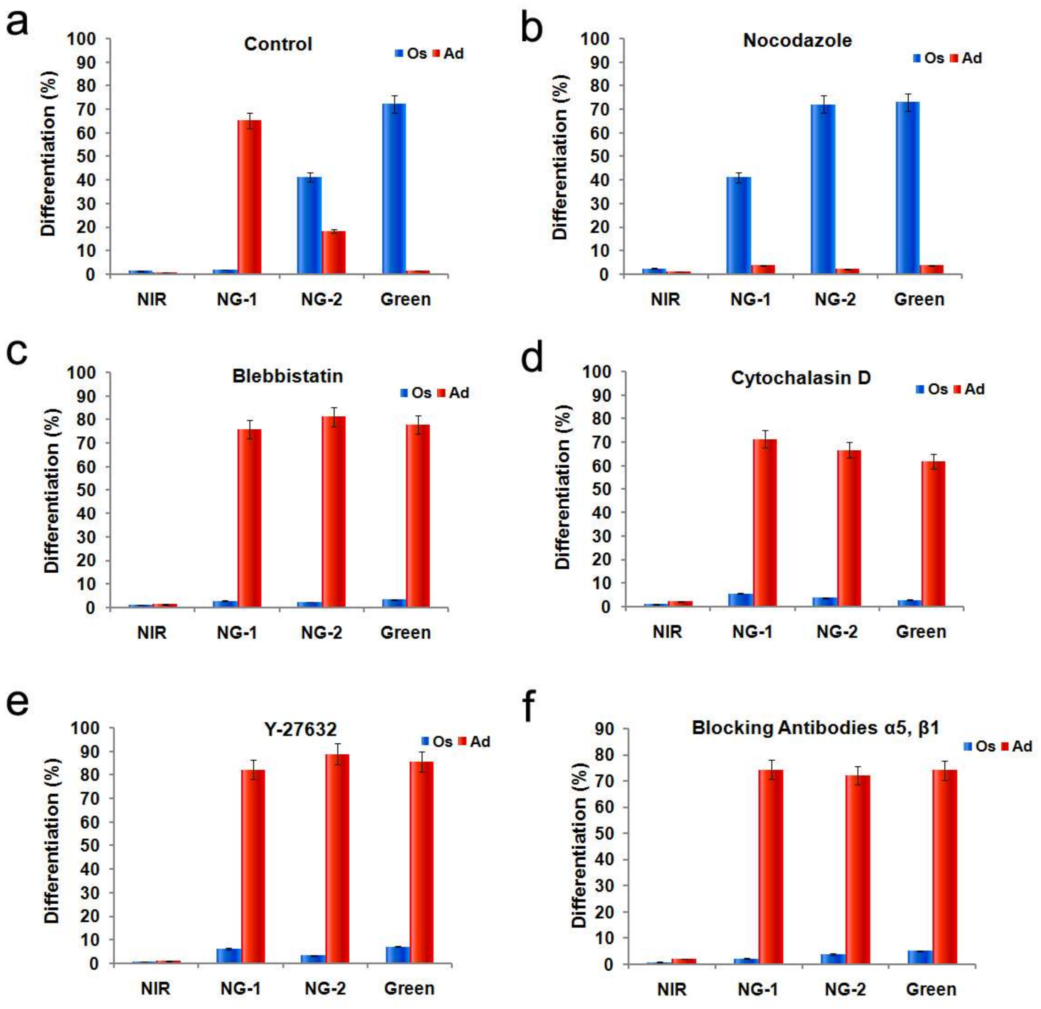

Figure 4.11. Percentage of cells in hydrogels exposed to different light conditions differentiating to adipocytes (stained by Oil red O) or osteoblasts (stained by Fast Blue salt) in normal bipotential differentiation media (**a**) or in the presence of cytoskeleton disruptors and integrin blocking antibodies (**b-f**).

Chapter 5 Zwitterionic Star Polymer Hydrogel for Cell Expansion without Loss in Bioactivity

Cell-based therapies depend on the ability to expand useful cell populations *ex vivo* reliably and effectively while maintaining their functional bioactivity or multipotency. Culturing cells in 3D hydrogel niches to mimic an *in vivo* environment *ex vivo* is a promising strategy, but nonspecific interactions between most biomaterials and cells have been shown to trigger phenotype change, differentiation, and senescence. Encapsulating cells in hydrogels during radical-mediated reactions typically required for gelation can also cause cell damage while many hydrogels are difficult to degrade for cell recovery. Here, we have developed a hydrogel-based cell expansion platform based on star-shaped poly(carboxybetaine), a biocompatible zwitterionic material that presents no nonspecific interactions to proteins and cells. Star-shaped poly(carboxybetaine) is end-functionalized with complementary thiol or disulfide pyridine groups, which react without radical initiation under physiological conditions via a biocompatible disulfide exchange reaction and form a hydrogel. Zwitterionic star polymers with a molecular weight greater than about 50 kDa were nontoxic to all four cell lines tested, including human mesenchymal stem cells (hMSCs), and all cell lines expanded 25-30 fold over two weeks of culture without losing bioactivity. The differentiation behavior of star polymer-encapsulated hMSCs expanded in bipotential media was examined through histological staining, gene expression, and flow cytometry. hMSCs were found to retain their multipotency. Cell expansion inside hydrogels based on star-shaped poly(carboxybetaine) represents a valuable platform for *ex vivo* cell expansion, and may relieve a current clinical bottleneck in cell-based therapy.

5.1 Introduction

Regenerative medicine and cell-based therapies are related to many exciting recent medical breakthroughs, enabling highly effective treatment and even promising to cure diseases once considered lethal. As the clinical importance of cell-based therapies continues to grow, *ex vivo* cell expansion of sufficient cells is key to fully realize the promises of tissue engineering and regenerative medicine. Cells frequently lose bioactivity and change their phenotype when expanded using typical culture platforms, which dramatically reduces their therapeutic value. Bioactivity loss in cells cultured on a 2D hydrophobic surface is closely linked to the loss of telomeric repeats and associated with cellular senescence. Hydrophobic materials in bioreactors can also provide cells with nonspecific signals that trigger phenotype change and differentiation. Stem cell differentiation is particularly hard to control or prevent during *ex vivo* expansion, deeply affecting the study and application of these expanded cells. For example, as a large number of mesenchymal stem cells (hMSCs) are needed for their clinical use, the limited cells obtained from a primary culture or patient must be further expanded through multiple passages. HMSCs can grow *ex vivo* at a rather constant rate during the first two to three weeks. However, cell doubling times start to increase along with the passage number until senescence stops growth. After their initial culture, hMSCs also progressively lose multipotency in classical media and other culture conditions.

One promising strategy to tackle this long-standing problem is culturing cells in a biomimetic 3D niche that more accurately models their *in vivo* environment. However, very few biomaterials are suitable for 3D culture platforms due to concerns about their long-term biocompatibility and immunogenic potential. Among these materials, zwitterionic poly(carboxybetaine) (pCB) is unique in several aspects. First, it is structurally similar to glycine betaine, a solute vital to the osmotic regulation of living organisms. Second, pCB shows undetectable nonspecific protein adsorption (<0.3 ng cm^{-2}) from complex physiological media such as undiluted human serum and plasma. A hydrogel matrix constructed exclusively from pCB will thus provide no nonspecific signals to encapsulated cells, and we recently found this complete absense of nonspecific interactions to result in mesenchymal stem cells temporarily ‘losing' their ability to differentiate inside pCB hydrogels. Third, each CB monomer contains one carboxyl group that can be functionalized to immobilize biomolecules using EDC/NHS chemistry, while the carboxylic acids unreacted after functionalization can be easily restored to their original nonfouling state. These combined attributes make pCB particularly amenable to specifically targeting desired molecules while remaining highly resistant to any other non-specific adhesion. In comparison, the popular biomaterial polyethylene glycol (PEG) is relatively difficult to functionalize, and unreacted functional groups (such as -COOH or -NH2) still carry charge and remain as fouling moieties after this process.

We have typically used free radical polymerization to produce pCB hydrogels in our previous work. This often makes dialysis or prolonged soaking necessary to remove unreacted monomers and initiators, and the free radicals generated can irreversibly damage encapsulated cells and compromise their viability and function. Hydrogels incorporating zwitterionic components that can form under physiological conditions and without free radical initiation have also been reported. However, all of these “injectable" hydrogels are based on copolymers of zwitterionic and hydrophobic portions; if used as a stem cell scaffold, the hydrophobic content in these copolymers will trigger differentiation as we have demonstrated. A strategy to form a purely zwitterionic hydrogel under physiological conditions is highly desirable for this reason.

Here, we use star-shaped pCB polymers to form a fully zwitterionic hydrogel. We prepared four-arm star poly(carboxybetaine acrylamide) (spCB) polymers using a tetrafunctional initiator, and modified the terminal groups of each star polymer to contain either thiol groups (spCB-SH) or disulfide pyridine groups (spCB-DP). These two functionalized polymers were then simply mixed to form a hydrogel via a disulfide exchange reaction. As this gelation process generates no cytotoxic species or radicals, cells can be encapsulated during gel formation without the potential for damage. In addition, the purely zwitterionic network does not provide any nonspecific interactions to encapsulated cells and thus restrains their differentiation.

5.2 Experimental Section

5.2.1. Synthesis of zwitterionic star polymers

PCBAA star polymers were synthesized using atom-transfer radical polymerization (ATRP), as previously reported. In brief, appropriate amounts of carboxybetaine acrylamide (CBAA) or cRGD-functionalized CBAA monomer, 2,2'-bipyridine (BPY), catalysts, and tetrafunctional initiator pentaerythritol tetrakis(2-bromoisobutyrate) were placed in a 10 mL reaction tube. The mixture was subjected to three freeze-pump-thaw cycles, and equilibrated at room temperature for 20 min before water and methanol were added at a 1:1 ratio. The polymerization reaction was stirred at room temperature for 8 h, after which the polymer product was treated with alumina, recovered, and purified by preciptation twice into acetone. Desired molecular weights of the polymer were tuned by adjusting the stoichiometric ratio between the monomer and the initiator. Star-shaped pCBAA (spCB) samples with targeted molecular weights of 5, 20, 50, 80 and 120 kDa were synthesized.

5.2.2. functionalization of star polymer

Purified spCB polymers were first end-functionalized with azide (N_3) groups by reacting 2 g of each polymer with 50 mg of sodium azide for 48 h in water at room temperature. N_3-functionalized polymers were purified using dialysis and lyophilized. Azide groups were then reduced to NH_2 using a MCM-Silylamine Pd(II) Complex, which was prepared as previously reported. Here, 1.5 g of azide-terminated spCB and 10 mg of MCM-Silylamine Pd(II) Complex were dissolved in 10 mL of methanol and reacted for 3 h at room temperature, after which the complex was removed by filtration and the polymer dried under vacuum.

To functionalize spCB with thiol or disulfide pyridine groups, 3-mercaptopropionic acid or 3-(2-Pyridyldithio) propanoic acid were functionalized to the star polymers, respectively. In brief, appropriate amounts of N-(3-Dimethylaminopropyl)-N'-ethylcarbodiimide hydrochloride (EDC) (Sigma) and N-hydroxysuccinimide (NHS) (Sigma) were added to 3-Mercaptopropionic acid or 3-(2-Pyridyldithio) propanoic acid solution. After incubation at 25°C for 1 h to activate the carboxylate group, 1g NH_2-terminated spCB was added to the activated system. The molar concentration of in the reaction solution was set at 100μM. The molar ratio of EDC, NHS and functionalization reagent (I or II) was fixed at 1:1:1. The reaction was allowed to proceed at 25°C for 24 hours before purification via LC-MS. The efficiency of the reaction was also calculated by LC-MS (Yield 68%). Scheme 1 outlines the full synthesis and functionalization procedure.

5.2.3. Characterization of functionalized polymers

An Agilent 1200 LC 6520 Q-Tof MS system (Agilent Technologies, Santa Clara, CA) was employed to purify the functionalized star polymers and quantify the efficiency of the conjugation reactions. In brief, after the reaction, functionalized star polymer sample was injected. The chromatographic separation was performed in hydrophilic interaction chromatography (HILIC) mode on a SeQuant ZIC-cHILIC column (150 x 2.1 mm, 3.0 µm particle size, Merck KGaA, Darmstadt, Germany). The flow rate was 0.500 mL/min, auto-sampler temperature was kept at 4°C, the column compartment was set at 40°C, and total separation time for both ionization modes was 40 min. The mobile phase was composed of Solvents A (5 mM ammonium acetate in 90% H_2O/10% acetonitrile + 0.2% acetic acid) and B (5 mM ammonium acetate in 90% acetonitrile/10% H_2O + 0.2% acetic acid). The gradient conditions are shown in Table 5.1.

TIME RANGE (MIN)	SOLVENT A (%)	SOLVENT B (%)
0 – 1	25	75
1 – 5	from 25 to 70	from 75 to 30
5 – 9	70	30
9 - 9.1	from 70 to 25	from 30 to 75
9.1 – 40	25	75

Table 5.1 Description of LC program

The Q-Tof mass spectrometer was equipped with an electrospray ionization (ESI) source. The instrument was controlled by an Agilent Mass Hunter Workstation (Agilent Technologies, Santa Clara, CA). The ESI voltage was set at 3800 volts. The source gas was N_2 (99.999% purity). The ion source conditions in positive mode were: drying gas = 10 L/min, nebulizer gas = 45 psi, temperature=325°C. The extracted ion chromatography (EIC, 3-Mercaptopropionic acid m/z=106.14, 3-(2-Pyridyldithio) propanoic acid m/z=312.36) peaks were integrated using Agilent Mass Hunter Qualitative Analysis software (Agilent Technologies, Santa Clara, CA). The functionalized star polymers were purified by the LC system and obtained via lyophilization.

The functionalization efficiency was determined using $(V_c - V_f)/ V_c \times 100$ (%), where V_f is the integrated value of the free 3-Mercaptopropionic acid or 3-(2-Pyridyldithio) propanoic acid after the reaction and V_c is the integrated value of the free 3-Mercaptopropionic acid or 3-(2-Pyridyldithio) propanoic acid in the aqueous solutions in which no coupling agents (EDC or NHS) were added.

Molecular weights of the polymers were determined using aqueous gel permeation chromatography (GPC) (Waters 2695 Separations Module) fitted with a Waters 2414 refractive index detector and a Waters Ultrahydrogel 250 column (7.8 mm 300 mm). The buffer solution (0.05 M Tris buffer + 1.0 M NaCl) was used as the eluent with a flow rate of 0.5 mL/min at 35 C. All samples were filtered through 0.2 micron PTFE filters prior to injection. The system was calibrated with narrow molecular weight polyethylene oxide standards.

5.2.4. Cytotoxicity evaluation

The polymers were dissolved directly in the cell culture medium at 10 mg/mL. NIH-3T3, COS-7, HEK293 and hMSC cell lines (ATCC, Manassas, VA) were plated at 2×10^4 cells/mL in a 96-well tissue culture treated plate and incubated at 37°C in 5% CO2 and 100% relative humidity. After culture for 24 h, the culture medium was removed and 100 uL of monomer solution was added in each well. Fresh medium was used as a control. After the cells were exposed to the polymer-containing medium for how long, the medium was removed and the cells were rinsed with PBS. An MTT assay was then used to evaluate cell viability after exposure to each spCB polymer. 100 uL of MTT solution (5 mg of MTT/mL serum-free DMEM) was added to each well and incubated for 4 h, then replaced with 100uL of DMSO per well. The optical absorbance of formazan production was measured at 570 nm (OD_{570}) and 630 nm (OD_{630}). The relative cell viability was calculated using the following equation: relative cell viability (% of control) = (OD_{570} - OD_{630} of treated wells)/(OD_{570} - OD_{630} of the control) x 100%.

5.2.5. Hydrogel preparation and characterization

Degradable spCB hydrogels were prepared via a disulfide exchange reaction between spCB-SH and spCB-DP. SpCB-SH was dissolved in 100 uL PBS to make a 5% (w/v) solution. Three amounts of spCB-DP (0.5, 1, and 2 mg) were added to the spCB-SH solution and mixed briefly to initate gelation. Gelation was monitored by inverting the tubes until the gel solution stopped flowing.

The mechanical properties of the spCB hydrogels formed were tested using an Instron 5543A mechanical tester (Instron Corp., Norwood, MA). Five0.5 cm-diameter disks of each formulation (1.5 mm thickness when cast) were compressed at a rate of 1 mm/min using a 10 kN load cell. The Young's modulus was calculated from 3% to 13% strain to avoid any complications in an instance in which the top plate may not be completely engaged with the specimen when compression begins.

Dynamic viscoelasticity of the spCB hydrogels was measured with a Kinexus Pro rheometer (Malvern Instruments Ltd) using parallel plates 40-mm in diameter and a plate-to-plate distance of 900µm. The frequency-sweep spectra were recorded in a constant-strain (10%) mode over the frequency range of 0.1-100 rad/s at 25ºC. The time-sweep spectra were recorded at a constant-strain (10%) mode and constant frequency of 10 rad/s over time at 25ºC. The strain-sweep spectra were recorded in a constant frequency of 10 rad/s over the strain range of 0.01-10 at 25ºC. The temperature dependence of the storage and loss moduli was determined by oscillatory shear deformation over a temperature range of 20ºC to 50ºC.

5.2.6. Cell encapsulation, expansion, and recovery

Four cell types (NIH3T3, COS-7, HEK293, and hMSC, all from ATCC) were encapsulated in the spCB hydrogels, all at seeding densities of $2x10^5$ cells/mL. To encapsulate cells, cells were suspended in their appropriate media and mixed with media aliquots containing spCB-SH and spCB-DP, with each star polymer at a final concentration of 5% (w/v) to allow gelation. The resulting hydrogels embedded with cells were incubated at 37^oC in 5% CO_2 and 100% relative humidity to promote cell expansion. Immediately after encapsulation, selected cell-hydrogel constructs for each cell type were assayed for viability. For this viability test, constructs were stained with 1 mg/ml fluorescein diacetate (FDA) and 1 mg/ml propidium iodide (PI) for 30 min at 37oC in the dark. The samples were then washed with a large amount of PBS and observed under a Nikon Eclipse TE2000-U flurorescence microscope. The initial viability was calculated as the number of live cells/the number of total cells*100(%).

After a specified number of days of culture (3, 5, 7, 9, 11, and 15), the cell-laden hydrogels were incubated with hydrogel-dissociation medium (cell medium containing 2 mM L-cysteine) at 37 C for 30 min, and cells were recovered upon hydrogel decomposition and then collected by centrifugation. Cells were stained with Trypan blue, and their viability and proliferation rate was calculated using a hemacytometer. The rate of cell expansion was also determined by staining for DNA and glycosaminoglcan (GAG) content in each hydrogel. After each chosen time point, cell-hydrogel constructs from each group (n=5) were recovered and dehydrated by lyophilization. The dried constructs were then crushed with a tissue grinder and digested in 1 mL of papainase for 15 h at 60ºC. The DNA content (nanograms of DNA per milligram dry weight of the hydrogel) was determined by staining with Hoechst 33258 and measuring fluorescence (Ex 352 nm, Em 461 nm). The GAG content was determined by chondroitin sulfate using dimethylmethylene blue dye.

5.2.7. HMSC differentiation

Multicolor analysis for progenitor and stem cell phenotyping was performed on a LSR II flow cytometer (Becton Dickinson). Cells were stained in staining media (HBSS supplemented with FBS 2% and EDTA 2 mM) at 4°C for 1 h with Alexa Fluor® 647 anti-STRO-1 (Biolegend), FITC anti-ALCAM (AbD Serotec), then washed with staining media and analyzed. At least 10,000 events were acquired for each analysis.

To test gene expression of hMSCs cultured in spCB hydrogels, constructs were removed from culture media at specified time points and assayed with quantitative real-time PCR (qRT-PCR). The constructs were transferred to TRI Reagent (Sigma) in RNase-free test tubes and homogenized with a tissue homogenizer. Total RNA was extracted according to the manufacturer's instructions. Total RNA for each sample was quantified with a UV spectrophotometer and converted to cDNA using the QuantiTect Reverse Transcription Kit. After amplification using SYBR Green PCR Master mix (Qiagen), thermocycling was carried out in a solution with primers (Integrated DNA Technologies) and cDNA. PCR conditions were as follows: 15 s at 94ºC, 30 s at 55ºC, and 30 s at 72ºC. Here, we used RNase-free DNase (Qiagen) to prevent genomic DNA contamination.

To test for differentiation of expanded hMSCs encapsulated in spCB hydrogels, cell-hydrogel constructs were first cultured in basal medium for 3 days. Following this time point, the basal medium was replaced with bipotential differentiation medium to promote adipogenic and osteogenic differentiation of hMSCs. This medium contained: low glucose DMEM supplemented with 20% FBS and 1% penicillin/streptomycin (Invitrogen); an adipogenic supplement: 1μM dexamethasone, 50 μM indomethacin (Sigma), 0.5 μM 3-isobutyl-1-methylxanthine (IBMX; Sigma) and 10μg/mL human recombinant insulin (Invitrogen); and an osteogenic supplement: 10 mM β-glycerol phosphate (Sigma) and 50 μg/mL ascorbic acid (Sigma). Media changes were performed every 3 days. As a parallel control, a mixed adipogenic/osteogenic inductive media was made by combining commercially available osteogenic and adipogenic inductive media (R&D Systems) in a 1:1 ratio and supplementing with 1% (v/v) penicillin-streptomycin (Gibco). The mixed media was also used for differentiation experiments and no significant difference was observed compared to the lab-made bipotential differentiation medium.

After incubation for one week, cell-hydrogel constructs were fixed in 4% paraformaldehyde in PBS for 8 hours, transferred to 30 wt% sucrose for 72 h, frozen in Cryo-gel (Instrumedics, Inc.) and cryosectioned (10 μm sections) to prepare for histological staining. Osteogenic marker alkaline phosphatase (ALP) was visualized by staining with Fast Blue BB (Sigma), while lipid accumulation was examined by staining with Oil Red O (Sigma) to assay adipogenic activity. The total cell counts were obtained by staining the nuclei with DAPI. The percentage of hMSCs that differentiated down an osteogenic or adipogenic pathway was calculated by dividing the number of cells stained positive for ALP or lipids by the total cell counts, respectively. Color micrographs were acquired using a Nikon E800 upright microscope.

5.2.8. Statistical analysis

Examination and quantification of histological sections was done by three independent researchers blinded to sample identity with at least five random images/fields in each section per sample. A two-tailed Student's t-test was used for all statistical analyses, with *$p<0.01$ being considered as statistically significant.

5.3 Results and Discussion

5.3.1. Star polymer cytotoxicity and hydrogel mechanical properties

We synthesized spCBs targeting a wide range of molecular weights (MWs) from 5 kDa to 120 kDa. Modifying the ratio between monomer and initiator in the initial polymerization reaction tuned the degree of polymerization. We found the conversion to be high (between 70-80%) upon characterizing the polymers with GPC. The targeted and characterized MWs of all spCBs along with their polymerization conditions are shown in Table 5.2.

Polymer (MW target)	Initiator (mM)	Monomer (mM)	Mn (Da)	Conversion (%)
spCB-5K	1	5	4211	73.3
spCB-20K	1	20	17844	75.7
spCB-50K	1	50	42682	76.1
spCB-80K	1	80	72659	80.0
spCB-120K	1	120	103200	78.6

Table 5.2. spCB samples synthesized and their target and characterized molecular weights and polymerization conditions.

Then, we exposed cell lines to each spCB sample to ascertain their cytotoxicity. As shown in Figure 1a, the higher MW spCBs were nontoxic to all cell lines, as we expected based on the demonstrated cytocompatibility of linear pCB. The lower MW spCB polymers and oligimers (each 'arm' of 5-kDa spCB is only ~4-5 monomers in length) resulted in lower cell viability, possibly due to the reduced ratio of nontoxic zwitterionic moieties to the required initiator component. We thus used high MW spCB for further cell encapsulation and expansion experiments.

We next examined how the molecular weight of spCBs influenced the mechanical and viscoelastic properties of corresponding spCB hydrogels. As all hydrogels formed were designed to be very soft to allow robust cell expansion, the tensile strength and compressive modulus measured with an Instron instrument were imprecise and rotational rheometry proved to be a better characterization approach. To measure the dynamic viscoelasticity of each spCB sample, we conducted a time sweep at constant strain (10%) and frequency (10 rad/s) and assessed the maximum storage (G') and loss (G'') moduli reached upon gelation. When functionalized spCBs of a low MW (spCB-5K and spCB-20K) were mixed to initiate crosslinking and examined rheologically, G'' remained greater than G' through the time sweep, indicating insufficient crosslinking to form a free-standing elastic hydrogel at the concentration used for cell encapsulation. In comparison, spCBs of higher MW displayed higher elasticity, forming soft elastic hydrogels with G' and G'' both between 200 and 400 Pa. This data is shown in Figure 1b.

5.3.2. Cell expansion in and recovery from spCB hydrogels

We encapsulated cells in spCB hydrogels and assessed their viability after 14 days of expansion. As shown in the Live/Dead-stained micrographs in Figure 2a, all cells showed excellent (over 95%) viability after expansion in spCB gels. To quantify expansion, we immersed cell-hydrogel constructs in dissociation media and counted viable cells after recovery. Figure 2b displays the expansion rate of each cell line, which was all between 25 and 30x. This expansion rate was corroborated by quantifying total DNA and glycosaminoglycan (GAG) content in dried cell-hydrogel constructs using fluorescent markers; DNA content increased between 3000 and 3500% and GAG content increased between 4000 and 6000%. The DNA and GAG content found at each time point are shown in Figure 2c-d.

5.3.3. Preservation of mesenchymal stem cell bioactivity

Robust cell expansion is only clinically useful if expanded therapeutic cells maintain their bioactivity or specific functionality. In the case of hMSCs, multipotency after expansion must be maintained so their differentiation pathway can be deliberately chosen for optimal therapeutic benefit. To test the multipotency of hMSCs expanded in spCB gels, we used immunofluorescence staining to visualize the expression of multipotency biomarkers ALCAM and STRO-1. As shown in Figure 3a, we used flow cytometry to count cells expressing these biomarkers after one week of culture in spCB gels or in standard tissue culture flasks and compared them to the multipotent cells initially seeded. The hMSCs expanded in spCB hydrogels displayed positive expression of both biomarkers, equivalent to the population initially seeded. In contrast, hMSCs expanded in a flask were heterogeneous in ALCAM and STRO-1 expression, with around half of the population appearing to lose multipotency.

To further examine hMSC differentiation or multipotency, we used qRT-PCR to quantify the expression of mRNA characteristic to adipogenic (ADIPOQ, FABP4, LPL, PPARG) or osteogenic (COL1A1, OCN, OPN, RUNX2) lineages. After one week, none of these genes showed significantly enhanced expression in hMSCs cultured in spCB hydrogels, suggesting neither adipogenic nor osteogenic fates had been chosen by the cells. The expression measured for all genes relative to the initial population is shown in Figure 3b. Notably, hMSCs that have conclusively chosen an adipogenic or osteogenic lineage typically show between 100x and 10000x higher expression of these characteristic mRNAs.

We finally recovered the hMSCs expanded in spCB gels or in flasks and cultured them in bipotential (adipogenic and osteogenic) differentiation-promoting media. In this way, we could assay their functional bioactivity and therapeutic potential after expansion. After one week of culture, cells were fixed and histologically stained with Fast Blue salts to mark osteogenic expression of alkaline phosphatase (ALP), and with Oil Red O to examine lipid accumulation characteristic of adipogenesis. There was no difference in the differentiation capacity of the initial hMSC population and cells expanded in spCB gels, indicating their full bioactivity was preserved during expansion. Conversely, hMSCs expanded in flasks displayed a significantly reduced ability to differentiate down adipogenic and osteogenic lineages, signifying loss in functional bioactivity.

5.4 Discussion

Physicians and clincians see the profound impact that personalized cell-based medicine can bring to patients, but the challenge of expanding a patient's lifesaving cells *ex vivo* while maintaining their bioactivity. They calls for interdisciplinary collaboration. In the case of stem cell expansion, it becomes clear that biochemical signals and physical interactions between a stem cell and its niche are both key to triggering differentiation or maintaining multi- or pluiripotency. Polymeric hydrogels have become popular platforms for studying stem cell differentiation and expanding cell populations, as cell microenvironment can be tuned to resemble *in vivo* conditions much more closely than on flat 2D substrates. While several have reported that hydrogel scaffold *stiffness* is the key physical trigger of differentiation lineage in these systems, we believe that this is not a complete picture of the phenomena observed. Many biomaterials, including popular poly(ethylene glycol) (PEG), are not purely hydrophilic, For example, PEG is amphiphilic and is under increasing scrutiny as its immunogenicity reported suggest that it is not as bioinert as originally thought. Truly hydrophilic poly(zwitterions), especially poly(caryboxybetaine) (pCB), have unlocked deeper studies of cell-biomaterial interactions since pCB itself presents no nonspecific cues to cells, but can be easily functionalized to induce specific signaling or binding. Notably, when we cultured mesenchymal stem cells in pCB hydrogels in our previous work, we found the material stiffness is *irrevelvant* to whether stem cells remain multipotent or commit to a differentiated lineage. Instead, precise tuning of *nonspecific interaction sites* in the hydrogel drives fate choice, and these can be controlled independent of modulus. Pure pCB hydrogels can maintain stem cell multipotency for an unprecedented length of time. If we add photoswitchable moieties to the network, we can reversibly trigger differentiation through specified wavelength exposure.

This advance encouraged us to explore key applications in which premature cell phenotype change or scenescence *in vitro* is bottlenecking advances in cell-based regenerative medicine. Many treatments require growing a substantially expanded, yet homogeneous cell population in which expanded cells must retain their potency and specific bioactivity. Although cell populations are routinely expanded in flasks and bioreactors, nonspecific interactions from growth surfaces or aggregation reduce the usefulness of the population as they exhaust their limited lifespan and change phenotype unpreditably. Many of these same cell types are sensitive to external inputs such as UV light. Thus, encapsulation through a radical-mediated gelation reaction can also cause damage. We endeavored to combine the unique control enabled by pCB hydrogels with a more cytocompatible encapsulation strategy.

The spCB zwitterionic star polymers we developed in this work present several advantages for cell expansion. First, polymerization and end-group functionalization both occur independent of any cell interactions. Thus, we were able to carefully tune spCB molecular weight through robust living polymerization procedures as detailed in Table 2. Any unreacted reagents were removed after functionalization with LC-MS purification so sensitive cells are only exposed to a pure, well-defined material. This high level of control proved useful when optimizing spCB cytocompatibility and efficient gelation, as shown in Figure 1. Second, the star-shaped architecture ensures that each functionalized "point" of the star can quickly react with a complementary point on another. Therefore, simple mixing in the presence of cells rapidly establishes a soft yet elastic supportive network that maintains high cell viability, as presented in Figure 2a. Many cytocompatible reactions in the growing toolbox of bioorthogonal chemistries could be used to crosslink this platform while maintaining the overall zwitterionic nature of the network. In this work, we used a disulfide exchange reaction to add degradable disulfide linkages between star building blocks, which allowed us to easily break down the hydrogel by adding L-cysteine after expanding cells. These mild conditions enable the robust expansion rate as shown in Figure 2b-d to translate to a large population of viable recovered cells. Finally, this flexible new strategy did not hinder the ability of pCB niches to reliably maintain the multipotency and full differentiation capacity of encapsulaed hMSCs. As shown in Figure 3, we combined immunofluorescence labeling, quantification of mRNA expression and histological staining to test the bioactivity of expanded cells. Even at a 25-fold rate of expansion, cells in the dramatically enlarged population demonstrated equivalent potency and function to those cells in the initial seeded culture. Many cell-based therapies have a success rate directly proportional to the number of functional cells available for infusion. Thus, a simple platform mediating high expansion, simple cell recovery, and high bioactivity of recovered cells will broaden the reach, reduce the cost, and improve the success rate of these lifesaving treatments immediately.

5.5 Conclusions

We have developed a robust platform for expanding cell populations while maintaining their full bioactivity, based on encapsulated culture in zwitterionic hydrogels that form spontaneously by simply mixing two poly(carboxybetaine) star polymers end-functionalized with bioorthogonal reactive groups. This strategy extends the excellent reported capacity of zwitterionic pCB hydrogels to act as cytocompatible scaffolds for tissue culture and regenerative medicine applications. The unique star architecture, spontaneous crosslinking and controlled degradation without external input or radical generation is a gentle and facile way to expand and recover valuable cell lines without loss in functionality. Reliable and broadly-applicable methods to magnify rare cell populations could extend the reach of cutting-edge personalized medicine.

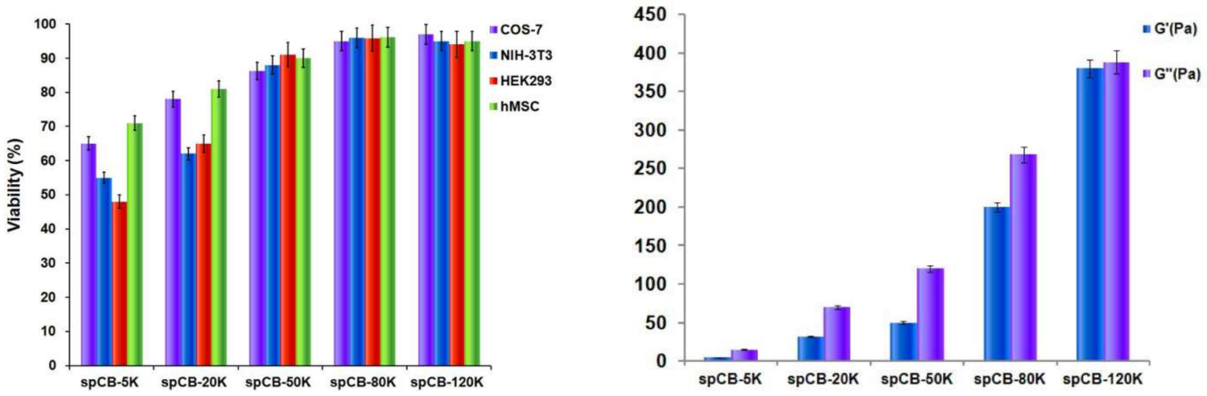

Figure 5.1. a) Cell viability after incubation with spCB samples overnight, and b) Rheological characterization (time sweep to gelation, strain = 10%, frequency = 10 rad/s)

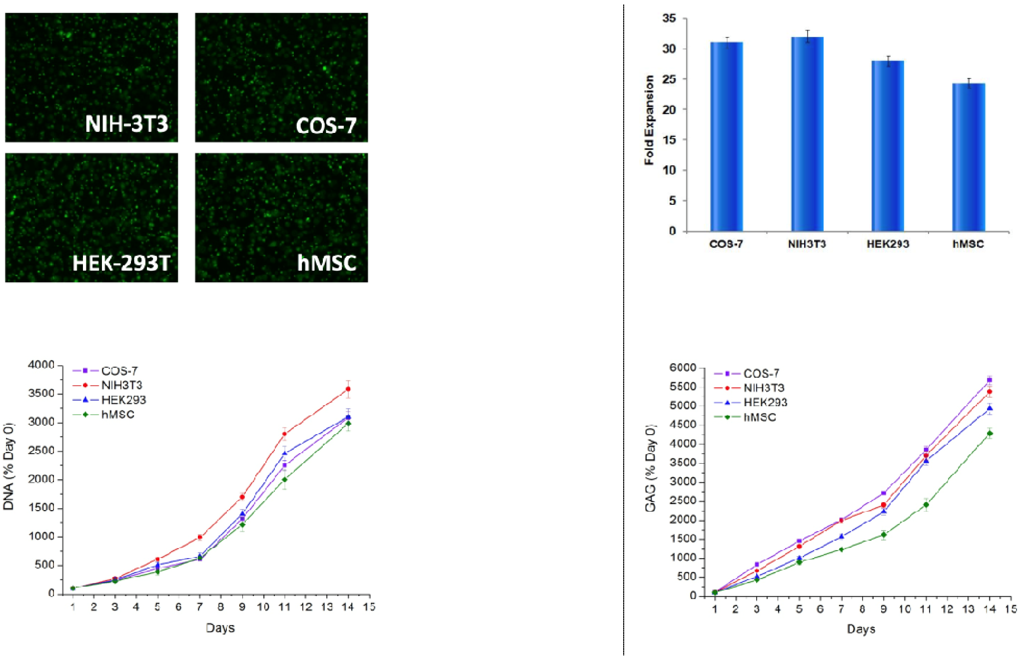

Figure 5.2. Cell viability and expansion in spCB hydrogels.

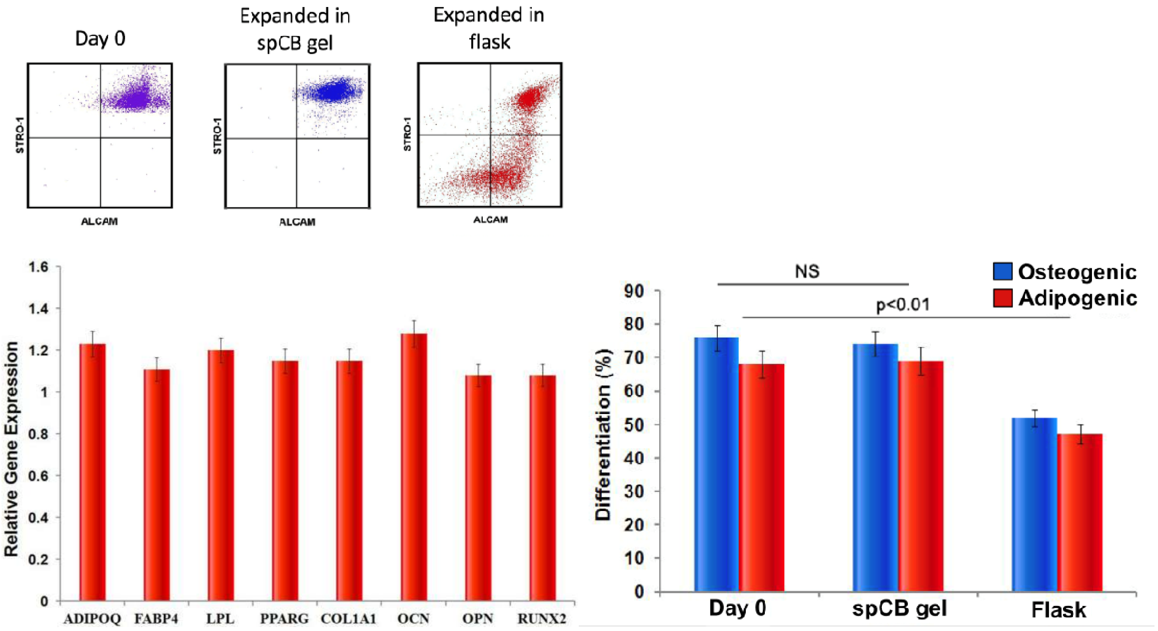

Figure 5.3. Analysis of hMSC differentiation. a) Flow cytometry analysis of immunofluorescently stained hMSCs expanded in spCB hydrogels or standard TC flasks, compared to the initial population. ALCAM and STRO-1 are multipotency markers, and dual positive expression indicates cell multipotency. b) Expression of mRNAs characteristic to adipogenic (left four) or osteogenic (right four) differentiation in the spCB-cultured cells, as assayed with qRT-PCR. c) Differentiation capacity of hMSCs expanded in spCB hydrogels or on flasks, when induced to choose a lineage with bipotential media.

Chapter 6 Nonfouling Zwitterionic Hydrogel Restrains the Differentiation of Hematopoietic Stem Cells in *Ex vivo* Expansion

The ability to *ex vivo* expand hematopoietic stem and progenitor cells (HSPC) without differentiation during culture is critical to fully realize the potential of hematopoietic stem cell based therapies. This is particularly true for therapies such as cord blood transplantation that have been proven clinically effective but are limited in clinical use due to low HSPC numbers. Through use of a 3D zwitterionic hydrogel, we achieved significant expansion of phenotypically primitive CD34+ cord blood and bone marrow-derived HSPCs with reduced metabolic activity. No differentiation was observed. Importantly, the cultured HSPCs were capable of human hematopoietic reconstitution for at least 24 weeks in immunocompromised mice, and resulted in a 70-fold increase in long-term hematopoietic stem cell (LT-HSC) frequency as demonstrated by limiting dilution assays. Deeper analysis showed that 3D zwitterionic hydrogel culture mitigates defects in HSPC self-renewal by inhibiting the excessive production of reactive oxygen species (ROS). Eliminating nonspecific cell-background interactions through use of a degradable zwitterionic matrix enables differentiation-free HSPC expansion and should facilitate clinical hematopoietic stem cell therapies.

6.1 Introduction

Hematopoietic cell transplantation (HCT) is an effective and widely used therapy with curative intent for a number of hematologic malignancies and non-malignant disorders. A total of 88,063 hematopoietic cell transplants were performed in the USA between 2009 and 2013, with 37,768 of these being from allogeneic related and unrelated stem cell donors [1]. However, the majority of patients in need of an HCT will not have the preferred donor, namely an HLA-matched related donor. In addition, only approximately 50% of Caucasian patients and far fewer patients of mixed race/minority backgrounds will be able to identify an unrelated, suitably matched and available adult donor [2]. For these patients, umbilical cord blood (CB) is now commonly used as an HSC source for allogeneic HCT. Cord blood has the distinct advantage of less stringent HLA-matching requirements between donor and host, allowing nearly all patients to identify CB donors without an increased risk of graft-versus-host disease, even in the setting of mismatched donors. Cord blood transplant (CBT) recipients have also been shown to have lower disease relapse rates post-transplant compared with those receiving bone marrow (BM) or peripheral blood transplants. Furthermore, our recent study evaluated the impact of pre-transplant minimal residual disease in patients undergoing a first allogeneic stem cell transplant and demonstrated that cord blood transplant recipients had a survival advantage compared to matched and mismatched unrelated donor transplant recipients[3]. Despite these advantages, the low stem cell dose available in a single- or double-unit CBT significantly delays hematopoietic recovery and results in a higher risk of graft failure and early transplant-related mortality, limiting the more widespread use of this stem cell source [4-6].

To increase the absolute numbers of HSPCs available for clinical applications, especially in the setting of HCT with CB donors, researchers have long sought to identify culture conditions suitable for *ex vivo* expansion of HSPC populations [7]. Early cytokine-mediated expansion strategies promote HSPC proliferation, but also trigger notable cell differentiation, diminishing their therapeutic value [8,9]. More recent efforts have focused on the use of small molecules or targeted *ex vivo* manipulation of molecular pathways known to play a role in hematopoietic stem cell fate [10]. For example, HSPCs exposed to an optimized balance of stimulatory and inhibitory factors in a fed-batch reactor have exhibited promising expansion rates and repopulation properties [11]. Our group has focused on the use of an engineered Notch ligand (Delta1) to activate endogenous Notch signaling in CB-derived HSPCs, thereby inhibiting *ex vivo* differentiation and resulting in a significant increase in the absolute number of $CD34^+$ HSPCs available for clinical applications. This approach has been evaluated in a number of clinical trials and shown to be safe while reducing the time to hematopoietic recovery in the myeloablative CBT setting [12,13]. A number of small molecules under clinical investigation, such as the aryl hydrocarbon antagonist SR1 and the pyrimidoindole derivatives (UM family of molecules) [14,15], have also been shown to promote the expansion of CB-derived HSPCs that possess robust repopulation activity. Despite these notable advances, and evidence of their ability to reduce the time to neutrophil recovery in a number of CBT trials, none of these state-of-the-art culture strategies are able to avoid significant HSPC differentiation and none are applicable for the expansion of adult BM-derived HSPCs [10].

Like many cell lines, HSPCs are commonly cultured in hydrophobic polystyrene flasks, exposing them to surroundings that differ greatly from their *in vivo* niche—a three-dimensional (3D) environment dominated by hydrophilic and zwitterionic cell membrane lipids [16]. Hydrophobic materials provide abundant nonspecific interactions to all cell ligands [17], and we hypothesize that this continuous nonspecific stimulation of cells plays a key role in triggering nonspecific HSPC differentiation *in vitro*. To explore this hypothesis, we endeavored to more closely model the *in vivo* niche by culturing HSPCs inside a 3D zwitterionic hydrogel matrix. Zwitterionic polymers and peptides are super-hydrophilic and uniquely resistant to nonspecific interactions, and polyzwitterionic surfaces can completely eliminate protein attachment in complex physiological fluids including undiluted plasma and serum [18]. In contrast to hydrophobic and amphiphilic materials, zwitterionic materials have no effect on the activity of nearby or conjugated proteins [19], are able to resist collagenous capsule formation when implanted in mice [20], and circumvent antibody production during bloodstream circulation [21]. Here, we encapsulated and cultured both CB- and BM-derived HSPCs inside zwitterionic poly(carboxybetaine)-based hydrogels using a specifically selected metalloproteinase-cleavable zwitterionic peptide to reversibly crosslink the gels [22-24]. All components were designed to completely avoid nonspecific interactions with the encapsulated HSPCs, and the degradable crosslinks facilitated gradual growth and eventual cell recovery.

6.2 Methods

6.2.1 Star-shaped Polymer synthesis: The polymerization was conducted as reported before. In brief, CBMA, 2,2'-bipyridine (bpy), catalysts, tetrafunctional initiator, pentaerythritol tetrakis(2-bromoisobutyrate), were placed in a 10 mL reaction tube, and the mixture was subjected to three freeze-pump-thaw cycles. The mixture stayed under room temperature for 20 min, and water and methanol were added at a 1:1 ratio. The reaction was allowed to continue at room temperature under stirring for 8 h. The polymer product was recovered after treatment with alumina, and finally purified by precipitation twice into acetone. The molecular weight of the polymer can be tuned by the stoichiometric ratio between the monomer and the initiator. Star-shaped polymers with target molecular weights of 50000 was synthesized.

6.2.2 Synthesis of N_3-functionalized star-shaped pCB polymers. After purification, 2g star-shaped pCB polymer was mixed and tired with 50mg sodium azide in water. The reaction was allowed at room temperature for 48 hours. The product was purified by dialysis and dried on lyophilization .

6.2.3 Synthesis of NH_2-functionalized star-shaped pCB polymers. The azide group on this star-shaped pCB was reduced into NH_2 by using a MCM-Silylamine Pd(II) Complex. MCM-Silylamine Pd(II)Complex was prepared as reported before. In this work, 1.5g Azide-terminated pCB polymer and 10mg MCM-Silylamine Pd(II) Complex was dissolved in 10ml methanol. The reaction was allowed for 3 hours at room temperature and then the complex was filtered and the polymer was dried under vacuum.

6.2.4 Synthesis of click-functionalized star-shaped pCB polymers As we reported before, DIFO3 was functionalized to the end of star-shaped pCB polymer. In brief, appropriate amounts of N-(3-Dimethylaminopropyl)-N'-ethylcarbodiimide hydrochloride (EDC) (Sigma) and N-Hydroxysuccinimide (NHS) (Sigma) were added to DIFO3 solution. After incubation at 25°C for 1 hour to activate the carboxylate group, 1g NH_2-terminated polymer was added to the activated system. The molar concentration of DIFO3 in the reaction solution was set at 100μM. The molar ratio of EDC, NHS and peptides was fixed at 1:1:1. The reaction was allowed to proceed at 25°C for 24 hours before purification. The efficiency of the reaction was calculated by ^{1}H-NMR.

6.2.5 Surface-initiated atom transfer radical polymerization

Surface-initiated ATRP was carried out on SAM-coated gold substrates following a method similar to one previously reported[1]. Briefly, CuBr, $CuBr_2$, BPY, and gold chips with immobilized initiators were placed in a sealed reaction tube and deoxygenated via vacuum and nitrogen purging. CBAA monomer was deoxygenated in a separate sealed tube, and then dissolved in a deoxygenated solution of methanol and pure water in a 10:1 volume ratio. The monomer solution was transferred to the reaction tube using a syringe under nitrogen protection. In a shaker at 120 RPM and 25℃, PCBAA was allowed to react for 3 h. After polymerization, chips were removed, rinsed with pure water and PBS, and stored overnight in PBS. Chips were rinsed with Milli-Q water and dried with filtered air just prior to any experiments. Dry film thickness was measured with an ellipsometer (J.A. Woollam, Alpha-SE), and chips with thicknesses of 20-30 nm were used for SPR measurements.

6.2.6 Preparation of mix charged peptide SAMs. Peptides (CGG$(KE)_{20}$GPQG and CGG$(KE)_{20}$IWGQ) were ordered from Synthetic Biomolecules (San Diego, CA) at a purity of >95%. Gold-coated chips were cleaned by rinsing with Millipore water and ethanol (Decon Laboratories, Inc., King of Prussia, PA) and then drying with filtered air. They were placed in the UV cleaner for 20 min. Cleaned gold chips were incubated in a phosphate buffered saline (PBS) solution (pH 7.4 and ionic strength 150 mM, Sigma-Aldrich, St. Louis, MO) containing 0.14 mM peptide for 24 h. Once removed, the gold chips were rinsed with Millipore water and dried by filtered air.

6.2.7 Preparation of Cell lysates. HSCs were pelleted (1000 rpm, 4°C) and lysed into RIPA buffer (Sigma) which enables efficient cell lysis and protein solubilization while avoiding protein degradation and interference with the proteins' immunoreactivity and biological activity. The protein content of purified cell lysates was determined via BCA assay.

6.2.8 Measurements of protein adsorption

For protein adsorption tests, 1% HSCs lysates and 5GF-SFEM II were used for the protein absorption assay. This study used a custom-built surface plasmon resonance (SPR) sensor from the Institute of Photonics and Electronics, Academy Sciences (Prague, Czech Republic). A prepared chip was attached to the base of the prism and optical contact was established using refractive index matching fluid (Cargille). A quadruple-channel flow cell with four independent parallel flow channels was used to contain liquid samples during experiments. A peristaltic pump (Ismatec) was utilized to deliver liquid samples to the four channels of the flow cell. A stable baseline was first established with water, PBS, or divalent salt solution with different concentrations of running buffer, then serum solution was delivered to the surface at a flow rate of 0.050 mL/min for 30 min, and the same buffer flowed again for 10 min before determining final wavelength shifts. A surface-sensitive SPR detector was used to monitor surface interactions in real time, and wavelength shift was used as an indication of changes on the surface.

6.2.9 Metabolites analysis. Cell-hydrogel constructs were washed in PBS and crushed with a tissue grinder before metabolites were extracted using an extraction solvent (1:3:1 Chloroform: Methanol: Water), and placed on a rotary shaker for 1 hour at 4℃. The solution was then centrifuged for 3 minutes at 13000g at 4℃ after which supernatant were collected and dried at 30 °C for ~2hr in a SpeedVac. The samples were analyzed using LC-MS QqQ method system as described below.

6.2.10 Liquid chromatography conditions. The LC system was composed of two Agilent 1260 binary pumps, an Agilent 1260 auto-sampler, and Agilent 1290 column compartment containing a column-switching valve (Agilent Technologies, Santa Clara, CA). Each sample was injected twice, 10 µL for analysis using negative ionization mode and 2 µL for analysis using positive ionization mode. Both chromatographic separations were performed in hydrophilic interaction chromatography (HILIC) mode on two SeQuant ZIC-cHILIC columns (150 x 2.1 mm, 3.0 µm particle size, Merck KGaA, Darmstadt, Germany) connected in parallel. Our setup allows one column performing separation while the other column is getting reconditioned and ready for the next injection. The flow rate was 0.300 mL/min, auto-sampler temperature was kept at 4℃, the column compartment was set at 40℃, and total separation time for both ionization modes was 20 min. The mobile phase was composed of Solvents A (5 mM ammonium acetate in 90% H_2O / 10% acetonitrile + 0.2% acetic acid) and B (5 mM ammonium acetate in 90% acetonitrile/ 10% H_2O + 0.2% acetic acid). The gradient conditions for both separations were identical and are shown below.

Time min.	Segment,	Solvent A, %	Solvent B, %
0 - 2		25	75
2 - 5		from 25 to 70	from 75 to 30
5 - 9		70	30
9 - 11		from 70 to 25	from 30 to 75

11 - 20	25	75

The metabolite identities were confirmed by spiking the sample used for method development with mixtures of standard compounds (each mixture contained five standard metabolites). All the samples were analyzed over a 12-day period and the retention times (RT) did not undergo any significant shift (each peak was within 6 seconds throughout 12 days of analysis), which proved the robustness of our HILIC method.

6.2.11 Mass spectrometry conditions. After the chromatographic separation, MS ionization and data acquisition were performed using an AB Sciex QTrap 5500 mass spectrometer (AB Sciex, Toronto, ON, Canada) equipped with an electrospray ionization (ESI) source. The instrument was controlled by Analyst 1.5 software (AB Sciex, Toronto, ON, Canada). Targeted data acquisition was performed in multiple-reaction-monitoring (MRM) mode. We monitored 99 and 59 MRM transitions in negative and positive mode, respectively (158 transitions in total). The source and collision gas was N_2 (99.999% purity). The ion source conditions in negative/positive mode were: curtain gas (CUR) = 25 psi, collision gas (CAD) = high, ion spray voltage (IS) = -3.8/3.8 KV, temperature (TEM) = 500℃, ion source gas 1 (GS1) = 50 psi, and ion source gas 2 (GS2) = 40 psi.. The extracted MRM peaks were integrated using MultiQuant 2.1 software (AB Sciex, Toronto, ON, Canada).

6.2.12 Data analysis, model development and cross validation. A custom metabolite database incorporating HMDB was used to identify compounds. After exporting from MultiQuant software, spectral data were normalized using average values from the data of quality control (QC) injections (at least five in each batch, 33 QC samples in total). Means and standard errors of the mean were generated for all groups of picked peaks.

6.2.13 Cell sources

We obtained human umbilical cord blood samples for research purpose from normal deliveries under Swedish Medical Center's Institutional Review Board (Seattle) approval and after consent was obtained. Unit processing and CD34+ cell selection were performed as described previously (Delaney, 2010 & 2005).

Cryopreserved immobilized peripheral blood stem cell and bone marrow stem cells were purchased from Cell Processing Facility at the Fred Hutchinson Cancer Research Center.

6.2.14 CD34$^+$ Cells expansion in ZTG

Hydrogels were created by mixing 10 wt% total star-shaped polymer and difunctionalized peptide in media between Rain-X-treated glass slides spaced at a known distance (300 um), and reacted for 30 min at 37℃.

HSCs were encapsulated in the ZT Gel, at various seeding densities. To encapsulate cells, cells were suspended in HSC expansion media consisting of StemSan SFEM II (StemCell Technologies) supplemented with human 50ng/ml stem cell factor (SCF), 50ng/ml FMS-like trysine kinase 3 ligand (FLT3), 50ng/ml thrombopoietin (TPO), 50ng/ml interleukin-6 (IL-6) and 10ng/ml interleukin-3 (IL-3) (Invitrogen). Media aliquots containing zwitterionic polymers and peptides, with each polymer at a final concentration of 10% (w/v) to allow gelation. The slides were separated and the cell-encapsulating hydrogels were equilibrated in media. During the first 5-hour equilibration, the media was refreshed every hour, and then refreshed every day. The resulting hydrogels embedded with cells were incubated at 37^{o}C in 5% CO_2 and 100% relative humidity to promote cell expansion.

As control, selected CD34+ cells were cultured directly in tissue culture polystyrene flask or in 2.5ug/ml Delta1 ext-IgG coated flask (Delaney, 2010 & 2005). Culture media and supplement were the same as above. For no growth factors experiment, CD34+ cells were cultured in either hydrogel or TCPS using SFEM II media without other supplements.

6.2.15 Flow Cytometric Analysis

Cell phenotypes in fresh and expanded cells were measured using a combination of the following antibodies and fluorophores: Primitive panel: APC-anti-huCD34, PECY7-huCD45RA, AF700-huCD38, PE-huCD90, FITC-huCD49f; Differential panel: AF700-huCD34, PE-huCD7, PeCy7-huCD56, APC.Cy7-huCD14, FITC-huCD15, APC-huCD19 antibodies.

For CFSE labeling, CD34$^+$ CB cells (1x10^6 cells/ml) were labeled with 5 μM carboxyfluorescein diacetate succinimidyl ester (CFSE, Invitrogen) according to the manufacturer's guidelines. Labeled cells were encapsulated in ZTG to culture for 7 days, or cultured in a 6 well tissue culture plate for 4 days. Cells were harvested and stained with APC-labelled anti-human CD34.

Cell events were collected with an LSR II Flow Cytometer (BD Biosciences), and flow data was analyzed using FlowJo software (TreeStar, Ashland, OR).

6.2.16 Assessment of Cell Morphology

Cell morphology was assessed using slides prepared by Cytospin using a cytocentrifuge (Cytospin 2, Shandon Scientific) at 500rpm for 3 min followed by Wright-Giemsa staining. The bright field slides were scanned with Aperio Scanscope AT. The images were recorded and analyzed using Aperio ImageScope v12.2.1.5005. Briefly, the diameter of 50 randomly selected cells from each group were averaged and then compared between the groups.

6.2.17 *In vitro* colony-forming unit assays

Frequencies of colony-forming cells were estimated by plating 200 or 500 fresh or expanded CD34+ cells in methylcellulose containing media (MethoCult H4434, StemCell Technologies) supplemented with thrombopoietin, and Flt-3 ligand, each at a final concentration of 50ng/ml. After 14 days in culture, plates were visually scored for CFU-multilineage colonies.

6.2.18 *In vivo* repopulation studies

All experiments with animals were conducted under protocols approved for use by the Fred Hutchinson Cancer Research Center Institutional Animal Care and Use Committee (IACUC). NOD/LtSz-scidIL2rg−/− (NSG) mice were obtained from the Jackson Laboratory (Bar Harbor, ME) and bred in the animal care facility at the Fred Hutchinson Cancer Research Center. Fresh CB CD34+ cells or their progeny present in different cultures were injected into sub-lethally irradiated (275 cGy) 5-10 weeks old NSG mice one day prior to infusion via tail vein. We assessed their repopulating ability at 4 weeks and 12-14 weeks after transplant with marrow removed from the knee joint of anesthetized mice. At 20-30 weeks after transplant, we killed the mice and assessed both femurs and tibias for the number and types of human cells. For secondary transplants, 50% of the bone marrow isolated from each recipient mouse was transplanted into one secondary sub-lethally irradiated NSG mouse.

Human cell engraftment was monitored by flow cytometric analysis of bone marrow cells obtained from different time point using PE.Cy5-anti-human CD45 and APC.Cy7-anti-mouse CD45.1 antibodies. The subsets of human CD45+ cells were further determined using PE.Cy7-anti-huCD33, APC-anti-huCD19, PE-anti-huCD56, APC.Cy7-anti-huCD3, PE-anti-huCD41, FITC-anti-huCD235a, AlexaFluro700-anti-huCD34 or APC-anti-huCD34 and AlexaFluro700-anti-huCD38 antibodies.

We determine the frequency of SCID repopulating cell (SRC) by limiting dilution analysis (LDA). HSCs either from fresh isolated CB CD34+ cells or from cultured cells were diluted serially to the desired cell doses. The frequency of SRC were calculated using the ELDA software (http://bioinf.wehi.edu.au/software/elda/index.html) provided by the Walter and Eliza Hall Institute.

6.2.19 Cell cycle Analysis

For the combinatory staining of surface markers and cell cycle, HSCs were stained with APC-anti-CD34 as described above. After a washing step, the cells were fixed and permeabilized with 70% ethanol, then intracellularly stained with FITC conjugated Ki-67. After washing, cells were stained with Hoechst33342 for 10 minutes and washed before resuspension in 100 μl PBS. Cells were subsequently analyzed using the LSRII flow cytometer (BD biosciences).

6.3 Results and Discussions

To enable gentle cell encapsulation in situ, we used a bioorthogonal and cytocompatible strain-promoted azide-alkyne cycloaddition (SPAAC) “click” reaction to form the hydrogels. Four-arm poly(carboxybetaine acrylamide) (pCBAA) was terminated with difluorinated cyclooctynes ($DIFO_3$) and reacted with a bis(azide)-functionalized polypeptide (Azide–GG-$(KE)_{20}$-GPQGIWGQ-$(KE)_{20}$-GG-Azide) to form an idealized three-dimensional network with minimal local defects (Fig. 1a-c, Supplementary table S1 and Fig. S1) [22,25]. To maximize the crosslinker hydrophilicity, we added zwitterionic segments of twenty alternating lysine (K) and glutamic acid (E) residues on each side of the metalloproteinase-cleavable motif previously reported [24,25]. Particularly in contrast to hydrophobic polystyrene (the most common material for cell culture flasks), we did not detect any nonspecific interactions between HSPC lysate or media proteins and either the pCBAA polymer or KE-dominated peptide (Supplementary Fig. S2). In addition, compared with the commercial hyaluronic acid and polyethylene glycol-based HyStem® hydrogel, which is designed to minimize cell attachment, the ZTG hydrogel showed much less interaction with encapsulated HSPCs (Supplementary Fig. S3). This finding suggests these materials can completely eliminate cell-background interactions in the culture platform, acting as a truly "blank slate" for 3D stem cell culture.

We isolated fresh human CD34$^+$ HSPCs from CB, encapsulated this purified cell population within the aforementioned zwitterionic hydrogel (ZTG) in optimized growth factors and media, and monitored proliferation responses. HSPCs secrete small amounts of metalloproteinase, which gradually cleaves some of the peptide crosslinks during proliferation and allows the hydrogel to swell and accommodate the growing population. After an initial 14-day expansion period, additional metalloproteinase was added to fully disassemble the constructs and free the expanded cells. As presented in Supplementary Fig. S4-6, the ZTG condition exhibited much better biocompatibility than the control flask substrate, promoting HSPC survival and self-renewal under different culture conditions. The isolated cells were immunophenotyped and evaluated for differentiation (defined as loss of CD34 expression). As presented in Fig. 1d, when HSPCs were cultured on a hydrophobic tissue culture polystyrene (TCPS) substrate, a sharp decrease in CD34 expression was observed. While aforementioned UM171, SR1 and Delta1 culture can maintain CD34 expression at a much higher level, hydrophilic 2D substrates such as IgG protein coatings, ZTG hydrogels, and HyStem® can also significantly delay the differentiation process. Importantly, 3D culture showed a striking effect in preserving CD34 expression during this 14-day culture. Expanded HSPCs from the commercial HyStem® culture exhibited 62.1% expression of CD34. Among all experimental groups, a surprisingly high frequency of CD34$^+$ cells in the final harvested cell population (95.9%±3%) was achieved in 3D ZTG culture. This encouraged us to pursue further expansion using 3D ZTG culture. We investigated the cell cycle status of cells in the 3D ZTG culture condition by staining with anti-Ki-67 and

Hoechst 33342. As presented in Supplementary Fig. S7, the cells began to exhibit G1 and S+G2/M phases in the first few days of 3D ZTG culture. Then, due to contact inhibition, cells in the G_1 and $S+G_2/M$ phases gradually decreased and almost all cells converged into the G_0 phase by Day 14. In addition, when cells were transferred to regular cell culture flasks, we observed that both fresh cells and ZTG-expanded cells were able to enter into cell cycles (Supplementary Fig. S8).

As presented in Fig. 1e, after the initial 14-day expansion period, expanded cells were passaged into a new ZTG at an optimal seeding density for another 10 days of culture; contact inhibition led to a significant proliferation rate decrease after this 10-day culture (Supplementary Fig. S9a). In this work, we used the 24-day protocol as the optimized condition for $CD34^+$ HSPC culture in the ZTG (ZTG_{opt}), in which expanded cells showed a higher cell number increase and minimized phenotype change (Supplementary Fig. S9b-d). The final cell population was harvested for further evaluation and functional stem cell assays (Fig. 1d, bottom). Over this 24-day culture period, we achieved a 322-fold expansion of total nucleated cells (TNC) with excellent viability (94.2%±3%) and a surprisingly high frequency of $CD34^+$ cells in the final harvested cell population (94.6%±2%). Cells harvested after the second 10-day culture period in the ZTG were more robust in terms of *in vitro* CFU assays and *in vivo* engraftment, compared to cells cultured in the ZTG for only 14 days (Fig. 1, f, g).

Given our prior experience with *ex vivo* expansion of human CB-derived $CD34^+$ HSPCs in the presence of an engineered Notch ligand, and our clinical translation of these methods, we compared the ZTG_{opt} expansion methodology with an optimized $Delta1^{ext\text{-}IgG}$ culture system (DXI_{opt}) and HSPC culture in unmodified flasks (Control). Highly purified fresh CB $CD34^+$ cells (93% ± 2% CD34) were used to initiate cultures in all conditions. These cells were homogeneously small and round, with scant and agranular cytoplasm and round eccentric nuclei (Fig. 2a). The homogeneity of this population was retained after culture in the ZTG_{opt}, while both DXI_{opt} and control conditions resulted in heterogeneous populations of large cells with granular cytoplasm and irregular nuclei, indicating some degree of cell differentiation (Fig. 2a). ZTG_{opt} culture conditions maintained a high percentage of $CD34^+$ cells throughout the culture period with 94.6% ± 2% of the cultured cells expressing CD34.

In comparison, 33.6% ± 2% of the DXI_{opt} expanded cells and only 5.1% ± 4% of the control culture remained $CD34^+$ (Fig. 2b). More importantly, even though a significant portion of DXI_{opt} expanded cells continued to express CD34, only 4.8% ± 4% of these cells were also negative for lineage markers (CD7, CD14, CD15, CD19 and CD56), similar to the control condition result (3.8% ± 3%).

In stark contrast, 93.1% ± 1% of ZTG_{opt} cells were both $CD34^+$ and Lin^-, again showing no significant difference from fresh HSPCs (91.8% ± 1%) (Fig. 2b). ZTG_{opt} cells maintained a phenotype very similar to fresh HSPCs, as well as a high frequency of $CD34^+CD45RA^-$ cells at 74.5% ± 9% of the total final cell population, compared to 77.6% ± 5% of the initial purified starting population. This is in contrast to the reduced $CD34^+CD45RA^-$ frequencies observed after culture in the DXI_{opt} (3.9% ± 3%) and control (0.3% ± 0.5%) cultures (Fig. 2c). The fold expansions of both total cell count (TCC) and primitive HSPC subsets (Supplementary Fig. S10) are summarized in Fig. 2c. Higher overall TCC proliferation was seen in the DXI_{opt} (530-fold) and control (1450-fold) conditions, but a substantial fraction of these cells were negative for CD34. In contrast, ZTG_{opt} expansion produced a 322-fold TCC increase that was matched by a 319-fold increase in $CD34^+$ cells and a 284-fold increase in the most phenotypically primitive subset ($CD34^+CD38^-CD45RA^-CD49f^+CD90^+$) (Supplementary Fig. S10). These results are remarkable when compared with the fold increase of the same populations in DXI_{opt} (122-fold increase in $CD34^+$ and 6-fold increase in $CD34^+CD38^-CD45RA^-CD49f^+CD90^+$ cells) and control conditions (22-fold increase in $CD34^+$ and 30% decrease in $CD34^+CD38^-CD45RA^-CD49f^+CD90^+$ cells) (Fig. 2d).

The negligible expansion of $CD34^-$ cells (0.3-fold increase) and low expression of differentiation markers in the ZTG_{opt}-expanded population suggests the zwitterionic hydrogel is particularly capable of inhibiting HSPC differentiation during expansion. To investigate whether the 24-day ZTG_{opt} cells behaved similarly to freshly isolated (non-cultured) HSPCs in our DXI_{opt} system, we initiated cultures as per our DXI_{opt} methods using cells harvested after ZTG_{opt} culture (Supplementary Fig. S11a). We demonstrated that these 24-day ZTG_{opt} cells continued to retain their *ex vivo* expansion capacity signaled by $Delta1^{ext\text{-}IgG}$ stimulation, as expected in this system (Supplementary Fig. S11, b, c). As with freshly isolated HSPCs,

ZTG_{opt}-cultured cells subsequently expanded in DXI_{opt} conditions rapidly reconstituted in NSG recipients, matching our experiments using freshly isolated HSPCs from CB for Delta1$^{ext-IgG}$ expansion (Supplementary Fig. S11d) [12].

Having demonstrated that CB-derived $CD34^+$ cells cultured with the ZTG_{opt} method maintained their *in vivo* repopulating ability, we next conducted limiting dilution analysis (LDA) to determine the frequencies (adjusted to the numbers of $CD34^+$ cells at day 0) and absolute numbers of long-term repopulating hematopoietic cells (LT-HSCs), comparing ZTG_{opt} cultured cells with non-cultured cells (Fig. 3a, Supplementary Tables S2 and S3) [26]. When analyzed at 24 and 30 weeks post-transplantation, the LT-HSC frequency in ZTG_{opt} expanded populations was measured to be 1 per 12 $CD34^+$ starting cells (95% confidence interval of 6.8 to 21.5), whereas in non-cultured $CD34^+$ CB cells, a LT-HSC frequency of 1 per 880 $CD34^+$ starting cells (95% confidence interval of 495 to 1542) was measured (Fig. 3b, c). This represented a 73-fold increase in the frequency of day-0-equivalent LT-HSCs in ZTG_{opt} cultured populations when compared with non-cultured cells (Fig. 3c), a five-fold increase over DXI_{opt} expanded cells (1/59), and a 110-fold increase over the control-expanded cells (1/1320) (Supplementary Table S2b). At all evaluated time points (short [4 weeks], medium [12-14 weeks], and long [24-30 weeks] term post-transplant) ZTG_{opt} expanded cells demonstrated higher levels of human engraftment than non-cultured $CD34^+$ cells and those expanded in DXI_{opt} and control cultures (Supplementary Table S2-3). Notably, a ZTG_{opt}-expanded population generated from 100 fresh $CD34^+$ cells had a similar level of sustained engraftment in NSG mice (24.7%) as 10,000 uncultured $CD34^+$ cells (22.4%) at 24-30 weeks post-transplantation (Fig. 3d, e). In addition, both lymphoid and myeloid engraftment were detected in mice that received the non-cultured and ZTG_{opt}-cultured cells (Fig. 3d).

We next examined whether ZTG_{opt}-expanded cells retained the multi-lineage potential of the starting non-cultured HSPCs. To exclude the impact of different graft levels on lineage contribution, we compared two groups that had similar human engraftment: the group receiving ZTG_{opt} cells derived from the expansion of 100 fresh HSPCs, and the group receiving 10,000 fresh HSPCs. The similar levels of human engraftment in both groups indicated that ZTG-expanded populations retained full HSPC multi-lineage repopulation capabilities (Fig. 3e). Importantly, we observed similar levels of $CD34^{+}CD38^{-}$ (0.73% vs 0.67%) cells, signifying the continued presence of LT-HSCs in the BM of NSG recipients (Fig. 3e, Supplementary Table S2-3).

In addition to LDA, secondary transplants were conducted to further determine the presence of LT-HSC engraftment. Primary recipients transplanted with ZTG_{opt} cells were sacrificed at 24 weeks post-transplantation and half of their marrow was transplanted into secondary mice. We observed human engraftment (defined as >0.1% human $CD45^{+}$ cells) in the marrow of 4 out of 5 secondary recipients (Supplementary Table S4), supporting the sustained presence of an LT-HSC population and showing that ZTG-expanded HSPCs remained competent in secondary recipients.

To date, most *ex vivo* HSPC expansion methodologies have had limited success with adult HSPCs. After demonstrating the ability of our ZTG_{opt} method to support *ex vivo* expansion of CB-derived HSPCs with primitive phenotypes and *in vivo* functionality, we applied this same strategy to expand BM-derived HSPCs *ex vivo*. Similar to ZTG_{opt} cultures initiated with CB HSPCs, ZTG_{opt} expansion of BM-derived HSPCs inhibited differentiation while promoting expansion and maintenance of cells expressing primitive markers (Supplementary Fig. S12 a, b). ZTG_{opt} cultures initiated with BM-derived HSPCs exhibited a 238-fold TCC increase, which was again nearly matched by the 230-fold increase in $CD34^{+}$ cells (Supplementary Fig. S12c). Both *in vitro* and *in vivo* functional assays demonstrated strong ZTG_{opt} repopulating capacity and no significant difference was found between fresh and ZTG_{opt} groups (Supplementary Fig. S12d and S13). All of these results corroborate our CB-derived cell findings.

We next sought to explore the mechanism by which the nonfouling ZTG culture environment influences HSPC activity, and thereby their self-renewal or differentiation decisions. Biomaterials are known to induce production of reactive oxygen species (ROS), which leads to a number of possible pathophysiological outcomes including cytotoxicity and foreign body reactions such as fibrosis, atherogenesis and granulomas et al[27,28]. Reactive oxygen species can nonspecifically react with a number of redox-sensitive molecules, resulting in oxidative modifications including cysteine oxidation, cysteine nitrosylation, cysteine glutathionylation, methionine oxidation, protein carbonylation, and protein hydroxylation[29]. These oxidative modifications can directly or indirectly affect the function and activation of transcription factors (e.g. EOXO, p53, PRDM16, NRF2, HIF et al.), as well as kinases (e.g. mTOR, p38 MAPK, AKT et al.) and phosphatases (e.g. PTEN)[29,30]. Other regulators, such as the signal transducer β-Catenin, the cytokine signaling inhibitor LNK, the modulator KEAP1, the E3 ubiquitin ligase MDM2, and the cell cycle inhibitors p16INK4A and p19ARF, can also be affected by ROS levels. It has been reported that increased ROS levels can inhibit HSPC self-renewal pathways such as Wnt/β-Catenin[31,32] while activating pathways that can result in defective self-renewal such as p38 MAPK[33], mTOR[34] et al.[35]. These ROS-induced pathway activation and deactivation processes appear to be nonspecific. In nature, primitive HSPCs reside in a low-oxygenic niche that limits ROS production and provides the cells with long-term protection[36]. Here, we tried to elucidate whether 3D ZTG culture can also limit ROS production and protect the encapsulated HSPCs. Since the pioneering work in the Anderson and Langer labs[37], it has been noticed that culture in a hydrophilic environment significantly mitigates excessive ROS production and reduces the degree of fibrosis. In our previous work, we also found superhydrophilic zwitterionic hydrogels to resist this fibrosis[20]. We hypothesize that culture in hydrophobic environments provides cells with nonspecific interactions and induces excessive ROS production; as a result, these excessive ROS will nonspecifically activate HSPC differentiation pathways while inhibiting HSPC self-renewal pathways (Fig. 4a). In contrast, the lack of nonspecific interactions in zwitterionic cultures may inhibit ROS-induced nonspecific pathway activation/deactivation, enabling differentiation-free HSPC expansion to be achieved in zwitterionic hydrogel cultures. As presented in Fig. 4b-c, after one day of culture in each system, cellular ROS and mitochondrial superoxide levels slightly decreased in the ZTG group, while significant ROS production was observed in both DXI and Control groups. We further examined the activation or deactivation of ROS-related signaling pathways in each culture system. Inhibition of the p38 MAPK[38] and mTOR[39,40] pathways, along with activation of the Wnt/β-Catenin[41] pathway, have been demonstrated to significantly enhance HSPC self-renewal. In our analysis of these culture platforms, we first noticed increased ROS levels to clearly correlate with increased p38 activation (Fig. 4d) in the DXI and Control cultures, likely leading to defective self-renewal. In addition, DXI and Control cultures exhibited β-Catenin and mTOR signaling behavior opposite to that expected for healthy self-renewal, with β-Catenin exhibiting reduced expression and mTOR showing significant activation in these cultures (Fig. 4e-f). On the other hand, we found the inhibited production of excessive ROS in the 3D ZTG culture to correlate with the desired pathway responses, enhancing self-renewal and avoiding defective self-renewal behavior.

We further analyzed mitochondrial mass and membrane potential, as well as metabolic activity markers, in the 14-day ZTG (ZTG_{14}), 24-day ZTG (ZTG_{opt}), and other expanded populations. As presented in Fig. 5a and b, mitochondrial mass and mitochondrial membrane potential marginally decreased in ZTG_{14} and ZTG_{opt} cells—these results sharply contrast the significant increases in both mass and membrane potential observed in the DXI_{opt} and Control groups, which was again correlated with excessive ROS production in these platforms. Moreover, since metabolic activity is another key regulator of stem cell self-renewal[42,43], we measured glucose consumption, lactate secretion, and amino acid metabolism in all expansion cultures. After 14 days, cells in the Control and DXI_{opt} systems exhibited significantly higher glucose consumption and lactate secretion than ZTG cells, which correlated to the increased energy required for differentiation and the specialized functions of differentiated progeny (Fig. 5b, c)[44,45]. In comparison, no significant changes in these metabolic activities were found in ZTG_{14} and ZTG_{opt} populations. Then, using a triple quadrupole (QqQ) LC/MS, we tested HSPCs expanded with each platform for levels of the twenty canonical amino acids necessary for polypeptide biosynthesis. The signal from each amino acid was first normalized to the total DNA content and then to the corresponding signal from fresh HSPCs. We found moderately upregulated biosynthesis in DXI_{opt} and control cultures, but sharply downregulated biosynthesis in ZTG-cultured HSPCs (Fig. 5c). Again, no significant difference was found between ZTG_{14} and ZTG_{opt} cells, suggesting that HSPCs in zwitterionic hydrogels interpret the nonfouling background as a signal to slow their metabolic rate. We believe this reduced activity is critical to keeping the stem cells in a naïve state for an extended time.Finally, for more advanced insight on the activity of CD34$^+$ stem cells in a purely zwitterionic background, we conducted expression profiling employing mRNA deep-sequencing (RNA-seq). As presented in Supplementary Fig. S14, while 778 genes were found to be significantly up-regulated and 926 genes were found to be significantly down-regulated, expression of more than 10,000 genes showed no significant change in ZTG populations compared to fresh HSPCs. Gene ontology (GO) enrichment analysis of the biological process terms (GO:BP) for the up- and down-regulated gene sets was done (Fig. 6a-b). After compressing GO terms (see Methods), we found 875 general GO:BP terms to be statistically enriched in the down-regulated gene set, including those for cell differentiation, cell activation, cytokine production et al., again indicating slowed metabolic processes. Strikingly, we found only four terms, all associated with cell adhesion, statistically enriched in the up-regulated gene set, suggesting the encapsulated cells were trying to adapt to their new niche. A complete list of up-/down-regulated GO terms can be found in the Supplementary Information. Similar to the GO enrichment analysis, a complete canonical pathway analysis predicted activation of four pathways in ZTG expanded cells, including self-renewal-related pathways such as Wnt/ β-Catenin and PPAR signaling[43]. Furthermore, inhibition was predicted for twenty-four pathways in this platform, again including several tied to self-renewal—p38 MAPK signaling[33], ROS production[30], Gα12/13 signaling[46] and others. Inhibition of AMP-mediated signaling and IL-6 signaling are correlated with the reduced metabolism in growing cells from ZTG culture[47,48]. A complete canonical pathways analysis can be found in Supplementary Fig. S15.

6.4 Conclusions

Our findings establish that HSPC culture in zwitterionic hydrogels promotes significant and clinically meaningful expansion of CB and BM-derived HSPCs with long-term repopulating ability while blocking their differentiation *ex vivo*. This methodology therefore has clinical implications beyond increasing the absolute number of CD34$^+$ cells for use in CBT; it may also be useful in gene therapy settings in which genetically modified/corrected HSPCs can be expanded prior to infusion. This work complements previous efforts to improve HSPC expansion *in vitro*, including through fed-batch culture[11], aryl hydrocarbon antagonists[14], the

UM family of molecules[15], Notch ligand signaling[12], copper chelators[49] or the expression of HOX genes[50]. Next, it will be important to explore the clinical potential of this strategy either by itself or in synergy with these other approaches.

Reference

1 Center for International Blood and Marrow Transplant Research, Transplant Activity Report Covering 2009-2013.

2 Gragert, L. *et al.* HLA match likelihoods for hematopoietic stem-cell grafts in the US registry. *New England Journal of Medicine* **371**, 339-348 (2014).

3 Milano, F. *et al.* Cord-Blood Transplantation in Patients with Minimal Residual Disease. *New England Journal of Medicine* **375**, 944-953, doi:doi:10.1056/NEJMoa1602074 (2016).

4 Wagner, J. E. *et al.* Transplantation of unrelated donor umbilical cord blood in 102 patients with malignant and nonmalignant diseases: influence of CD34 cell dose and HLA disparity on treatment-related mortality and survival. *Blood* **100**, 1611-1618 (2002).

5 Ballen, K. K., Gluckman, E. & Broxmeyer, H. E. Umbilical cord blood transplantation: the first 25 years and beyond. *Blood* **122**, 491-498 (2013).

6 Smith, A. R. & Wagner, J. E. Alternative haematopoietic stem cell sources for transplantation: place of umbilical cord blood. *British journal of haematology* **147**, 246-261 (2009).

7 Dahlberg, A., Delaney, C. & Bernstein, I. D. *Ex vivo* expansion of human hematopoietic stem and progenitor cells. *Blood* **117**, 6083-6090 (2011).

8 Murray, L. J. *et al.* Thrombopoietin, flt3, and kit ligands together suppress apoptosis of human mobilized CD34+ cells and recruit primitive CD34+ Thy-1+ cells into rapid division. *Experimental hematology* **27**, 1019-1028 (1999).

9 Ratajczak, M. Z. Phenotypic and functional characterization of hematopoietic stem cells. *Current opinion in hematology* **15**, 293-300 (2008).

10 Pineault, N. & Abu-Khader, A. Advances in umbilical cord blood stem cell expansion and clinical translation. *Experimental hematology* **43**, 498-513 (2015).

11 Csaszar, E. *et al.* Rapid expansion of human hematopoietic stem cells by automated control of inhibitory feedback signaling. *Cell stem cell* **10**, 218-229 (2012).

12 Delaney, C. *et al.* Notch-mediated expansion of human cord blood progenitor cells capable of rapid myeloid reconstitution. *Nature medicine* **16**, 232-236 (2010).

13 Delaney, C. *et al.* Infusion of a non-HLA-matched ex-vivo expanded cord blood progenitor cell product after intensive acute myeloid leukaemia chemotherapy: a phase 1 trial. *The Lancet Haematology* (2016).

14 Boitano, A. E. *et al.* Aryl hydrocarbon receptor antagonists promote the expansion of human hematopoietic stem cells. *Science* **329**, 1345-1348 (2010).

15 Fares, I. *et al.* Pyrimidoindole derivatives are agonists of human hematopoietic stem cell self-renewal. *Science* **345**, 1509-1512 (2014).

16 Bretscher, M. S. Mammalian plasma membranes. *Nature* **258**, 43-49 (1975).

17 Steele, J. G., Dalton, B. A., Johnson, G. & Underwood, P. A. Adsorption of fibronectin and vitronectin onto Primaria™ and tissue culture polystyrene and relationship to the mechanism of initial attachment of human vein endothelial cells and BHK-21 fibroblasts. *Biomaterials* **16**, 1057-1067 (1995).

18 Jiang, S. & Cao, Z. Ultralow‐fouling, functionalizable, and hydrolyzable zwitterionic materials and their derivatives for biological applications. *Advanced Materials* **22**, 920-932 (2010).

19 Keefe, A. J. & Jiang, S. Poly (zwitterionic) protein conjugates offer increased stability without sacrificing binding affinity or bioactivity. *Nature chemistry* **4**, 59-63 (2012).

20 Zhang, L. *et al.* Zwitterionic hydrogels implanted in mice resist the foreign-body reaction. *Nature biotechnology* **31**, 553-556 (2013).

21 Zhang, P. *et al.* Zwitterionic gel encapsulation promotes protein stability, enhances pharmacokinetics, and reduces immunogenicity. *Proceedings of the National Academy of Sciences* **112**, 12046-12051 (2015).

22 DeForest, C. A., Polizzotti, B. D. & Anseth, K. S. Sequential click reactions for synthesizing and patterning three-dimensional cell microenvironments. *Nature materials* **8**, 659-664 (2009).

23 Anderson, S. B., Lin, C.-C., Kuntzler, D. V. & Anseth, K. S. The performance of human mesenchymal stem cells encapsulated in cell-degradable polymer-peptide hydrogels. *Biomaterials* **32**, 3564-3574 (2011).

24 West, J. L. & Hubbell, J. A. Polymeric biomaterials with degradation sites for proteases involved in cell migration. *Macromolecules* **32**, 241-244 (1999).

25 DeForest, C. A. & Anseth, K. S. Cytocompatible click-based hydrogels with dynamically tunable properties through orthogonal photoconjugation and photocleavage reactions. *Nature chemistry* **3**, 925-931 (2011).

26 Ito, M. *et al.* NOD/SCID/gamma(c)(null) mouse: an excellent recipient mouse model for engraftment of human cells. *Blood* **100**, 3175-3182, doi:10.1182/blood-2001-12-0207 (2002).

27 Nel, A., Xia, T., Mädler, L. & Li, N. Toxic potential of materials at the nanolevel. *science* **311**, 622-627 (2006).

28 Kaplan, S., Basford, R., Mora, E., Jeong, M. & Simmons, R. Biomaterial‐induced alterations of neutrophil superoxide production. *Journal of biomedical materials research* **26**, 1039-1051 (1992).

29 Bigarella, C. L., Liang, R. & Ghaffari, S. Stem cells and the impact of ROS signaling. *Development* **141**, 4206-4218 (2014).

30 Ray, P. D., Huang, B.-W. & Tsuji, Y. Reactive oxygen species (ROS) homeostasis and redox regulation in cellular signaling. *Cellular signalling* **24**, 981-990 (2012).

31 Shin, S. Y. *et al.* Hydrogen peroxide negatively modulates Wnt signaling through downregulation of β-catenin. *Cancer letters* **212**, 225-231 (2004).

32 Reya, T. *et al.* A role for Wnt signalling in self-renewal of haematopoietic stem cells. *Nature* **423**, 409-414 (2003).

33 Ito, K. *et al.* Reactive oxygen species act through p38 MAPK to limit the lifespan of hematopoietic stem cells. *Nature medicine* **12**, 446-451 (2006).

34 Yoshida, S. *et al.* Redox regulates mammalian target of rapamycin complex 1 (mTORC1) activity by modulating the TSC1/TSC2-Rheb GTPase pathway. *Journal of Biological Chemistry* **286**, 32651-32660 (2011).

35 Ito, K. *et al.* Regulation of oxidative stress by ATM is required for self-renewal of haematopoietic stem cells. *Nature* **431**, 997-1002 (2004).

36 Jang, Y.-Y. & Sharkis, S. J. A low level of reactive oxygen species selects for primitive hematopoietic stem cells that may reside in the low-oxygenic niche. *Blood* **110**, 3056-3063 (2007).

37 Liu, W. F. *et al.* Real-time *in vivo* detection of biomaterial-induced reactive oxygen species. *Biomaterials* **32**, 1796-1801 (2011).

38 Wang, Y., Kellner, J., Liu, L. & Zhou, D. Inhibition of p38 mitogen-activated protein kinase promotes *ex vivo* hematopoietic stem cell expansion. *Stem cells and development* **20**, 1143-1152 (2011).

39 Huang, J., Nguyen-McCarty, M., Hexner, E. O., Danet-Desnoyers, G. & Klein, P. S. Maintenance of hematopoietic stem cells through regulation of Wnt and mTOR pathways. *Nature medicine* **18**, 1778-1785 (2012).

40 Luo, Y. *et al.* Rapamycin enhances long-term hematopoietic reconstitution of *ex vivo* expanded mouse hematopoietic stem cells by inhibiting senescence. *Transplantation* **97** (2014).

41 Fleming, H. E. *et al.* Wnt signaling in the niche enforces hematopoietic stem cell quiescence and is necessary to preserve self-renewal *in vivo*. *Cell stem cell* **2**, 274-283 (2008).

42 McGraw, T. E. & Mittal, V. Stem cells: Metabolism regulates differentiation. *Nature chemical biology* **6**, 176-177 (2010).

43 Ito, K. & Suda, T. Metabolic requirements for the maintenance of self-renewing stem cells. *Nature reviews Molecular cell biology* **15**, 243-256 (2014).

44 Folmes, C. D., Dzeja, P. P., Nelson, T. J. & Terzic, A. Metabolic plasticity in stem cell homeostasis and differentiation. *Cell stem cell* **11**, 596-606 (2012).

45 Enver, T., Pera, M., Peterson, C. & Andrews, P. W. Stem cell states, fates, and the rules of attraction. *Cell stem cell* **4**, 387-397 (2009).

46 Nishida, M. *et al.* Gα12/13-and reactive oxygen species-dependent activation of c-Jun NH2-terminal kinase and p38 mitogen-activated protein kinase by angiotensin receptor stimulation in rat neonatal cardiomyocytes. *Journal of Biological Chemistry* **280**, 18434-18441 (2005).

47 Long, Y. C. & Zierath, J. R. AMP-activated protein kinase signaling in metabolic regulation. *The Journal of clinical investigation* **116**, 1776-1783 (2006).

48 Carey, A. L. *et al.* Interleukin-6 increases insulin-stimulated glucose disposal in humans and glucose uptake and fatty acid oxidation *in vitro* via AMP-activated protein kinase. *Diabetes* **55**, 2688-2697 (2006).

49 De Lima, M. *et al.* Transplantation of *ex vivo* expanded cord blood cells using the copper chelator tetraethylenepentamine: a phase I/II clinical trial. *Bone marrow transplantation* **41**, 771-778 (2008).

50 Antonchuk, J., Sauvageau, G. & Humphries, R. K. HOXB4-induced expansion of adult hematopoietic stem cells *ex vivo*. *Cell* **109**, 39-45 (2002).

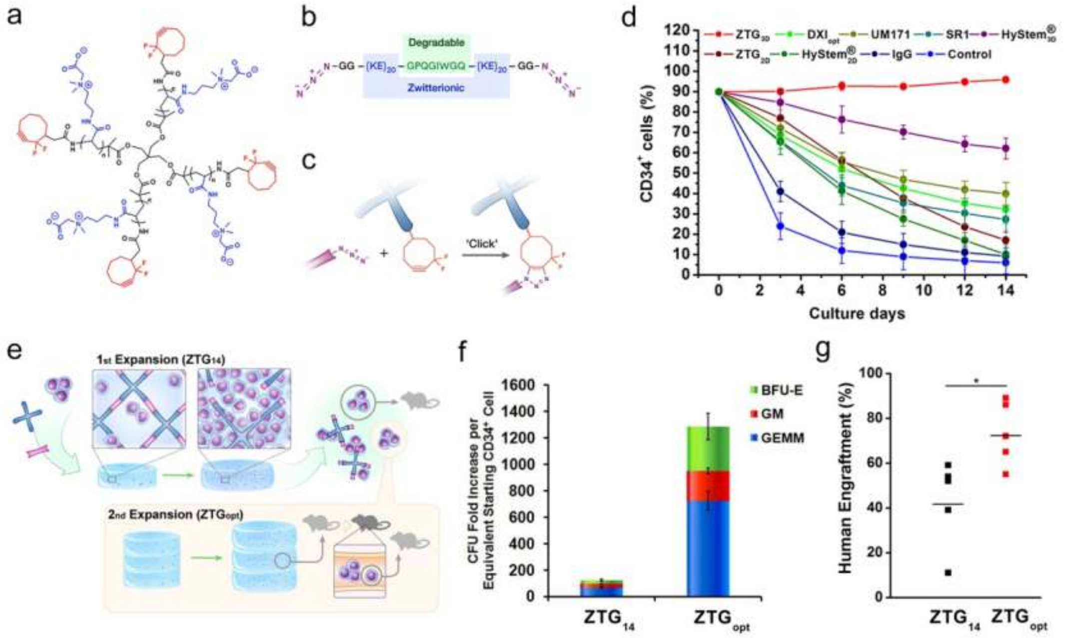

Figure 6.1. Construction of biodegradable zwitterionic hydrogel allows the expansion of CD34$^+$ CB stem cells. (a-c) Chemical structures of the hydrogel components; a Huisgen cycloaddition was used to form a 3D ideal network hydrogel through a step-growth polymerization mechanism. (**d**) Dynamic changes in CD34 expression by using various culture systems. (**e**) Schematic illustration of the ZTG$_{opt}$ culture procedure and experimental outline: freshly isolated HSPCs were mixed with the click-reactive zwitterionic components to form cell-hydrogel constructs, which were cultured in expansion media for 14 days (ZTG$_{14}$). A second expansion was performed by dividing the ZTG$_{14}$ population among new zwitterionic gels at an optimal seeding concentration and culturing them for another 10 days before final harvest for further experimentation. The resulting ZTG$_{opt}$ cells will be injected into NSG mice for primary and secondary transplantation. (**f**) Fold increase in CFUs after the first and second expansions in zwitterionic hydrogels. **(g)** Mice were injected with 200,000 cells harvested at the end of Day-14 or Day-24, which corresponded to the progeny of 10,000 and 667 day 0 CD34$^+$ cells, respectively. The level of human engraftment (% hCD45) in mouse bone marrow 20 weeks after transplantation. Horizontal lines indicate the average value for each group. * indicates a significant difference (P<0.05)

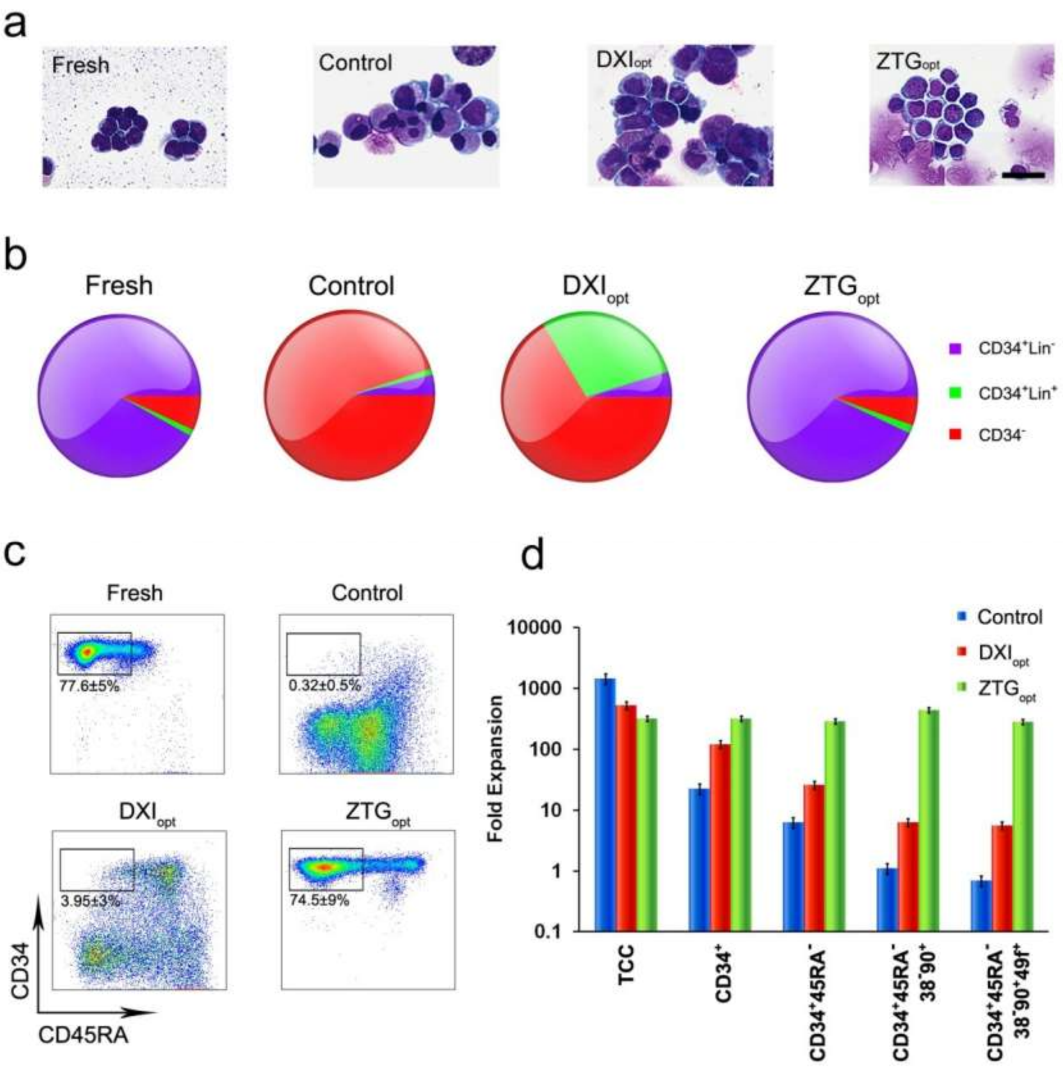

Figure 6.2. Zwitterionic hydrogel inhibits the differentiation of CD34$^+$ CB cells during *ex vivo* expansion. (a) Photomicrograph of Wright-Giemsa-stained fresh HSPCs and cells after culture in different conditions. Scale bar: 30um. (**b)** The distribution of fresh, control-, DXI$_{opt}$-, and ZTG$_{opt}$-cultured cells according to CD34 and lineage (CD7, CD14, CD15, CD19 and CD56) marker expression determined by flow cytometry**. (c)** Representative FACS profiles of CD34$^+$CD45RA$^-$ populations in fresh, control-, DXI$_{opt}$-, and ZTG$_{opt}$-cultured cells. (**d)** Fold expansion of defined hematopoietic cell subsets after culture in each condition. Values represent means ±SD.

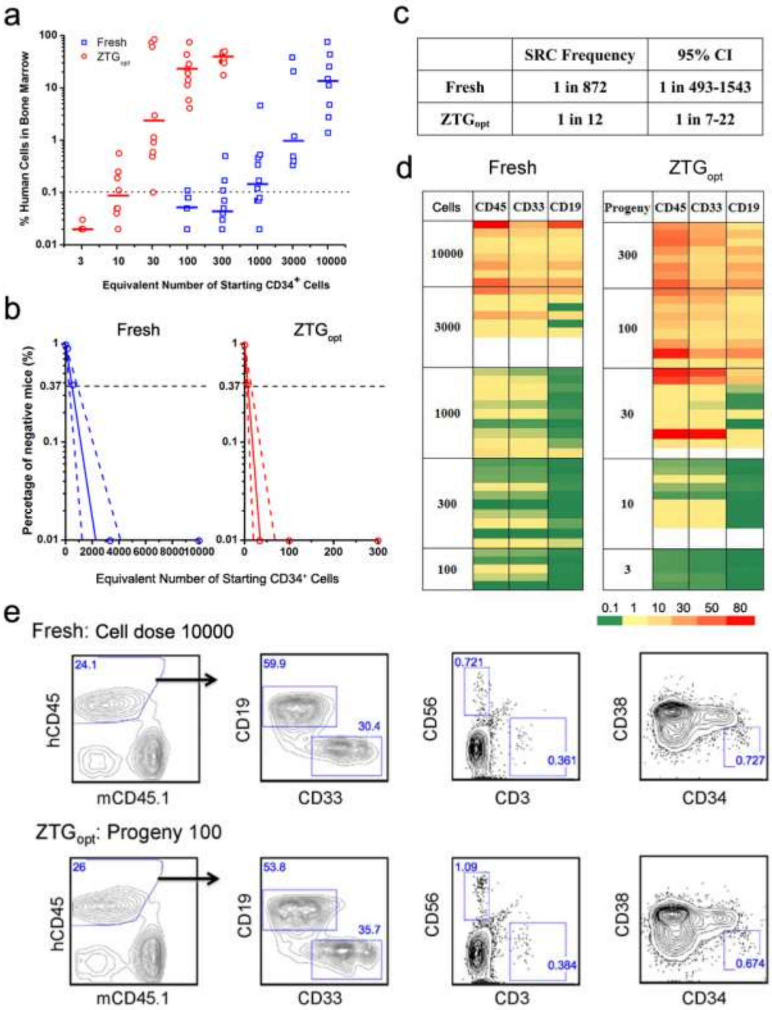

	SRC Frequency	95% CI
Fresh	1 in 872	1 in 493-1543
ZTG_{opt}	1 in 12	1 in 7-22

Figure 6.3. Culture of $CD34^+$ CB cells in the ZTG_{opt} condition promotes expansion of LT-HSCs. (a) Mice were injected with either fresh cord blood $CD34^+$ HSPCs or ZTG_{opt}-expanded progeny at doses normalized to their founding HSPC population. The percentage of human $CD45^+$ cells in the mouse bone marrow at week 24-30 is shown. Horizontal lines indicate the average value for each group. **(b)** Linear regression analysis of data from Fig. 3a. Solid lines indicate the best-fit linear regression model for each data set. Dotted lines represent 95% confidence interval. Fresh group is shown in blue and ZTG_{opt} group is shown in red. (**c**) LT-HSC numbers before and after culture in the ZTG_{opt} condition. (**d)** Levels of human engraftment in NSG mice transplanted with different cell doses. (**e)** ZTG_{opt} culture does not affect the lineage repopulating ability. Representative flow cytometry dot plots from BM samples flushed from transplanted mice at week 24. Pooled BM samples were analyzed (top: Pooled BM from 4 mice receiving 10,000 fresh HSPCs; bottom: Pooled BM from 5 mice receiving ZTG_{opt} cells expanded from 100 fresh HSPCs). Progeny: $CD34^+$ starting cells (day 0 equivalent).

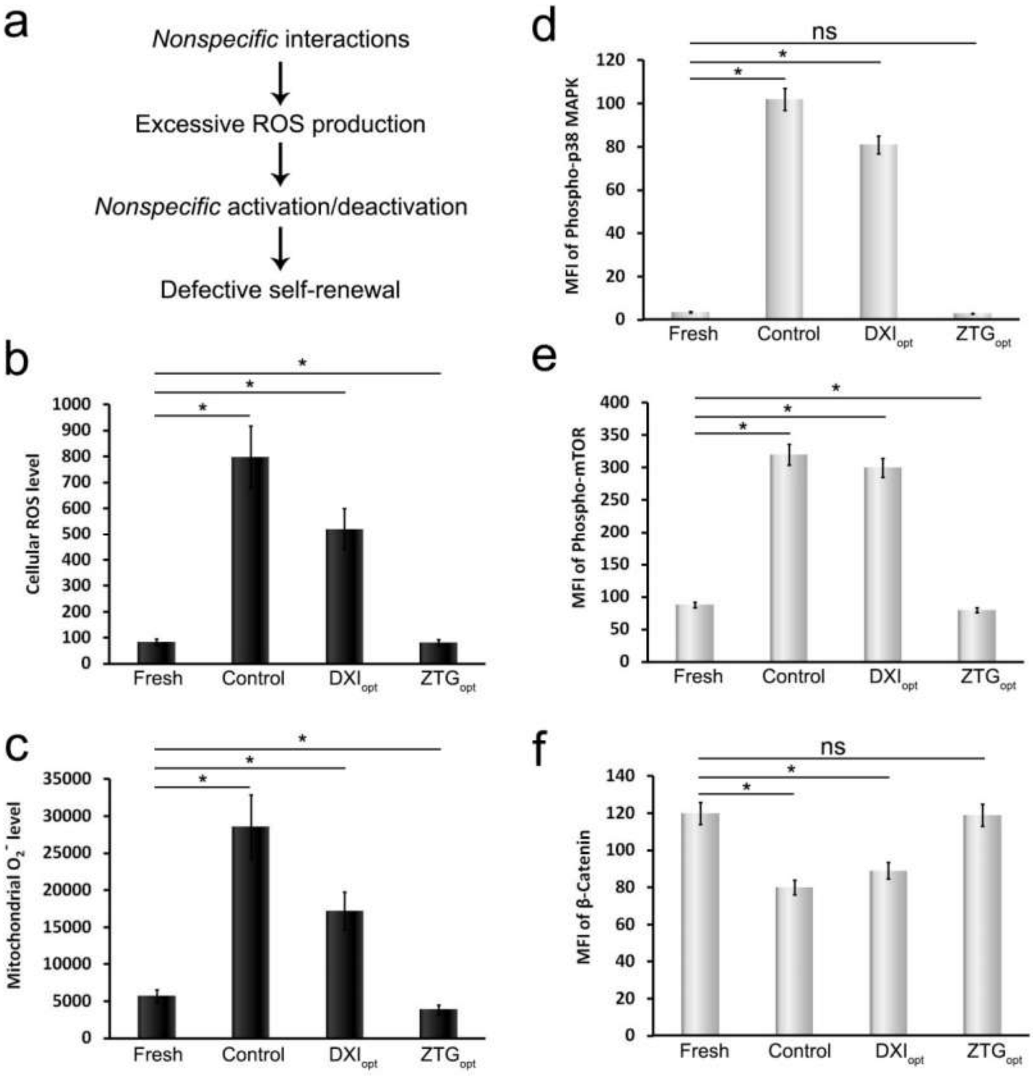

Figure 6.4. 3D zwitterionic culture avoids excessive ROS production and nonspecific pathway activation/deactivation. (a) Hydrophobicity-induced nonspecific cell-matrix/substrate interaction leads to excessive ROS production. These generated ROS can nonspecifically activate and deactivate intracellular pathways and result in defective self-renewal of HSPC. **(b-c)** Intracellular ROS was measured with DCFH2-DA and Mitochondrial superoxide was measured with MitoSOX™ Red after 1-day culture. **(d-f)** Mean fluorescent intensity of phospho-p38 (**d**), phospho-mTOR (**e**) and β-Catenin (**f**) were examined after 1-day culture. ns indicates no significant difference. * indicates a significant difference ($P<0.05$). Values represent means ±SD.

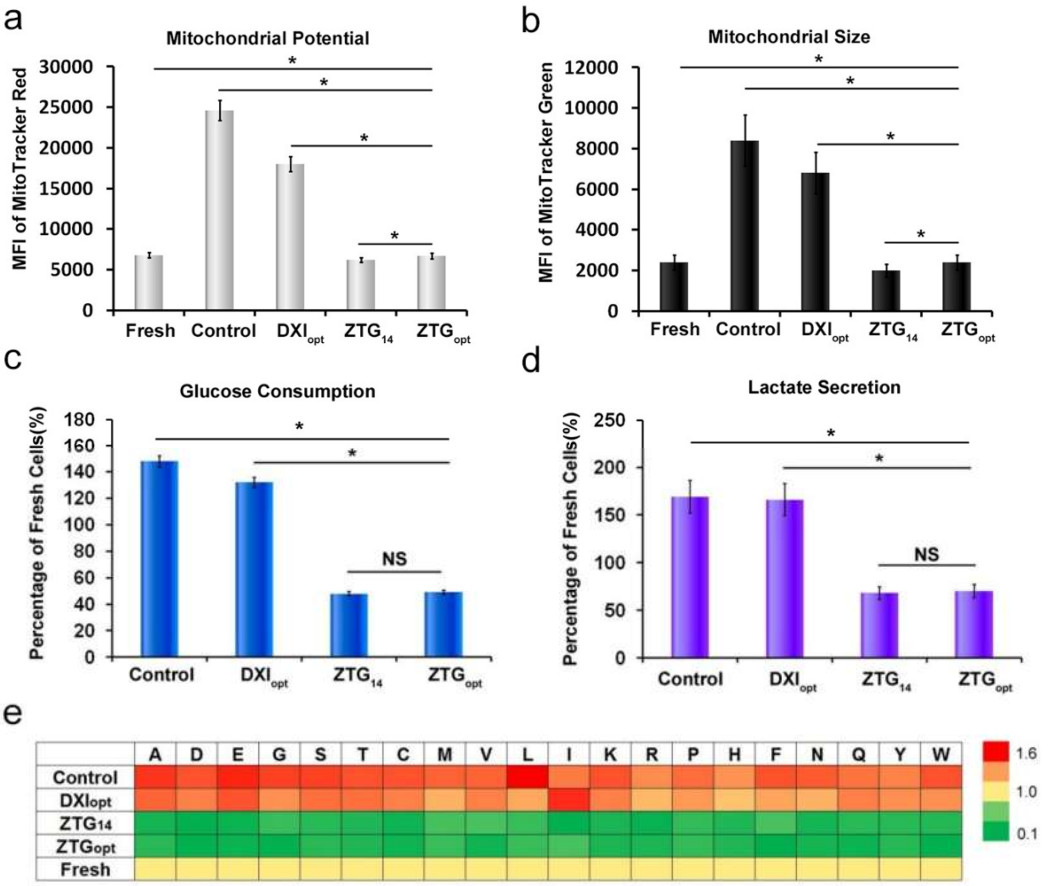

Figure 6.5. ZTG$_{opt}$ culture induces CD34^{+} CB cells to reduce their metabolisms. (a-b) Difference of mitochondrial potential and size of CB cells after *ex vivo* culture in each condition was presented by the mean fluorescent intensity of MitoTracker red and MitoTracker green. **(c-d)** Percentage change of glucose consumption and lactate secretion by CB cells after *ex vivo* culture in each condition. **(e)** Amino acid metabolism of CB cells before and after culture in control, ZTG$_{opt}$ and DXI$_{opt}$ conditions. NS indicates no significant difference. * indicates a significant difference ($P<0.05$). Values represent means ±SD.

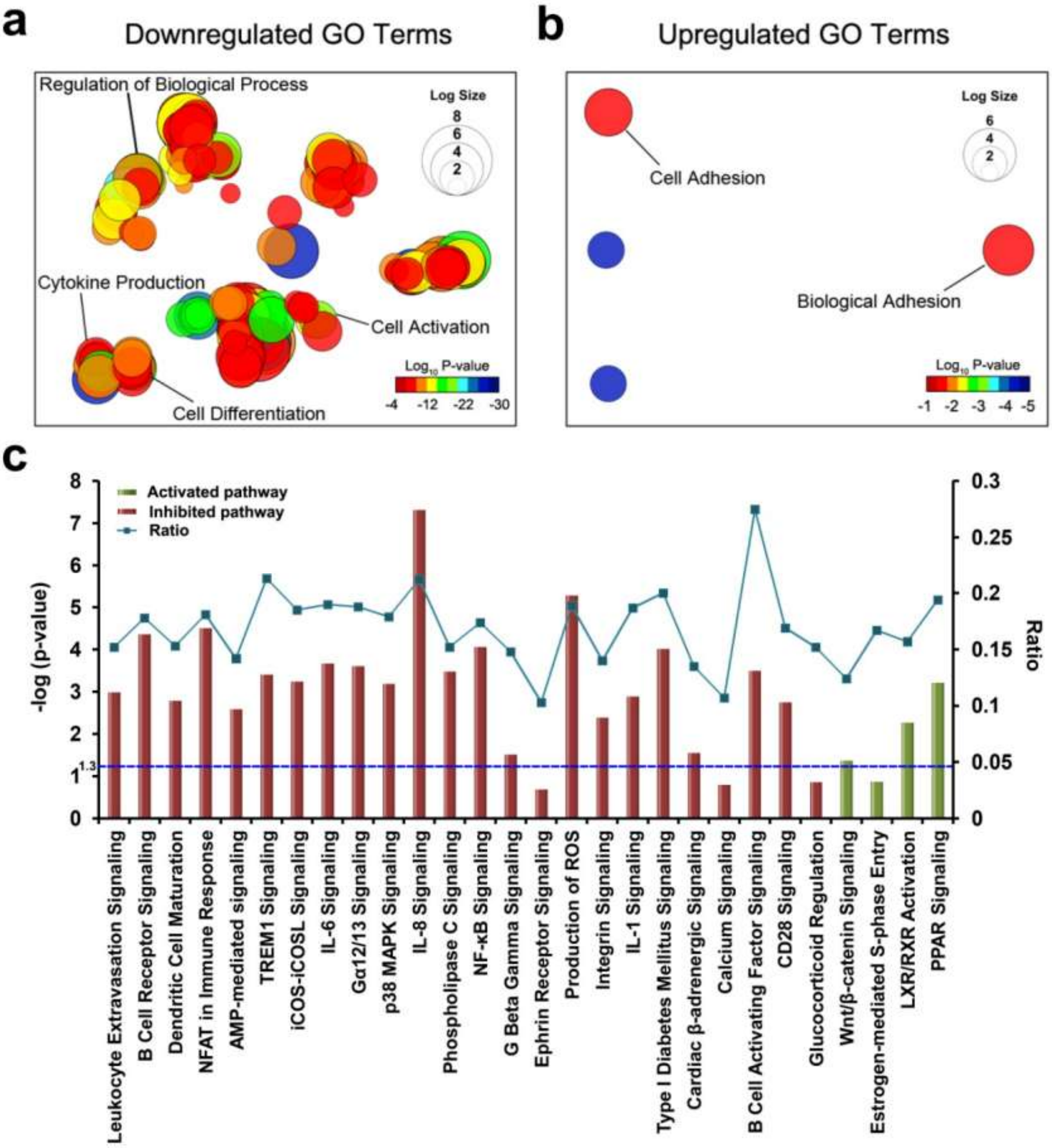

Figure 6.6. RNA expression indicates HSPCs cultured in ZTG$_{opt}$ condition are not activated for differentiation. (a-b) Gene ontology enrichment analysis of differentially expressed genes show statistically enriched GO categories for down-regulated **(a)** and up-regulated genes **(b)**. **(c)** activated and inhibited pathways in cells from ZTG$_{opt}$ culture were predicted by Ingenuity pathway analysis (IPA). The first y-axis (left) shows the significance score (−log of P-value) calculated by the Benjamini-Hochberg (B-H) method; the B-H method was used to adjust the right-tailed Fisher's exact test P-value, which indicates the significance of each pathway. The blue dash line indicates −log of P-value 1.3 (P-value 0.05). The second y-axis (right) shows the ratio indicating the number of differentially expressed genes that map to the pathway divided by the total number of genes that map to the canonical pathway.

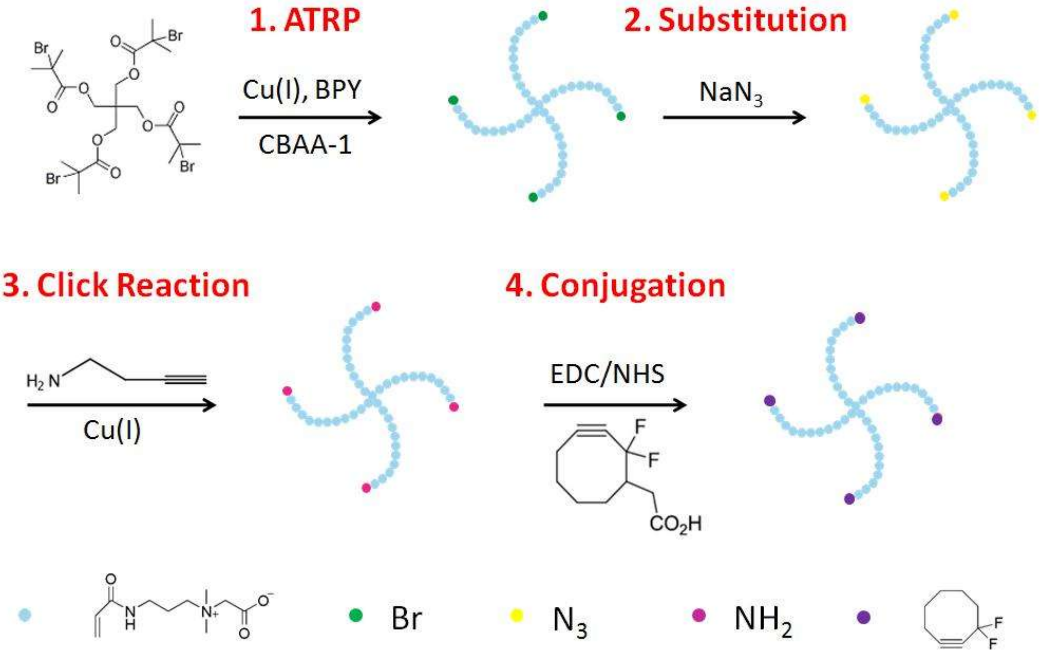

Figure 6.7. Synthesis of zwitterionic star-shaped polymer. N_3-terminated star-shaped pCBAA was produced by atom-transfer radical-polymerization and subsequent azide substitution. Then, The azide groups on pCBAA were converted into NH_2 groups using a 'click' reaction. Finally, $DIFO_3$ was functionalized to the end of pCBAA polymer via an EDC/NHS reaction.

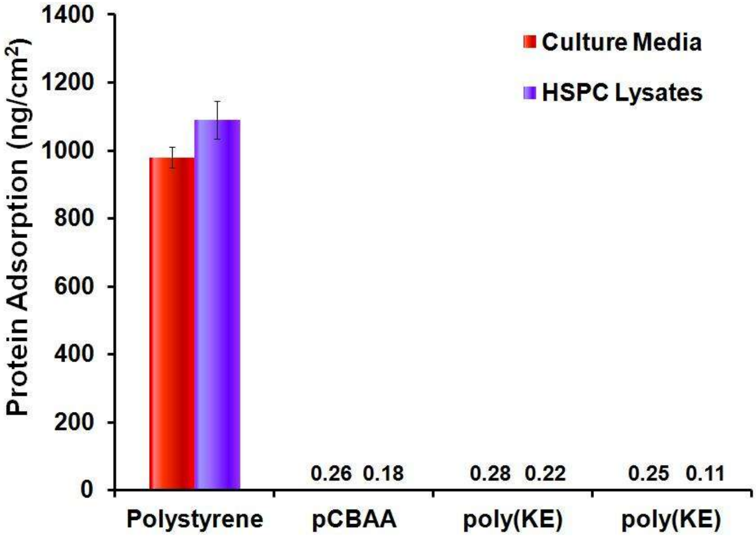

Figure 6.8. Zwitterionic polymer and peptide are ultra-low fouling in complex protein solutions. Total protein adsorption was measured on an SPR sensor after injection of cell culture medium and fresh HSPC lysates on polystyrene, pCBAA and poly(KE)$_1$: CGG(KE)$_{20}$GPQG and poly(KE)$_2$: CGG(KE)$_{20}$IWGQ films.

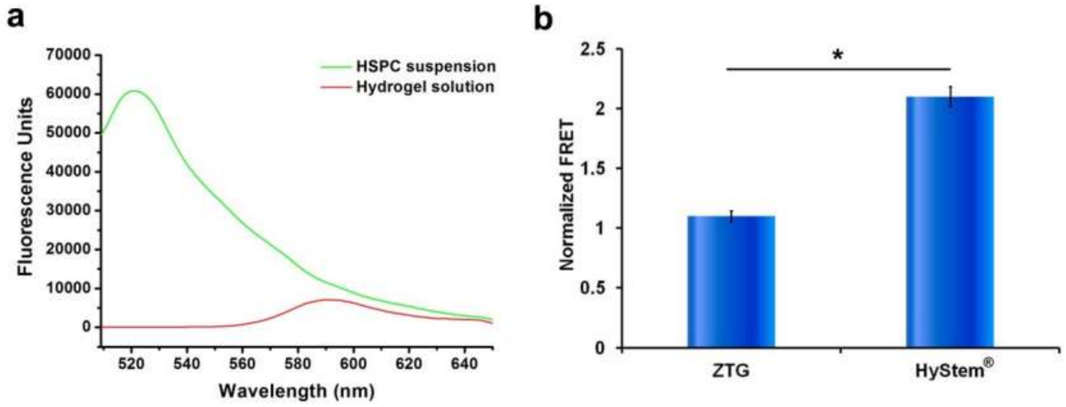

Figure 6.9. FRET measurement of nonspecific interactions between HSPC and hydrogel matrix. (a) When the TAMRA fluorophore is presented on the matrix, 480nm excitation yields weak 590nm (red) emission ('Hydrogel solution' sample). When the HSPCs membrane is labeled with 5-hexadecanoylaminofluorescein, 480nm excitation yields 525nm (green) emission ('HSPC suspension' sample), unless TAMRA labeled components are bound to HSPCs, in which case 525nm emission is diminished and 580 nm (red) emission is enhanced (FRET effect). **(b)** Normalized FRET of HSPCs-encapsulated ZTG and HyStem$^{®}$ hydrogels. Asterisks designate statistical significance as per students' t-test performed between indicated groups; N=4, $p<0.05$.

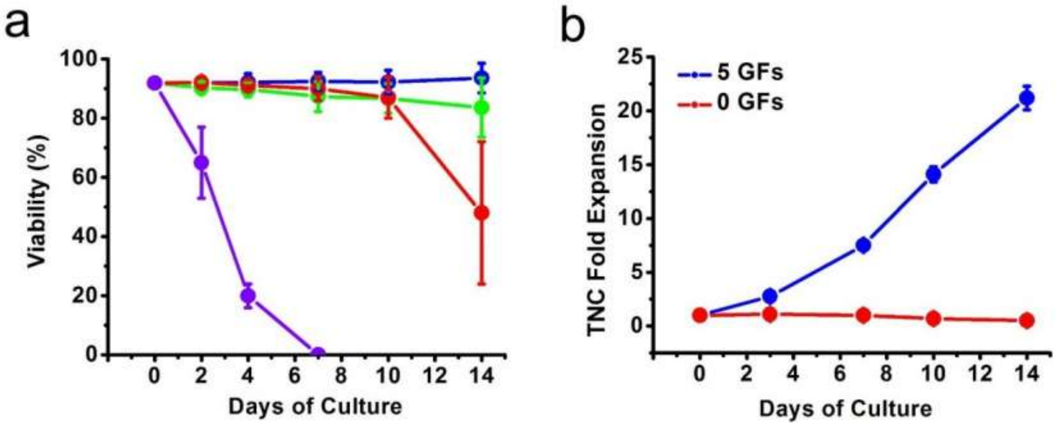

Figure 6.10. ZTG culture prolongs the viable time of HSPCs but cell division in ZTG requires growth factors (GFs). a, b) ZTG-encapsulated cord blood CD34$^+$ HSPCs were cultured in SFEM II medium with (blue) or without (red) 5 growth factors, while cells cultured in control conditions with (green) or without (purple) growth factors were set as controls. Mean ± SEM is shown; n=3 independent experiments.

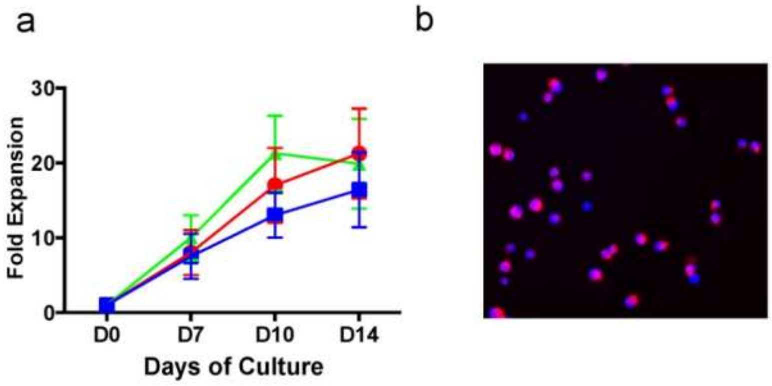

Figure 6.11. Examination of HSPC seeding density for ZTG culture. a) Kinetics of TNC expansion at different seeding densities in ZTG culture (Blue: 0.6x10^{6} cells/ml; Red: 1.2x10^{6} cells/ml; Green: 2.5x10^{6} cells/ml). 1.2x10^{6} cells/ml was selected as the optimal seeding density. Mean ± SEM is shown; n=3 independent experiments. **b)** Immunofluorescence for ZTG$_{14}$ cells with 1.2x10^{6} cells/ml seeding density after staining with DAPI (blue) and anti-CD34 antibody (pink).

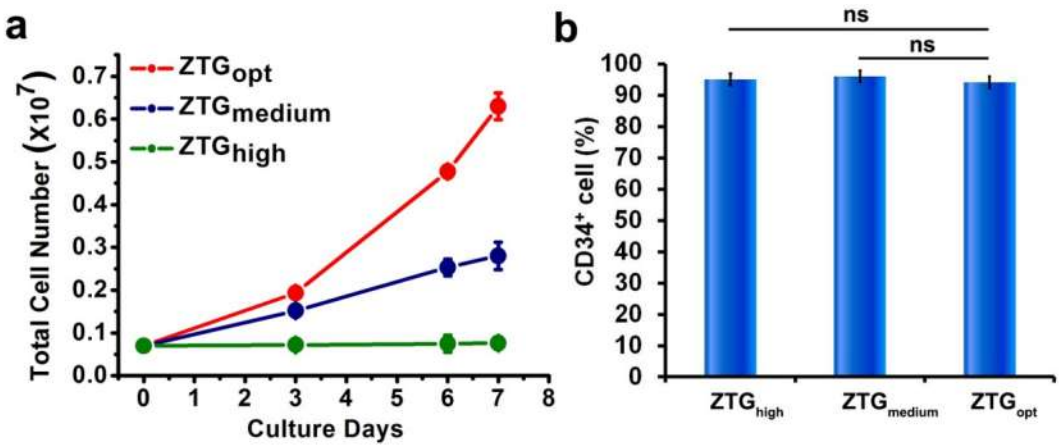

Figure 6.12. Effect of mechanical property on expanded cells from ZTG culture. a) Dynamic total cell number increase in zwitterionic hydrogels with different mechanical properties. **b)** Percentage of CD34$^+$ cells after each culture condition. ns indicates no significant difference.

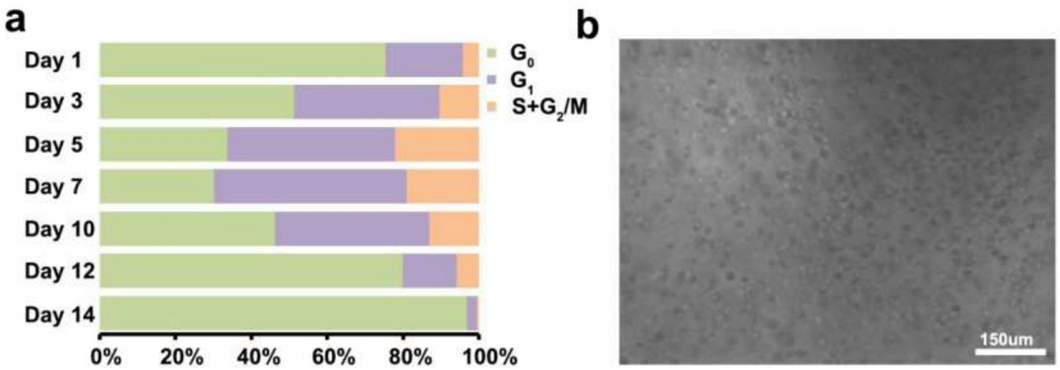

Figure 6.13. Dynamic cell cycle analysis. a) Dynamic cell cycle analysis by FACS using anti-Ki-67 and Hoechst 33342 staining for HSPCs in ZTG$_{opt}$ culture. **b)** Representative phase contrast image of ZTG$_{opt}$ cell at day 24 in culture.

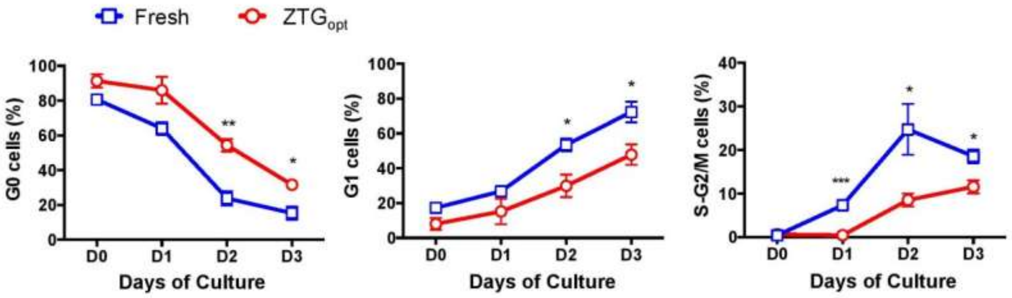

Figure 6.14. ZTG$_{opt}$ cells show delayed entry into cell cycles. Dynamic change of cell cycle subsets after transferring cells before (Fresh) and after ZTG$_{opt}$ culture into control conditions. Mean ± SEM is shown; n=3 independent experiments. *p<0.05, **p<0.001, ***p<0.0005 by 2-tail t-test.

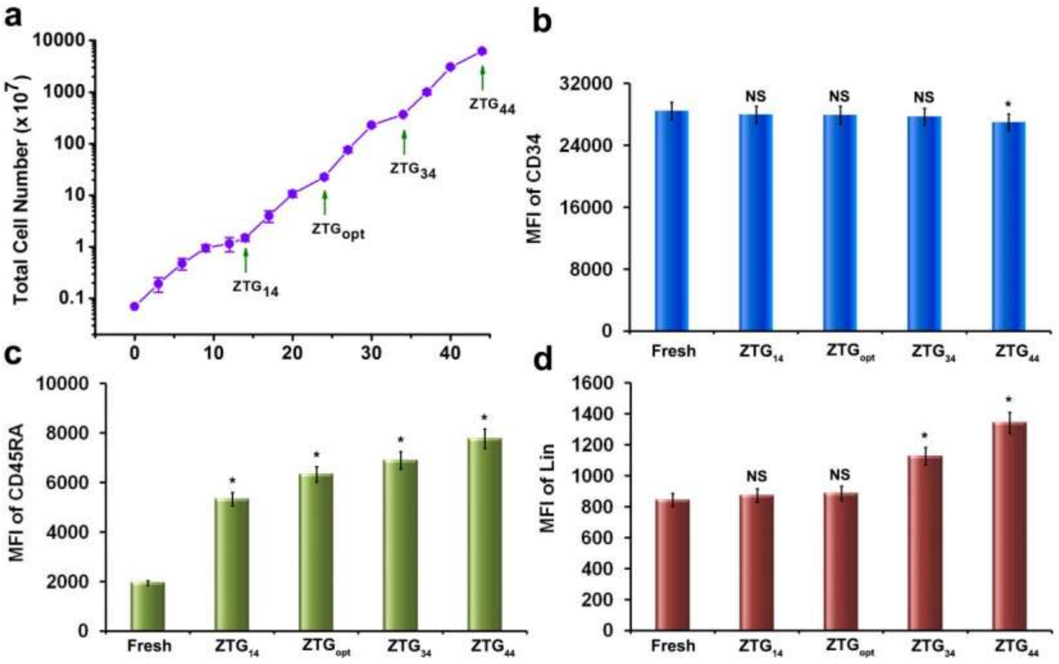

Figure 6.15. Effect of additional passages on expanded cells from ZTG culture. a) Dynamic total cell number increase in ZTG culture. (b-d) Mean fluorescent intensity of CD34 (b), CD45RA (c) and lineage marker cocktail (d) at different time point. NS indicates no significant difference. * indicates a significant difference ($P<0.05$). Values represent means ±SD.

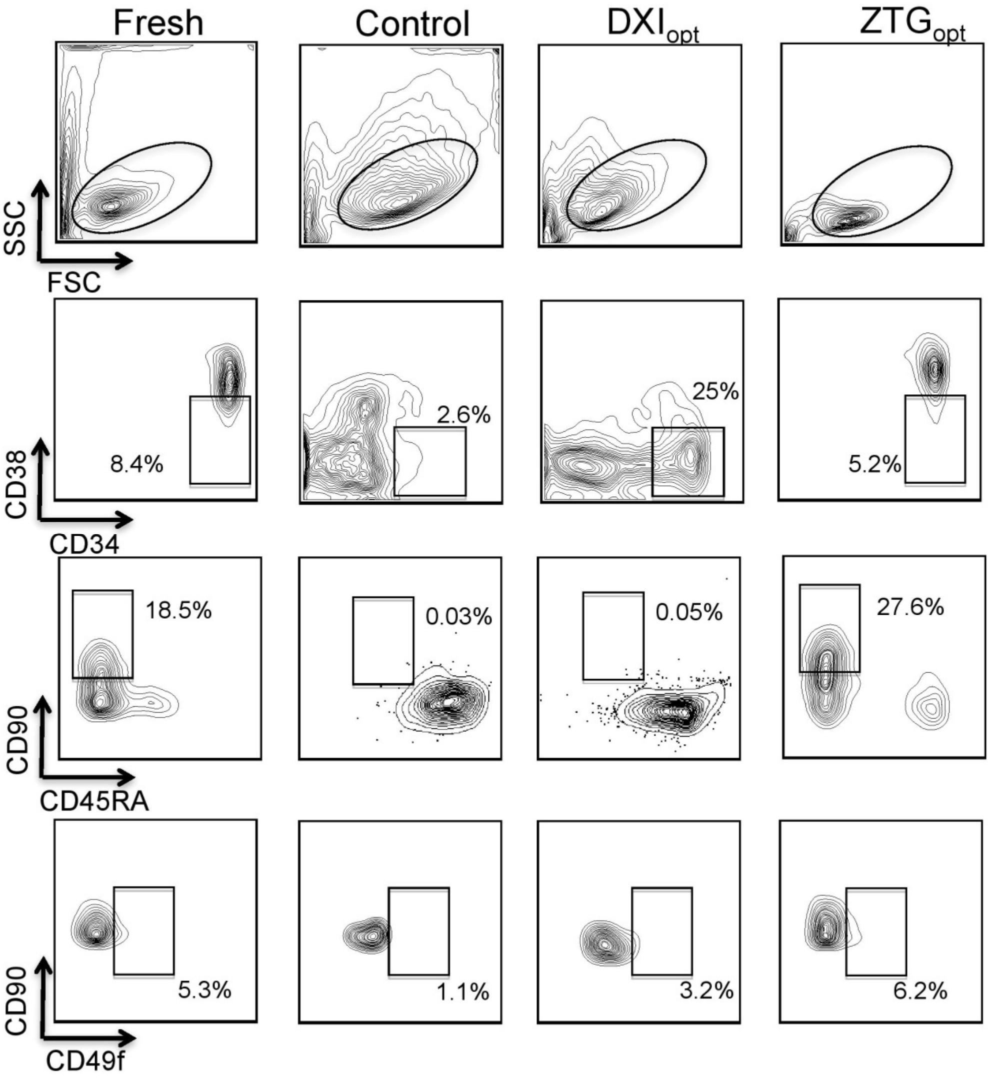

Figure 6.16. ZTG$_{opt}$-cultured HSPCs remain phenotypically primitive. Representative FACS profiles of the most primitive HSPC phenotype subset ($CD34^+CD38^-CD45RA^-CD90^+CD49f^+$) from fresh, control, DXI$_{opt}$ and ZTG$_{opt}$ conditions. Consecutive gating was applied from top to down.

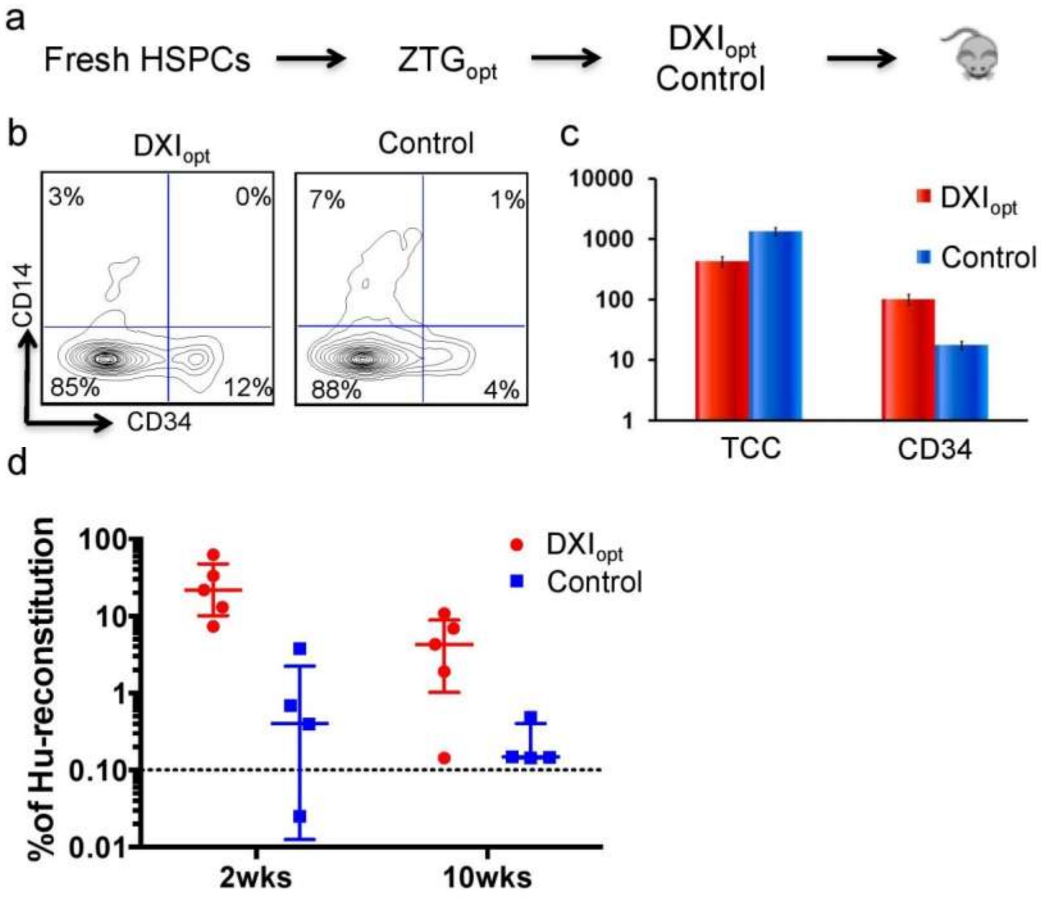

Figure 6.17. HSPCs retain their capacity for subsequent expansion after ZTG$_{opt}$ culture. a) Schematic representation of the experimental design. Cord blood CD34$^+$ HSPCs were expanded in the ZTG$_{opt}$ condition, after which cells were harvested and further expanded in DXI$_{opt}$ and control conditions. These secondary groups of expanded cells were harvested and injected into NSG mice, with progeny doses based on a founding CD34$^+$ population of 1000 for each group. **b)** Flow cytometry analysis of subsequently expanded HSPCs. **c)** Fold change of the subsequent expansion in DXI$_{opt}$ or control conditions. **d)** human engraftment in NSG BM after indicated time points.

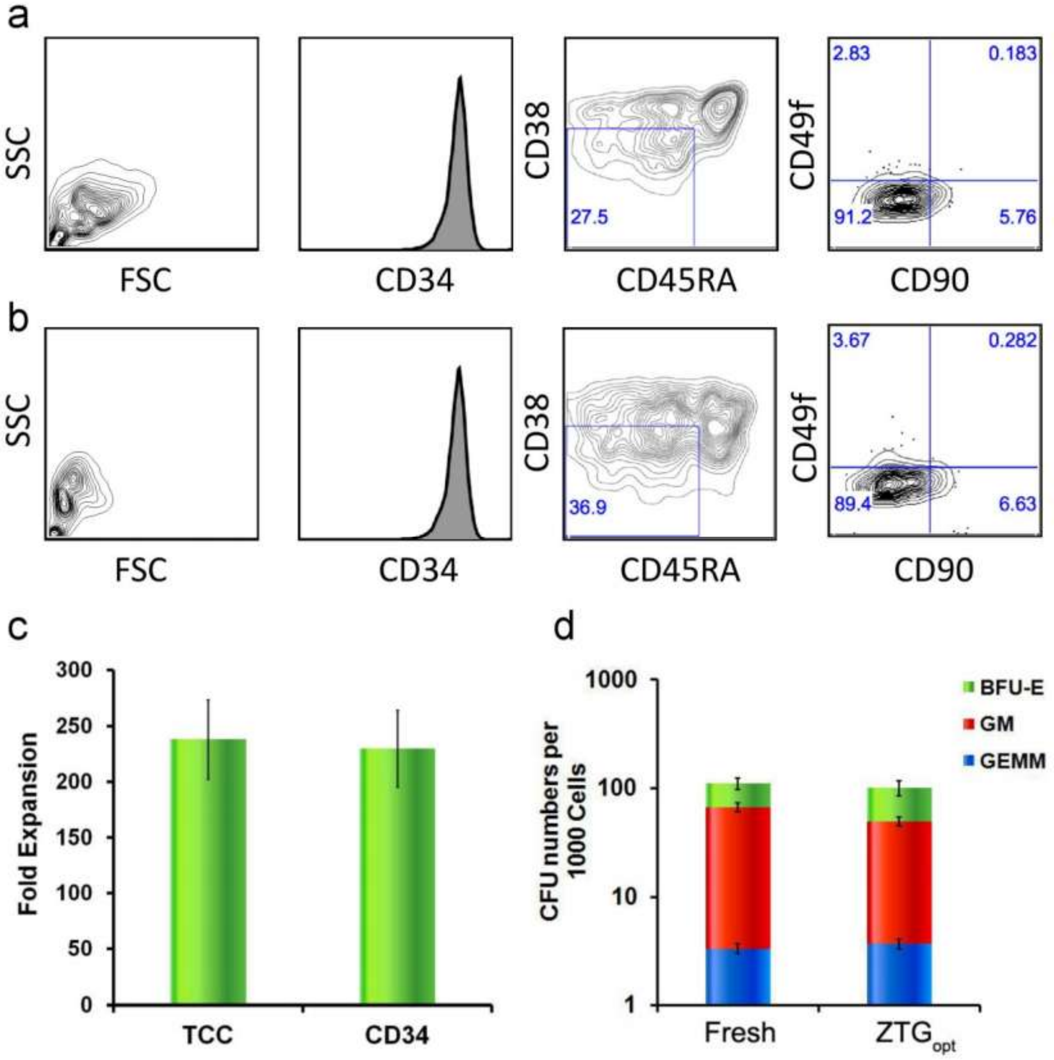

Figure 6.18. Zwitterionic hydrogel restrains the differentiation of bone marrow HSPCs during *ex vivo* expansion. a-b) Representative flow cytometry dot plot for fresh (**a**) and ZTG$_{opt}$ (**b**) cells. FSC: forward scatter; SSC: side scatter. **c)** Fold expansion of total and CD34$^+$ cells after ZTG$_{opt}$ culture. **d)** CFU numbers per 1000 Fresh or ZTG$_{opt}$ cells.

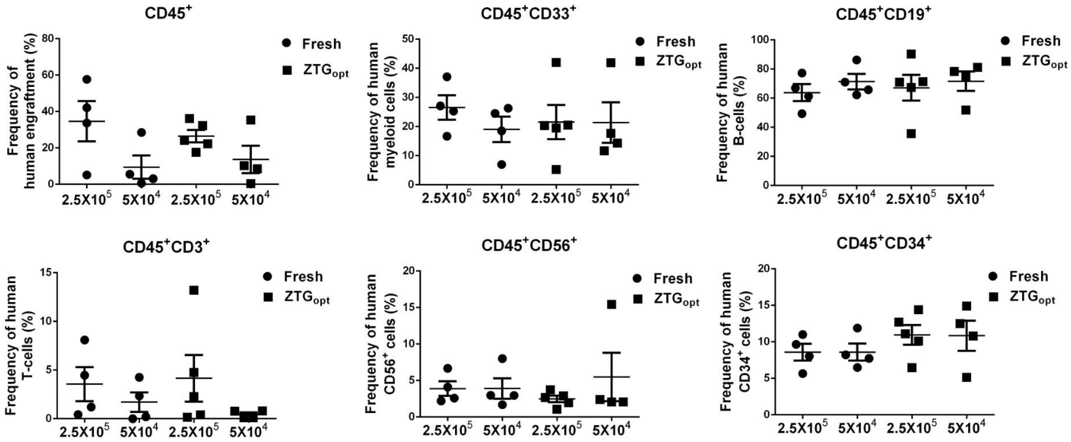

Figure 6.19. ***In vivo*** **function of expanded BM-CD34$^+$ HSPCs from ZTG$_{opt}$ culture.** Levels of human engraftment and lineage repopulating in NSG mice transplanted with different cell doses at week 24.

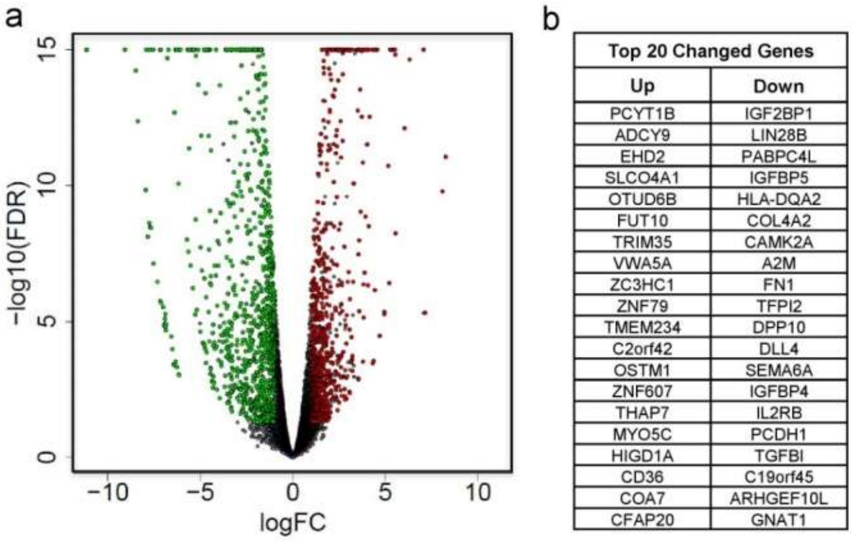

Top 20 Changed Genes	
Up	**Down**
PCYT1B	IGF2BP1
ADCY9	LIN28B
EHD2	PABPC4L
SLCO4A1	IGFBP5
OTUD6B	HLA-DQA2
FUT10	COL4A2
TRIM35	CAMK2A
VWA5A	A2M
ZC3HC1	FN1
ZNF79	TFPI2
TMEM234	DPP10
C2orf42	DLL4
OSTM1	SEMA6A
ZNF607	IGFBP4
THAP7	IL2RB
MYO5C	PCDH1
HIGD1A	TGFBI
CD36	C19orf45
COA7	ARHGEF10L
CFAP20	GNAT1

Figure 6.20. 14.3% genes changed significantly after ZTG$_{opt}$ culture. a) Volcano plots of statistical significance against fold-change between cord blood CD34$^+$ HSPCs cultured in ZTG$_{opt}$ and fresh cord blood CD34$^+$ HSPCs demonstrating that 1704 out of 11912 genes are found to be significantly differentially expressed. There are 778 genes up-regulated (red) and 926 genes down regulated (green). More than 10000 genes (black) did not show significant change after ZTG$_{opt}$ culture. **b)** Top 20 up- or down-regulated genes.

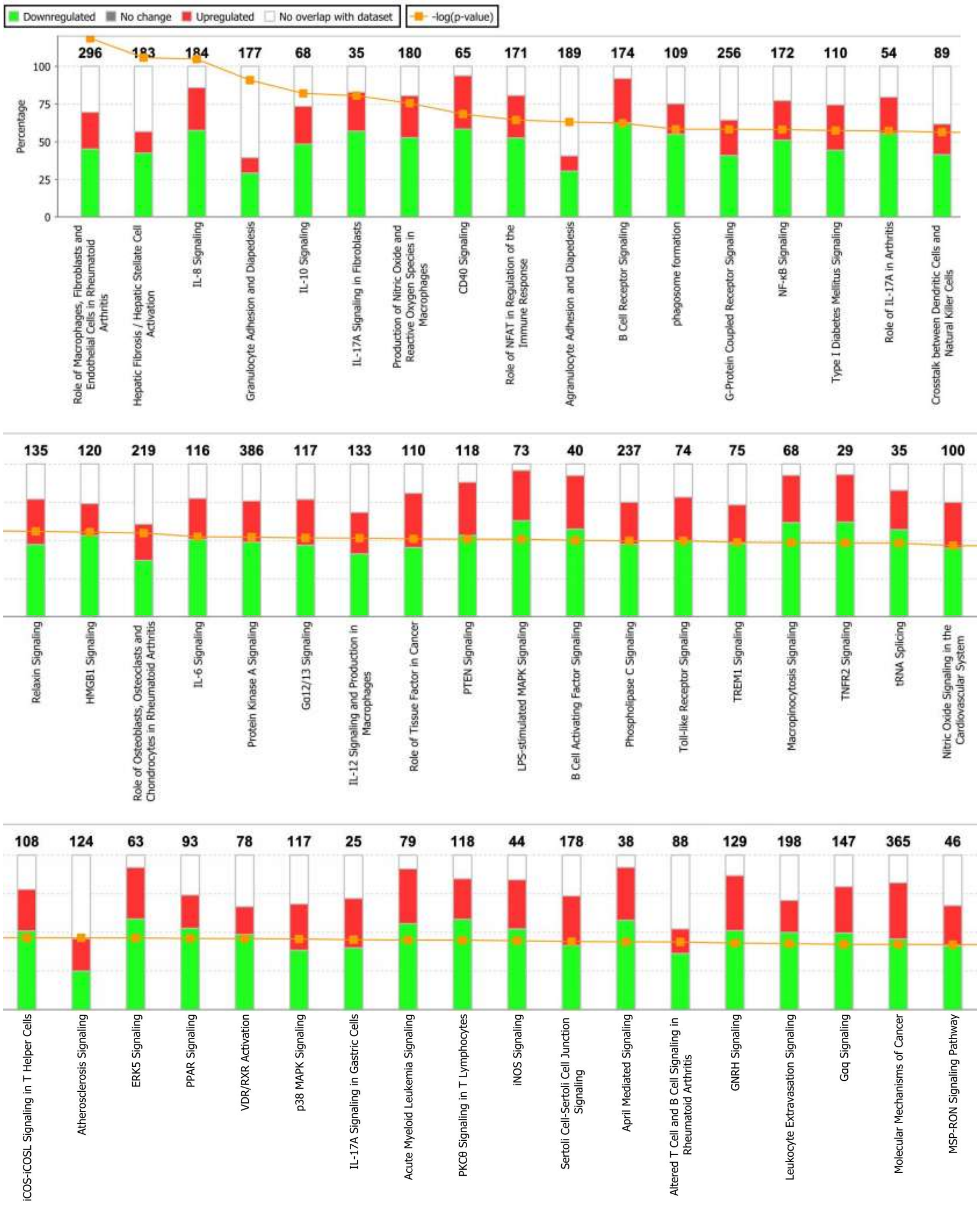
🟩 Downregulated
▨ No change
🟥 Upregulated
☐ No overlap with dataset
-log(p-value)
Percentage
100
75
50
25
0
296
183
184
177
68
35
180
65
171
189
174
109
256
172
110
54
89
Role of Macrophages, Fibroblasts and Endothelial Cells in Rheumatoid Arthritis
Hepatic Fibrosis / Hepatic Stellate Cell Activation
IL-8 Signaling
Granulocyte Adhesion and Diapedesis
IL-10 Signaling
IL-17A Signaling in Fibroblasts
Production of Nitric Oxide and Reactive Oxygen Species in Macrophages
CD40 Signaling
Role of NFAT in Regulation of the Immune Response
Agranulocyte Adhesion and Diapedesis
B Cell Receptor Signaling
phagosome formation
G-Protein Coupled Receptor Signaling
NF-κB Signaling
Type I Diabetes Mellitus Signaling
Role of IL-17A in Arthritis
Crosstalk between Dendritic Cells and Natural Killer Cells
135
120
219
116
386
117
133
110
118
73
40
237
74
75
68
29
35
100
Relaxin Signaling
HMGB1 Signaling
Role of Osteoblasts, Osteoclasts and Chondrocytes in Rheumatoid Arthritis
IL-6 Signaling
Protein Kinase A Signaling
Gα12/13 Signaling
IL-12 Signaling and Production in Macrophages
Role of Tissue Factor in Cancer
PTEN Signaling
LPS-stimulated MAPK Signaling
B Cell Activating Factor Signaling
Phospholipase C Signaling
Toll-like Receptor Signaling
TREM1 Signaling
Macropinocytosis Signaling
TNFR2 Signaling
tRNA Splicing
Nitric Oxide Signaling in the Cardiovascular System
108
124
63
93
78
117
25
79
118
44
178
38
88
129
198
147
365
46
iCOS-iCOSL Signaling in T Helper Cells
Atherosclerosis Signaling
ERK5 Signaling
PPAR Signaling
VDR/RXR Activation
p38 MAPK Signaling
IL-17A Signaling in Gastric Cells
Acute Myeloid Leukemia Signaling
PKCθ Signaling in T Lymphocytes
iNOS Signaling
Sertoli Cell-Sertoli Cell Junction Signaling
April Mediated Signaling
Altered T Cell and B Cell Signaling in Rheumatoid Arthritis
GNRH Signaling
Leukocyte Extravasation Signaling
Gαq Signaling
Molecular Mechanisms of Cancer
MSP-RON Signaling Pathway

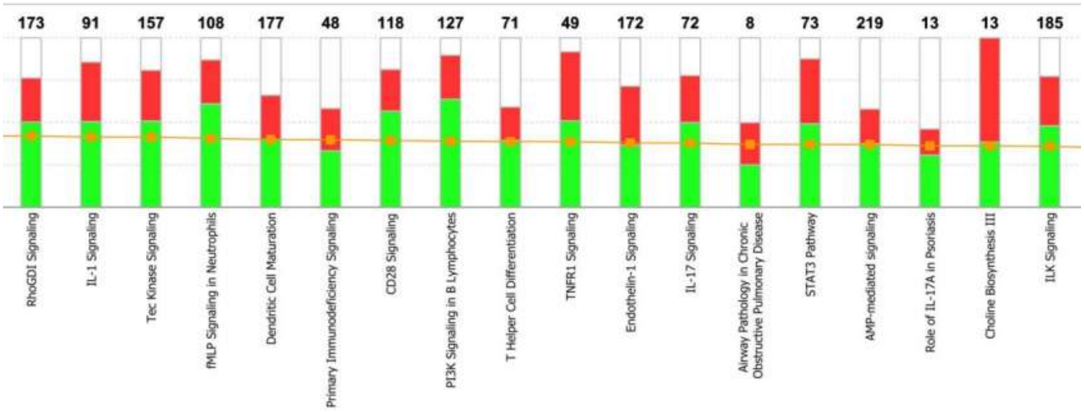
173
91
157
108
177
48
118
127
71
49
172
72
8
73
219
13
13
185
RhoGDI Signaling
IL-1 Signaling
Tec Kinase Signaling
fMLP Signaling in Neutrophils
Dendritic Cell Maturation
Primary Immunodeficiency Signaling
CD28 Signaling
PI3K Signaling in B Lymphocytes
T Helper Cell Differentiation
TNFR1 Signaling
Endothelin-1 Signaling
IL-17 Signaling
Airway Pathology in Chronic Obstructive Pulmonary Disease
STAT3 Pathway
AMP-mediated signaling
Role of IL-17A in Psoriasis
Choline Biosynthesis III
ILK Signaling

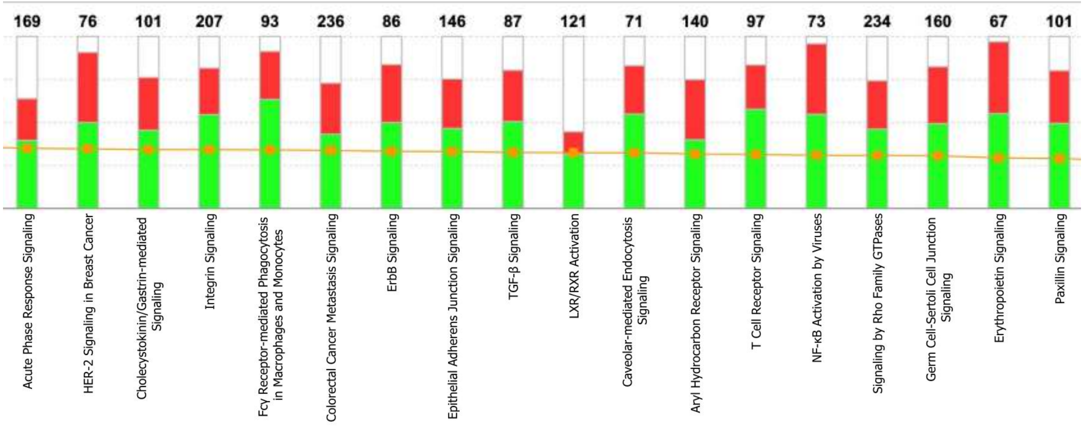
169
76
101
207
93
236
86
146
87
121
71
140
97
73
234
160
67
101
Acute Phase Response Signaling
HER-2 Signaling in Breast Cancer
Cholecystokinin/Gastrin-mediated Signaling
Integrin Signaling
Fcγ Receptor-mediated Phagocytosis in Macrophages and Monocytes
Colorectal Cancer Metastasis Signaling
ErbB Signaling
Epithelial Adherens Junction Signaling
TGF-β Signaling
LXR/RXR Activation
Caveolar-mediated Endocytosis Signaling
Aryl Hydrocarbon Receptor Signaling
T Cell Receptor Signaling
NF-κB Activation by Viruses
Signaling by Rho Family GTPases
Germ Cell-Sertoli Cell Junction Signaling
Erythropoietin Signaling
Paxillin Signaling

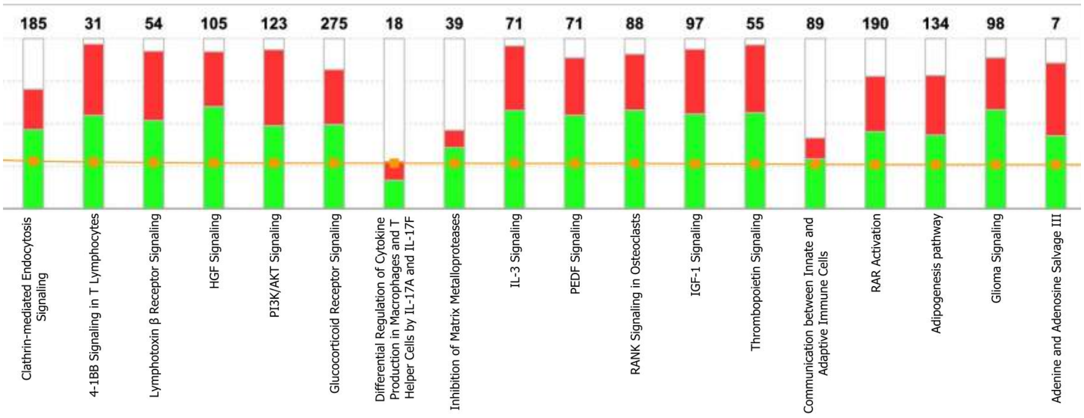
185
31
54
105
123
275
18
39
71
71
88
97
55
89
190
134
98
7
Clathrin-mediated Endocytosis Signaling
4-1BB Signaling in T Lymphocytes
Lymphotoxin β Receptor Signaling
HGF Signaling
PI3K/AKT Signaling
Glucocorticoid Receptor Signaling
Differential Regulation of Cytokine Production in Macrophages and T Helper Cells by IL-17A and IL-17F
Inhibition of Matrix Metalloproteases
IL-3 Signaling
PEDF Signaling
RANK Signaling in Osteoclasts
IGF-1 Signaling
Thrombopoietin Signaling
Communication between Innate and Adaptive Immune Cells
RAR Activation
Adipogenesis pathway
Glioma Signaling
Adenine and Adenosine Salvage III

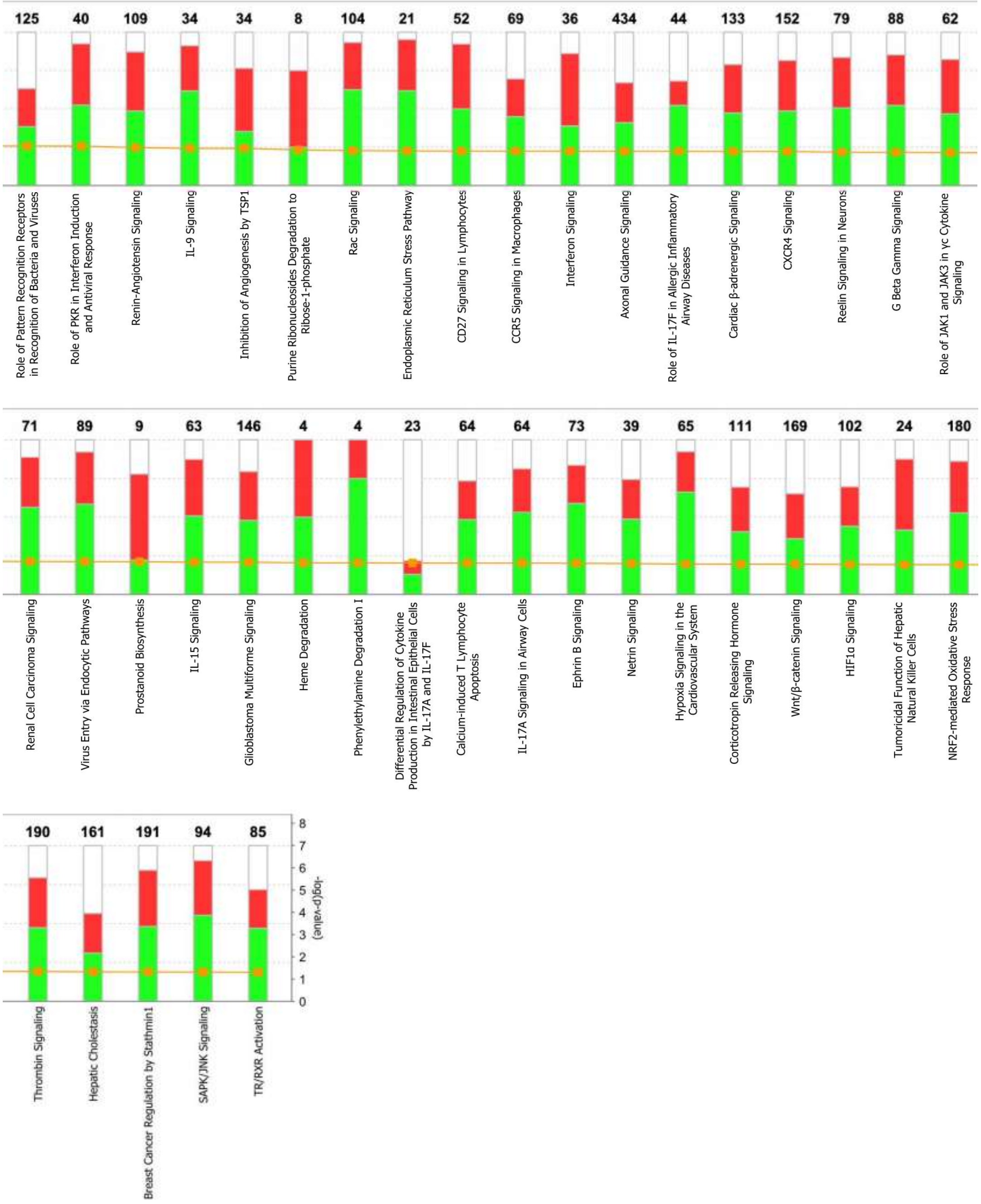

Figure 6.21. Effect of ZTG_{opt} culture on canonical pathways. Significantly changed canonical pathways in ZTG_{opt}-cultured cells compared to Fresh cells was analyzed by Ingenuity Pathway Analysis (IPA). The stacked bar chart displays the percentage of genes that were upregulated (red), downregulated (green), and genes not overlapping with our data set (white) in each canonical pathway. The numerical value at the top of each bar represents the total number of genes in the canonical pathway. The secondary y-axis (right) shows the −log of P-value calculated by the Benjamini-Hochberg (B-H) method; the B-H method was used to adjust the right-tailed Fisher's exact test P-value, which indicates the significance of each pathway.

Table 6.1 Molecular description of prepared star-shaped pCBAA polymers. Summary of functionalized polymer weight detected by NMR or GPC and conversion rate of each step.

	NMR	GPC		Conversion (%)
Name	M_n (kDa)	M_n(kDa)	M_w/M_n	
pCBAA-N_3	20.1	20.2	1.17	85%
pCBAA-NH_2	20.0	19.7	1.13	99%
pCBAA-$DIFO_3$	20.5	20.1	1.15	78%

Table 6.2 Limiting dilution analysis of NSG engraftment. a) Summary of primary NSG engraftment data from different time points. HSPCs from different conditions were injected into NSG mice at different doses. Human engraftment was examined at different time intervals. Human engraftment higher than 0.1% was considered as positive response. **b)** Poisson statistics were applied to the data in **a** and SRCs were calculated and presented in different scenarios. Progeny: CD34$^+$ starting cells (day 0 equivalent). Cell dose: Actual total cells infused.

a

Conditions	Number per mouse		Responses			%human engraftment (mean±SEM)		
	Progeny	Cell dose	4 W	12-14 W	24-30 W	4 W	12-14 W	24-30 W
Fresh	100	100	2/5	0/5	1/5	1.3±0.83	0.08±0.08	0.15±0.09
	300	300	6/10	2/10	3/10	0.62±0.51	0.09±0.05	0.1±0.05
	1000	1000	6/10	7/9	6/9	1.56±0.79	1.5±1.3	0.65±0.44
	3000	3000	7/8	6/6	6/6	1.2±0.52	5.4±3.9	10.2±6.5
	10000	10000	10/10	9/9	8/8	9.8±3.9	10.9±3.9	22.4±9.1
ZTG$_{opt}$	3	840	3/5	0/5	0/5	0.27±0.09	0.01±0.01	0.02±0.02
	10	2800	5/10	4/10	4/8	0.9±0.62	0.2±0.13	0.16±0.06
	30	8400	5/10	8/9	9/9	0.39±0.17	3.3±2.0	28±13.2
	100	28000	10/10	9/9	9/9	9.3±5.7	5.1±2.6	24.7±7.4
	300	84000	10/10	10/10	8/8	12.4±4.7	29.1±6.6	35.9±3.8
DXI$_{opt}$	100	57000	2/5	0/5	4/5	0.1±0.03	0.02±0.01	0.2±0.02
	300	171000	4/5	2/5	5/5	0.54±0.34	0.5±0.46	1.8±1.4
	1000	570000	5/5	5/5	5/5	0.76±0.28	1.4±0.66	5.5±2.8
Control	300	415000	3/4	0/5	1/5	0.11±0.02	0.02±0.01	0.09±0.05
	1000	1050000	4/5	1/5	3/4	0.04 ±0.02	0.08±0.05	0.16±0.05
	3000	4150000	4/5	4/5	4/5	0.15±0.07	6.4±5.6	0.82±0.51

b

Time	Conditions	SRC frequency per progeny cell	95% Confidence Interval	SRC per 10^6 CD34$^+$ starting cells	SRC frequency per injected cell	95% Confidence Interval
4 weeks	Fresh	1/808	1/466-1/1401	1136	1/808	1/466-1/1401
	ZTG$_{opt}$	1/22	1/13-1/38	83333	1/6160	1/3640-1/10640
	DXI$_{opt}$	1/186	1/83-1/415	16949	1/106000	1/47310-1/236600
	Control	1/853	1/387-1/1881	758	1/895700	1/406400-1/1975000
12-14 weeks	Fresh	1/833	1/465-1/1490	1136	1/833	1/465-1/1490
	ZTG$_{opt}$	1/17	1/10-1/31	83333	1/4760	1/2800-1/8680
	DXI$_{opt}$	1/480	1/210-1/1049	16949	1/273600	1/124800-1/597900
	Control	1/2782	1/1158-1/6684	758	1/2921100	1/1215900-1/7018200
24-30 weeks	Fresh	1/880	1/499-1/1553	1136	1/880	1/499-1/1553
	ZTG$_{opt}$	1/12	1/7-1/22	83333	1/3360	1/1960-1/6160
	DXI$_{opt}$	1/59	1/22-1/157	16949	1/33630	1/12540-1/89500
	Control	1/1320	1/593-1/2937	758	1/1386000	1/622700-1/3083900

Table 6.3. *In vivo* data analyzed at indicated time post-transplantation presented as heat-map

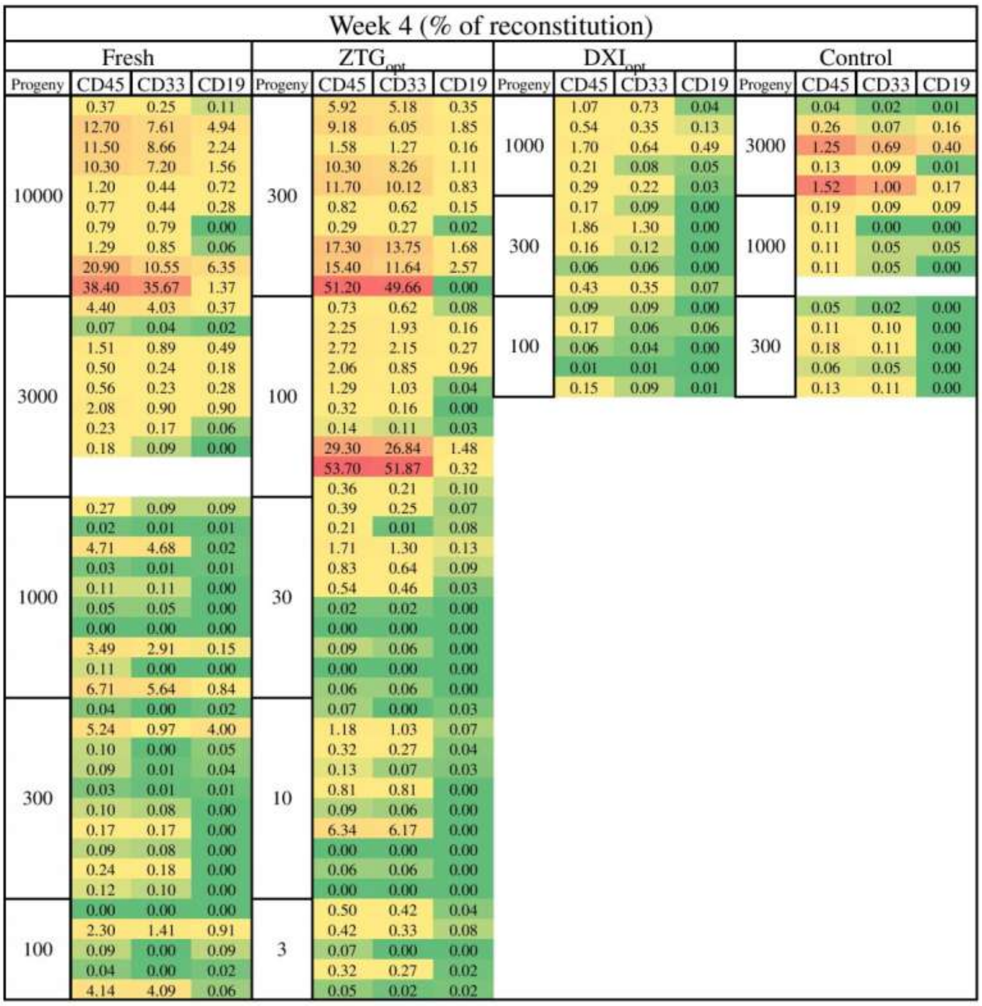

Week 4 (% of reconstitution)															
Fresh				ZTG$_{opt}$				DXI$_{opt}$				Control			
Progeny	CD45	CD33	CD19	Progeny	CD45	CD33	CD19	Progeny	CD45	CD33	CD19	Progeny	CD45	CD33	CD19
10000	0.37	0.25	0.11	300	5.92	5.18	0.35	1000	1.07	0.73	0.04	3000	0.04	0.02	0.01
	12.70	7.61	4.94		9.18	6.05	1.85		0.54	0.35	0.13		0.26	0.07	0.16
	11.50	8.66	2.24		1.58	1.27	0.16		1.70	0.64	0.49		1.25	0.69	0.40
	10.30	7.20	1.56		10.30	8.26	1.11		0.21	0.08	0.05		0.13	0.09	0.01
	1.20	0.44	0.72		11.70	10.12	0.83		0.29	0.22	0.03		1.52	1.00	0.17
	0.77	0.44	0.28		0.82	0.62	0.15	300	0.17	0.09	0.00	1000	0.19	0.09	0.09
	0.79	0.79	0.00		0.29	0.27	0.02		1.86	1.30	0.00		0.11	0.00	0.00
	1.29	0.85	0.06		17.30	13.75	1.68		0.16	0.12	0.00		0.11	0.05	0.05
	20.90	10.55	6.35		15.40	11.64	2.57		0.06	0.06	0.00		0.11	0.05	0.00
	38.40	35.67	1.37		51.20	49.66	0.00		0.43	0.35	0.07				
3000	4.40	4.03	0.37	100	0.73	0.62	0.08	100	0.09	0.09	0.00	300	0.05	0.02	0.00
	0.07	0.04	0.02		2.25	1.93	0.16		0.17	0.06	0.06		0.11	0.10	0.00
	1.51	0.89	0.49		2.72	2.15	0.27		0.06	0.04	0.00		0.18	0.11	0.00
	0.50	0.24	0.18		2.06	0.85	0.96		0.01	0.01	0.00		0.06	0.05	0.00
	0.56	0.23	0.28		1.29	1.03	0.04		0.15	0.09	0.01		0.13	0.11	0.00
	2.08	0.90	0.90		0.32	0.16	0.00								
	0.23	0.17	0.06		0.14	0.11	0.03								
	0.18	0.09	0.00		29.30	26.84	1.48								
					53.70	51.87	0.32								
					0.36	0.21	0.10								
1000	0.27	0.09	0.09	30	0.39	0.25	0.07								
	0.02	0.01	0.01		0.21	0.01	0.08								
	4.71	4.68	0.02		1.71	1.30	0.13								
	0.03	0.01	0.01		0.83	0.64	0.09								
	0.11	0.11	0.00		0.54	0.46	0.03								
	0.05	0.05	0.00		0.02	0.02	0.00								
	0.00	0.00	0.00		0.00	0.00	0.00								
	3.49	2.91	0.15		0.09	0.06	0.00								
	0.11	0.00	0.00		0.00	0.00	0.00								
	6.71	5.64	0.84		0.06	0.06	0.00								
300	0.04	0.00	0.02	10	0.07	0.00	0.03								
	5.24	0.97	4.00		1.18	1.03	0.07								
	0.10	0.00	0.05		0.32	0.27	0.04								
	0.09	0.01	0.04		0.13	0.07	0.03								
	0.03	0.01	0.01		0.81	0.81	0.00								
	0.10	0.08	0.00		0.09	0.06	0.00								
	0.17	0.17	0.00		6.34	6.17	0.00								
	0.09	0.08	0.00		0.00	0.00	0.00								
	0.24	0.18	0.00		0.06	0.06	0.00								
	0.12	0.10	0.00		0.00	0.00	0.00								
100	0.00	0.00	0.00	3	0.50	0.42	0.04								
	2.30	1.41	0.91		0.42	0.33	0.08								
	0.09	0.00	0.09		0.07	0.00	0.00								
	0.04	0.00	0.02		0.32	0.27	0.02								
	4.14	4.09	0.06		0.05	0.02	0.02								

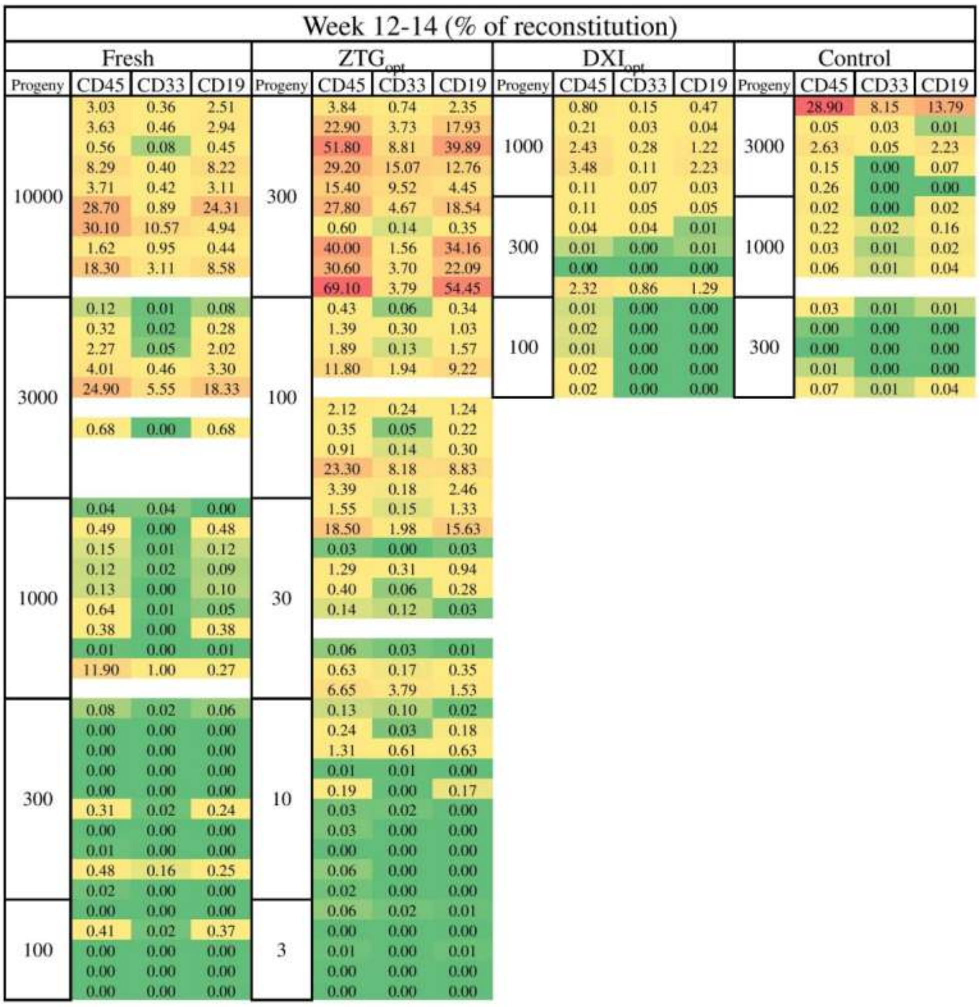

Week 12-14 (% of reconstitution)															
Fresh				ZTG$_{opt}$				DXI$_{opt}$				Control			
Progeny	CD45	CD33	CD19	Progeny	CD45	CD33	CD19	Progeny	CD45	CD33	CD19	Progeny	CD45	CD33	CD19
10000	3.03	0.36	2.51	300	3.84	0.74	2.35	1000	0.80	0.15	0.47	3000	28.90	8.15	13.79
	3.63	0.46	2.94		22.90	3.73	17.93		0.21	0.03	0.04		0.05	0.03	0.01
	0.56	0.08	0.45		51.80	8.81	39.89		2.43	0.28	1.22		2.63	0.05	2.23
	8.29	0.40	8.22		29.20	15.07	12.76		3.48	0.11	2.23		0.15	0.00	0.07
	3.71	0.42	3.11		15.40	9.52	4.45		0.11	0.07	0.03		0.26	0.00	0.00
	28.70	0.89	24.31		27.80	4.67	18.54	300	0.11	0.05	0.05	1000	0.02	0.00	0.02
	30.10	10.57	4.94		0.60	0.14	0.35		0.04	0.04	0.01		0.22	0.02	0.16
	1.62	0.95	0.44		40.00	1.56	34.16		0.01	0.00	0.01		0.03	0.01	0.02
	18.30	3.11	8.58		30.60	3.70	22.09		0.00	0.00	0.00		0.06	0.01	0.04
					69.10	3.79	54.45		2.32	0.86	1.29				
3000	0.12	0.01	0.08	100	0.43	0.06	0.34	100	0.01	0.00	0.00	300	0.03	0.01	0.01
	0.32	0.02	0.28		1.39	0.30	1.03		0.02	0.00	0.00		0.00	0.00	0.00
	2.27	0.05	2.02		1.89	0.13	1.57		0.01	0.00	0.00		0.00	0.00	0.00
	4.01	0.46	3.30		11.80	1.94	9.22		0.02	0.00	0.00		0.01	0.00	0.00
	24.90	5.55	18.33						0.02	0.00	0.00		0.07	0.01	0.04
					2.12	0.24	1.24								
	0.68	0.00	0.68		0.35	0.05	0.22								
					0.91	0.14	0.30								
					23.30	8.18	8.83								
					3.39	0.18	2.46								
1000	0.04	0.04	0.00	30	1.55	0.15	1.33								
	0.49	0.00	0.48		18.50	1.98	15.63								
	0.15	0.01	0.12		0.03	0.00	0.03								
	0.12	0.02	0.09		1.29	0.31	0.94								
	0.13	0.00	0.10		0.40	0.06	0.28								
	0.64	0.01	0.05		0.14	0.12	0.03								
	0.38	0.00	0.38												
	0.01	0.00	0.01		0.06	0.03	0.01								
	11.90	1.00	0.27		0.63	0.17	0.35								
					6.65	3.79	1.53								
300	0.08	0.02	0.06	10	0.13	0.10	0.02								
	0.00	0.00	0.00		0.24	0.03	0.18								
	0.00	0.00	0.00		1.31	0.61	0.63								
	0.00	0.00	0.00		0.01	0.01	0.00								
	0.00	0.00	0.00		0.19	0.00	0.17								
	0.31	0.02	0.24		0.03	0.02	0.00								
	0.00	0.00	0.00		0.03	0.00	0.00								
	0.01	0.00	0.00		0.00	0.00	0.00								
	0.48	0.16	0.25		0.06	0.00	0.00								
	0.02	0.00	0.00		0.02	0.00	0.00								
100	0.00	0.00	0.00	3	0.06	0.02	0.01								
	0.41	0.02	0.37		0.00	0.00	0.00								
	0.00	0.00	0.00		0.01	0.00	0.01								
	0.00	0.00	0.00		0.00	0.00	0.00								
	0.00	0.00	0.00		0.00	0.00	0.00								

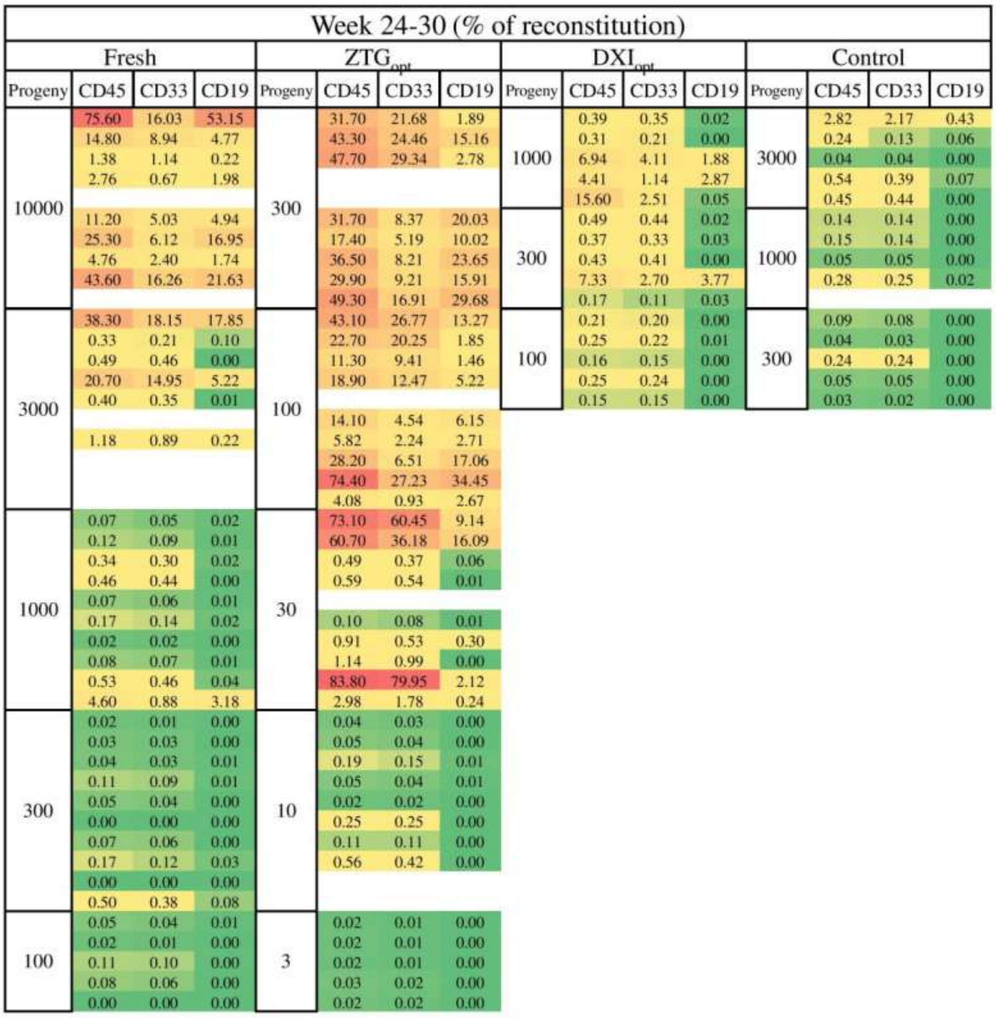

Week 24-30 (% of reconstitution)															
Fresh				ZTG_{opt}				DXI_{opt}				Control			
Progeny	CD45	CD33	CD19	Progeny	CD45	CD33	CD19	Progeny	CD45	CD33	CD19	Progeny	CD45	CD33	CD19
10000	75.60	16.03	53.15	300	31.70	21.68	1.89	1000	0.39	0.35	0.02	3000	2.82	2.17	0.43
	14.80	8.94	4.77		43.30	24.46	15.16		0.31	0.21	0.00		0.24	0.13	0.06
	1.38	1.14	0.22		47.70	29.34	2.78		6.94	4.11	1.88		0.04	0.04	0.00
	2.76	0.67	1.98						4.41	1.14	2.87		0.54	0.39	0.07
									15.60	2.51	0.05		0.45	0.44	0.00
	11.20	5.03	4.94		31.70	8.37	20.03	300	0.49	0.44	0.02	1000	0.14	0.14	0.00
	25.30	6.12	16.95		17.40	5.19	10.02		0.37	0.33	0.03		0.15	0.14	0.00
	4.76	2.40	1.74		36.50	8.21	23.65		0.43	0.41	0.00		0.05	0.05	0.00
	43.60	16.26	21.63		29.90	9.21	15.91		7.33	2.70	3.77		0.28	0.25	0.02
					49.30	16.91	29.68		0.17	0.11	0.03				
3000	38.30	18.15	17.85	100	43.10	26.77	13.27	100	0.21	0.20	0.00	300	0.09	0.08	0.00
	0.33	0.21	0.10		22.70	20.25	1.85		0.25	0.22	0.01		0.04	0.03	0.00
	0.49	0.46	0.00		11.30	9.41	1.46		0.16	0.15	0.00		0.24	0.24	0.00
	20.70	14.95	5.22		18.90	12.47	5.22		0.25	0.24	0.00		0.05	0.05	0.00
	0.40	0.35	0.01						0.15	0.15	0.00		0.03	0.02	0.00
					14.10	4.54	6.15								
	1.18	0.89	0.22		5.82	2.24	2.71								
					28.20	6.51	17.06								
					74.40	27.23	34.45								
					4.08	0.93	2.67								
1000	0.07	0.05	0.02	30	73.10	60.45	9.14								
	0.12	0.09	0.01		60.70	36.18	16.09								
	0.34	0.30	0.02		0.49	0.37	0.06								
	0.46	0.44	0.00		0.59	0.54	0.01								
	0.07	0.06	0.01												
	0.17	0.14	0.02		0.10	0.08	0.01								
	0.02	0.02	0.00		0.91	0.53	0.30								
	0.08	0.07	0.01		1.14	0.99	0.00								
	0.53	0.46	0.04		83.80	79.95	2.12								
	4.60	0.88	3.18		2.98	1.78	0.24								
300	0.02	0.01	0.00	10	0.04	0.03	0.00								
	0.03	0.03	0.00		0.05	0.04	0.00								
	0.04	0.03	0.01		0.19	0.15	0.01								
	0.11	0.09	0.01		0.05	0.04	0.01								
	0.05	0.04	0.00		0.02	0.02	0.00								
	0.00	0.00	0.00		0.25	0.25	0.00								
	0.07	0.06	0.00		0.11	0.11	0.00								
	0.17	0.12	0.03		0.56	0.42	0.00								
	0.00	0.00	0.00												
	0.50	0.38	0.08												
100	0.05	0.04	0.01	3	0.02	0.01	0.00								
	0.02	0.01	0.00		0.02	0.01	0.00								
	0.11	0.10	0.00		0.02	0.01	0.00								
	0.08	0.06	0.00		0.03	0.02	0.00								
	0.00	0.00	0.00		0.02	0.02	0.00								

Table 6.4 Summary of secondary NSG engraftment plan and data.

Conditions	Human $CD45^+$Cell Dose	Human $CD34^+38^-$ Cell Dose	Secondary Transplant Responses
Fresh	$5x10^6$	$3.74x10^4$	2/2
	$1.5x10^6$	$1.12x10^4$	2/2
ZTG_{opt}	$7.5x10^6$	$3.98x10^4$	3/3
	$2.5x10^6$	$1.33x10^4$	3/4
	$7.5x10^5$	$3.98x10^3$	1/4
	$2.5x10^5$	$1.33x10^3$	0/4

Chapter 7 Conclusions

This thesis explores and investigates the unique properties of zwitterionic hydrogels for biomedical application. The strategy and design of zwitterionic hydrogels for specific applications are described.

The first part of the thesis (Chapter 2) discusses the self-healing properties of zwitterionic hydrogels. The biomedical applications of current self-healing materials are largely impeded by their healing conditions, which usually require heating, UV exposure or harsh pH environments. At the same time, for very few existing spontaneously self-healing materials, healing can only be achieved immediately after rupture occurs. In this chapter, we provided a spontaneously healing material, driven by a new mechanism, "zwitterionic fusion", which is repairable independent of time after damage under physiological conditions. We also tested the anti-fatigue property of this zwitterionic hydrogel. Furthermore, we utilized this zwitterionic fusion to link different cell-hydrogel constructs together.

The second part of the thesis (Chapters 3 and 4) explores the strategy to employ zwitterionic hydrogel as a platform to control the self-renewal and differentiation of mesenchymal stem cells. In Chapter 3, we demonstrate for the first time that nonfouling hydrogels composed of pure poly(carboxybetaine) (PCB) allow hMSCs to retain their stem cell phenotype and multipotency, independent of differentiation-promoting media, cytoskeletal manipulation agents, and the stiffness of the hydrogel matrix. Moreover, encapsulated hMSCs can be specifically induced to differentiate down osteogenic or adipogenic pathways by controlling the content of fouling moieties in the PCB hydrogel. This work examines the critical role of nonspecific interactions in stem cell differentiation and highlights the importance of materials chemistry in maintaining stem cell multipotency and controlling differentiation.

In Chapter 4, we provide a photodynamic zwitterionic hydrogel capable of reversibly triggering and suspending the differentiation process via manipulating nonspecific interactions between cultured stem cells and the hydrogel. The state of differentiated stem cells can be altered when the hydrogel is exposed to a selected light program, while the differentiation can be immediately suspended when the hydrogel is converted into a pure zwitterionic form by light. Unlike other existing studies controlling the fate of stem cells via specific interactions, this work provides a completely different approach, allowing reversible, real-time and site-specific manipulation of the fate choice of stem cells via nonspecific interactions.

The third part of the thesis (Chapters 5 and 6) explores the strategy to employ biodegradable zwitterionic hydrogels as a platform to expand mesenchymal stem cells and haematopoietic stem cells. In Chapter 5, we have developed a hydrogel-based cell expansion platform with star-shaped poly(carboxybetaine), a biocompatible zwitterionic material that presents no nonspecific interactions to cells. Star-shaped poly(carboxybetaine) is end-functionalized with complementary thiol or disulfide pyridine groups, which react without radical initiation under physiological conditions via a biocompatible disulfide exchange reaction and form a hydrogel. Zwitterionic star polymers with a molecular weight greater than about 50 kDa were nontoxic to all four cell lines tested, including human mesenchymal stem cells, and all cell lines expanded 25-30 fold over two weeks of culture without losing bioactivity.

Cord blood-derived hematopoietic stem cells (HSCs) are known to vigorously and spontaneously differentiate when expanded *ex vivo*, impeding their clinical utility. In Chapter 6, by using a 3D culture platform based on a zwitterionic hydrogel devoid of nonspecific cell-matrix interactions, we achieved 322-fold expansion of HSCs without prompting differentiation. The expanded cells obtained through this strategy are able to reconstitute human hematopoiesis in NSG mice for at least 24 weeks. Notably, cells encapsulated within zwitterionic hydrogels became more quiescent and primitive. Eliminating nonspecific cell-background interactions by culturing cells in a zwitterionic matrix can provide differentiation-free HSC expansion and should facilitate clinical HSC therapy.

Based on the unique properties of zwitterionic hydrogels in restraining nonspecific differentiation of stem cells, it is possible to expand their usage in other cell types such as T cells, islets, platelets, cardiovacular cells and other applications such as gene therapy.

Tao Bai

University of Washington, Department of Chemical Engineering, Seattle, WA, 98195
Taobai@u.washington.edu, Phone: (206) 495-2068

EDUCATION

Ph.D. (Chemical Engineering) 2011-2017
University of Washington, Seattle, WA, USA (Supervisor: Shaoyi Jiang)
B.Sc. (Materials Science and Engineering) 2007-2011
Tianjin University, Tianjin, China (Supervisor: Wenguang Liu)

RESEARCH EXPERIENCE

1) Development and Applications of Zwitterionic Hydrogel

- Differentiation-free expansion of hematopoietic stem cell (HSC), mesenchymal stem cell (MSC) and regulatory T cell (Treg) in zwitterionic hydrogels
- Directed differentiation of MSCs in functionalized zwitterionic hydrogels
- Zwitterionic hydrogels resistant to the immunogenicity and fibrous encapsulation in mice
- Time-independent self-healing zwitterionic hydrogels
- Long-life zwitterionic material-coated biosensors in whole blood

2) Development of Long-circulating Zwitterionic Nanomaterials

- Long-circulating and therapeutic protein-encapsulated zwitterionic nanogels
- Immunogenicity-free zwitterionic nanoparticles

3) Development and Applications of High-strength Hydrogels

- Construction of ultra-high strength hydrogels
- High-strength hydrogel-based gene transfection platform
- Develop shape-memory effect for high-strength hydrogel
- Directed differentiation of MSCs on a shape-memory hydrogel

SKILLS

- **Biological Skills:** Murine injection, Blood sampling and biodistribution, Cell culture, Cell encapsulation, Cell transfection, Cell differentiation, Multicolor flow cytometry, PCR, Immunohistochemistry (IHC), Histological staining, Immunological assays.
- **Polymer and Small Molecules Synthesis Skills:** Synthesis, purification and characterization of linear, branched, blocked and 3D crosslinked polymers, Multi-step synthesis, isolation and characterization of small molecules, Polymer functionalization, Bioconjugations.
- **Analytical Instruments:** Spectroscopy (NMR, FTIR, UV-VIS, Raman etc.), Chromatography (GC, HPLC, GPC), Thermal Analysis (DSC, TGA, etc.), Mechanical Testing (Tensile, compression, cyclic, etc.), Microscopy (FESEM, TEM), XPS, XRD
- **Others:** Proficiency in experimental design and proposal/grant writing.

AWARDS

2015 National Award for Outstanding Chinese Students Study Abroad
2016 High Impact Publication Award, Chemical Engineering, University of Washington

JOURNAL PUBLICATIONS (Total: 30, Citations: 900+, H-index: 16)

1. **Tao Bai**, Jianqiang Li, Suzan Imren, Andrew Sinclair, Fabiola Merriam, Fang Sun, Cynthia Nourigat, Priyesh Jain, Jeffrey J. Delrow, Ryan S. Basom, Hsiang-Chieh Hung, Peng Zhang, Shelly Heimfeld, Shaoyi Jiang, Colleen Delaney, 'Culture in Zwitterionic Hydrogels Promotes Expansion of Human Hematopoietic Stem Cells ', ***Nature***, In Revision.

2. **Tao Bai**, Fang Sun, Lei Zhang, Andrew Sinclair, Sijun Liu, Jean-Rene Ella-Menye, Ying Zheng, and Shaoyi Jiang, 'Restraint of the Differentiation of Mesenchymal Stem Cells by a Nonfouling Zwitterionic Hydrogel', ***Angewandte Chemie International Edition***, 126 (2014), 12943-48.

3. Lei Zhang, Zhiqiang Cao, **Tao Bai**, Louisa Carr, Jean-Rene Ella-Menye, Colleen Irvin, Buddy D Ratner, and Shaoyi Jiang, 'Zwitterionic Hydrogels Implanted in Mice Resist the Foreign-Body Reaction', ***Nature Biotechnology***, 31 (2013), 553-56.

4. **Tao Bai**, Andrew Sinclair, Fang Sun, Priyesh Jain, Hsiang-Chieh Hung, Peng Zhang, Jean-Rene Ella-Menye, Wenguang Liu, and Shaoyi Jiang, 'Harnessing Isomerization-Mediated Manipulation of Nonspecific Cell/Matrix Interactions to Reversibly Trigger and Suspend Stem Cell Differentiation', ***Chemical Science***, 7 (2016), 333-38.

5. **Tao Bai**, Sijun Liu, Fang Sun, Andrew Sinclair, Lei Zhang, Qing Shao, and Shaoyi Jiang, 'Zwitterionic Fusion in Hydrogels and Spontaneous and Time-Independent Self-Healing under Physiological Conditions', ***Biomaterials***, 35 (2014), 3926-33.

6. **Tao Bai**, Yanjiao Han, Peng Zhang, Wei Wang, and Wenguang Liu, 'Zinc Ion-Triggered Two-Way Macro-/Microscopic Shape Changing and Memory Effects in High Strength Hydrogels with Pre-Programmed Unilateral Patterned Surfaces', ***Soft Matter***, 8 (2012), 6846-52.

7. **Tao Bai**, Peng Zhang, Yanjiao Han, Yuan Liu, Wenguang Liu, Xiaoli Zhao, and William Lu, 'Construction of an Ultrahigh Strength Hydrogel with Excellent Fatigue Resistance Based on Strong Dipole–Dipole Interaction', ***Soft Matter***, 7 (2011), 2825-31.

8. Yanjiao Han, **Tao Bai (Co-first Author)**, and Wenguang Liu, 'Controlled Heterogeneous Stem Cell Differentiation on a Shape Memory Hydrogel Surface', ***Scientific Reports***, (2014), 4.

9. Yanjiao Han, **Tao Bai (Co-first Author)**, Yuan Liu, Xinyun Zhai, and Wenguang Liu, 'Zinc Ion Uniquely Induced Triple Shape Memory Effect of Dipole–Dipole Reinforced Ultra-High Strength Hydrogels', ***Macromolecular Rapid Communications***, 33 (2012), 225-31.

10. Bing Xu, **Tao Bai (Co-first Author)**, Andrew Sinclair, Wei Wang, Qian Wu, Fei Gao, Huizhen Jia, Shaoyi Jiang, Wenguang Liu, 'Directed neural stem cell differentiation on polyaniline-coated high strength hydrogels', ***Materials Today Chemistry***, 1 (2016), 15-22.

11. Fang Sun, Hsiang-Chieh Hung, Andrew Sinclair, Peng Zhang, **Tao Bai**, Daniel David Galvan, Priyesh Jain, Bowen Li, Shaoyi Jiang, Qiuming Yu, 'Hierarchical zwitterionic modification of a SERS substrate enables real-time drug monitoring in blood plasma', ***Nature Communications***, 7 (2016), 13437.

12. Xiyang Dai, Yinyu Zhang, Lina Gao, **Tao Bai**, Wei Wang, Yuanlu Cui, and Wenguang Liu, 'A Mechanically Strong, Highly Stable, Thermoplastic, and Self-Healable Supramolecular Polymer Hydrogel', ***Advanced Materials***, 23 (2015), 3566-3571.

13. Peng Zhang, Fang Sun, Caroline Tsao, Sijun Liu, Priyesh Jain, Andrew Sinclair, Hsiang-Chieh Hung, **Tao Bai**, Kan Wu, and Shaoyi Jiang, 'Zwitterionic Gel Encapsulation Promotes Protein Stability, Enhances Pharmacokinetics, and Reduces Immunogenicity', ***Proceedings of the National Academy of Sciences*** (2015), 201512465.

14. Wei Yang, **Tao Bai**, Louisa R Carr, Andrew J Keefe, Jiajie Xu, Hong Xue, Colleen A Irvin, Shengfu Chen, Joseph Wang, and Shaoyi Jiang, 'The Effect of Lightly Crosslinked Poly (Carboxybetaine) Hydrogel Coating on the Performance of Sensors in Whole Blood', ***Biomaterials***, 33 (2012), 7945-51.

15. Andrew Sinclair, **Tao Bai**, Louisa R Carr, Jean-Rene Ella-Menye, Lei Zhang, and Shaoyi Jiang, 'Engineering Buffering and Hydrolytic or Photolabile Charge Shifting in a Polycarboxybetaine Ester Gene Delivery Platform', ***Biomacromolecules***, 14 (2013), 1587-93.

16. Fang Sun, **Tao Bai**, Lei Zhang, Jean-Rene Ella-Menye, Sijun Liu, Ann K Nowinski, Shaoyi Jiang, and Qiuming Yu, 'Sensitive and Fast Detection of Fructose in Complex Media Via Symmetry Breaking and Signal Amplification Using Surface-Enhanced Raman Spectroscopy', ***Analytical Chemistry***, 86 (2014), 2387-94.

17. Ya Zhao, **Tao Bai**, Qing Shao, Shaoyi Jiang, and Amy Q Shen, 'Thermoresponsive Self-Assembled Nipam-Zwitterion Copolymers', ***Polymer Chemistry***, 6 (2015), 1066-77.

18. Fang Sun, Peng Zhang, **Tao Bai**, Daniel David Galvan, Hsiang-Chieh Hung, Nan Zhou, Shaoyi Jiang, and Qiuming Yu, 'Functionalized Plasmonic Nanostructure Arrays for Direct and Accurate Mapping Extracellular Ph of Living Cells in Complex Media Using Sers', ***Biosensors and Bioelectronics***, 73 (2015), 202-07.

19. Lei Tang, Yang Yang, **Tao Bai**, and Wenguang Liu, 'Robust MeO$_2$Ma/Vinyl-4, 6-Diamino-1, 3, 5-Triazine Copolymer Hydrogels-Mediated Reverse Gene Transfection and Thermo-Induced Cell Detachment', ***Biomaterials***, 32 (2011), 1943-49.

20. Ying-Nien Chou, Fang Sun, Hsiang-Chieh Hung, Priyesh Jain, Andrew Sinclair, Peng Zhang, **Tao Bai**, Yung Chang, Ten-Chin Wen, and Qiuming Yu, 'Ultra-Low Fouling and

High Antibody Loading Zwitterionic Hydrogel Coatings for Sensing and Detection in Complex Media', ***Acta Biomaterialia***, 40 (2016), 31-37.

21. Yongmao Li, Bing Xu, **Tao Bai**, and Wenguang Liu, 'Co-Delivery of Doxorubicin and Tumor-Suppressing P53 Gene Using a Poss-Based Star-Shaped Polymer for Cancer Therapy', ***Biomaterials***, 55 (2015), 12-23.

22. Qing Shao, Luo Mi, Xia Han, **Tao Bai**, Sijun Liu, Yuting Li, and Shaoyi Jiang, 'Differences in Cationic and Anionic Charge Densities Dictate Zwitterionic Associations and Stimuli Responses', ***The Journal of Physical Chemistry B***, 118 (2014), 6956-62.

23. Fang Sun, Jean-Rene Ella-Menye, Daniel David Galvan, **Tao Bai**, Hsiang-Chieh Hung, Ying-Nien Chou, Peng Zhang, Shaoyi Jiang, and Qiuming Yu, 'Stealth Surface Modification of Surface-Enhanced Raman Scattering Substrates for Sensitive and Accurate Detection in Protein Solutions', ***ACS Nano***, 9 (2015), 2668-76.

24. Ning Wang, Yanjiao Han, Yuan Liu, **Tao Bai**, Han Gao, Peng Zhang, Wei Wang, and Wenguang Liu, 'High-Strength Hydrogel as a Reusable Adsorbent of Copper Ions', ***Journal of Hazardous Materials***, 213 (2012), 258-64.

25. Yuping Wei, Hsiang-Chieh Hung, Fang Sun, **Tao Bai**, Peng Zhang, Ann Kate Nowinski, and Shaoyi Jiang, 'Achieving Low-Fouling Surfaces with Oppositely Charged Polysaccharides Via Lbl Assembly', ***Acta Biomaterialia***, 40 (2016), 16-22.

26. Wei Yang, Jean-Rene Ella-Menye, Sijun Liu, **Tao Bai**, Daqian Wang, Qiuming Yu, Yuting Li, and Shaoyi Jiang, 'Cross-Linked Carboxybetaine Sams Enable Nanoparticles with Remarkable Stability in Complex Media', ***Langmuir***, 30 (2014), 2522-29.

27. Wei Yang, Sijun Liu, **Tao Bai**, Andrew J Keefe, Lei Zhang, Jean-Rene Ella-Menye, Yuting Li, and Shaoyi Jiang, 'Poly (Carboxybetaine) Nanomaterials Enable Long Circulation and Prevent Polymer-Specific Antibody Production', ***Nano Today***, 9 (2014), 10-16.

28. Xinyun Zhai, Peng Zhang, Changjun Liu, **Tao Bai**, Wenchen Li, Liming Dai, and Wenguang Liu, 'Highly Luminescent Carbon Nanodots by Microwave-Assisted Pyrolysis', ***Chemical Communications***, 48 (2012), 7955-57.

29. Lei Zhang, Zhiqiang Cao, Yuting Li, Jean-Rene Ella-Menye, **Tao Bai**, and Shaoyi Jiang, 'Softer Zwitterionic Nanogels for Longer Circulation and Lower Splenic Accumulation', ***ACS Nano***, 6 (2012), 6681-86.

30. Peng Zhang, Priyesh Jain, Caroline Tsao, Andrew Sinclair, Fang Sun, Hsiang-Chieh Hung, **Tao Bai**, Kan Wu, and Shaoyi Jiang, 'Butyrylcholinesterase Nanocapsule as a Long Circulating Bioscavenger with Reduced Immune Response', ***Journal of Controlled Release***, 230 (2016), 73-78.

PATENT

Shaoyi Jiang, **Tao Bai**, Harihara Subramanian, Andrew William Sinclair, Jene-rene Ella-Menye, Priyesh Jain, Functionalized zwitterionic and mixed charge polymers, related hydrogels, and methods for their use, WO 2016040489 A1.

CONFERENCE PROCEEDINGS AND PRESENTATIONS

Tao Bai and Shaoyi Jiang, Restraint of the Differentiation of Mesenchymal Stem Cells By a Nonfouling Zwitterionic Hydrogel. 2015 Annual Meeting

Tao Bai and Shaoyi Jiang, Zwitterionic Fusion in Hydrogels and Spontaneous and Time-Independent Self-Healing Under Physiological Conditions. 2014 Annual Meeting

Tao Bai, Lei Zhang and Shaoyi Jiang. Construction of an Integrated Zwitterionic Device of Continuous Blood Glucose Monitoring, Real Time Self-Regulated Insulin-Releasing and Non-Fouling Capabilities. 2012 Annual Meeting

Tao Bai, Lei Zhang and Shaoyi Jiang Construction of Zero-Order Release Nanoparticle with Non-Fouling Surface. 2012 Annual Meeting

Lei Zhang, Hongyan Ma, James D. Bryers and **Tao Bai** A Biodegradable Scaffold That Inhibits Nosocomial Infections While Promoting Healing. 2013 Annual Meeting

Lei Zhang, **Tao Bai** and Shaoyi Jiang Inhibition of Foreign Body Capsule Formation By Implanted Zwitterionic Hydrogels. 2013 Annual Meeting

Andrew Sinclair, **Tao Bai**, Lei Zhang, Shaoyi Jiang and Ann Nowinski Polycarboxybetaine Esters for Gene Delivery: Molecular Tuning, Controlled Degradation and Vaccine Applications. 2013 Annual Meeting